Ph.D. DISSERTATION

Applicability of No-insulation High-temperature Superconductor Saddle-shaped Dipole Magnet to Particle Accelerator

무절연 고온초전도 안장형 이극 자석의 입자 가속기 적용성 연구

BY

Geonyoung Kim

FEBRUARY 2025

DEPARTMENT OF ELECTRICAL AND COMPUTER ENGINEERING
COLLEGE OF ENGINEERING
SEOUL NATIONAL UNIVERSITY

Ph.D. DISSERTATION

Applicability of No-insulation High-temperature Superconductor Saddle-shaped Dipole Magnet to Particle Accelerator

무절연 고온초전도 안장형 이극 자석의
입자 가속기 적용성 연구

BY

Geonyoung Kim
FEBRUARY 2025

DEPARTMENT OF ELECTRICAL AND COMPUTER ENGINEERING
COLLEGE OF ENGINEERING
SEOUL NATIONAL UNIVERSITY

Applicability of No-insulation High-temperature Superconductor Saddle-shaped Dipole Magnet to Particle Accelerator

무절연 고온초전도 안장형 이극 자석의
입자 가속기 적용성 연구

지도교수 한 승 용
이 논문을 공학박사 학위논문으로 제출함

2025년 2월

서울대학교 대학원

전기정보공학부

김 건 영

김건영의 공학박사 학위 논문을 인준함

2025년 2월

위 원 장:	최 성 휘	
부위원장:	한 승 용	
위 원:	이 상 진	
위 원:	최 세 용	
위 원:	한 가 람	

Abstract

Particle accelerators are intricately connected to our lives, from applications in cancer treatment to advancing cutting-edge scientific research such as particle physics. Countries worldwide are actively developing technologies to enhance the performance of existing accelerators or to create new facilities. A representative example is CERN's Large Hadron Collider (LHC) in Europe, which successfully detected the Higgs boson, the particle mediating mass, and is currently developing the High-Luminosity LHC to explore the mysteries of modern physics, including the Standard Model. Particle beams manipulated by accelerators include electrons, protons, and heavy ions, which require precise control of their position and velocity for specific operational conditions. A key mechanism for controlling charged particles is the Lorentz force exerted by magnetic fields, making high-field magnets essential for particle accelerators. Low-field regions around 1 T primarily use copper-based conventional magnets, while higher magnetic field regions rely on NbTi low-temperature superconductor (LTS) magnets. Recently, the focus has shifted towards the development of Nb_3Sn LTS magnets. In addition, efforts to enhance accelerator performance have led to attempts to apply high-temperature superconducting (HTS) magnets by increasing magnetic field strength. However, these efforts are still in the early stages and require further research.

Efforts to develop dipole magnets for accelerators using HTS materials, such as REBCO conductors, have been previously undertaken. However, no successful attempt has been made to develop dipole magnets utilizing no-insulation (NI) technology. Challenges such as the complex geometry of dipole magnets and the instability in magnetic field uniformity caused by the current bypassing characteristic of NI magnets have made the adoption of NI technology challenging. Additionally, several issues intrinsic to HTS materials must be resolved before these magnets can be applied in practical fields. One of the main challenges lies in accurately predicting the criti-

cal current of magnets made from REBCO conductors. The critical current varies not only with the magnitude of the applied magnetic field but also with its angle, leading to significant variations in critical current across the conductor width. This complexity makes the design and operation of such magnets more difficult. Other issues, such as screening current, mechanical stress, and quench phenomena in NI magnets, also require further investigation.

This study explores the feasibility of applying NI HTS dipole magnets to particle accelerators. To achieve this, we improved existing magnet analysis models and developed new ones, applying them to magnet design and analysis. The research consists of three main parts: 1) development of analysis models, 2) design, fabrication, and operation of the dipole magnet, and 3) evaluation of measurement results and improvement of magnetic field uniformity. Due to the saddle-shaped geometry of dipole magnets, conventional finite-element-method-based screening current analysis is difficult. To overcome these challenges, we devised circuit-based analysis methods, techniques to accelerate inductance calculations, and 3D magnetic field analysis models using distributed-circuit approaches. To address the critical current challenges of HTS conductors, we proposed a standard dataset and introduced the widthwise average method, which was validated through experiments.

To verify the performance of NI dipole magnets and the developed models, we designed a dipole magnet with a central magnetic field of 0.7 T and developed winding and assembly techniques to fabricate the magnet. We also constructed a conduction cooling system for magnet cooling and a mapping system for measuring magnetic field uniformity. Using these setups, we successfully operated the NI dipole magnet for the first time and validated that the target central magnetic field was achieved. Magnetic field uniformity measurements were performed, and discrepancies with the analysis model were evaluated. Furthermore, to improve the measured magnetic field uniformity, we introduced the ferroshim technique, designed and fabricated ferroshims, and

verified uniformity improvements through additional experiments. Finally, we identified areas for improvement and outlined future research directions for the development of high-field NI HTS dipole magnets.

Keywords: Dipole magnet, High-temperature superconductor, No-insulation, Particle Accelerator, Saddle-shaped magnet

Student Number: 2020-27571

Contents

List of Tables

List of Figures

Nomenclature

Superconducting Properties

T_c	Critical temperature [K]
I_c	Critical current [A]
J_c	Critical current density [A/m^2]
B_c	Critical magnetic field [T]
B_{c1}	Lower critical magnetic field in type-II superconductor [T]
B_{c2}	Upper critical magnetic field in type-II superconductor [T]
E_c	Critical electric field [V/m]
n	Index value for E-J power-law
δ	Thickness of superducting layer [m]

Superconductor Magnet Parameters

I_{op}	Operating current [A]
T_{op}	Operating temperature [K]
I_θ	Azimuthal current [A]
I_r	Radial current [A]

R_c Characteristic resistance [Ω]

ρ_{ct} Contact resistivity [Ωm^2]

L Self-inductance [H]

M Mutual inductance [H]

V Coil voltage [V]

V_{sc} Superconducting index voltage [V]

l Length of conductor [m]

W Width of conductor [m]

Physical Variables

$\mathbf{B}$ Magnetic field vector [T]

$\mathbf{A}$ Magnetic vector potential [T·m]

$\mathbf{J}$ Current density vector [A/m^2]

$\mathbf{T}$ Current vector potential [A/m]

$\mathbf{K}$ Surface current density vector [A/m]

$\mathbf{E}$ Electric field vector [V/m]

T Temperature [K]

t Time [s]

$\mathbf{u}$ Displacement vector [m]

Material Properties

μ_0 Vacuum permittivity [H/m]

μ Permittivity [H/m]

ρ Electrical resistivity [Ω·m]

σ Electrical conductivity [S/m]

Other Symbols

$k_0, k_1, \alpha_0, \alpha_1, \beta_0, \beta_1, \phi, c, \eta$ Critical current fitting parameters

Abbreviations

HTS High-temperature superconductor

LTS Low-temperature superconductor

NI No-insulation

LN2 Liquid nitrogen

DC Direct current

AC Alternating current

FEM Finite element method

SCF Screening-current-induced-field

SCS Screening-current-induced-stress

CSR Current sweep reversal

Chapter 1

INTRODUCTION

1.1 Superconducting Dipole Magnet System for Future High-field Particle Accelerators

1.1.1 Global Projects for High-Performance Particle Accelerators through High-Field Magnet Development

The development of high-performance particle accelerators is a key driver of progress in fundamental physics, medical applications, and industrial technologies. One of the main challenges in the development of these accelerators is the creation of high-field magnets that can generate stronger magnetic fields while maintaining stability and efficiency [1–8]. These magnets are crucial for steering, focusing, and accelerating charged particles within accelerators, particularly in next-generation designs [9, 10]. Currently, numerous projects are underway worldwide to develop such superconducting magnets as shown in Figure 1.1.

Building upon the success of the Large Hadron Collider (LHC) [11,12], CERN has proposed the Future Circular Collider (FCC) as a next-generation facility to explore the frontiers of particle physics [13–18]. The FCC aims to achieve collision energies significantly beyond those of the LHC, facilitating a deeper understanding of fundamental

forces, particles, and the universe's origins. The FCC is envisioned as a 100-kilometer circular collider, dwarfing the 27-kilometer LHC. This ambitious design is intended to explore phenomena such as dark matter, precision Higgs boson measurements, and the search for new particles. It will initially operate as FCC-ee before transitioning into FCC-hh capable of achieving center-of-mass energies of up to 100 TeV—more than seven times the energy of the LHC. Extensive research is underway to optimize Nb_3Sn and explore next-generation materials like high-temperature superconductors (HTS). These materials will play a critical role in achieving the high magnetic fields necessary for steering and focusing high-energy beams within the FCC's massive structure.

The Muon Collider has the potential to revolutionize particle physics by enabling precise measurements of the Higgs boson's properties, exploring multi-TeV energy scales, and providing a clean experimental environment for new physics discoveries. The project has garnered global interest, with collaborations involving CERN, Fermilab, and institutions worldwide [19–21]. Feasibility studies, including simulations and prototype testing, are actively underway. The compact nature of a Muon Collider necessitates high-field magnets capable of efficiently bending and focusing the muon beams. These magnets must operate in challenging conditions due to the short lifetime of muons (2.2 μs at rest) and the high levels of radiation produced during muon decay. Advanced superconducting materials, such as Nb_3Sn and HTS, are being explored to meet these demands. The Muon Collider is envisioned to achieve center-of-mass energies of several TeV, comparable to or exceeding the capabilities of future proton colliders like the FCC-hh. This makes it an ideal candidate for studying phenomena such as Higgs boson pair production, electroweak symmetry breaking, and potential new particles beyond the Standard Model.

The Electron-Ion Collider (EIC) is a next-generation particle accelerator currently under development in the United States [22–24]. It aims to provide unprecedented insights into the internal structure of protons, neutrons, and nuclei by colliding high-energy electrons with various ion species. Located at the Brookhaven National Lab-

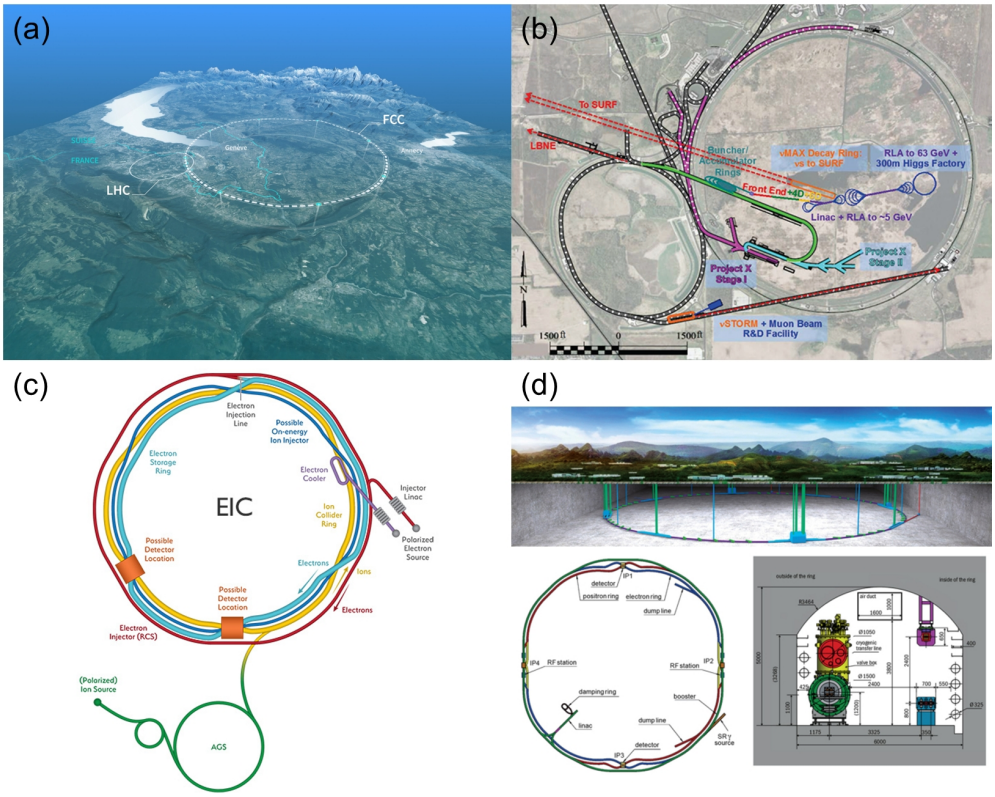

Figure 1.1: Global projects for particle accelerators with high-field magnet. (a) CERN's FCC project [25], (b) Fermilab's Muon Collider project [26], (c) BNL's Electron-Ion Collider project [27], (d) China's Circular Electron-Positron Collider project [28].

oratory (BNL), the EIC will expand our understanding of quantum chromodynamics (QCD), the fundamental theory describing the strong interaction. Decades after the discovery of the proton's spin, its origin remains one of the most intriguing mysteries in particle physics. The EIC will help quantify the contributions of quarks, gluons, and orbital angular momentum to the proton's overall spin. Advanced superconducting magnets will steer and focus the electron and ion beams. These magnets must provide high field strength and stability to accommodate the high-energy collisions.

The Circular Electron-Positron Collider (CEPC) is a next-generation particle ac-

celerator proposed by China to explore the Higgs boson and other fundamental aspects of the universe [29–31]. As part of the nation's growing commitment to advancing particle physics, the CEPC is envisioned to be the world's largest electron-positron collider, with a circumference of approximately 100 kilometers—comparable to the proposed FCC in Europe. The CEPC aims to act as a 'Higgs factory,' producing millions of Higgs bosons in a clean electron-positron collision environment. This will enable highly precise measurements of the Higgs boson's couplings, decay channels, and self-interactions, which are crucial for understanding electroweak symmetry breaking. High-field superconducting magnets are essential for bending and focusing the beams within the CEPC's large circular structure. Research is focused on enhancing the performance and cost-effectiveness of Nb_3Sn and other advanced materials.

1.1.2 Previous Dipole Magnets and Key Challenges

In accelerator systems, dipole magnets are indispensable components that play a critical role in guiding, controlling, and stabilizing the trajectory of charged particle beams. These magnets generate a uniform magnetic field, which interacts with the electric charge of the particles, forcing them to move along a curved path. This bending action is fundamental for maintaining the circular or elliptical trajectories required in most accelerators, such as synchrotrons and colliders. The ability of dipole magnets to precisely guide particles is determined by their magnetic field strength, which must be carefully calibrated to match the momentum and energy of the particle beam [32, 33].

As particles are accelerated to higher energies, their momentum increases, necessitating stronger magnetic fields to maintain the desired curvature of their path. Dipole magnets are designed to adapt to these changing conditions by varying the magnetic field strength in real-time, ensuring that the particles remain confined to their designated orbit. Without this dynamic adjustment, the beam could deviate from its intended path, resulting in beam loss or damage to the accelerator components.

In addition to trajectory control, dipole magnets are extensively used in beam steer-

ing applications. They are crucial for deflecting the particle beam into specific directions, such as injecting the beam into the main accelerator ring or extracting it for delivery to experimental targets. This precision steering is vital for ensuring that the beam enters and exits the system efficiently and with minimal loss. Furthermore, dipole magnets are employed in beamline corrections, where they counteract small deviations or misalignments in the particle trajectory. This corrective capability is essential for maintaining the overall stability, focus, and quality of the beam [10, 34].

High-energy accelerators, which are used in particle physics and advanced materials research, place even greater demands on dipole magnet performance. In these systems, the magnets must bend particle beams traveling at relativistic speeds, where the momentum is extremely high. To achieve the required magnetic fields, advanced superconducting dipole magnets are often used. These magnets, constructed using materials like Nb_3Sn or NbTi, can generate magnetic fields exceeding 10 T while minimizing energy losses due to electrical resistance. Their ability to sustain strong and stable fields under extreme conditions makes them indispensable for next-generation accelerators, such as the High-Luminosity Large Hadron Collider (HL-LHC) and future circular colliders [35–39].

Beyond their primary role in trajectory control and beam steering, dipole magnets also contribute to the broader functionality of accelerators. For example, they are instrumental in creating specific experimental conditions by selectively bending and separating particles of different energies or charge states. This capability is particularly useful in experiments requiring highly controlled beam parameters or in facilities that operate with multiple particle types simultaneously.

These dipole magnets have been constructed using various methods depending on the target central magnetic field strength. For magnets generating relatively low fields below 2 T, copper electromagnets or permanent magnets have predominantly been used instead of superconducting materials. In contrast, to create dipole magnets with fields exceeding 2 T, NbTi superconducting wires were historically the primary

material of choice. Figure 1.3 illustrates dipole magnets that have either been successfully operated or designed, plotted against their central magnetic field strength by year. Copper electromagnet dipole magnets have been employed in various storage rings worldwide, including South Korea's PLS-II [40] as shown in Figure 1.2 (a), Japan's KEKB [41], Canada's CLS [42, 43], and so on [44–49]. Additionally, prominent examples of NbTi superconducting magnets include those used in CERN's LHC [50] as shown in Figure 1.2 (b), Brookhaven National Lab's RHIC [51], Fermilab's Tevatron [52], and many more [53–58]. Increasing the central magnetic field allows for accelerating higher-energy particle beams and enhancing the accelerator's performance by increasing luminosity, driving a continuous effort to achieve higher field strengths. However, due to the critical magnetic field limit of NbTi, magnets surpassing 8 T have been designed using materials like Nb_3Sn, which possess superior critical magnetic field properties [59–62]. Currently, the HL-LHC magnets are designed to operate at 11 T, with their construction and operation forthcoming.

Since the 2010s, the design and fabrication of dipole magnets using HTS wires have been actively explored. In particular, efforts to utilize REBCO-coated conductors, commercially available under the name 2G HTS conductor, have been increasing [63–67]. Additionally, a 20 T magnet design combining Bi-2212 and Nb_3Sn wires has been proposed [68]. However, employing HTS wires remains challenging due to the relatively immature state of magnet technology development. As a result, large-scale projects or high-field magnet development initiatives involving HTS are rare, and the verified magnetic field levels of existing HTS magnets remain relatively low, below 3 T [69–72].

From the perspective of HTS magnets as shown in Figure 1.2 (c) and (d), the key challenges lie in the consistency and reliability of the superconducting wires, as well as in addressing quench protection issues [76, 77]. Compared to conventional LTS wires, HTS wires exhibit lower consistency and are more vulnerable to problems such as delamination. Unlike NbTi wires, which can be easily wound or cabled due to

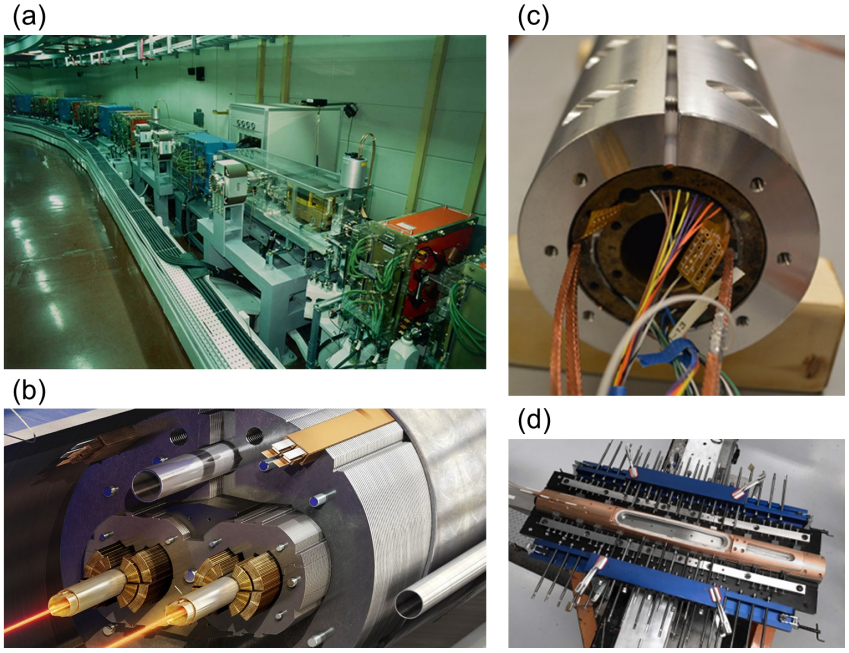

Figure 1.2: Dipole magnets made with various conductors. (a) Copper dipole magnet of PLS-II [73], (b) LTS dipole magnet of CERN LHC [74], (c) Bi2212 HTS dipole magnet of LBNL [75], (d) REBCO HTS dipole magnet of CERN [65].

their metallic properties, HTS wires present significant hurdles for practical applications. The advent of NI magnet technology [78] has provided a potential solution to the quench protection problem; however, quenches in HTS magnets still pose serious risks, including potential damage or even melting of the magnet. Furthermore, REBCO magnets face the additional challenge of mitigating the degradation of magnetic field uniformity caused by screening currents [79–81]. Unlike LTS wires, which consist of very thin filaments, REBCO wires have a thin but wide geometry that can result in significant nonuniform current distribution. This nonuniformity directly impacts magnetic field uniformity, a critical parameter for particle accelerators where performance heavily depends on precise magnetic fields. Addressing these issues is essential for the successful integration of HTS magnets into particle accelerator applications.

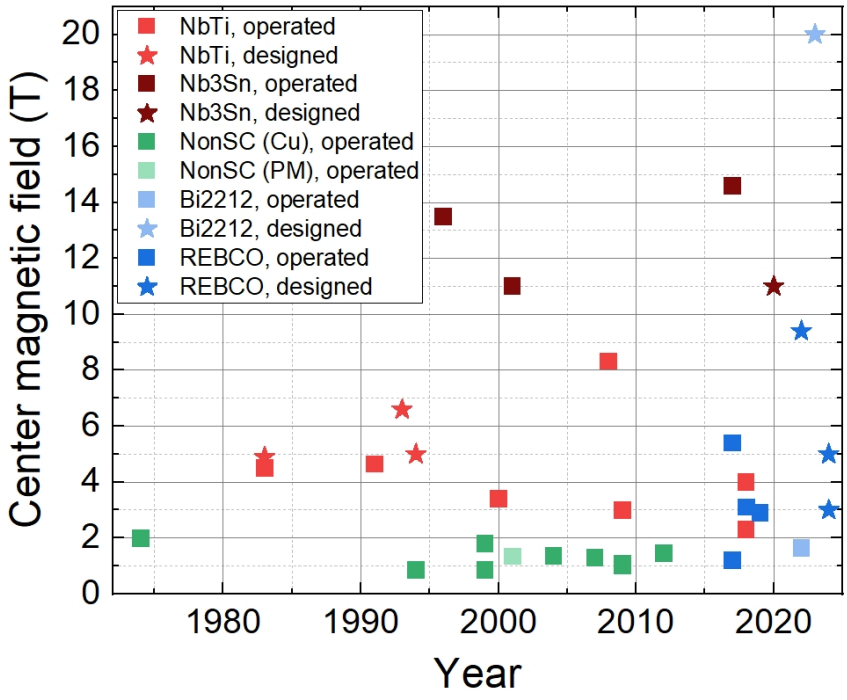

Figure 1.3: Comparison of coil conductor materials and magnetic field strengths of dipole magnets developed or designed in the history of particle accelerators.

The cooling method for magnets is also a critical issue. Traditional superconducting magnets have relied on liquid helium for cooling, resulting in large-scale cooling systems and high operating costs [82, 83]. This reliance stems from the low critical temperature of LTS materials, which require extremely low temperatures around 4 K to achieve optimal performance, with some high-performance applications even utilizing pressurized superfluid helium at approximately 1.8 K [84]. In contrast, REBCO has a significantly higher critical temperature of around 93 K and can maintain sufficient performance at temperatures in the range of 10 to 20 K, eliminating the necessity for liquid helium cooling. This opens up options such as conduction cooling systems using cryocoolers [85,86] or gas helium cooling systems [87,88]. Developing technology to operate these cooling systems efficiently and manufacture them in a compact form is essential for advancing HTS magnet applications.

1.2 High-temperature Superconducting Magnet as Potential Technical Solution for Dipole Magnet

1.2.1 Background and Applicability of No-insulation High-temperature Superconducting Magnet Technique

Since the HTS NI magnet technique was first proposed in 2011 [78], various high-field magnets have been developed using the NI approach. The NI technique is implemented by removing the insulation between the wires within the coil as shown in Figure 1.4 (a). Since the resistance of a superconductor becomes zero below its critical temperature, current flows along the winding direction even without insulation between turns during steady-state operation. The contact resistance between turns provides sufficient insulation under such conditions, enabling nominal operation without dedicated insulation. Furthermore, if a local hot spot arises due to an internal defect or an external disturbance at a specific turn, the current can bypass through turn-to-turn contacts, aiding in coil protection and enhancing operational reliability. The key advantages and disadvantages of the NI HTS coil are summarized as follows:

- **(Pros 1) Defect and disturbance tolerance:** NI HTS coils demonstrate stable operation even in the presence of internal defects or external disturbances, enabling the fabrication and operation of highly reliable coils.

- **(Pros 2) Enhanced mechanical properties:** Removing insulation materials between turns allows for a more compact coil structure with improved mechanical robustness due to the absence of soft insulating layers.

- **(Pros 3) Mitigation of permanent thermal damage:** In insulated HTS coils, a quench can result in local hot spots causing irreversible thermal damage. Conversely, in NI HTS coils, the current can bypass these hot spots, significantly reducing the likelihood of local thermal runaway.

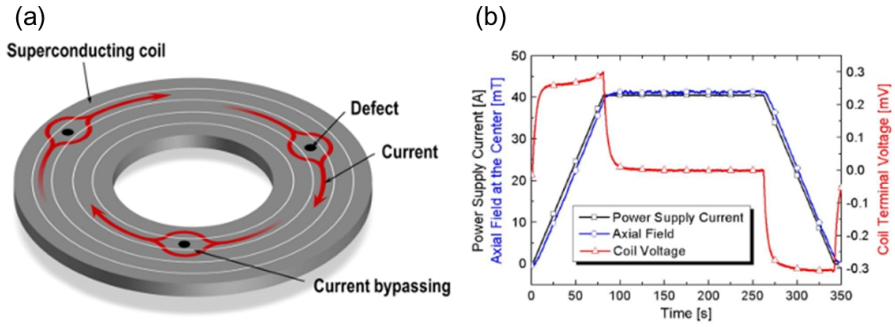

Figure 1.4: A basic explanation of NI characteristics. (a) Schematic diagram illustrating the current bypassing characteristics of NI coils [89], (b) Charging delay phenomenon caused by current bypassing characteristics [78].

- **(Cons 1) Charging delay caused by bypassing current through turn-to-turn contacts:** In NI HTS coils, bypassing current through turn-to-turn contacts can lead to delays during charging and discharging processes as shown in Figure 1.4 (b). Furthermore, transient operations such as changes in external magnetic fields or fluctuations in operating current may generate bypassing currents, causing temporary fluctuations in the magnetic field.

- **(Cons 2) Joule loss due to bypassing current:** Currents passing through the contact resistance between turns result in Joule losses. For NI HTS coils, evaluating this extra inter-turn Joule loss is essential for optimizing the cryogenic system design.

- **(Cons 3) Difficulty in achieving uniform contact resistance:** Contact resistivity in NI magnets is influenced by pressure and surface conditions, making it challenging to control during the winding process. Additionally, predicting contact resistivity before coil testing is nearly impossible.

NI magnet technology is regarded as a crucial option for high-field magnet development and has been successfully implemented, demonstrating the intended performance [90,91]. Initially, technological validation was primarily conducted on solenoid-

type high-field magnets. The 26 T magnet as shown in Figure 1.5 (a) developed by MIT and SuNAM demonstrated for the first time that REBCO magnets could achieve magnetic field levels unattainable with LTS materials [92]. Following this, REBCO magnets utilizing NI technology were successfully employed in practical applications, such as the 18 T axion detection magnet [93] and the 9.4 T NMR magnet [94] as shown in Figure 1.5 (b). The 45.5 T LBC3 magnet, which reached the world's highest DC magnetic field, proved that NI magnets could endure extremely high magnetic field environments [95].

Efforts to mitigate the limitations of NI technology through modifications are also ongoing. Japan's RIKEN developed a magnet employing the 'intra-layer NI' technique, achieving a magnetic field of 31.4 T [96, 97]. France's CNRS Grenoble succeeded in reaching 32.5 T using a magnet based on the metal insulation method [98, 99]. Meanwhile, China's Chinese Academy of Sciences achieved 32.35 T, setting the record for the highest magnetic field among all-superconducting magnets [100]. These continuous attempts to enhance magnetic field performance through NI and modified NI technologies demonstrate the growing potential of these approaches.

These advancements are also being applied to devices in other fields. Notably, the fusion energy sector, which requires compact high-field magnets, has seen significant efforts in this direction. Commonwealth Fusion Systems, a spin-off from MIT, is utilizing NI technology to manufacture TF coils for the SPARC project as shown in Figure 1.5 (c), achieving a record magnetic field of 20 T [101]. Similarly, the UK-based Tokamak Energy is applying NI technology to develop magnets, progressing through milestones aimed at building fusion devices [102].

In the accelerator field, initiatives employing NI technology are also underway. CERN has proposed the GaToroid concept [103] as shown in Figure 1.5 (d), which involves using NI magnets for particle therapy. In Korea, the Pohang Accelerator Laboratory (PAL) has developed a 5 T wavelength shifter insertion device for the PLS-II storage ring, conducting various experiments to further refine the technology [104].

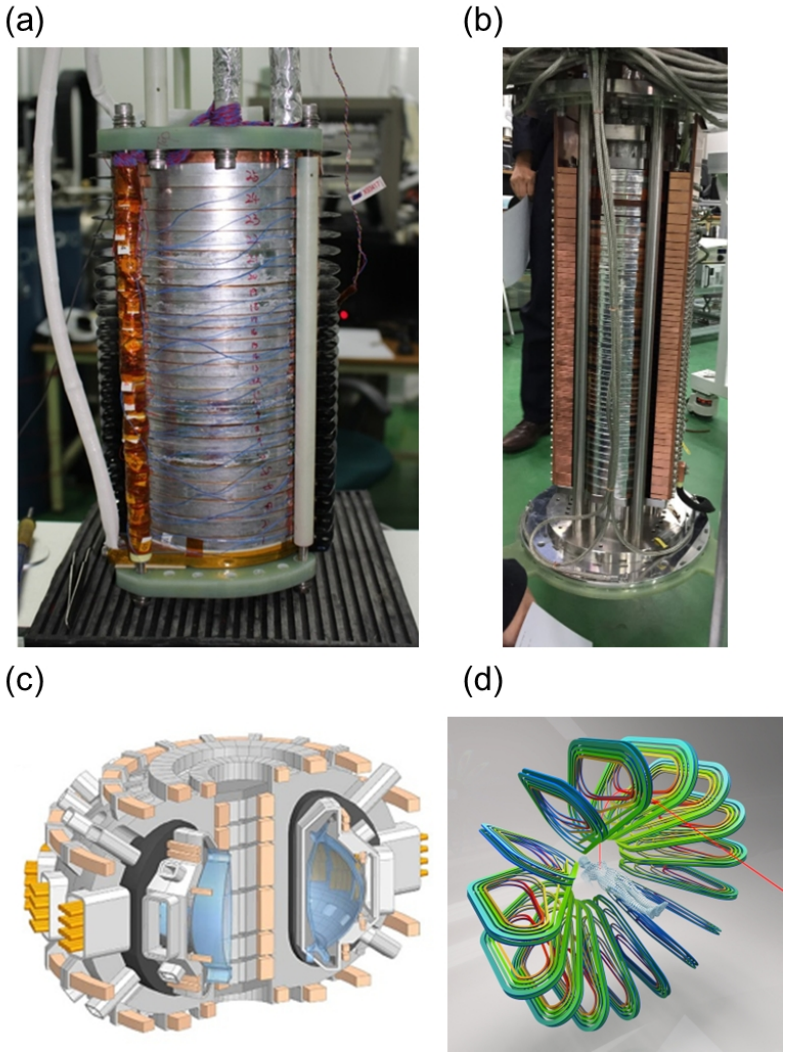

Figure 1.5: Examples of a no-insulation magnet development. (a) 26 T solenoid NI magnet developed by MIT and SuNAM [92], (b) 9.4 T NI magnet for NMR developed under the leadership of KBSI [94], (c) Tokamak design based on NI magnets by Commonwealth Fusion Systems [105], (d) GaToroid design based on NI magnets by CERN [103].

1.2.2 Requirements for Development of High-temperature Superconducting Dipole Magnet: Analysis Methods and Experimental Study

There have been rare previous cases of using NI magnet technology to fabricate saddle-shaped dipole magnets. Existing attempts can largely be categorized into those utilizing insulated magnets and those employing CORC cables. NI technology was considered more challenging for magnets requiring high magnetic field uniformity due to the occurrence of bypassing currents. In the case of REBCO conductors, significant screening currents arise, and this uncertainty in current distribution poses difficulties for developing dipole magnets.

To address these issues, improvements in analysis and design methodologies, along with their validation, are necessary. This study focuses on resolving these challenges. Specifically, the required developments can be summarized as follows:

- The analysis of NI magnets can be broadly divided into three parts: electromagnetic, mechanical, and thermal, with ongoing research in each area. In the electromagnetic domain, key issues include screening currents and critical current estimation. For solenoid magnets, FEM-based methods such as H formulation and T-A formulation have been used to analyze screening currents. However, for saddle-shaped magnets, which are representative of dipole magnet geometries, a well-established analysis method for screening currents has yet to be developed. Circuit models, which are widely studied, face challenges in calculating inductance for non-planar magnet geometries. Additionally, predicting the critical current, a fundamental property of superconducting magnets, is particularly difficult for REBCO magnets. This challenge arises from the anisotropic nature of REBCO conductors' critical current with respect to magnetic field strength and angle. Accurately estimating critical current affects screening current distribution and is closely related to quench phenomena, underscoring the need for advancements in analytical methods.

- Mechanical analysis also requires the establishment of methods tailored for dipole magnets. In particular, bending strain at the coil-end part is critical for saddle-shaped magnets. While the 'constant perimeter winding' technique is well-known, its direct application during the winding process is often impractical due to factors such as conductor thickness and design constraints. Thus, an analysis method that incorporates more realistic conditions is necessary. Similarly, thermal analysis must consider the comprehensive effects of Joule heating caused by bypassing currents and the magnet's cooling conditions. Developing such integrated analysis methods is essential for ensuring the effective design and operation of these magnets.

- Challenges also exist in experimental validation. Since there are no prior examples of fabricating NI saddle-shaped magnets, basic verification of manufacturing techniques, including winding processes, is essential. Additionally, because the magnetic field uniformity produced by the magnet plays a critical role in particle accelerator applications, experiments to measure and evaluate this uniformity are necessary. For experiments employing conduction cooling systems without cryogenic liquids, it is crucial to design and implement a system capable of providing sufficient cooling and to conduct validation through these experiments.

1.2.3 Role of Saddle-shaped Dipole Magnet in Synchrotron

Synchrotrons are vital components of modern particle accelerators, enabling high-energy particle collisions and facilitating numerous applications in science, medicine, and industry. Dipole magnets are essential in synchrotrons, providing the magnetic fields needed to bend charged particle beams along their circular trajectory. Among various dipole magnet designs, saddle-shaped dipole magnets have emerged as a promising solution for enhancing synchrotron performance, particularly in achieving higher magnetic field uniformity and compact accelerator layouts [106].

A synchrotron operates by accelerating charged particles, such as electrons or protons, within a circular trajectory while synchronized electromagnetic fields maintain beam stability and energy. Dipole magnets play a critical role in bending the particle trajectory and confining the beam within the synchrotron's circular path. Saddle-shaped dipole magnets stand out in this application due to their ability to generate uniform magnetic fields over the beam path, a crucial factor for beam stability and efficient particle acceleration. Additionally, the compact design of saddle-shaped magnets allows for more efficient use of space, enabling the construction of smaller synchrotron facilities without compromising performance.

The development of saddle-shaped dipole magnets addresses several challenges associated with synchrotron design and operation. One key challenge is maintaining magnetic field uniformity, which is critical for high-energy beams to ensure consistent particle trajectories and minimize beam loss. Saddle-shaped magnets, with their optimized geometry and advanced winding techniques, provide a highly uniform magnetic field, making them ideal for synchrotrons operating at high energy levels. Furthermore, as synchrotrons aim to achieve higher beam energies, compact accelerator designs become increasingly important. Saddle-shaped dipole magnets achieve high magnetic field strengths within smaller dimensions, facilitating the construction of compact and cost-effective synchrotrons.

Another advantage of saddle-shaped dipole magnets is their compatibility with advanced cryogenic cooling systems. Unlike traditional superconducting magnets that require liquid helium cooling to operate at temperatures near 4 K, HTS saddle-shaped magnets can function efficiently at temperatures of 10-20 K. This reduces the dependence on liquid helium, lowers cooling costs, and simplifies the overall cryogenic system design. These attributes make saddle-shaped dipole magnets particularly attractive for synchrotrons that require high-field magnets but seek to reduce operational complexity and costs.

Saddle-shaped dipole magnets also have applications beyond beam bending in syn-

chrotron rings. They are particularly advantageous in synchrotrons designed for high-energy physics experiments, medical particle therapy, and synchrotron light sources. For instance, compact synchrotrons used in cancer treatment rely on the high field strengths and uniformity provided by saddle-shaped magnets to deliver precise and effective treatments. Similarly, synchrotron light sources, which produce high-intensity radiation for material science and biological research, benefit from the improved magnetic field quality and control offered by these magnets.

Despite these advantages, saddle-shaped dipole magnets must address challenges such as mitigating screening currents and achieving precise magnetic field uniformity. Techniques such as ferroshimming, where small ferromagnetic pieces are strategically placed to correct magnetic field distortions, have been successfully applied to enhance field uniformity. These innovations ensure that saddle-shaped dipole magnets can meet the stringent requirements of modern synchrotrons.

Thus, saddle-shaped dipole magnets represent a significant advancement in synchrotron technology. By addressing challenges related to magnetic field uniformity, compact design, and thermal management, they enable synchrotrons to achieve enhanced performance across a wide range of applications. As the demand for high-performance particle accelerators continues to grow, the integration of saddle-shaped dipole magnets will play a pivotal role in advancing synchrotron technology for scientific, medical, and industrial purposes.

1.3 Goal and Significance of This Study

This study focuses on the applicability of NI HTS saddle-shaped dipole magnets to particle accelerators. Among the various criteria necessary for application to particle accelerators, the research examines the effects of screening currents on magnetic field uniformity and operational stability. Therefore, the primary objective of this study was not the production of a high-field dipole magnet itself. Instead, establishing and val-

idating the foundational technologies for the design, fabrication, and operation of NI saddle-shaped dipole magnets will serve as a stepping stone toward acquiring the techniques required for developing high-field magnets. The specific objectives of this study are as follows:

- Proposal of analysis models and fabrication methods for an NI HTS saddle-shaped dipole magnet
- Design and construction of the first NI HTS saddle-shaped cosine-theta dipole magnet
- Experimental validation of operation characteristics and performance of NI HTS saddle-shaped dipole magnet
- Design, fabrication, and installation of ferroshim for enhancement of magnetic field uniformity

The significance of this study, in connection with the aforementioned objectives, is as follows:

- **First suggestion of various analysis models for NI HTS saddle-shaped dipole magnet:** This study introduces the first analytical models related to saddle-shaped magnets. These include a distributed circuit model for analyzing screening currents in nonplanar coil configurations and a high-speed inductance calculation method for utilizing the model. Additionally, a predictive model for the critical current of magnets is proposed, along with a practical method incorporating hard-way bending-free conditions for coil-end parts. Furthermore, a thermal analysis model for conduction cooling characteristics is applied to analyze the temperature profile.
- **Validation on applicability of NI HTS dipole magnet through experiments:** Fabrication of an NI saddle-shaped magnet was undertaken for the first time, followed by experimental validation. Structures for winding, such as a universal

joint, were devised and utilized to manufacture the coil. Additionally, essential structures for assembling the magnet were designed and their effectiveness validated. The magnet was cooled without cryogens using a conduction cooling system, and its performance was verified by measuring magnetic field uniformity with a field-mapper, alongside assessments of the cooling system's efficiency.

- **First validation of passive shimming method:** A ferroshim technique for saddle-shaped magnets was developed and its performance was validated. A design model was established to adapt the ferroshim technique, previously used for NMR magnets, to saddle-shaped magnets. This model was applied to the magnetic field distribution of the fabricated saddle-shaped magnet to design and create the ferroshim. The ferroshim was then installed in the bore of the magnet, and its effectiveness in improving magnetic field uniformity was measured and confirmed.

1.4 Thesis Structure

This thesis consists of six chapters. The first chapter 'INTRODUCTION' discusses the background, objectives, and significance of the research. It introduces the background of dipole magnets used in particle accelerators and ongoing developments in high-field accelerator magnets. Additionally, it explains the NI technology that can be utilized in the development of such magnets and the requirements for applying this technology to saddle-shaped magnets. The chapter also defines the challenges addressed in this study and outlines the research objectives and the significance of the accomplishments achieved during the research process.

Chapter 2 'ANALYSIS METHODS FOR SADDLE-SHAPED DIPOLE MAGNET ADOPTING NO-INSULATION TECHNIQUE' discusses the analytical models for saddle-shaped magnets. It advances existing circuit analysis models for screening current evaluation and develops an inductance calculation method. To address the chal-

lenging issue of predicting the critical current of REBCO magnets, the widthwise average method is introduced. Additionally, harmonic analysis techniques for magnetic field distribution are incorporated into the magnet design process. Finally, a practical end-coil optimization method is developed to minimize hard-way bending during design.

Chapter 3 'DESIGN, CONSTRUCTION, AND OPERATION OF SADDLE-SHAPED DIPOLE MAGNET' outlines the overall design, fabrication, and experimental setup for operating the magnet at the core of this study. The magnet used in this research is designed for a central magnetic field of 0.7 T with a winding diameter of 110 mm, and optimization techniques were applied during the design process. Mechanical and thermal analyses were conducted to refine the design, addressing challenges encountered during fabrication to construct the magnet based on these final specifications. Additionally, the chapter describes the experimental setup for conduction cooling experiments. Furthermore, it includes details about the demonstration magnet used for experiments such as fast ramping tests.

Chapter 4 'EXPERIMENTAL RESULTS AND ANALYSIS OF HTS SADDLE-SHAPED DIPOLE MAGNET' presents the experimental results of the magnet. The measured magnetic field uniformity using a field mapper is detailed, and the effects of screening current on magnetic field uniformity are analyzed. Harmonic analysis of the magnetic field distribution is conducted to evaluate the temporal stability of the magnetic field. Additionally, ferroshim was designed, installed in the magnet's bore, and its effectiveness in improving magnetic field uniformity was assessed. Lastly, the chapter discusses the analysis of errors in magnetic field uniformity caused by geometric deformation observed in the demonstration magnet experiments, as well as the results of fast ramping tests.

The last chapter 'CONCLUSION' presents the conclusion of the thesis and provides a summary of the overall content.

Chapter 2

ANALYSIS METHODS FOR SADDLE-SHAPED DIPOLE MAGNET ADOPTING NO-INSULATION TECHNIQUE

The saddle-shaped magnet, due to its unique nonplanar structure, requires different analytical techniques from those used for conventional high-temperature superconducting (HTS) magnets. When conducting experiments to evaluate the performance of the saddle-shaped magnet after construction, the measurable electromagnetic parameters mainly include voltage, critical current, and magnetic field distribution. To reproduce these parameters through analysis, an appropriate analytical model is required, but such a model has not been sufficiently developed in the past.

In this study, a distributed circuit model was developed to analyze the voltage and current distribution within the saddle-shaped magnet. A numerical method was proposed to quickly calculate the inductance required when applying the distributed circuit. Additionally, the precise critical current estimation problem, which has been considered a challenge for HTS magnets, was solved using the distributed circuit approach. We also analyzed the magnetic field generated by the saddle-shaped magnet and conducted calculations for the harmonic coefficient, which significantly affects the characteristics of the actual beam. A method was developed to assess the impact of screening currents and ferroshim on the harmonic coefficient.

Meanwhile, in the mechanical analysis of the saddle-shaped magnet, the key issue lies in the bending strain at the magnet's ends. Since the well-known constant perimeter winding technique cannot be directly applied to actual windings, a practical solution is suggested. Furthermore, a mechanical analysis model was developed to address the operational characteristics of the magnet.

2.1 Nonuniform Current Distribution and Voltage Simulation Method

Traditionally, the finite element method (FEM) has been extensively employed to replicate the behavior of superconducting magnets. Techniques such as the H formulation, T-A formulation, and H-ϕ formulation have been utilized to model the nonlinear properties of superconducting materials. However, no-insulation (NI) HTS coils exhibit distinct voltage-current characteristics due to the bypass current flowing between adjacent turns, prompting the adoption of various circuit models to describe the electromagnetic behavior of these coils. These models incorporate an additional bypass path into the conventional circuit model of insulated HTS coils, which typically includes only inductance and an index resistance governed by the superconductivity power-law. To accurately represent this bypass path, the contact resistivity (R_{ct}) of the REBCO conductor is taken into account. Despite this, researchers are still investigating the factors influencing contact resistivity and exploring methods to effectively control it. From the contact resistivity, the resistive circuit element named characteristic resistance (or contact resistance) can be calculated as follows [107]:

$$R_c = \frac{\rho_{ct}}{S_{ct}}, \tag{2.1}$$

where S_{ct} represents the contacted area.

In this study, two advanced circuit analysis models are suggested: 1) the FEM-circuit sequential model, which combines FEM with the circuit analysis model to analyze screening currents and NI characteristics, and 2) the widthwise-segmented circuit

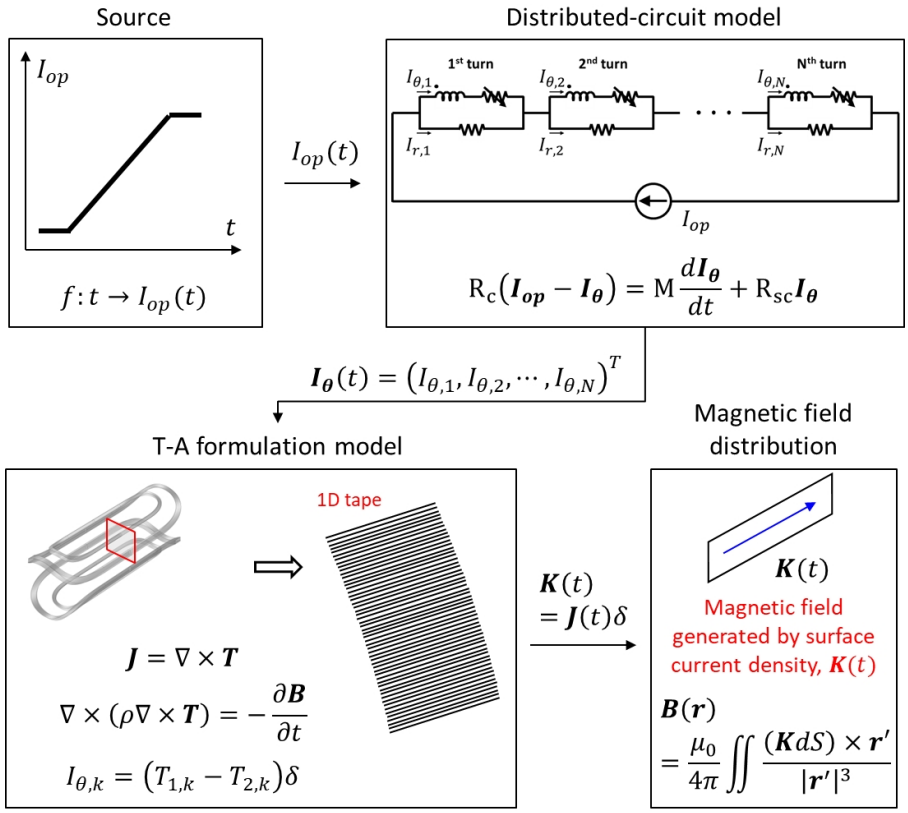

Figure 2.1: A flowchart for suggested sequential simulation model consisting of distributed-circuit model and T-A formulation method.

model, which divides the width of the REBCO conductor to incorporate the analysis of both aforementioned aspects.

2.1.1 FEM-circuit Sequential Model

The T-A formulation accurately simulates the screening current distribution in insulated magnets, as demonstrated through AC loss measurement experiments. However, in the case of NI magnets, additional bypass current paths form between turns, making it impossible to analyze them using the conventional T-A formulation. Thus, a sequential simulation method, as shown in Figure 2.1, was suggested consisting of

both distributed-circuit and T-A formulation models to analyze the current distribution caused by both turn-to-turn contact and the screening current [108]. The simulation sequence is as follows:

- Define the operating current function, $I_{op}(t)$, for a specific time domain.
- Import the operating current function into the distributed-circuit model's source. The azimuthal current, I_θ, and the radial current, I_r, for each turn are calculated and exported.
- Import the azimuthal current simulated from the previous step into the T-A formulation model. The azimuthal current for each turn is considered as the transport current in this model. The current density along one dimensional layer, $J(t)$ are calculated and exported.
- Consider the surface current density, $K(t) = J(t)\delta$, and calculate the magnetic field distribution based on two dimensional integration of Biot-Savart law.

Therefore, the effect of current distribution due to the radial current and the screening current on magnetic field distribution can be analyzed by this method, and the simulation results will be compared with the experimental results in the following sections.

2.1.2 Widthwise-segmented Circuit Model

FEM-based analysis models still have the drawback of requiring significant computation time. An efficient circuit analysis model can quickly calculate the electromagnetic characteristics of NI magnets during operation. To achieve this, this study proposes the widthwise-segmented circuit model. This approach involves dividing the HTS tape along its width, enabling the construction of a simplified circuit model by omitting many components, as the potential along the widthwise direction remains

nearly equipotential [109, 110]. If it is assumed that the current gradient within a single turn does not vary significantly, the model can be extended by incorporating the azimuthal components of the turn-distributed-circuit model as shown in Figure 2.2. Then, the governing equation can be derived as follows:

$$V_i = \mathbf{M}_{\zeta(i-1)+j}\frac{dI_{\theta,\zeta(i-1)+j}}{dt} + V_{sc,\zeta(i-1)+j}(I_{\theta,\zeta(i-1)+j}) = R_{c,i}I_{r,i}, \tag{2.2}$$

$$\mathbf{M} = \begin{pmatrix} L_1 & M_{1,2} & \cdots & M_{1,\zeta N} \\ M_{2,1} & L_2 & \cdots & M_{2,\zeta N} \\ \vdots & \vdots & \ddots & \vdots \\ M_{\zeta N,1} & M_{\zeta N,2} & \cdots & L_{\zeta N} \end{pmatrix} = \begin{pmatrix} \mathbf{M}_1 \\ \mathbf{M}_2 \\ \vdots \\ \mathbf{M}_{\zeta N} \end{pmatrix}, \tag{2.3}$$

$$V_{sc,\zeta(i-1)+j}(I_{\theta,\zeta(i-1)+j}) = E_c l_i (\frac{I_{\theta,\zeta(i-1)+j}}{I_{c,\zeta(i-1)+j}})^n, \tag{2.4}$$

$$I_{r,i} = I_{op} - \sum_{j=1}^{\zeta} I_{\theta,\zeta(i-1)+j}, \tag{2.5}$$

$$\therefore \frac{d\mathbf{I}_\theta}{dt} = \mathbf{M}^{-1}(\mathbf{R}_c I_{op} - \mathbf{V}_{sc}(\mathbf{I}_\theta) - \mathcal{R}\mathbf{I}_\theta), \tag{2.6}$$

$$\mathbf{I}_\theta = (I_{\theta,1}, I_{\theta,2}, \cdots, I_{\theta,\zeta N})^T, \tag{2.7}$$

$$\mathbf{R}_c = (R_{c,1}, R_{c,1}, \cdots, R_{c,1}, R_{c,2}, \cdots, R_{c,2}, \cdots\cdots, R_{c,N})^T, \tag{2.8}$$

$$\mathcal{R}_{\zeta(i-1)+j,\zeta(i-1)+k} = \begin{cases} R_{c,i} & (1 \le i \le N, 1 \le j,k \le \zeta) \\ 0 & (\text{otherwise}) \end{cases}, \tag{2.9}$$

$$\mathbf{V}_{sc}(\mathbf{I}_\theta) = (E_c l_1 (\frac{I_{\theta,1}}{I_{c,1}})^n, E_c l_2 (\frac{I_{\theta,2}}{I_{c,2}})^n, \cdots, E_c l_{\zeta N} (\frac{I_{\theta,\zeta N}}{I_{c,\zeta N}})^n)^T, \tag{2.10}$$

where $I_{\theta,i}$, $I_{r,i}$, $I_{c,i}$, L_i, $M_{i,j}$, l_i, $R_{c,i}$, ζ, and N represent the azimuthal current flowing through i^{th} element, radial current flowing through i^{th} turn, critical current of i^{th} element (which is determined by magnetic field, inclination angle, and temperature), self-inductance of i^{th} element, mutual inductance between i^{th} and j^{th} element, length of i^{th} element, characteristic resistance of i^{th} element, the number of widthwise segments of each turn, and the number of total turns, respectively.

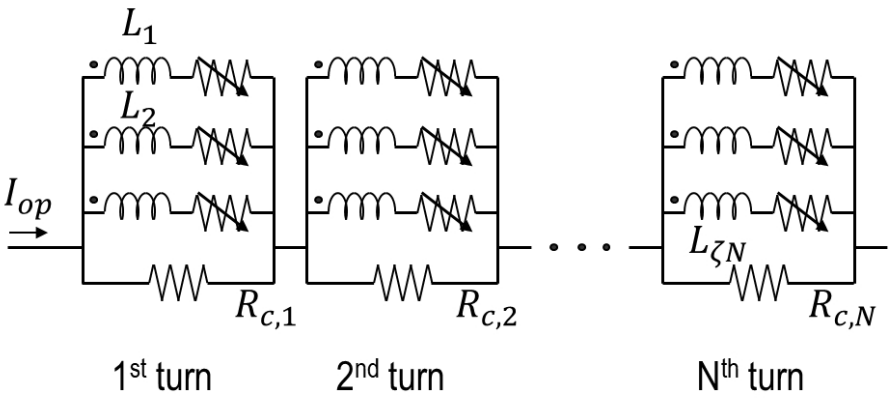

Figure 2.2: Widthwise-segmented circuit model of an NI HTS coil for simulation of screening current

2.2 Fast Inductance Calculation Method

To calculate the aforementioned circuit models, the inductance should first be calculated. When considering the magnet as larger segments, as in the lumped circuit model, the inductance can be calculated by either evaluating the magnetic energy through FEM or finding a closed-form inductance formula based on the Neumann formula. However, for the distributed circuit model, where the magnet is divided into smaller units, these methods become impractical or inefficient. Traditional numerical integration methods required for inductance calculation have the drawback of being time-consuming. In this study, a computational method that leverages vectorization and symmetry conditions to reduce the computation time for inductance is suggested.

2.2.1 Numerical Calculation of Inductance Based on Neumann Formula

The basic formula used to calculate inductance is the Neumann formula [111], which can calculate the mutual inductance between two finite line segments. The form of the formula is as follows:

$$M = \frac{\mu_0}{4\pi} \iint \frac{d\mathbf{x}_i \cdot d\mathbf{x}_j}{|\mathbf{x}_i - \mathbf{x}_j|}, \tag{2.11}$$

where $\mathbf{x}_i$ and $\mathbf{x}_j$ represent position vectors for the line segments.

The above equation provides four types of closed-form solutions depending on the positional relationship between two segments. These relationships are as follows: 1) two parallel segments; 2) two segments meeting at a single point; 3) two segments lying on the same plane but not intersecting; 4) two segments not located on the same plane. Considering that the superconducting layer of the REBCO tape is extremely thin, the inductance calculation for HTS magnets can be simplified to finding the mutual inductance between very thin rectangular pieces, ignoring their thickness. This mutual inductance can be calculated using the following equation:

$$M = \frac{\mu_0}{4\pi W_1 W_2} \int_0^{W_2} \int_0^{W_1} \int_0^{L_2} \int_0^{L_1} \frac{\hat{i_1} \cdot \hat{i_2}}{|\mathbf{r'}_1 - \mathbf{r'}_2|} dx_1 dx_2 dy_1 dy_2, \tag{2.12}$$

$$\mathbf{r'}_1 = x_1 \hat{i_1} + y_1 \hat{j_1} + \mathbf{r}_1, \tag{2.13}$$

$$\mathbf{r'}_2 = x_2 \hat{i_2} + y_2 \hat{j_2} + \mathbf{r}_2, \tag{2.14}$$

where W_1, W_2, L_1, L_2, $\mathbf{r}_1$, and $\mathbf{r}_2$ represent the width of the first piece, width of the second one, length of the first one, length of the second one, center of the first one, and the center of the second one, respectively. Detailed vector representations can be found in Figure 2.3.

The two inner integrals in the equation are formulated based on the solutions corresponding to the four types of positional relationships mentioned earlier. However, since closed-form solutions do not exist for the two outer integrals, numerical integration is required. In this study, Gaussian quadrature was used for the numerical integration. A detailed approach to approximating these outer integrals to reduce computation time for solenoid magnets can be found in [112]. However, that approach is difficult to adopt to nonplanar shaped coil such as saddle-shaped coil, so the other computational acceleration methods are suggested in the next subsection.

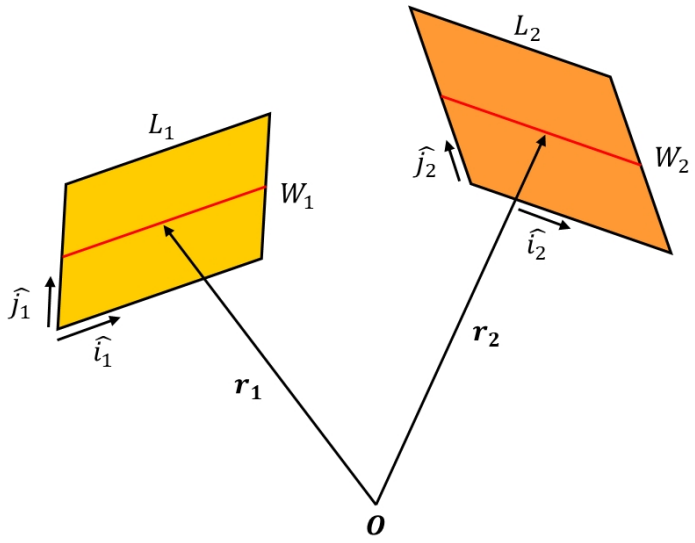

Figure 2.3: Schematic drawing of two rectangular pieces with display of notations

2.2.2 Computational Acceleration by Vectorization and Use of Symmetry

In this study, vectorization and symmetry were employed to reduce the computational load as shown in Figure 2.4. First, vectorization is a technique that speeds up operations by converting matrices into vectors for efficient computation. While basic numerical operations can be easily applied using functions provided by commercial numerical analysis software, inductance calculations are more complex because the equations vary depending on the positional relationships between elements. To address this, positional relationships were first classified, and then vectorization was applied to enhance calculation speed.

Second, the geometric symmetry of the coil was utilized to eliminate redundant calculations. This approach can be applied not only to saddle-shaped magnets but also to any magnet with a symmetrical structure. By implementing these two techniques, computation time was reduced to 90.4% of the original, significantly accelerating the circuit analysis process without loss of accuracy as shown in Figure 2.5 [113].

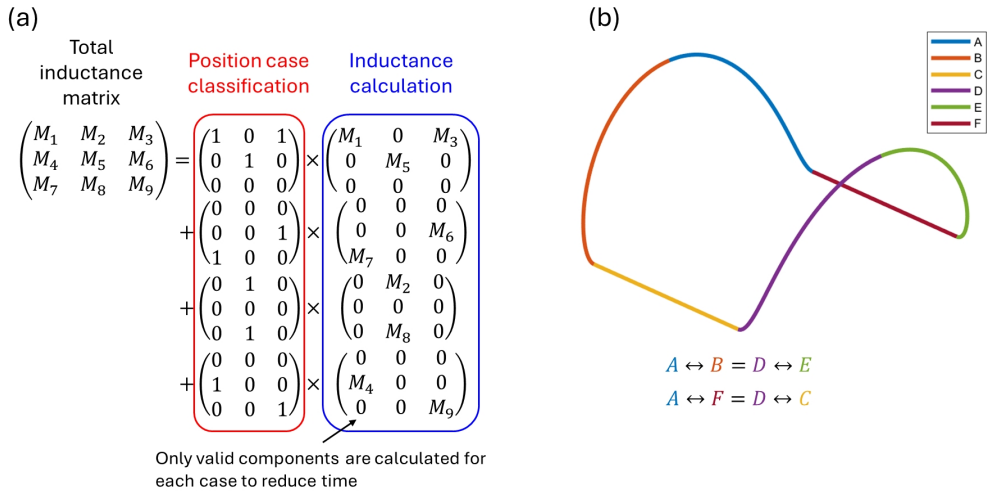

Figure 2.4: Methods for improving inductance calculation speed. (a) Schematic of the vectorization method, (b) example of symmetry in one turn of a saddle-shaped magnet.

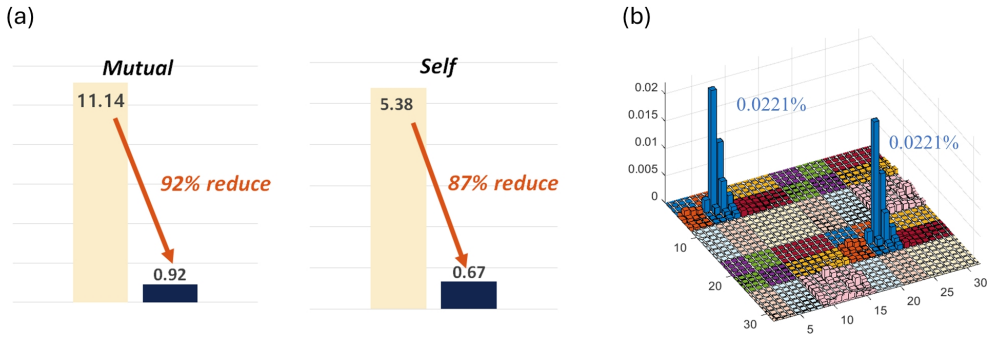

Figure 2.5: The effect of reducing inductance calculation time and its error. (a) Reduction in computation time when applying the inductance calculation speed enhancement method, (b) representation of computation error.

2.3 Critical Current Estimation of HTS Magnet

REBCO coated conductors exhibit a characteristic where the critical current varies depending on the strength and incident angle of the magnetic field. Additionally, due to the material's nature, it is manufactured with a wide width and thin thickness, leading

to significant variations in critical current across the width during magnet operation. As a result, unlike low-temperature superconducting (LTS) magnets, where the critical current could be predicted simply by considering the magnetic field strength, predicting the critical current in HTS magnets has been more challenging. Researchers have calculated critical currents using different criteria without a clear definition of effective critical current of magnet. In fact, a bigger issue is that researchers have used different critical current data, making it difficult to compare their analysis results. To address these challenges, this study suggests three approaches: 1) defining basis critical current data; 2) introducing a widthwise average method for effective critical current estimation; and 3) load-line margin estimation with consideration of temperature variance.

2.3.1 Anisotropic Property of REBCO Critical Current and Fit Function

Factors affecting the critical current of REBCO include the magnetic field strength, magnetic field angle of incidence, temperature, and strain. During the manufacturing and operation of the magnet, as many of these factors as possible should be considered to predict the critical current and provide sufficient current margin. However, predicting the magnet's temperature during the design phase is challenging, and temperature gradients can occur depending on the cooling conditions. Therefore, the critical current of the magnet is typically estimated based on the worst-case temperature scenario. Regarding strain, the magnetic field strength and current density are designed to prevent any reduction in critical current due to strain, making magnetic field strength and angle of incidence the most critical factors in predicting the magnet's critical current. Notably, REBCO conductors exhibit a unique dependence of critical current on the magnetic field angle, unlike other types of superconducting wires. As a result, it is common to use approximation formulae for critical current based on the magnetic field angle. In this study, an approximation formulae for the critical current using Hilton's fitting function [114], one of the most widely used models, was constructed. The for-

mulae used is as follows:

$$I_c(|\mathbf{B}|,\theta) = \frac{k_0}{(|\mathbf{B}|+\beta_0)^{\alpha_0}} + \frac{k_1}{(|\mathbf{B}|+\beta_1)^{\alpha_1}} \frac{1}{\xi(|\mathbf{B}|,\theta)}, \tag{2.15}$$

$$\xi(|\mathbf{B}|,\theta) = \sqrt{\omega^2(|\mathbf{B}|)\cos^2(\theta-\phi) + \sin^2(\theta-\phi)}, \tag{2.16}$$

$$\omega(|\mathbf{B}|) = c(|\mathbf{B}| + (\frac{1}{c})^{\frac{1}{\eta}})^{\eta}, \tag{2.17}$$

where θ is field incidence angle. The measurement results from the Robinson Research Institute [115] were used to determine the coefficients of the approximation formula. A genetic algorithm was employed to find the combination of coefficients that minimized the average error across all measured values. Additionally, it is possible to fit the coefficients' variation with respect to temperature, allowing the critical current to be expressed as a function of temperature, magnetic field strength, and magnetic field angle of incidence. The fitting functions for the temperature dependence of the coefficients for the conductor used in this study are as follows:

$$I_c(|\mathbf{B}|,\theta,T) = \frac{k_0(T)}{(|\mathbf{B}|+\beta_0(T))^{\alpha_0(T)}} + \frac{k_1(T)}{(|\mathbf{B}|+\beta_1)^{\alpha_1}} \frac{1}{\xi(|\mathbf{B}|,\theta,T)}, \tag{2.18}$$

$$\xi(|\mathbf{B}|,\theta,T) = \sqrt{\omega^2(|\mathbf{B}|,T)\cos^2(\theta-\phi) + \sin^2(\theta-\phi)}, \tag{2.19}$$

$$\omega(|\mathbf{B}|,T) = c(T)(|\mathbf{B}| + (\frac{1}{c(T)})^{\frac{1}{\eta}})^{\eta}, \tag{2.20}$$

$$k_0(T) = -7.221T + 635.1, \tag{2.21}$$

$$k_1(T) = -32.50T + 2845, \tag{2.22}$$

$$\alpha_0(T) = 0.03345e^{0.04672T} + 0.4190, \tag{2.23}$$

$$\beta_0(T) = 0.005326T + 0.005788, \tag{2.24}$$

$$c(T) = 2.713e^{0.02906T} - 2.713, \tag{2.25}$$

$$\alpha_1 = 0.1, \quad \beta_1 = 0.65, \quad \phi = 0, \quad \eta = 1.6. \tag{2.26}$$

Figure 2.6 shows fitting results of critical current at 1, 2, and 3 T of field range and 15, 20, 25 K of temperature range. The average error between the fitting function and reference is 6.5%.

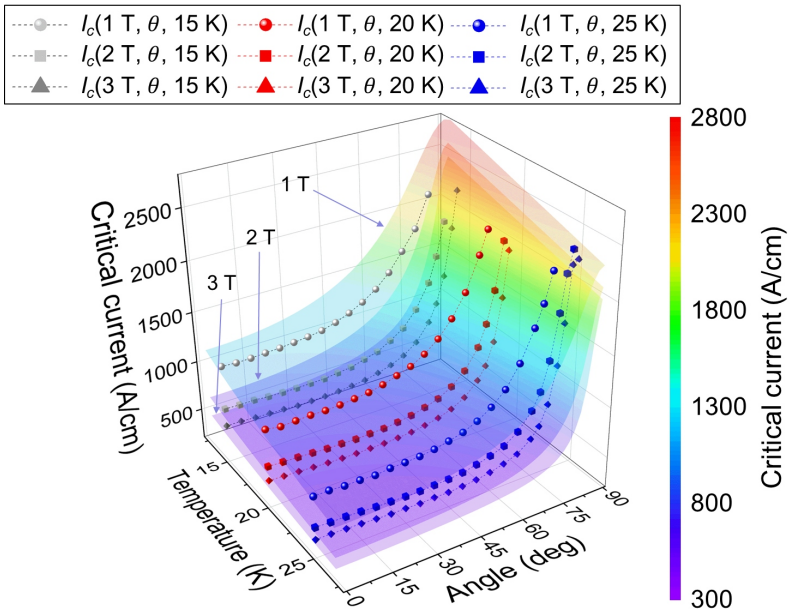

Figure 2.6: Comparison of the critical current fitting function with measured data for magnetic field strength, incident angle, and temperature.

2.3.2 Basis Critical Current Data

The first step in calculating the critical current of REBCO magnets is deciding which critical current data to use. The Robinson Research Institute, mentioned earlier, provides measurement data for various types of HTS conductors. However, due to the inconsistency in the critical current of HTS conductors, it is challenging to apply these measurements directly to magnet designs. In some cases, exceptionally high critical current values may have been recorded from high-quality sample conductors. As a result, many researchers conduct separate assessments to determine how much lower the critical current might be for the actual conductors used, compared to the measured values. Others use a proportional constant called the 'lift factor' to predict the critical current. However, since each researcher adopts a different approach, this lack of standardization creates challenges for research and magnet design.

In this study, we defined 'basis' critical current data and shared it with domestic

researchers to ensure that related studies and projects using the same superconducting conductors would utilize consistent data. This is the first attempt to standardize critical current data at the national level. A challenge in defining the basis critical current data was the limited range of available measurements. Since data for all temperature and magnetic field ranges were not available, appropriate extrapolation techniques had to be applied. The temperature and magnetic field angle were fixed at specific values, and extrapolation was performed for magnetic field strength to generate a critical current table covering values up to 50 T. The extrapolation function for magnetic field strength is as follows:

$$I_{c,\theta,T}(|\mathbf{B}|) = \frac{a}{(|\mathbf{B}|^{4.5} + b)^c}, \tag{2.27}$$

where a, b, and c are fitting parameters for extrapolation. The values within the critical current table were then used through interpolation.

2.3.3 Widthwise Average Method for Effective Critical Current Estimation

Finally, a key challenge in analyzing the critical current of HTS magnets is determining the effective critical current when there is a distribution of critical currents across the width of the conductor. Typically, two main approaches have been used: 1) using the minimum value of the critical current distribution across the width, and 2) using the average value. However, since no definitive research has established a clear answer, a mix of these methods has been applied in practice.

To address this issue, the distributed circuit model discussed in the previous section was used to simulate the REBCO conductor as shown in Figure 2.7 (a) [116]. The REBCO tape was divided into small units along both its width and length, with each unit modeled as a circuit element consisting of resistance and inductance. The critical current distribution across the width was then calculated by considering both the magnetic field generated by the current flowing through the conductor and the lift factor as shown in Figure 2.7 (b). Additionally, the voltage across both ends of the conductor

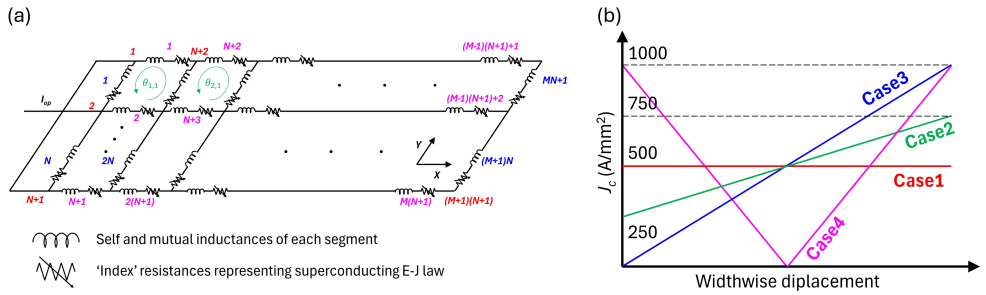

Figure 2.7: Circuit model and critical current distribution assumptions for validating the widthwise average method. (a) Distributed circuit model for critical current estimation, (b) representation of critical current distribution for each case.

Table 2.1: Analysis results of effective critical current for each case

	Case1	Case2	Case3	Case4
Average critical current	205 A			
Effective critical current	205.0 A	204.5 A	202.7 A	203.0 A

was calculated using the circuit model to determine the effective critical current.

The calculation results showed that the effective critical current was closer to the average value than the minimum value as displayed in Table 2.1, with the difference from the average value varying depending on the case but within 1.2%. These results were also demonstrated in the quench experiment results which will be described in following section.

2.3.4 Load-line Method with Consideration of Temperature Variation

The critical current value of a magnet under specific operating conditions is determined by the magnetic field generated by the magnet and an externally applied fixed magnetic field. However, to calculate the critical current margin of the magnet, it is necessary to consider the load-line margin [117]. This method accounts for the inverse relationship between critical current and the increasing magnetic field as the operating

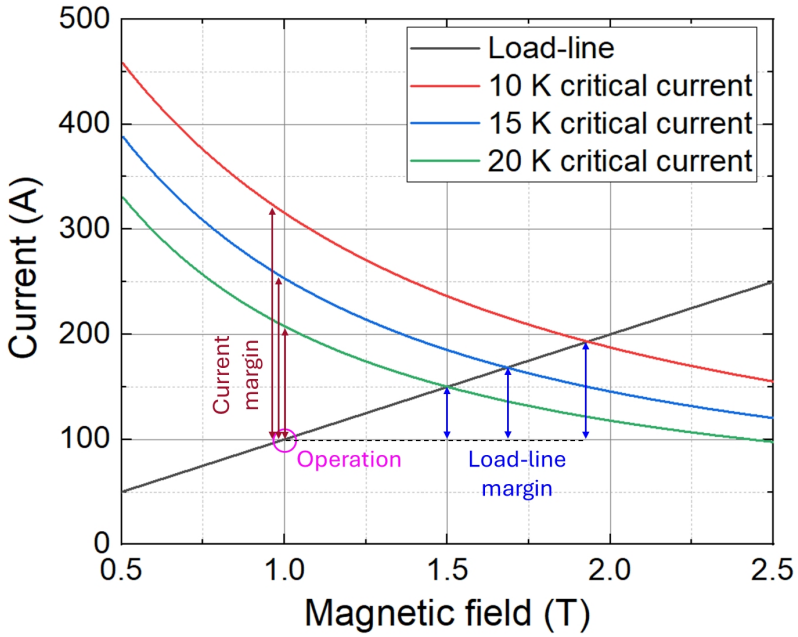

Figure 2.8: Example of calculating the load-line margin of the critical current considering temperature variations

current of the superconducting magnet rises. Traditional load-line margin calculations only considered the load-line due to current. However, in actual operating conditions, the increase in current also leads to greater heat generation in components such as current leads, resulting in a temperature rise. Therefore, when considering the load-line, it is essential to account for the reduction in critical current caused by both the increasing magnetic field and the associated temperature rise. In the previous section, a fitting function was proposed to account for changes in critical current with temperature. This function can be utilized to analyze the load-line.

As shown in Figure 2.8, if the operating conditions are set at 1 T and 100 A, with an assumed operating temperature of 10 K, the critical current margin is 68%, whereas the load-line margin is 47%. Although these values may vary depending on the situation, the load-line margin is generally about half of the critical current margin under such operating conditions. However, if the operating temperature rises due to

increased current flow in the magnet, it becomes necessary to consider the margin at higher temperatures. For example, if the operating temperature increases to 15 K or 20 K, the load-line margin decreases to approximately 40% and 33%, respectively. Since HTS magnets often exhibit high stability and are operated at margins lower than these values, it is essential to monitor temperature variations and estimate the margin accordingly.

2.4 Magnetic Field Calculation Method

For saddle-shaped dipole magnets used in particle accelerators, magnetic field uniformity is crucial. If the magnetic field is not sufficiently uniform, the beam may be lost, or the desired beam characteristics may not be achieved, rendering the particle accelerator unusable. In theory, applying a cosine-theta winding can create a uniform magnetic field with only a dipole component. However, that is practically impossible. In reality, the spatial distribution of the magnetic field generated by the dipole magnet contains not only dipole components but also other field components in different directions. When expressed in terms of spatial harmonic functions, these higher-order components are referred to as quadrupole, sextupole, octupole, and so on. This section describes the method of expressing harmonic functions for dipole magnets and explains how the harmonic coefficients are calculated in this study.

2.4.1 Harmonic Coefficient for Dipole Magnet

For magnets requiring magnetic field uniformity, representing the spatial distribution of the magnetic field using harmonic functions offers advantages. Magnetic field uniformity u is defined as follows [118–120]:

$$u = \max\left(\left|\frac{B_{y,R_{ref}} - B_{y,0}}{B_{y,0}}\right|\right), \tag{2.28}$$

where $B_{y,R_{ref}}$ and $B_{y,0}$ represent magnetic field in the direction of the dipole component within the reference radius, and magnetic field at the center, respectively. Even

if a magnet is designed and fabricated precisely, screening current or manufacturing tolerances can cause deviations from the intended magnetic field distribution. To correct this, active [121–123] and passive shimming [124–126] techniques are applied. Active shimming involves installing additional coils and adjusting the current to improve field uniformity, while passive shimming uses magnetizable iron shims rather than coils to enhance uniformity. Since the performance of these shimming techniques is influenced by each component of the harmonic function, the use of harmonic functions is essential. Furthermore, in particle accelerator magnets, higher-order terms of harmonic functions, which affect beam chromaticity and other factors, are directly output, making harmonic analysis crucial. As shown in Figure 2.9, the harmonic components of a magnetic field are named in order from lower to higher terms as dipole, quadrupole, sextupole, octupole, and so on. If an offset orthogonal component exists for each term, it is designated as skew dipole, skew quadrupole, etc.

To calculate the harmonic components in a dipole magnet, let's assume the designed dipole magnetic field direction is along the +y direction on a two-dimensional plane. To analyze the normal and skew magnetic field components, the position and direction of the magnetic field can be defined on the complex plane. Assuming a straight line carrying current I is located at position $z_0 = x_0 + \mathrm{i}y_0$, the magnetic field $B(z) = B_y(z) + \mathrm{i}B_x(z)$ at position $z = x + \mathrm{i}y$ can be expressed by the following equation [127, 128]:

$$\begin{aligned} B(z) = \tfrac{\mu_0 I}{2\pi(z-z_0)} &= -\tfrac{\mu_0 I}{2\pi z_0} \sum_{k=1}^{\infty} (\tfrac{R}{z_0})^{k-1} (\tfrac{z}{R})^{k-1} \\ &= \sum_{k=1}^{\infty} (B_k + \mathrm{i}A_k)(\tfrac{z}{R})^{k-1} \\ &= B_1(1 + 10^{-4} \sum_{k=2}^{\infty} (b_k + \mathrm{i}a_k)(\tfrac{z}{R})^{k-1}), \end{aligned} \quad (2.29)$$

where R is the reference radius for magnetic field distribution. If the magnetic field is symmetric about the y-axis, there will be no skew components, and even components of the normal term b_k will also be absent.

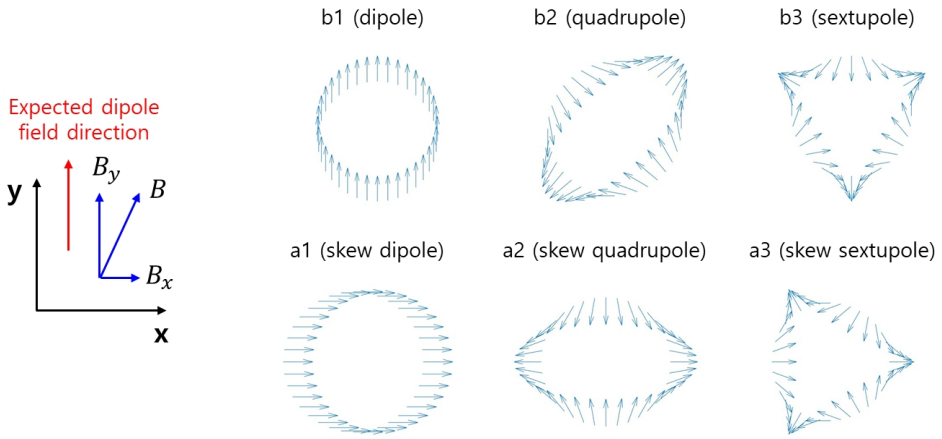

Figure 2.9: Representation of the direction of each magnetic field harmonic component

2.4.2 Magnetic Field and Harmonic Coefficient Generated by HTS Magnet

To design the magnet, the magnetic field generated by an infinite straight conductor in two dimensions can be calculated. The magnetic field produced by an infinite conductor is easily derived using Ampere's law. Now, as shown in Figure 2.10, the magnetic field generated by the area corresponding to the infinite conductor is computed. Considering the stacking structure of the REBCO tape, the current-carrying region can be parameterized as follows:

$$z_0 = r_0 e^{\mathrm{i}\theta'} + t e^{\mathrm{i}\theta_1}, \tag{2.30}$$

$$\text{where} \quad \theta_0 \leq \theta' \leq \theta_0 + \Delta\theta,$$

$$\text{and} \quad 0 \leq t \leq w,\ \theta_1 = \theta_0 + \alpha.$$

The position where the magnetic field is analyzed is defined as $z = Re^{\mathrm{i}\theta}$. Additionally, if a current J flows in the coil located in the first quadrant, a coil with a reverse current of $-J$ must exist in the second quadrant. Since the coils are positioned as pairs, a symmetric structure of coils must exist in the third quadrant with a current of $-J$, and in the fourth quadrant with a current of J. Therefore, the magnetic field

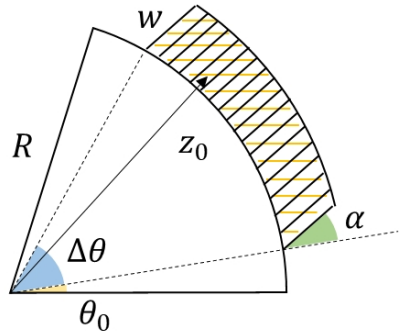

Figure 2.10: Schematic of the 2D coil geometry and parameter definitions

generated by these four current distributions can be expressed as follows:

$$\begin{aligned} B(z) &= -\frac{\mathrm{i}\mu_0 JR}{2\pi}\int_0^w\int_{\theta_0}^{\theta_0+\Delta\theta}\cos(\theta'-\theta_1)\times \\ &\qquad (\frac{1}{z_0^*-z^*}+\frac{1}{z_0^*+z^*}+\frac{1}{z_0^*-z}+\frac{1}{z_0^*+z})d\theta' dt, \\ &= -\frac{\mathrm{i}\mu_0 JR}{\pi}\int_0^w\int_{\theta_0}^{\theta_0+\Delta\theta}\frac{\cos(\theta'-\theta_1)}{z_0^*}\sum_0^{k=2n}((\frac{z^*}{z_0^*})^k+(\frac{z}{z_0^*})^k)d\theta' dt, \end{aligned} \tag{2.31}$$

$$\therefore B_k+\mathrm{i}A_k = -\frac{\mathrm{i}\mu_0 J}{\pi}\int_0^w\int_{\theta_0}^{\theta_0+\Delta\theta}\cos(\theta'-\theta_1)(1+e^{-\mathrm{i}2k\theta})\frac{R^{k+1}}{z_0^{k+1}}d\theta' dt, \tag{2.32}$$

where z^* and z_0^* represents conjugate complex numbers. The above equation cannot be expressed in a closed form and was calculated using numerical integration.

Designing an actual magnet requires more than assuming a magnetic field generated by an infinite straight conductor in two dimensions. Real magnets have a three-dimensional shape, and the effects of magnetic fields generated by curved sections, not just straight sections, should be considered. Since there is no closed-form solution for the magnetic field created by curved sections, numerical methods should be used. Similar to the method used for inductance calculation, the magnetic field generated by a current flowing through small rectangular segments can be calculated, allowing for the determination of the magnetic field distribution once the overall shape of the magnet is defined.

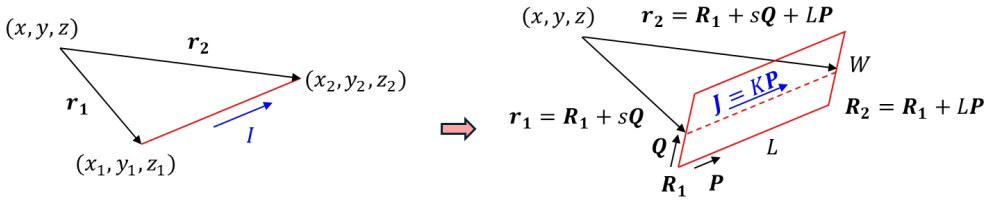

Figure 2.11: Derivation of the formula for the magnetic field generated by an arbitrary rectangle in 3D space based on the magnetic field created by a line segment with zero thickness

As shown in Figure 2.11, the magnetic field generated by a line segment is first calculated, and this result is used to compute the magnetic field created by a rectangular segment. If the starting point of the line segment is (x_1, y_1, z_1), the endpoint is (x_2, y_2, z_2), the current flowing through the segment is I, and the position where the magnetic field is calculated is (x, y, z), then the magnetic field can be calculated using the Biot-Savart law as follows:

$$\mathbf{B}(x,y,z) = \frac{\mu_0 I}{4\pi} \frac{\mathbf{r}_1 \times \mathbf{r}_2}{|\mathbf{r}_1||\mathbf{r}_2|} \frac{|\mathbf{r}_1| + |\mathbf{r}_2|}{|\mathbf{r}_1||\mathbf{r}_2| + \mathbf{r}_1 \cdot \mathbf{r}_2}, \tag{2.33}$$

$$\mathbf{r}_1 = (x_1 - x, y_1 - y, z_1 - z), \tag{2.34}$$

$$\mathbf{r}_2 = (x_2 - x, y_2 - y, z_2 - z). \tag{2.35}$$

Then, the magnetic field generated by thin rectangular segment can be expressed by using surface current density K as follows:

$$\mathbf{B}(x,y,z) = \frac{\mu_0 K}{4\pi} \int_0^W \frac{\mathbf{r}_1 \times \mathbf{r}_1}{|\mathbf{r}_1||\mathbf{r}_2|} \frac{|\mathbf{r}_1| + |\mathbf{r}_2|}{|\mathbf{r}_1||\mathbf{r}_2| + \mathbf{r}_1 \cdot \mathbf{r}_2} ds. \tag{2.36}$$

2.4.3 Calculation of Magnetic Field Generated by Magnetic Moment

In this study, a ferroshim design using iron shims was developed, fabricated, installed, and tested for performance. Consequently, it was also necessary to calculate the magnetic field generated by the magnetized iron shims. The shape of the iron shim was assumed to be part of the coil core, and as shown in Figure 2.12, the space occupied

by the shim can be defined in cylindrical coordinates as (r, θ, Z) where $r_1 \leq r \leq r_2$, $\theta_1 \leq \theta \leq \theta_2$, and $z_1 \leq Z \leq z_2$. Assuming the magnetic field generated by the magnet is in the +x direction, the magnetic vector potential created by the shim at (x, y, z) can be expressed as follows:

$$\mathbf{A}(x,y,z) = \frac{\mu_0 \delta m}{4\pi} \int_{z_1}^{z_2} \int_{\theta_1}^{\theta_2} \int_{r_1}^{r_2} \frac{(0, Z-z, y - r\cos\theta) r dr d\theta dZ}{((x - r\cos\theta)^2 + (y - r\sin\theta)^2 + (z-Z)^2)^{3/2}}, \tag{2.37}$$

$$\mathbf{m} = \int_{z_1}^{z_2} \int_{\theta_1}^{\theta_2} \int_{r_1}^{r_2} (\delta m, 0, 0) r dr d\theta dz, \tag{2.38}$$

where $\mathbf{m}$ and δm represent magnetization vector and volume density of magnetization, respectively. Therefore, magnetic field generated by the shim can be calculated as follows:

$$\begin{aligned} B_x(x,y,z) &= \frac{\partial A_z}{\partial y} - \frac{\partial A_y}{\partial z} \\ &= \frac{\mu_0 \delta m}{4\pi} \int_{z_1}^{z_2} \int_{\theta_1}^{\theta_2} \int_{r_1}^{r_2} \frac{\partial}{\partial y} \frac{(y - r\cos\theta) r dr d\theta dZ}{((x - r\cos\theta)^2 + (y - r\sin\theta)^2 + (z-Z)^2)^{3/2}} \\ &\qquad - \frac{\partial}{\partial z} \frac{(Z - z) r dr d\theta dZ}{((x - r\cos\theta)^2 + (y - r\sin\theta)^2 + (z-Z)^2)^{3/2}}. \end{aligned} \tag{2.39}$$

This integral does not have a closed-form solution, but an analytic solution can be derived up to a single integral remaining. The remained single integral can then be calculated using numerical integration techniques such as Gaussian quadrature.

2.5 End-coil Winding Path Optimization and Mechanical Analysis Method

The saddle-shaped magnet has a nonplanar structure, requiring a different structural analysis approach than planar magnets like solenoids or racetrack-shaped magnets. The most challenging area is the curved end-part of the coil. In the case of REBCO conductors with a wide, thin tape shape, the end-part can face issues related to hard-way bending. To prevent these issues, a mechanical optimization technique for the

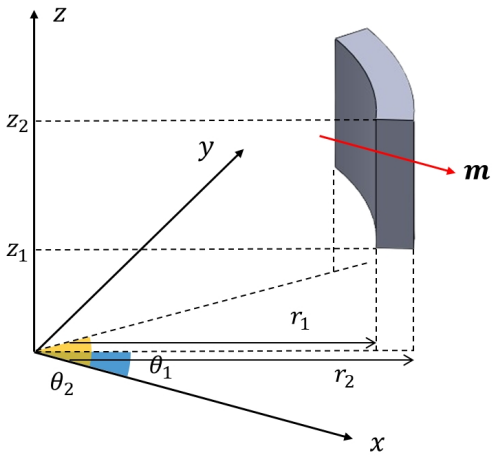

Figure 2.12: Definition of parameters for calculating the magnetic field generated by a magnetized iron piece in 3D space

end-part was developed. Additionally, an analysis model for the mechanical stresses caused by the magnetic field and thermal contraction-induced stress is presented.

2.5.1 Introduction to Frenet-Serret Frame

The Frenet-Serret frame is a mathematical framework that provides a natural coordinate system for describing the geometry of a curve in three-dimensional space [127, 129]. This frame is defined at each point along a differentiable curve, allowing the analysis of the curve's local geometric properties such as curvature and torsion. Consider a differentiable curve in 3D space, parameterized by $r(s)$, where s is the arc length, ensuring that the curve's parameterization has unit speed:

$$|\frac{dr}{ds}| = 1. \tag{2.40}$$

Then, the Frenet-Serret frame consists of three mutually orthogonal unit vectors at

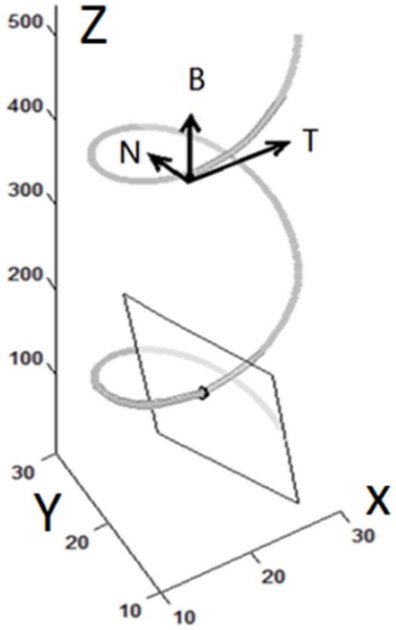

Figure 2.13: Schematic of the Frenet-Serret frame for a 3D curve [130].

each point on the curve:

$$T(s) = \frac{dr}{ds}, \tag{2.41}$$

$$N(s) = \frac{dT/ds}{|dT/ds|}, \tag{2.42}$$

$$B(s) = T(s) \times N(s), \tag{2.43}$$

where $T(s)$, $N(s)$, and $B(s)$ are named as a tangent vector, a normal vector, and a binormal vector, respectively. These three vectors form an orthonormal basis known as the Frenet-Serret frame as shown in Figure 2.13.

The evolution of the Frenet-Serret frame along the curve is governed by the Frenet-Serret equations, which describe how the frame rotates and changes:

$$\begin{pmatrix} \frac{dT}{ds} \\ \frac{dN}{ds} \\ \frac{dB}{ds} \end{pmatrix} = \begin{pmatrix} 0 & \kappa & 0 \\ -\kappa & 0 & \tau \\ 0 & -\tau & 0 \end{pmatrix} \begin{pmatrix} T \\ N \\ B \end{pmatrix}, \tag{2.44}$$

where κ and τ are the curvature and the torsion of the curve, respectively. The curvature indicates how sharply the curve bends while the torsion describes the deviation of the curve from being planar. A zero torsion indicates that the curve lies entirely in a plane. By decomposing motion and geometry into orthogonal components, it facilitates the understanding of complex trajectories and forces acting along them.

2.5.2 Practical End-coil Optimization Method with Constant Perimeter Winding Technique Incorporated

One of the purposes of the coil-end design is to minimize the strain energy due to the bending at the coil-end [127]. The so-called 'constant perimeter winding' technique, which refers to both edges of the REBCO conductor following the curves of the same length, was adopted. Using this approach, the hard-way bending can be reduced in the saddle-shaped coil.

To define the surface of the conductor wound with constant perimeter conditions, both edges' curves should be defined first. The edge lying on the cylindrical winding mandrel is named 'base edge,' while the counterpart is called 'free edge.' The base edge can follow any arbitrary smooth curve as long as it lies on the cylinder. Still, it has been generally modeled to follow an ellipse or superellipse on the cylinder due to the ease of modeling. Although ellipse modeling is more accessible than superellipse modeling, the curvature continuity is not satisfied at the part where the straight and coil-end sections of ellipse modeling are connected.

Theoretically, a perfect 'hard-way-bending-free' condition can be achieved by the angular velocity vector (or the Darboux vector field) to the base edge's curve [127]. However, for practical coil winding, the angular velocity vector is inadequate to determine the free edge's curve; thus, we developed a numerical method to determine the free edge's curve that satisfies the constant perimeter condition. First, the base edge's curve as shown in figure 2.14 (a), $X(t)$, can be expressed as follows:

$$X(t) = (r\sin(\psi\cos^{\frac{2}{m}}t), b\sin^{\frac{2}{m}}t, r\cos(\psi\cos^{\frac{2}{m}}t)), \quad (0 \leq t \leq \frac{\pi}{2}) \tag{2.45}$$

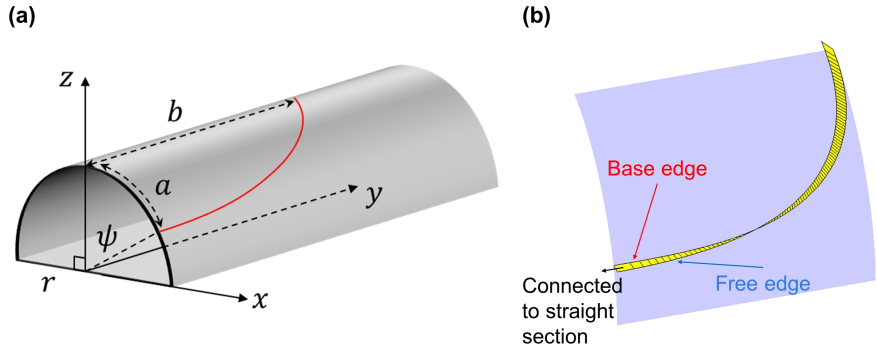

Figure 2.14: Parameter setting for the end-coil design optimization method. (a) A schematic of ellipse or superellipse on the surface of the cylinder. The red line represents the base edge's curve, $X(t)$. (b) An example modeling result of the practical coil-end design with constant perimeter winding technique incorporated.

where r, ψ, and b represent the radius of the cylinder, the end part angle from the Z-axis, and the semimajor axis, respectively. Then, the semiminor axis, a, can be determined as $a = \psi r$. The parameter m determines the shape of the base edge, so the base edge is ellipse when $m = 2$ while it is superellipse when $m > 2$.

Second, the free edge's curve, $Y(t)$, was modeled by the following steps:

- (Step 1) At $t = t_0$, consider the plane where the normal vector is the tangent vector of the base edge's curve. Find the line of intersection between the cylinder and the plane.
- (Step 2) Find the point P on the plane where $P - X(t_0)$ is inclined with the angle of $\theta(t_0)$. Also, the magnitude of $P - X(t_0)$ should be the width of the conductor.
- (Step 3) $Y(t)$ depends on the inclination angle function $\theta(t)$, so we determined an adequate inclination angle function satisfying the constant perimeter condition.

Thus, $Y(t)$ can be induced by the steps as stated above and the expression is as follows:

$$Y(t) = (y_x(t), y_y(t), y_z(t)), \quad (0 \leq t \leq \frac{\pi}{2}) \tag{2.46}$$

$$y_x(t) = (r + W\sin(\theta(t)))\sin(\psi\cos^{\frac{2}{m}} t) - \frac{bW\cos(\theta(t))}{\sqrt{b^2 + \psi^2 r^2 \tan^{\frac{4}{m}} t}}\cos(\psi\cos^{\frac{2}{m}} t), \tag{2.47}$$

$$y_y(t) = b\sin^{\frac{2}{m}} t - \frac{\psi r W\cos(\theta(t))}{\sqrt{b^2 + \psi^2 r^2 \tan^{\frac{4}{m}} t}}\tan^{\frac{4}{m}} t, \tag{2.48}$$

$$y_z(t) = (r + W\sin(\theta(t)))\cos(\psi\cos^{\frac{2}{m}} t) + \frac{bW\cos(\theta(t))}{\sqrt{b^2 + \psi^2 r^2 \tan^{\frac{4}{m}} t}}\sin(\psi\cos^{\frac{2}{m}} t). \tag{2.49}$$

Then, an example for the modeling results with the described procedure is presented in figure 2.14 (b) [108].

The equations for the path described above can be analyzed using the Frenet-Serret frame to calculate the bending strain. This approach can be found in references that calculate strain for REBCO conductors [131]. If the distance from the neutral axis of the conductor is defined as y, the bending strain can be calculated as follows:

$$\epsilon = y\frac{\kappa^2 + \tau^2}{\kappa}, \tag{2.50}$$

$$\epsilon_T = y\sqrt{\kappa^2 + \tau^2}, \tag{2.51}$$

$$\epsilon_B = y\frac{\tau}{\kappa}\sqrt{\kappa^2 + \tau^2}, \tag{2.52}$$

where ϵ, ϵ_T, and ϵ_B represent total bending strain, bending strain along the lengthwise direction, and that along the widthwise direction, respectively. The above equation was utilized in the design process to ensure that the strain limit was not exceeded.

2.5.3 Magnetic Stress Analysis for Saddle-shaped Magnet

The current flowing through the saddle-shaped magnet generates a magnetic field, and since this current flows within the magnetic field, the magnet experiences Lorentz

Table 2.2: Effective mechanical properties for REBCO conductor

Parameter	**Unit**	**Value**
Effective Young's modulus, E	[GPa]	175
Effective Poisson's ratio, ν		0.280
Effective Shear modulus, G	[GPa]	65.0

forces. This indicates that the magnet undergoes mechanical stress, and both stress and strain can affect magnet damage or critical current reduction, making it essential to design within safe limits. Unlike solenoid magnets, saddle-shaped magnets with nonplanar structures lack analytic approximations for stress calculations. Therefore, mechanical analysis should be conducted using FEM, and appropriate boundary conditions must be assumed for problematic areas. Even slight changes in boundary conditions can significantly affect the analysis results, so it is crucial to assume realistic conditions carefully.

In the manufacturing method introduced in the upcoming section, certain areas of the saddle-shaped magnet are constrained: the inner surface of whole area; and the outer and top surface of the coil's straight section. The inner surface is supported by the bobbin, and the outer surface is constrained by an external support structure. Additionally, the top surface is covered by a capping structure, allowing a boundary condition to be applied where no normal direction displacement occurs $(\mathbf{u} \cdot \hat{n} = 0)$ in the areas marked in blue in Figure 2.15 (a). The mechanical properties used in the analysis are shown in Table 2.2 [132].

When conducting FEM analysis under these conditions, as shown in Figure 2.15 (b), a displacement tendency arises where the curved section of the coil moves downward, while the straight section displaces outward through the top surface. However, since the coil is positioned on a cylindrical aperture, downward displacement is not allowed. Therefore, it is reasonable to apply an additional boundary condition where there is no vertical displacement on the underside of the curved section as shown in

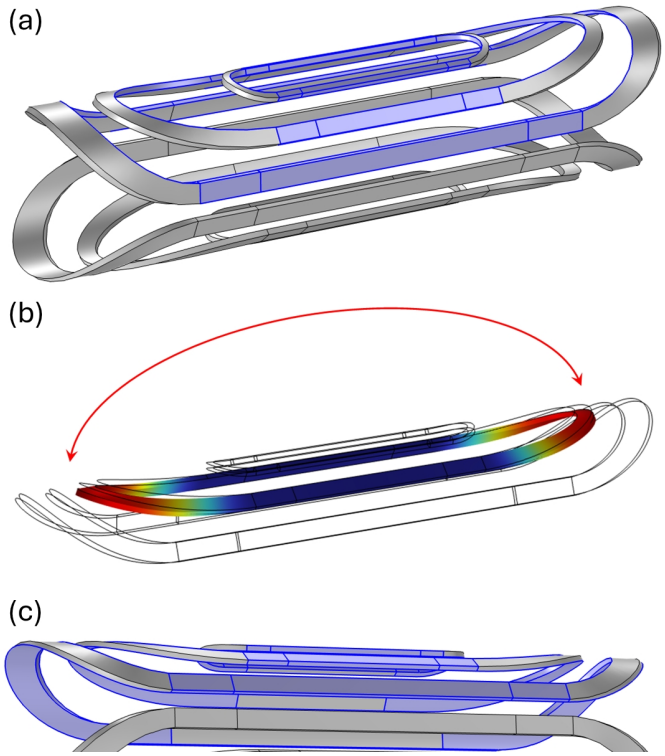

Figure 2.15: Development of an analytical model to determine boundary conditions. (a) Initial attempt for 3D boundary conditions, where blue boundaries represent conditions with no normal displacement. (b) Analytical results from (a), considering the direction of displacement in the curved section. (c) Modified 3D boundary conditions.

Figure 2.15 (c). For the top surface of the straight section, manufacturing tolerances might prevent the cover structure from completely constraining all areas. Thus, allowing vertical displacement with a maximum displacement limit for the top surface of the straight section would better reflect practical conditions.

Considering these boundary conditions, it is possible to perform a 2D analysis for the straight section's mechanical analysis without needing a computationally intensive 3D analysis. In this approach, boundary conditions were applied such that there was no vertical displacement on the inner and outer surfaces, with a displacement limit imposed on the top surface. The need for 2D analysis arises because it is challenging

to analyze the screening-current-induced-stress (SCS) phenomenon, which plays an essential role in HTS magnets, in a 3D context.

2.5.4 Stress due to Thermal Contraction of Magnet System

Since superconducting magnets can only operate in cryogenic environments, it is essential to account for thermal contraction. Most materials used in magnet systems are metals, and these metals have relatively similar thermal contraction rates. However, even small deformations due to thermal contraction can significantly impact the uniformity of the magnetic field generated by saddle-shaped magnets, making a thermal contraction analysis model necessary.

Unlike solenoid magnets, which allow analytic calculations in 2D, saddle-shaped magnets require 3D analysis for thermal contraction. Using the previously defined boundary conditions, thermal contraction analysis can be conducted under the condition of cooling from an initial room temperature to cryogenic temperatures. Since the coil and bobbin are made of different materials, differences in thermal contraction rates arise. The bobbin used in the experiment is made of aluminum 6061. The thermal expansion coefficients of REBCO and aluminum as a function of temperature, used in the thermal contraction analysis, are shown in Figure 2.16 [133–135]. Assuming an operating temperature of 15 K, the scenario of thermal contraction when cooling from room temperature (293 K) to 15 K can be analyzed.

The results of displacement analysis during the thermal contraction process of the coils are shown in Figure 2.17. Considering the boundary conditions, the curved sections of coil 1 and coil 2 exhibit displacement in an upward direction. In contrast, coil 3 does not exhibit this phenomenon. This trend was also observed experimentally, and the corresponding results will be discussed in a later chapter.

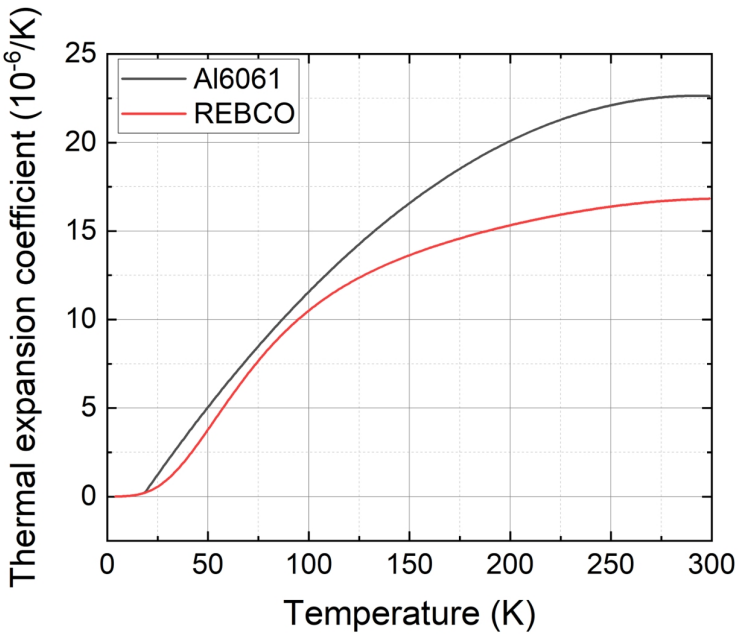

Figure 2.16: Thermal expansion coefficients used for thermal contraction analysis according to temperature

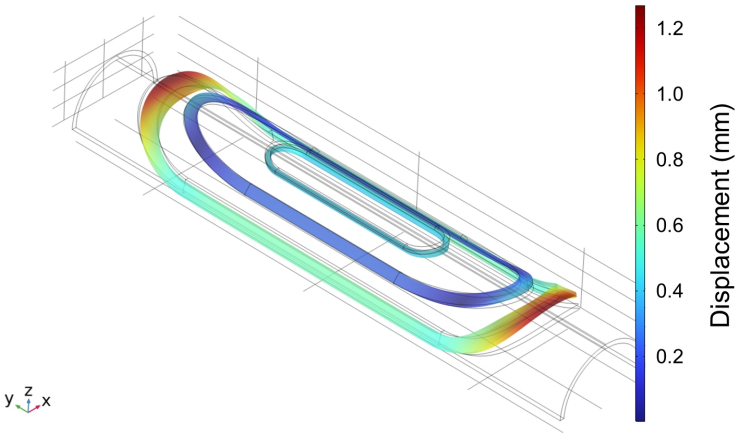

Figure 2.17: Example of displacement analysis under thermal contraction conditions down to the operating temperature

Chapter 3

DESIGN, CONSTRUCTION, AND OPERATION OF SADDLE-SHAPED DIPOLE MAGNET

This chapter describes the magnet design process, applying various design and analysis techniques discussed in the previous chapter. Additionally, the entire system, including external structures as well as the superconducting magnet, was designed. The chapter also discusses the detailed fabrication of the magnet, the installation process of the system, and the setup for operation in a conduction-cooled environment. The magnet constructed and operated in this study was designed with a maximum center magnetic field of 0.7 T, a winding diameter of 110 mm, and an operating temperature of 15 K.

3.1 Design of Main Magnet with a Center Field of 0.7 T and Winding Diameter of 110 mm

If only the design is considered, it is possible to assume a magnet with an extremely high magnetic field, such as 20 T. However, due to practical limitations, the dipole magnet was designed with a central magnetic field of 0.7 T and a winding diameter of 110 mm. This magnet, utilized for key experiments, is referred to as the ‘main magnet,’ while the simpler magnet used for preliminary tests is called the ‘demo magnet.’

The demo magnet was constructed earlier in sequence, and the issues identified and improvements made from it contributed to the successful operation of the main magnet. The central magnetic field strength was optimized to achieve the highest possible field while maintaining sufficient field uniformity, considering the limitations on the amount of conductor available. The winding diameter was determined based on the size of the warm bore needed for measuring magnetic field uniformity. Additionally, an analysis of the mechanical analysis that determines the operating conditions of the magnet was performed, along with a thermal analysis for a conduction-cooled environment. For the thermal analysis, a thermal circuit was proposed that includes both the conduction cooling system and the magnet.

3.1.1 Design Directions and Expected Limitations

Purpose of Magnet and Design Directions

The best approach to investigate the applicability of saddle-shaped magnets in particle accelerators is to fabricate a magnet that can be installed in an actual accelerator system for testing and validation. However, installing high-temperature superconductor (HTS) saddle-shaped magnet in a synchrotron used as a user magnet requires favorable conditions regarding budget, time, and technical maturity. Notably, the no-insulation (NI) HTS saddle-shaped dipole magnet developed in this study is the first of its kind, with even the analytical models not yet established. Therefore, this study aimed to design and fabricate a laboratory-scale dipole magnet that could validate the analysis model, to measure magnetic field uniformity in a conduction-cooled environment, and to develop techniques to improve that uniformity. The magnet and experimental system were designed based on the following three directions: (1) conduction cooling operation; (2) air-core magnet; and (3) application of an in-house 3-axis field mapper and ferroshim in a manner similar to NMR.

- **Conduction cooling operation**: The cooling system is involved in all stages of the superconducting magnet's design, fabrication, and operation, making it

one of the most major factors. Compared to cooling systems using cryogens, conduction cooling requires more structural complexity, as heat generated in the magnet must be removed solely through conduction, without direct contact with the coolant. In this study, a 2-stage GM cryocooler was used, and thermal channels were fabricated to facilitate conduction, achieving temperatures below 10 K.

- **Air-core magnet**: In the case of LTS or copper accelerator magnets, iron cores or yokes are commonly used. Utilizing iron core saturation can increase the central magnetic field in low-field regions, and optimizing the iron core shape is often sufficient to improve magnetic field uniformity without additional structures. However, for HTS high-field magnets, using an iron core does not necessarily enhance the central magnetic field and can sometimes even reduce it. Additionally, iron cores increase the overall weight and volume of the magnet system, so in this study, a magnet without an iron core was developed.

- **Field-mapper and ferroshim**: To measure magnetic field uniformity, a field mapper capable of precise sensor positioning is essential. An in-house field mapper with position control accuracy of 0.01 mm across three axes was installed to measure the magnetic field distribution. After measuring the magnetic field uniformity, ferroshim or active shim coils are needed to improve uniformity. The ferroshim method introduced in this study, due to the absence of an iron core, involves attaching iron shims (used in NMR magnets) to a cylindrical tray, which is then inserted into the warm bore.

Expected Limitations of Magnet

Based on the previously described objectives and design approach of the magnet, there are limitations to the elements that can be verified through the magnet as follows:

- **Thermal gradient due to conduction cooling operation**: The temperature of a magnet installed in a conduction-cooled environment typically shows a larger

temperature gradient compared to using cryogens. This is because heat transfer through conduction is affected by thermal contact resistance, which is difficult to estimate accurately before measurement. This temperature gradient can be a factor that degrades the performance of the magnet.

- **Relatively low performance of the test magnet**: In addition to the issue of the temperature gradient, limitations in the shape and size of the conduction cooling system where the magnet will be installed make it challenging to fully enhance the magnet's performance. Furthermore, constraints on the specifications and quantity of conductor used make it difficult to increase the central magnetic field to a practically usable level.

- **Measurement error due to field-mapper**: The field mapper used was able to achieve high positional accuracy by using a commercial stepper motor for position control. However, during installation, the bar with the attached Hall sensor may not be perfectly vertical. The angle between the bar and the magnet was measured to be less than 0.000436 rad. Additionally, vibrations from the mapper due to the stepper motor, as well as mechanical vibrations from the cooling system, could also contribute to measurement errors.

3.1.2 Optimization of Magnet Geometry Considering Magnetic Field Uniformity

Due to the shape of the saddle magnet, 3D analysis is essential to interpret specific parameters and base the design on these results. Additionally, optimization techniques must be applied for the design, requiring the establishment of objective functions and constraints. However, directly incorporating 3D analysis parameters into the optimization process significantly increases the computational load, unnecessarily prolonging analysis time. Therefore, optimization was first conducted using 2D analysis to refine parameters for the 3D analysis. Then, a second round of optimization was performed

Table 3.1: Assumptions for the main magnet design

Category	**Assumptions**
REBCO coated conductor	SuNAM's REBCO CC (4.05 mm × 0.135 mm)
Operating temperature	15 K
Maximum number of coil pairs	3
Maximum winding bore diameter	110 mm
Maximum coil axial length	550 mm
Maximum conductor usage	400 m
Maximum bending strain	0.4%
Minimum critical current margin	20%
Magnetic field uniformity at 15 mm radius	2.0×10^{-4}

with 3D analysis to finalize the design. Here, the 2D analysis assumed the coil as an infinitely long, straight conductor. Based on the design direction, specific design objectives were set, as shown in Table 3.1.

It was assumed that SuNAM's REBCO CC tape would be used, with a tape width and thickness of 4.05 mm and 0.135 mm, respectively. As previously mentioned, the operating temperature was set to 15 K using a conduction cooling system. Due to the shape and size of the system used in the experiment, the maximum winding bore diameter and maximum axial length were set to 110 mm and 550 mm, respectively. Additionally, a maximum bending strain of 0.4% and a minimum critical current margin of 20% were assumed, and a magnetic field uniformity of 2.0×10^{-4} or less was targeted over a reference radius of 15 mm. LTS saddle dipole magnets, which are already widely used in practical applications, achieve magnetic field uniformity of less than 1 and are in operation. To achieve this level of uniformity, active and passive shim techniques are employed. For example, the dipole magnets used in CERN's LHC exhibit magnetic field uniformity of 1 to 2 at a reference radius of 17 mm, similar to this

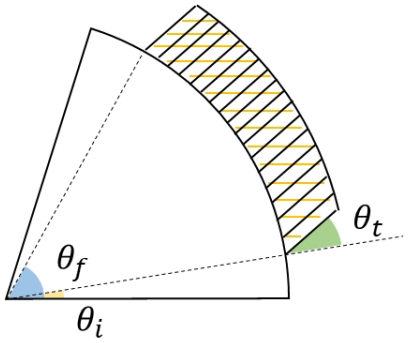

Figure 3.1: Definition of angles corresponding to the design variables for each coil

magnet [50].

Additionally, there are constraints on the coil's geometry. The overall shape of a cosine-theta saddle-shaped magnet is determined by two factors: 1) the number of coil pairs on the same circumference, and 2) the number of circumferential layers with coils. For the test magnet, the design conditions were limited to a maximum of 3 coil pairs on a single layer. The conductor usage was capped at 400 m. In the design process, the parameters that determine the shape of each coil include the coil start angle (θ_i), end angle (θ_f), and tape tilt angle (θ_t) in the 2D cross-section as shown in Figure 3.1, as well as the length of the straight (l_s) and curved (l_c) sections in the 3D structure. As previously mentioned, design was carried out sequentially through 2D analysis followed by 3D analysis, with the specific design stages outlined below.

- **Step 1:** The optimization range for parameters in the 2D design is set for a parameter sweep. When defining this range, design assumptions such as the maximum bending strain and maximum critical current margin are taken into account. For example, if the coil's end angle is too close to 90 degrees, excessive bending strain may occur in the innermost turn of the coil, so the end angle was limited to not exceed 80 degrees.

- **Step 2:** 2D design optimization is performed by first defining the number of coil pairs. The objective function for optimization is magnetic field uniformity, with

a target uniformity level of 1.0×10^{-4}, which is more stringent than the final goal of 2.0×10^{-4}. This target accounts for the expected decrease in uniformity when transitioning to 3D design optimization, compared to the 2D design assuming infinite conductors. Additionally, since the conductor length cannot be defined in 2D analysis, a constraint of 220 total turns was applied instead.

- **Step 3:** Based on the optimized shape, the optimization range for 3D design parameters is set. In this case, a condition was applied such that the sum of the lengths of the straight and curved sections does not exceed the maximum length of 550 mm.

- **Step 4:** For the length of the curved section, the tilt angle of the conductor that satisfies the constant perimeter winding condition was calculated. Using this, a lookup table was created to calculate the harmonic components of the magnetic field based on specific lengths of the curved and straight sections. This table includes a total of 225 data points, with 15 points for each of the curved and straight section lengths. The purpose of creating this lookup table is to avoid excessively long analysis times in the 3D design optimization process. Instead of recalculating from scratch with each parameter change, optimization can proceed by interpolating values from the lookup table.

- **Step 5:** 3D design optimization is performed based on the created lookup table. The objective function for optimization is magnetic field uniformity, with a target of 2.0×10^{-4}. The constraints for the optimization include the critical current margin and the amount of conductor used.

- **Step 6:** Through the above process, 100 design results were saved for each number of coil pairs, and the design with the highest central magnetic field was selected as the final design.

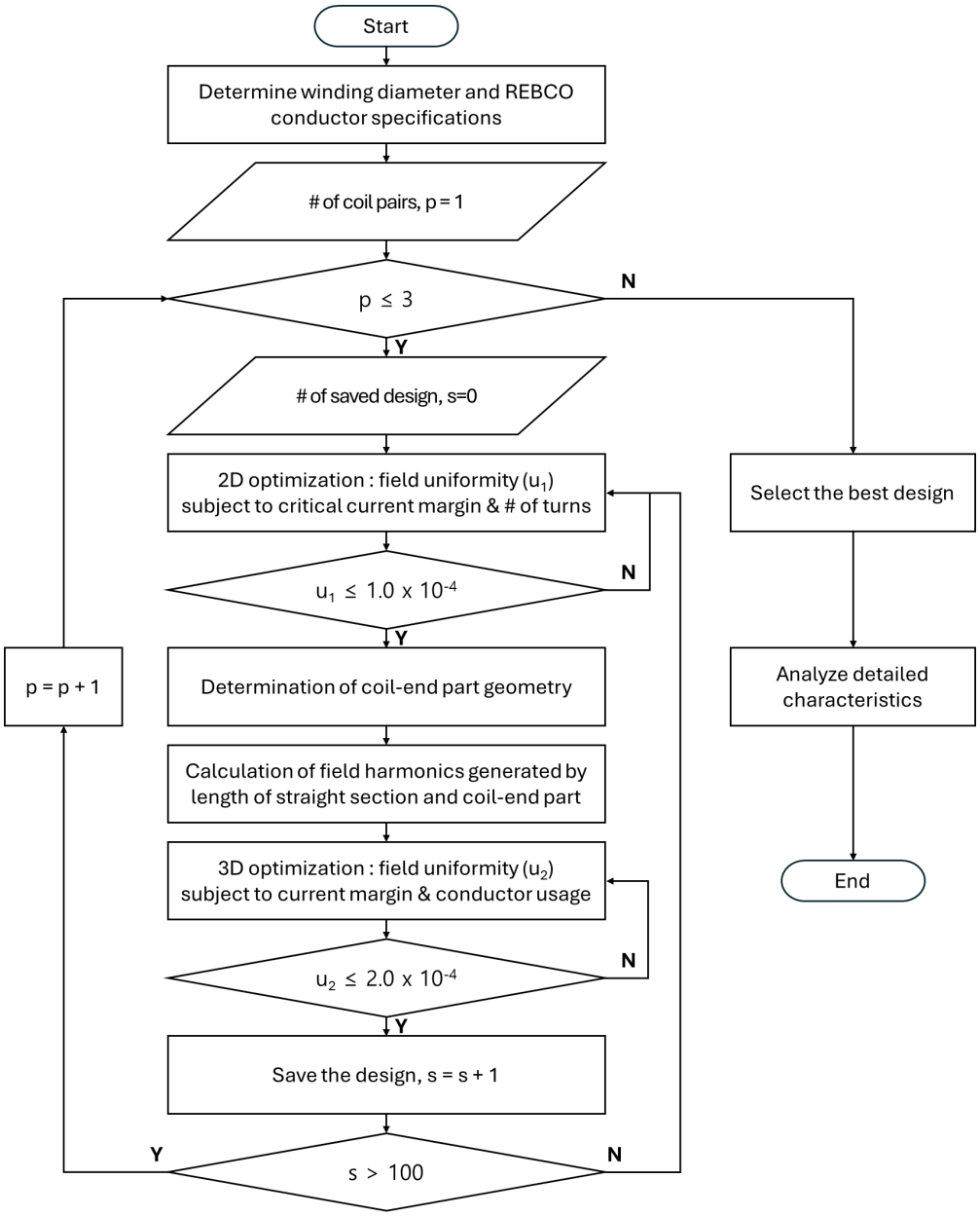

Figure 3.2: A flowchart illustrating the entire process of design optimization

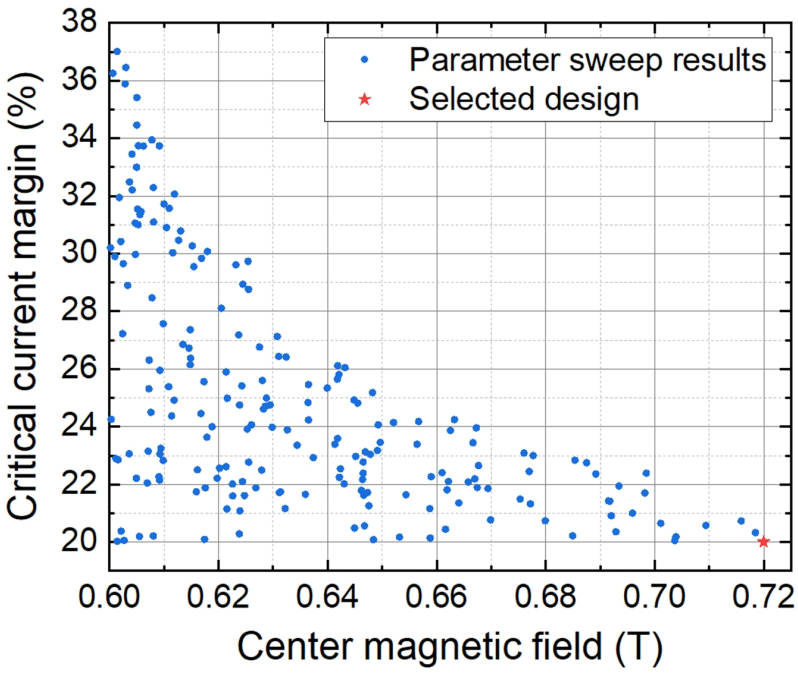

Figure 3.3: Results of the design parameter sweep and the selected design based on magnetic field strength and uniformity criteria

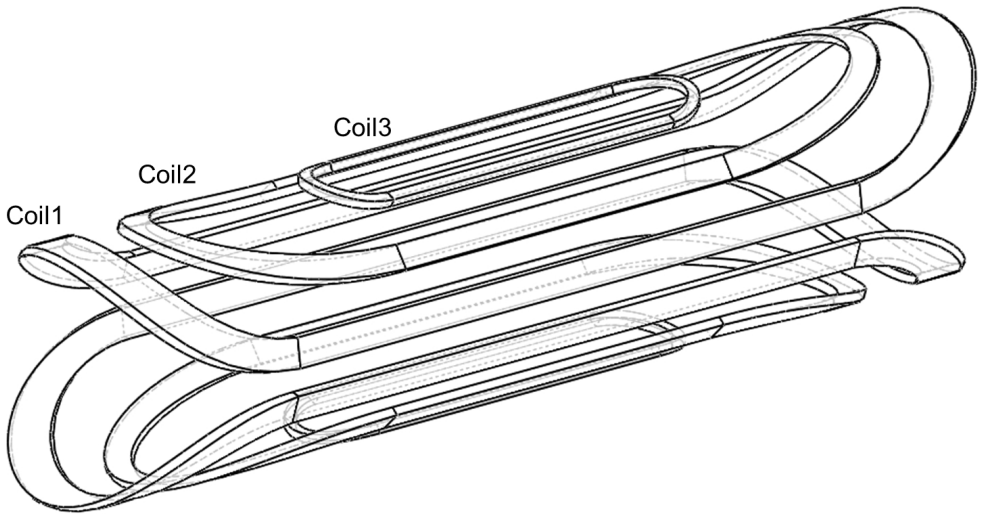

Figure 3.4: 3D configuration of the main magnet design composed of three pairs

Table 3.2: Summary of the selected design parameters and basic analysis results

Parameter	**Unit**	**Coil 1**	**Coil 2**	**Coil 3**
Coil start angle	[°]	6.1	34.8	66.7
Coil end angle	[°]	20.4	46.9	71.9
Tape tilt angle	[°]	2.4	2.2	-1.2
Length of straight section	[mm]	314.1	182.8	157.3
Length of curved section	[mm]	80.3	106.7	25.0
Conductor usage	[m]	103×2	67×2	24×2
Coil turns		97×2	82×2	35×2
Winding diameter	[mm]		109.6	
Operating current	[A]		295	
Critical current margin			20.0%	
Center magnetic field	[T]		0.720	
Magnet constant	[mT/A]		2.44	
Total inductance	[mH]		39.1	
Magnetic field uniformity			1.9×10^{-4}	
Effective magnetic length	[mm]		381.7	

Flowchart for overall optimization process is displayed in Figure 3.2. The interior-point method, a deterministic approach, was used for the 2D design optimization. This algorithm is well-suited for finding the minimum of a nonlinear multivariable function with constraints. However, being a deterministic method, the initial values were randomly varied within the given range to perform optimization process.

The design results showed that the optimization outcomes improved as the number of coil pairs increased. This appears to be a natural result of the increase in the number of variables available for optimization. Figure 3.3 shows the parameter sweep results for three coil pairs. Based on magnetic field strength and uniformity, the design with the highest magnetic field strength that met the uniformity criterion was selected.

The specific parameters for this design are shown in Table 3.2. The overall appearance of the designed coil is shown in Figure 3.4. The largest coil is named coil 1, the medium-sized coil is coil 2, and the smallest coil is coil 3. The design of various structures, including the bobbin and external support structures, was aligned with the coil positions and will be explained in detail in the following subsection.

3.1.3 Fundamental Analysis Results of Magnet Design

The magnetic field generated by the designed coils was calculated as shown in Figure 3.5. At an operating current of 295 A, the central magnetic field was calculated to be 0.72 T, demonstrating that the dipole component of the magnetic field is well-formed, as illustrated in Figure 3.5 (a). Figure 3.5 (b) shows the analysis results of magnetic field uniformity on the reference radius. For easier interpretation, the uniformity is expressed in $\log_{10}$, where the magnetic field uniformity of 1.9×10^{-4} corresponds to a $\log_{10}$ value of -3.7. This indicates that the magnetic field uniformity within the reference radius and its interior is well-designed.

The results of the harmonic analysis for the above magnetic field distribution are shown in Table 3.3. Since the design follows a perfectly symmetric structure, skew components are absent, and only the odd terms among the normal components remain. However, in practice, it is challenging to achieve a perfectly symmetrical structure during fabrication, so the experimental results may exhibit components that ideally should not exist.

The critical current analysis revealed that the minimum critical current occurred at the boundary between the straight section and the curved section for the innermost turn of Coil 1. The calculation was performed using the widthwise average method. The design initially assumed a margin of 20% without accounting for temperature variations. However, during actual operation, with temperature changes considered, the load-line margin was found to be around 15%. A comparison between the experimental measurements and the analysis results for the critical current will be discussed in the

Table 3.3: Harmonic components according to the reference radius

Reference radius	5 mm	10 mm	15 mm
b3 (sextupole)	0.0925	0.3697	0.8299
b5 (decapole)	-0.0004	-0.0054	-0.0108

following chapter.

The inductance of the coil was calculated to be 39.1 mH. It was determined by calculating the inductance matrix as shown in Figure 3.6 and summing the elements of this matrix for screening current analysis. Using the previously described technique for improving inductance calculation speed, it took approximately 33.6 hours to determine the inductance of this coil. In this case, each turn was divided into 16 segments along the width, resulting in an inductance matrix with 6848^2 ($6848 = 2\times(97+82+35)\times16$) elements. The matrix is symmetric with respect to the diagonal, and the elements are arranged in the order of top coil 1, coil 2, coil 3, bottom coil 1, coil 2, and coil 3. Within each coil, the elements are ordered from the innermost to the outermost turns, and within each turn, the elements are arranged from the bottom to the top segments.

The bending strain in the curved section was designed to be a maximum of 0.39%. The highest bending strain occurs in coil 3, which has a smaller winding radius than coil 1 and coil 2, as excessive bending strain can lead to a reduction in critical current. Figure 3.7 shows the strain values for the innermost turn in the curved section of each coil, where strain is highest. The lower part of the figure represents the area where the straight and curved sections meet, while the upper part shows the end of the curved section. The left and right directions represent the width of each tape. For this magnet, the REBCO surface is wound facing inward, causing the bending strain to act in a compressive direction. It is generally known that compressive strain is less likely to damage the conductor compared to tensile strain. Alongside the above bending strain analysis, the following section will present mechanical analysis results that account for external reinforcement structures, thermal contraction, and other relevant factors.

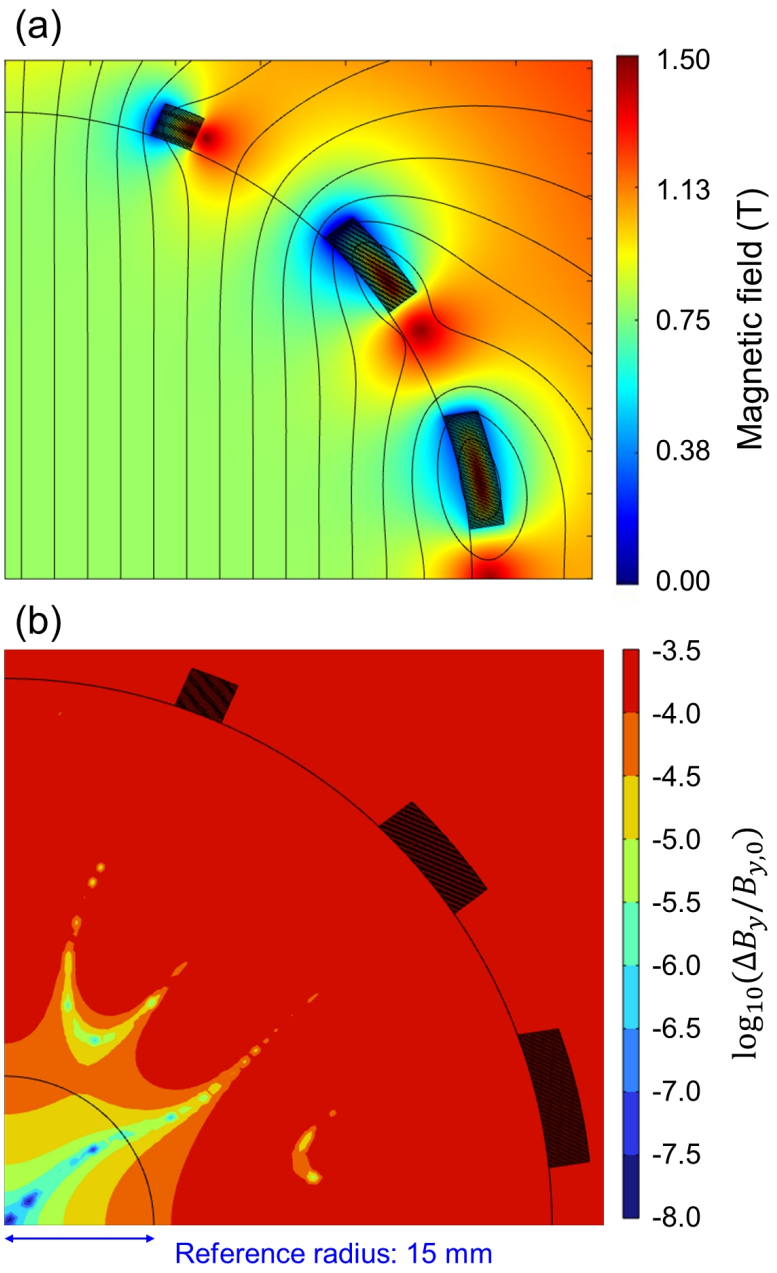

Figure 3.5: Magnetic field distribution analysis results for the designed magnet. (a) Analysis results of the central magnetic field distribution at the operating current, (b) Magnetic field uniformity on the reference radius.

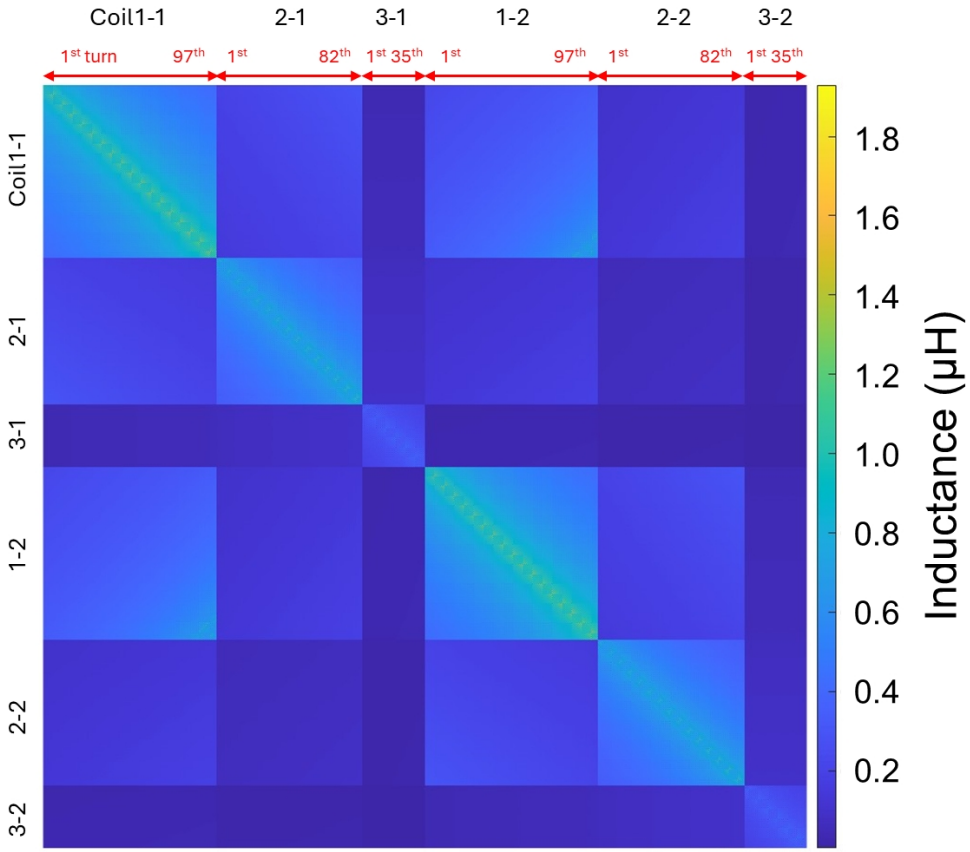

Figure 3.6: Calculation results of inductance matrix for designed coils.

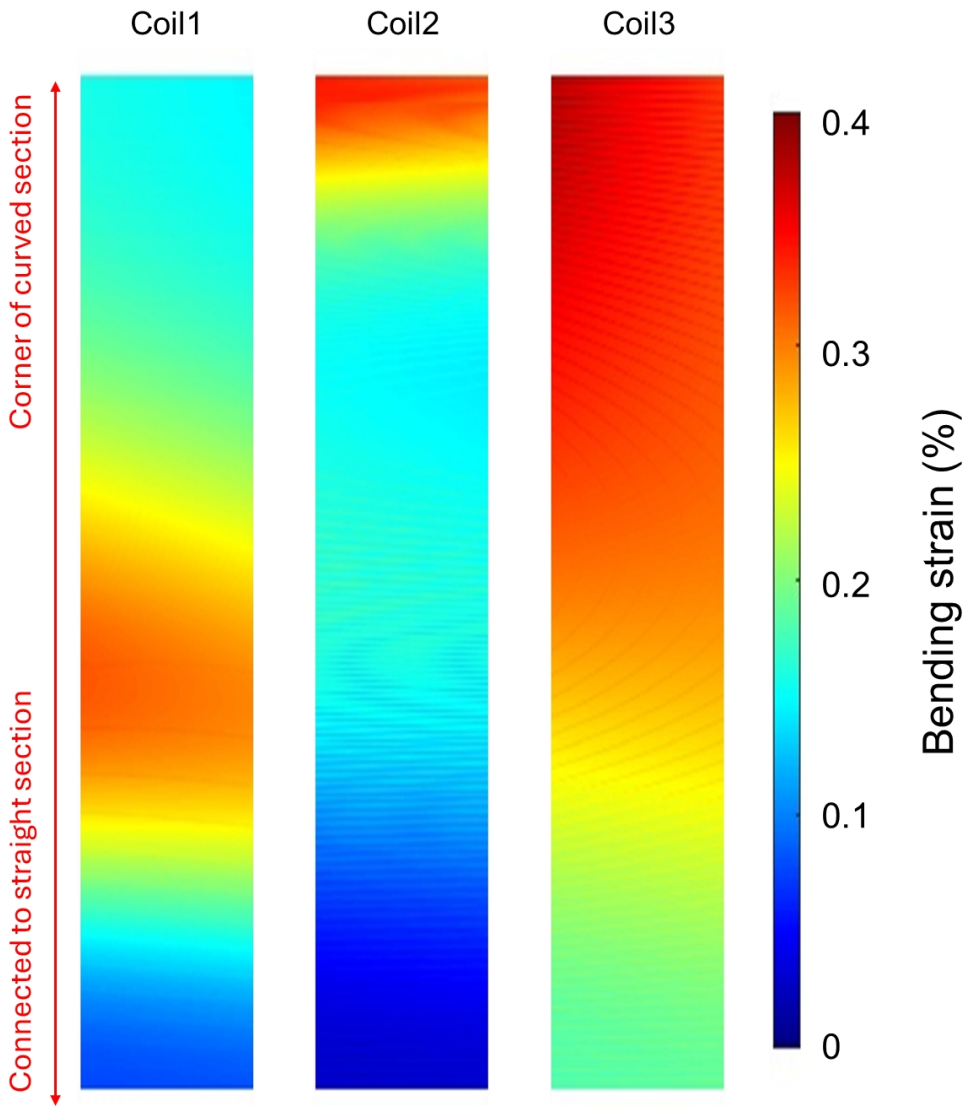

Figure 3.7: Analysis results of bending strain for the curved sections of each coil.

3.1.4 Mechanical Design for Support Structure

Although the coil has been designed, additional surrounding structures, including the bobbin, must be designed for actual fabrication. A particularly challenging technical aspect is how to reinforce the straight sections of the coil. For electrical connections between coils, the outer straight section of coil 3 must connect to the inner straight section of coil 2, the outer straight section of coil 2 to the inner straight section of coil 1, and the upper and lower outer straight sections of coil 1 must also be electrically connected. Two options were considered for this: 1) connecting with copper bulk current leads, and 2) inserting the conductor through gaps in the straight section reinforcement structure. Testing of both options indicated that connecting through the conductor minimized resistance.

Testing both options revealed that connecting via the conductor was the better choice. Figure 3.8 (a) and (b) shows each option as implemented. In the first option, using copper bulk current leads, the REBCO conductor was soldered to the top of the bulk to minimize resistance. However, issues such as conductor delamination during the soldering process and a limited contact surface length resulted in significantly higher resistance. The resistances for each coil-to-coil connection in the first option at 15 K were 4.2, 0.27, 0.23, 12.5, and 0.34 μΩ, respectively. Additionally, to address insulation issues with the aluminum bobbin, plastic bolts were used to secure the straight section supporting structure, but these bolts failed to provide sufficient mechanical stress.

Therefore, the straight section reinforcement structure was designed to include gaps through which the conductor could pass. By constructing the reinforcement structure's gaps as inclined surfaces, pressure could be applied on both sides along these surfaces, allowing the displacement from the inclined surfaces to apply pressure to the straight section. This structure was fabricated as shown in Figure 3.8 (c). Similar to the design of the coil's curved sections, curvature was added to the edges of the inclined surfaces to keep the local bending strain below 0.4%. Although this differs from the

end-coil optimization technique, it followed the same principle of designing to meet the bending strain conditions. The analysis result of the bending strain experienced by the wire when it is placed on the surface of the gap is shown in Figure 3.9. Strain occurs at the beginning and end sections where curvature is introduced, while in other areas, there is no strain as the wire follows the slope of a straight line.

Additionally, an overbanding structure for the coil was designed. There were two possible options: 1) overbanding the outer diameter of the coil with an insulating material, or 2) using a cover to prevent displacement of the coil's outer diameter. The latter option was chosen for the reinforcement structure. This choice was related to the coil winding process. As will be explained in more detail later, a universal joint was used to manually rotate the winding axis during coil winding, and without a cover structure, the coil winding tended to loosen. The cover not only facilitated the winding process but also served to reduce mechanical stress during operation. The actual appearance of this cover structure is shown in Figure 3.8 (b).

Considering this reinforcement structure, the stress experienced by the magnet during operation can be analyzed. Displacement from the inclined structure of the straight section and the displacement constraints from the cover structure were set as boundary conditions, allowing for analysis of the stress and strain due to electromagnetic forces. Strain was calculated by comprehensively considering the effects of bending strain and thermal contraction. The mechanical factors considered in the analysis are as follows:

- Magnetic strain due to Lorentz force
- Bending strain at the coil-end part
- Strain due to thermal contraction of magnet
- Strain due to pressure applied by wedge structure

The overall mechanical analysis was conducted using an iterative sequential method. Considering the actual sequence experienced by the magnet, strain first occurs due to

bending, followed by strain induced by the wedge structure. Subsequently, cooling leads to strain from thermal contraction, and finally, magnetic strain arises under operating conditions. To perform this time-sequential analysis, the strain results from previous stages were applied as external strain conditions for subsequent analyses.

Figure 3.10 illustrates the first principal strain calculated at each stage of the process. First, the bending strain of the coil-end part, as calculated in Figure 3.7, was applied as an external strain condition. Subsequently, an analysis was conducted on the pressure exerted by the wedge structure under this condition. The wedge structure is secured using two M4-sized bolts, each tightened with a torque T of 2 Nm. The relationship between torque and force is expressed by the following equation [136]:

$$F = \frac{T}{kd}, \tag{3.1}$$

where k and d are the torque coefficient and bolt diameter, respectively. Assuming a torque coefficient of 0.2 [137] and a bolt diameter of 4 mm, the force exerted by a single bolt was calculated to be approximately 2500 N. Given that the force is distributed over an area of 150 mm in length and 20 mm in height, the pressure applied to the outermost surface of the straight section is approximately 1.7 MPa. This assumption was incorporated into the analytical model to perform the analysis.

These results were applied to the thermal contraction analysis model described in the previous chapter. Finally, a mechanical analysis was conducted for the situation where current and magnetic fields are generated. As a result, the maximum tensile principal strain was calculated to be 0.27%, and the compressive principal strain was determined to be within 0.4%, confirming that there are no significant issues for the operation of the magnet. Although strain was not measured directly using methods like strain gauges, the processes corresponding to the analysis were followed during the actual fabrication and operation stages. Achieving the target performance successfully confirmed that the analysis results were within a reasonable and accurate range.

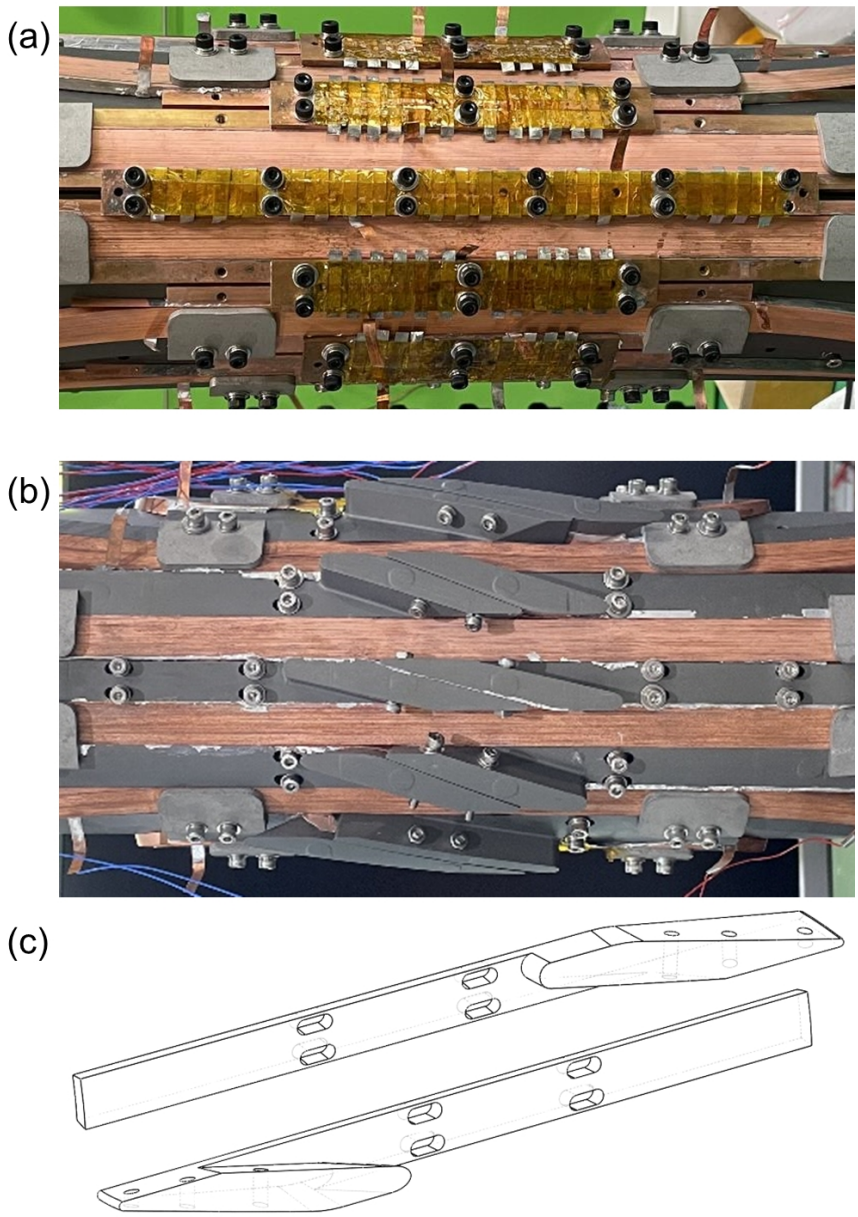

Figure 3.8: Introduction of a wedge structure for the straight section's mechanical support. (a) Straight section reinforcement structure made with copper leads, (b) straight section reinforcement structure using wedge design, (c) manufacturing drawing of the wedge structure.

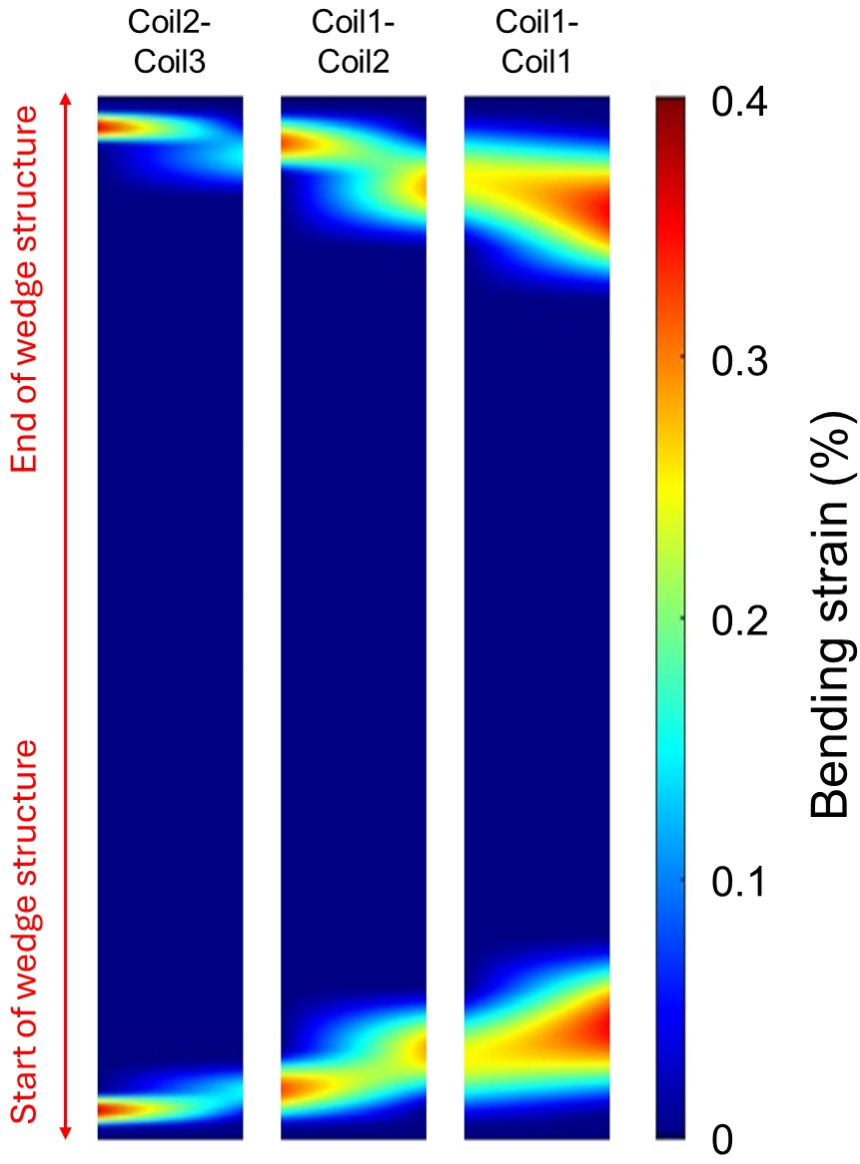

Figure 3.9: Bending strain acting on the conductor passing through the gap between the two wedge structures.

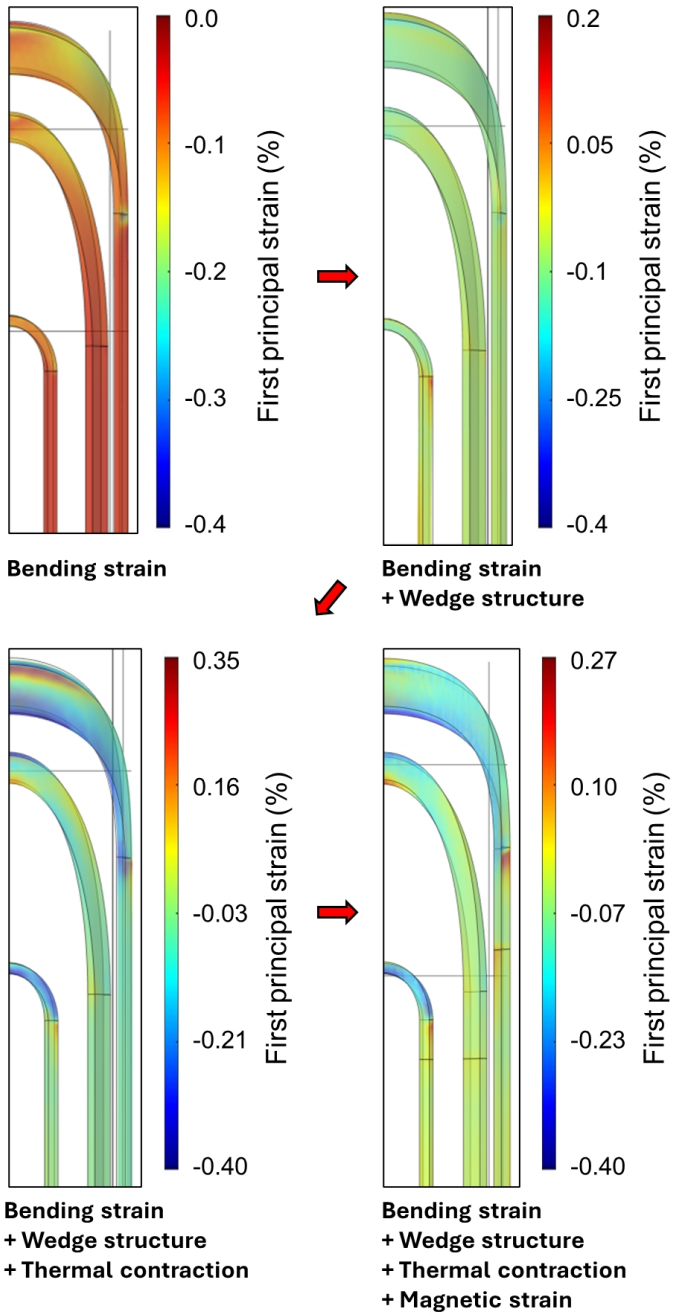

Figure 3.10: Sequential strain analysis results for the magnet fabrication and operation process.

3.1.5 Cryogenic Design for Conduction Cooling Operation

This magnet was cooled using a conduction cooling system. In this cooling method, the coolant does not directly contact the magnet for heat exchange; instead, the coolant circulates through a cryocooler driven by a compressor to remove heat. The cryocooler is thermally connected to the magnet through various metal thermal channels, ultimately lowering the magnet's temperature. Commonly used coolers for this purpose are Gifford-McMahon (GM) cryocooler and Stirling cryocoolers [138]. GM cryocooler, which was used for the experiments, operates by cyclically compressing and expanding helium gas to achieve low temperatures. In the first stage, helium is compressed and cooled, and then it flows through an expansion valve where it undergoes rapid expansion, lowering its temperature significantly. The cold helium is then directed to the cryogenic area, where it absorbs heat, and the cycle repeats, providing consistent cooling at cryogenic temperatures. The experiment used ULVAC's RM120ET 2-stage GM cryocooler [139], and to measure magnetic field uniformity, a system with a room-temperature bore at the center of the vacuum chamber was used. The cooling power map of the cryocooler is shown in Figure 3.11.

The overall configuration of the system is shown in Figure 3.12. The main focus is the thermal pathway setup between the cryocooler, current-carrying leads, and the magnet. Current enters through a room-temperature lead positioned at the bottom of the system. As it passes from the first to the second stage, it uses an HTS lead formed by attaching REBCO tape to a G10 plate to minimize thermal intrusion into the second stage. The current reaching the second stage is then directed to the magnet through copper braids connected to copper current leads. The copper current leads at the second stage are cooled via a copper block and copper plate attached to the second stage. Copper and brass blocks serve as thermal channels at the first and second stages, and a multi-layer insulation radiation shield is positioned between the first stage and the chamber to minimize radiation heat intrusion affecting the magnet. Information on the parts used as cooling channels is provided in Table 3.4.

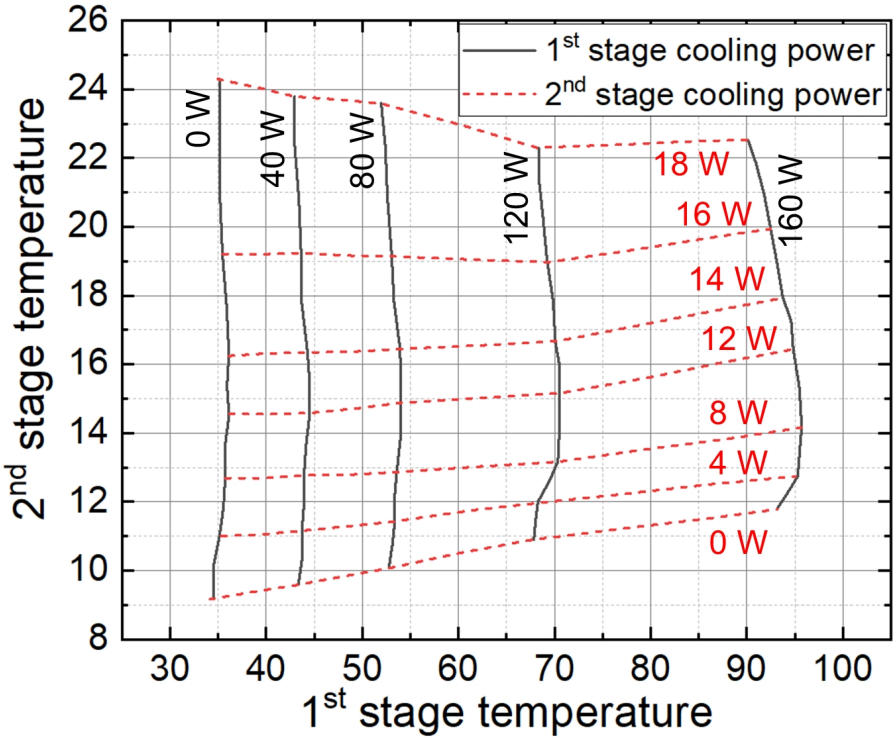

Figure 3.11: Cooling power map of ULVAC's RM120ET used in the experiment.

The magnet is also cooled by thermally contacting the copper plate of the second stage with the magnet's bobbin. However, relying solely on this method may result in a significant temperature gradient between the upper and lower parts of the magnet. To address this, an additional cooling path was established using copper braided wire as shown in Figure 3.13. This method involved creating 12 holes in the bobbin and connecting the second stage plate to the bobbin with copper wires, effectively adding parallel resistance from a thermal resistance perspective to facilitate smoother heat transfer.

To verify the effectiveness of this cooling path, a thermal circuit model, as shown in Figure 3.14, was used to assess the temperature gradient occurring in the coil. This thermal circuit model is primarily represented by two components. The first is the capacitive component of nodes, which represents parts or sections of an object, indicating

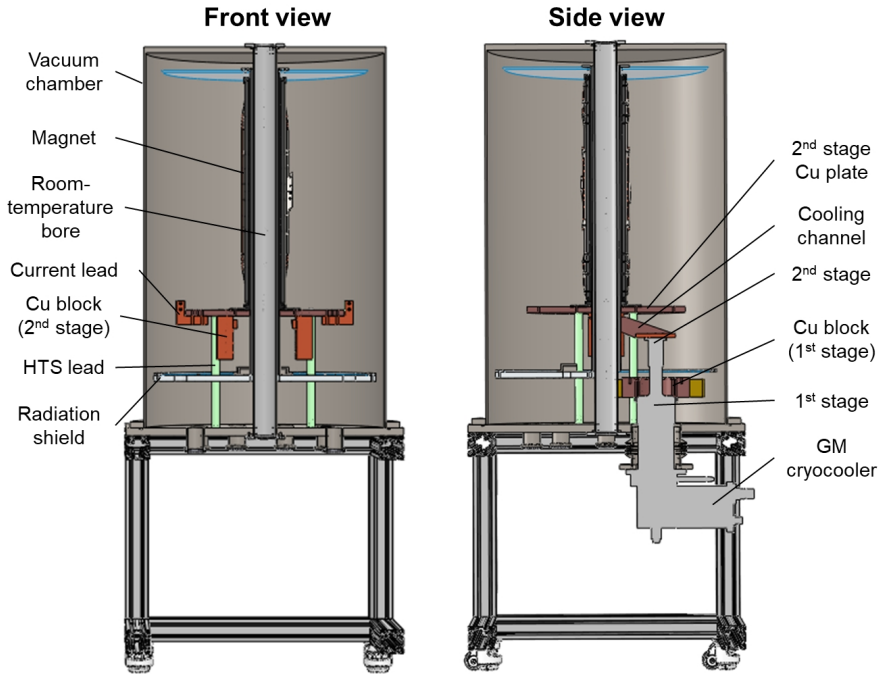

Figure 3.12: Overall schematic of the conduction cooling system used in the experiment.

the thermal capacity of each node. The second is the resistive component, representing conduction between nodes, which serves as the heat path in the conduction cooling system where no convection is present. It was assumed that no temperature gradient exists within each node, and the coil was segmented into multiple sections along the axial direction, each set as a node to analyze the coil's temperature gradient. The heat capacity values of the materials used in the analysis are shown in Figure 3.15. This analysis model will also be used later to examine the cooling profile and temperature rise during charging and discharging.

To analyze the model, a total of 46 nodes representing each object were set up, along with 96 connections between nodes. The conduction between nodes via thermal contact is determined by thermal contact resistance, but accurately predicting this value before measurement is nearly impossible. However, thermal contact resistance

Table 3.4: Properties and volumes of components in the conduction cooling system

Part Name	Material	Volume [cm^3]
Block attached to 1^{st} stage	Cu	1095
Cooling channel between 2^{nd} stage and block	Cu	259
Block at 2^{nd} stage	Cu	780
Plate at 2^{nd} stage	Cu	1774
Room-temperature current lead	Cu	31
1^{st} stage current lead	Cu	63
1^{st}-2^{nd} stage connecting current lead	Cu	14
2^{nd} stage current lead	Cu	14
Cooling channel between plate and current lead	Cu	51
Coil bobbin	Al	1619

values measured in previous experiments were incorporated as much as possible for this analysis. The primary variable in this analysis is the thermal resistance between the coil bobbin and the plate. Connecting more copper braided wires adds parallel resistance paths, thereby reducing the equivalent resistance and influencing the temperature gradient between the top and bottom of the coil. The analysis results are shown in Figure 3.16. It was observed that if the thermal resistance is sufficiently low, almost no temperature gradient occurs; however, if the thermal resistance increases, a temperature gradient of up to approximately 2 K can develop. In a later section, the cooling profile measurement results will be used to infer thermal resistance and to assess the potential critical current degradation due to the temperature gradient.

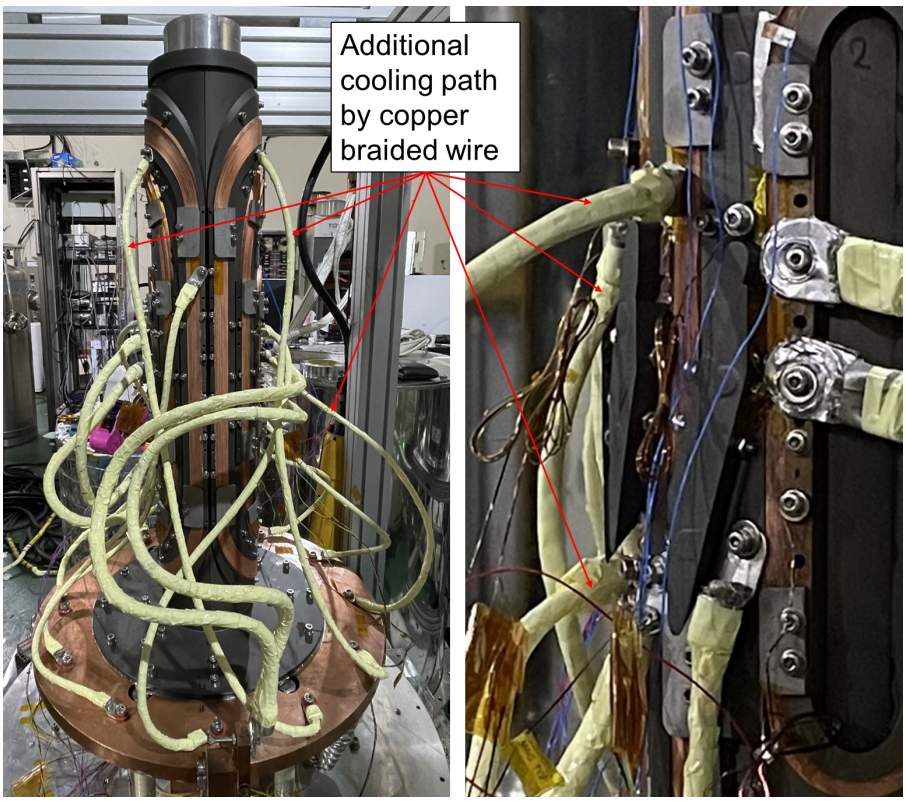

Figure 3.13: Configuration of additional cooling channels using copper braided wires.

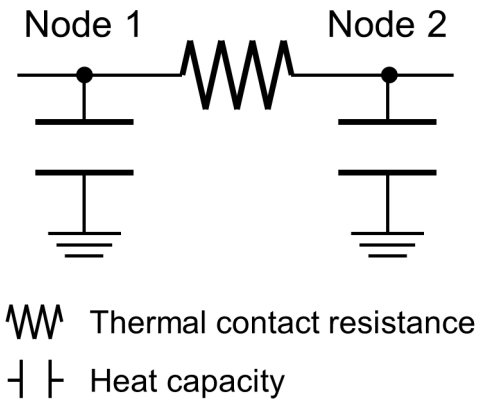

Figure 3.14: Thermal circuit model suggested for thermal analysis.

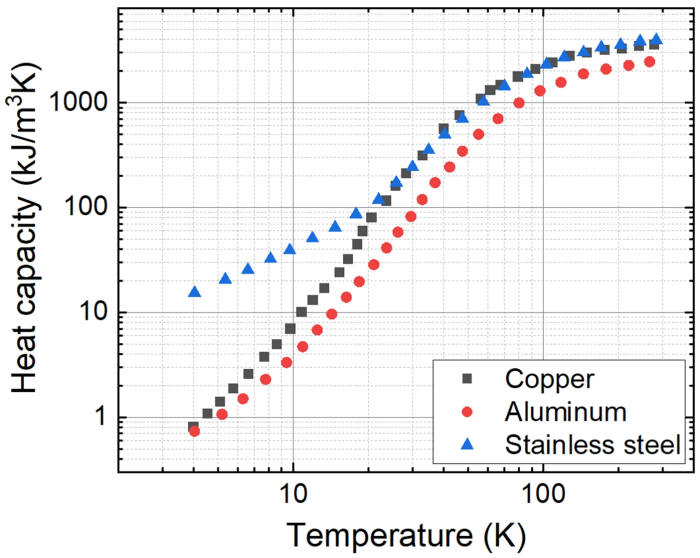

Figure 3.15: Heat capacity of materials as a function of temperature.

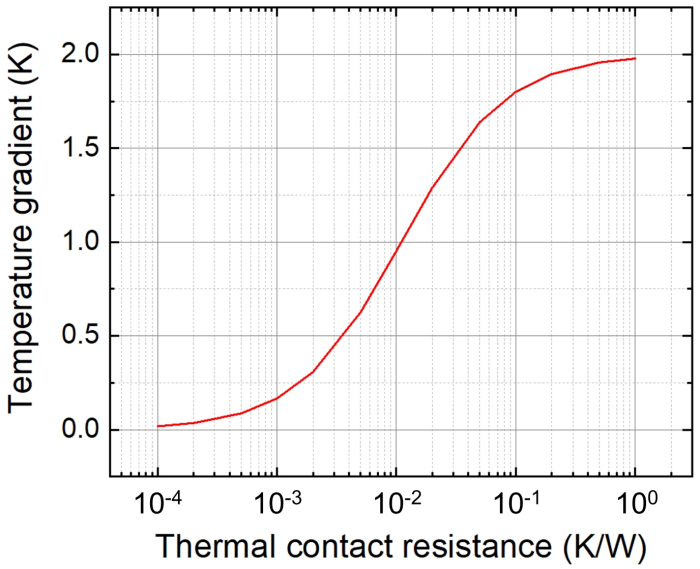

Figure 3.16: Analysis of temperature gradient within the coil based on thermal contact resistance.

3.2 Construction of Saddle-shaped Coils

The most challenging aspect of fabricating a saddle-shaped magnet is the winding process. Due to its tape form rather than round wire, the REBCO coated conductor poses difficulties in manufacturing nonplanar magnets. Precise winding is required to avoid damaging the conductor when hardway-bending occurs. To address this, winding machines based on robotic arms capable of controlling five or more axes of linear and rotational movement are being developed. However, in this study, a planar coil winding machine with only a single rotational and a single linear axis was used to fabricate the saddle-shaped magnet. A universal joint structure, which allows manual adjustment in three directions, was introduced to control the relative position and orientation of the conductor's entry to the bobbin. Additionally, a clamp structure was employed during the winding process to apply continuous pressure and prevent lifting in the straight sections.

As mentioned earlier, to solve the issue of electrical connections between coils, the conductor was routed through the gaps in the wedge structure designed for reinforcing the straight sections. Implementing this method required a lap joint to connect the conductors. It is known that chemicals in flux used in soldering can cause gradual but continuous damage to the conductor, so a solder-free lap joint was developed and used for electrical connections between coils. Finally, the previously designed reinforcement structure was installed to complete the magnet system.

3.2.1 Winding Method and Results

The tape form of REBCO coated conductors poses a challenge for winding saddle-shaped coils. Unlike other metallic superconducting materials, REBCO has a ceramic nature due to its unique crystal structure, making it susceptible to damage from hardway-bending, though it can withstand easyway-bending even in thin films. Consequently, planar coils, like solenoid coils, have typically been wound in a pancake shape along

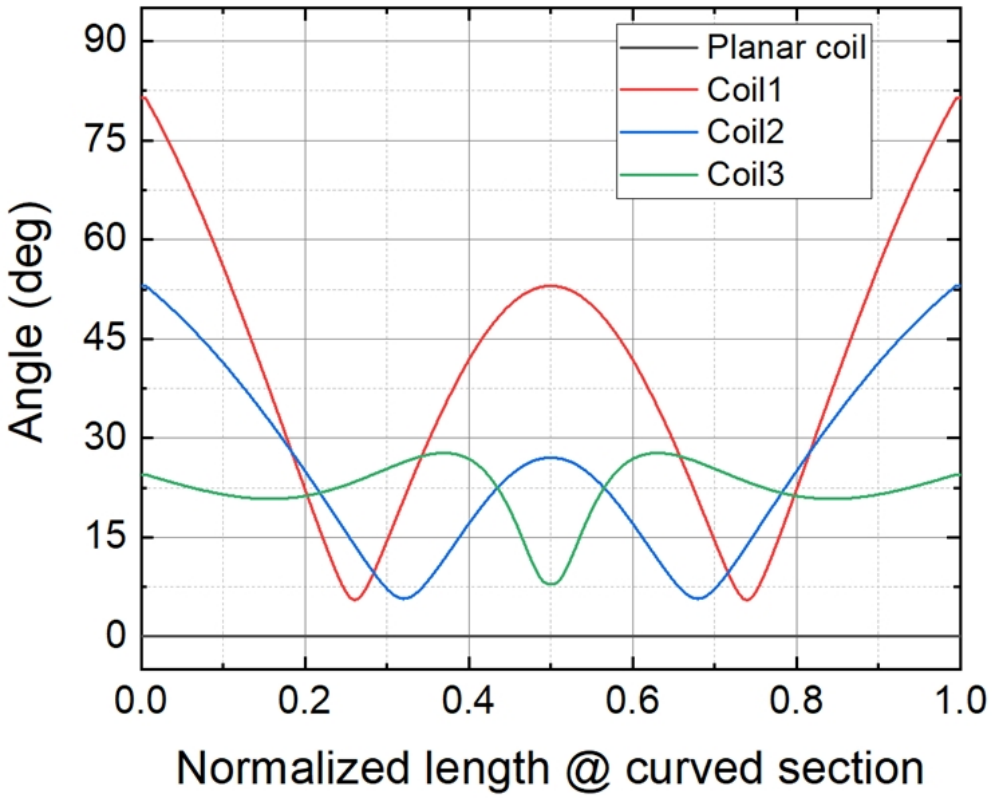

Figure 3.17: Varying rotation angle during winding for each coil

the easyway-bending direction. The winding machines used for these coils control winding speed and tension along one linear and one rotational axis. In contrast, winding nonplanar coils requires control over five or more axes for varying winding angle within coil as shown in Figure 3.17, and various studies are underway to address this. However, these specialized winding machines are not yet commercially available, and since this study marks the first attempt to produce a saddle-shaped NI magnet, a newly developed winding machine could not be used.

Therefore, to wind a nonplanar coil using the existing winding machine for planar coils, a universal joint was used as shown in Figure 3.18. A universal joint is a mechanical connection that allows rotation in multiple directions, enabling flexibility between two shafts that are not aligned. It is commonly used to transmit torque and movement

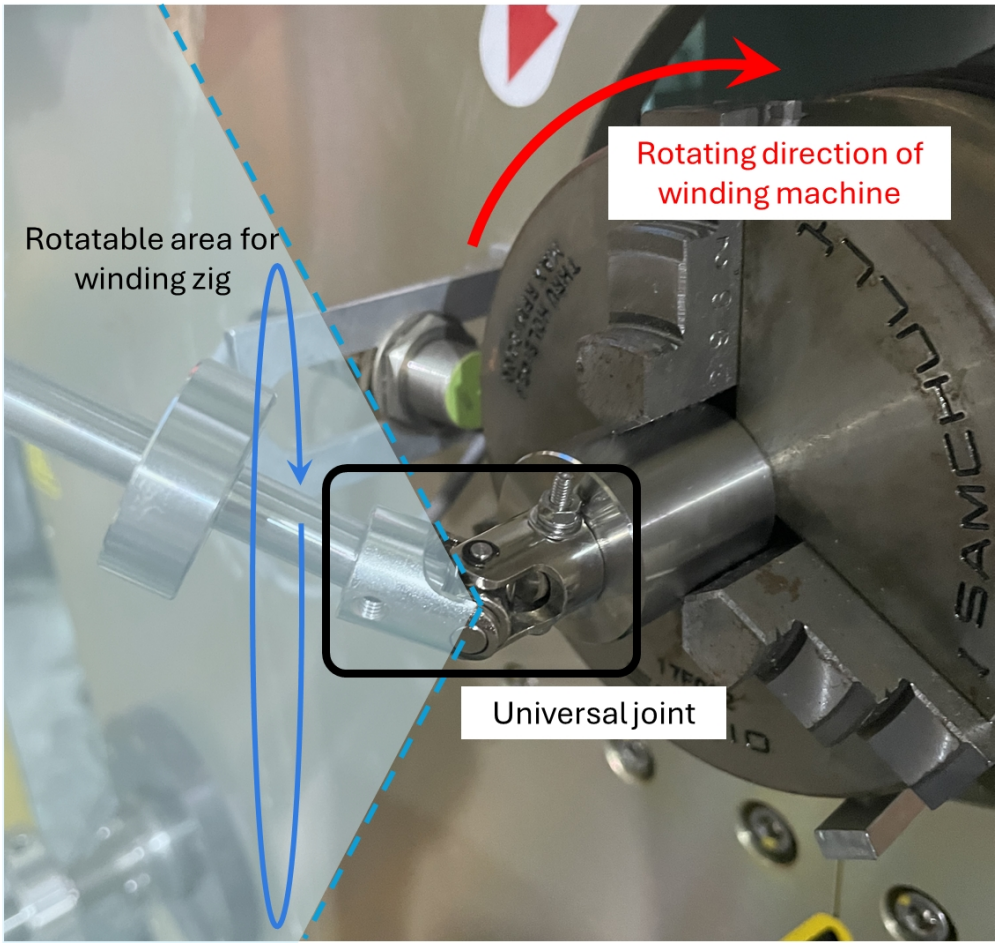

Figure 3.18: Installation of the universal joint for coil winding

in cases where angular misalignment is present. One end of the universal joint was fixed to the rotating axis of the winding machine, while the other end was connected to the winding jig for the coil, allowing manual adjustment of the coil's rotation direction. The winding machine rotated the coil for pancake winding and maintained consistent winding tension. The winding tension was set to 20 N.

A problem discovered during the winding practice was that the straight section of the coil did not receive vertical compressive winding stress, causing its shape to deviate from the design. This is a common issue with coils that have straight sections, which

require continuous pressure in those areas. Known methods to address this include using clamp structures or roller structures. In this study, a clamp structure that could be easily integrated into the existing winding machine was used during the winding process.

The entire winding process is as follows.

- **Step 1:** Attach the universal joint and winding jig to the coil bobbin. Additionally, attach a cover to the bobbin to prevent the conductor from slipping out. Then, secure the universal joint to the chuck located on the rotating axis of the winding machine.

- **Step 2:** Apply winding tension and rotate the bobbin 180 degrees. In the curved section, the winding is maintained by the tension, but in the straight section, the conductor may try to slip out. To keep it in place, insert the conductor between the cover and the bobbin. During rotation, manually adjust the direction of the universal joint to ensure the conductor's entry position and direction to the bobbin remain stable.

- **Step 3:** Stop the winding machine and install 2-3 clamps on the straight section. Apply pressure with the clamps from the front to the back of the winding, removing any extra space to minimize winding errors in the straight section.

- **Step 4:** Rotate the bobbin another 180 degrees and repeat the above steps until the desired number of turns is reached.

The above process is illustrated in detail in Figure 3.19.

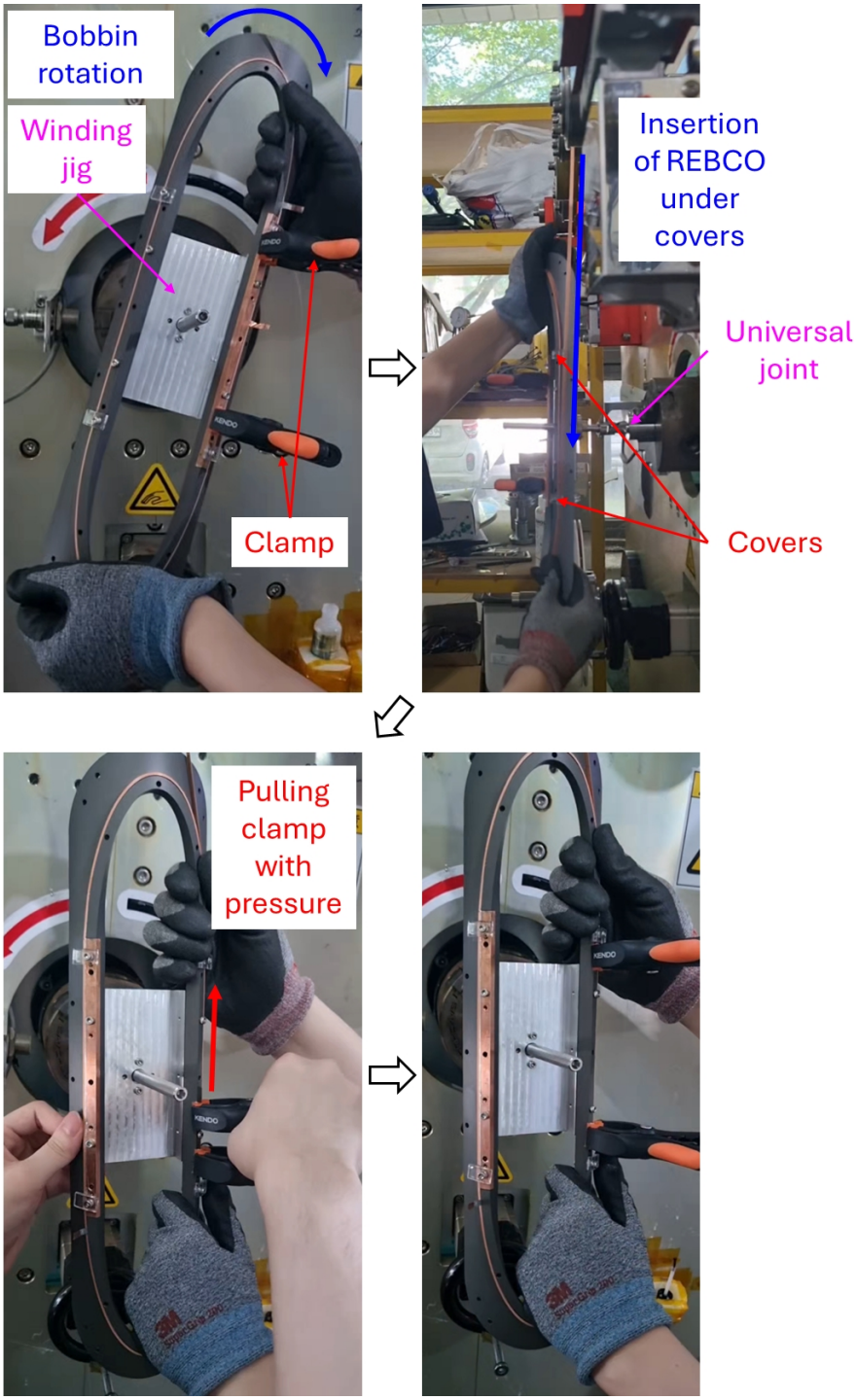

Figure 3.19: Detailed coil winding process

3.2.2 Solder-free Lap Joint for Electrical Connection and Magnet Assembly

Unlike LTS wire, achieving a superconducting joint with negligible resistance is extremely difficult with REBCO coated conductors. As a result, lap joints using soldering metals are the most commonly used method for connecting REBCO conductors [140]. The flux used in soldering to the copper stabilizer layer of REBCO tape removes copper oxide and reduces the surface tension of the solder, allowing for a reliable and conductive bond between conductors. However, excessive use of flux or inadequate cleaning can leave flux residues on the coil, where its chemical components may react with the copper, oxidizing or even eroding it in severe cases. This can weaken the mechanical properties of the superconducting tape, potentially causing delamination of the REBCO layer during cooling and operation, leading to serious operational issues for the magnet.

To address the above issue, a flux-free joining method was developed. It is known from current bypassing phenomena in NI HTS magnets that the electrical contact resistance between superconducting tapes can be determined by the applied pressure and contact area. Contact resistance decreases with increased pressure and a larger contact area. Thus, by applying sufficient pressure and maximizing contact area, a similar resistance level can be achieved without soldering. This method, termed a 'solder-free lap joint,' is shown in comparison with a soldered lap joint in Figure 3.20 (a) and (b). At the coil level, as shown in Figure 3.20 (c), this method was implemented by securing the end of the winding with an adhesive material, such as Kapton tape, and continuing with a new conductor spool, applying winding tension to maintain continuity.

This method was first tested on a solenoid double pancake coil to confirm its feasibility. The solenoid coil consisted of two 50-turn NI single pancake (SP) coils, with a solder-free lap joint inserted at the 8^{th} turn of one SP. The contact resistivity measured in a liquid nitrogen during charge-discharge testing was 16 $\mu\Omega cm^2$, which matched well with analytical results based on pressure and contact area considerations. This

Table 3.5: Resistance measurement results for each solder-free lap joint

Parameter	**Unit**	Joint inside top coil2		Joint inside bottom coil2		Joint between both coil1s	
Tested temperature	[K]	77	15	77	15	77	15
Contacted area	[cm^2]	35.6		35.6		90.7	
Joint resistance	[nΩ]	540	180	500	170	570	300
Contact resistivity	[$\mu\Omega cm^2$]	19	6.4	19	6.2	52	27

confirmed that the same technique could be applied to the magnet in this study.

For the saddle-shaped coil in this study, a total of three solder-free lap joints were inserted. The first was placed at the 37^{th} turn of coil 2, both top and bottom. The lap joint was created at this point because the length of the conductor used continuously from coil 3 was 50 meters. The end of this conductor was secured with an adhesive, and a new turn was wound over it. To maximize the contact area, the contact surface was extended across one turn. Another lap joint was implemented to connect the top and bottom coils 1. When winding each coil 1, a 2.5-meter excess length was left, and after combining the two coils on the bobbin, the excess lengths were crossed to form a lap joint that contacted the outermost turn of the opposite coil. Since this joint was located at the outermost part, where it was challenging to apply pressure through winding stress, the contact length was maximized, and pressure was applied using the wedge structure in the straight section to minimize contact resistance. The contact areas and resistance values for these solder-free lap joints are provided in Table 3.5. The resistance values varied with temperature, showing lower contact resistance at lower temperatures. Although the contact resistivity was observed to be significantly higher than the 0.1 $\mu\Omega cm^2$ value typical of soldered joints, maximizing the contact area allowed for achieving sub-$\mu\Omega$ resistance levels. Considering the conductor width of approximately 4.05 mm, the contact lengths were determined to be 0.88 m and 2.24 m, respectively.

The assembly process for the magnet is as follows.

- **Step 1:** Wind the smallest coil, coil3. The outermost turn of coil3 remains continuous, connecting directly to the innermost turn of coil2.
- **Step 2:** Pass the outermost turn of coil3 through the gap in the wedge structure. To prevent damage to the conductor, insert a soft metal like indium between the wedge structure and the conductor.
- **Step 3:** Press the wedge structure in the direction that applies force along each inclined surface. Then, while maintaining the applied force, secure the wedge structure and bobbin with bolts to hold the force in place.
- **Step 4:** Continue winding by using the outermost turn of coil3 as the innermost turn of coil2. At the 37^{th} turn of coil2, when the conductor length is exhausted, implement a solder-free lap joint and continue winding until reaching a total of 82 turns.
- **Step 5:** Repeat steps 2 and 3 for the final turn of coil2 and the wedge structure. Similarly, the final turn of coil2 connects to the innermost turn of coil1.
- **Step 6:** After winding a total of 97 turns for coil1, attach the set of coil1, coil2, and coil3 to the bobbin. Leave an extra 2.5 m at the end of the winding to allow for the connection between the two coil1s.
- **Step 7:** Repeat the steps above for the other set of coil1, coil2, and coil3, then attach them to the bobbin.
- **Step 8:** For the final turn of coil1, cross the extra lengths to create a solder-free lap joint. Apply pressure between the coil1 units using the wedge structure and complete the assembly.

The assembly process above is visualized in Figure 3.21.

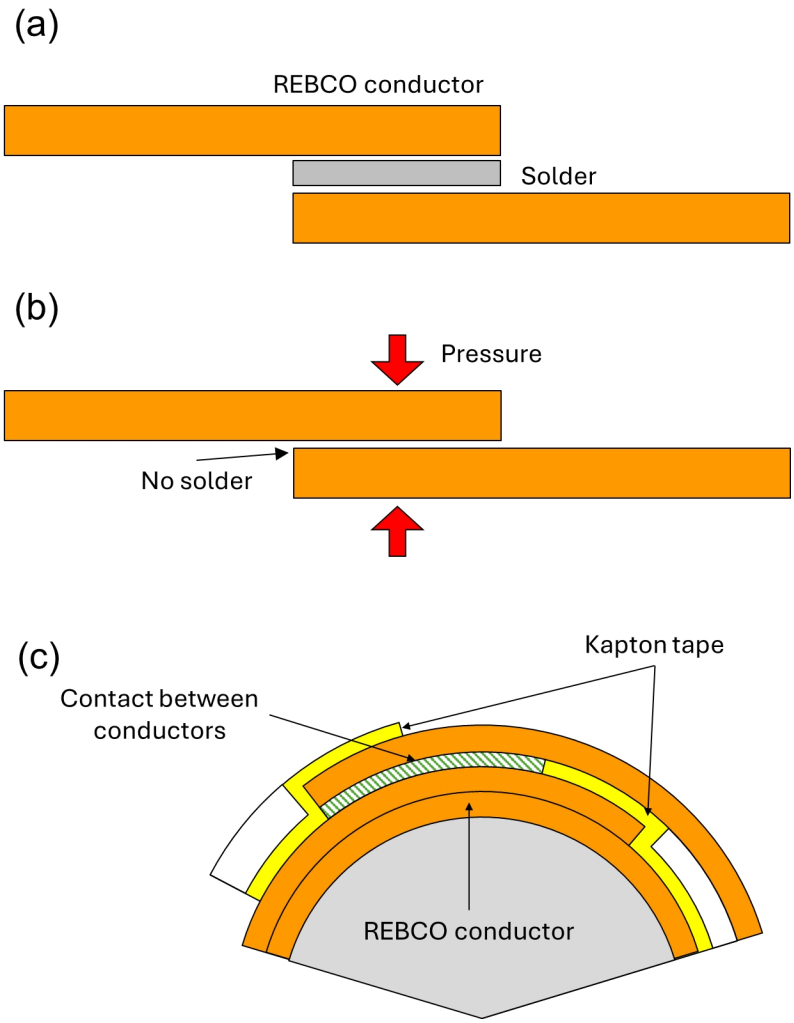

Figure 3.20: Introduction of a solder-free lap joint. (a) Traditional soldering lap joint, (b) Pressure-based solder-free joint, (c) Schematic of solder-free lap joint implementation within the coil.

Step1: Winding of coil 3

Step2: Insertion of the outermost turn of coil 3 into gap of wedge structure (Magenta arrow)

Step3: Pressing wedge structure from both sides and secure it with bolts (Red arrow)

Step4: Winding of coil 2 with conductor as the 1st turn pulled out in Step2

Step5: Repeating Step2 and Step3 for coil 2

Step6: Repeating Step4 for coil 1

Step7: Repeating the above processes for the opposite side

Step8: Constructing a solder-free lap joint by wrapping the conductors coming out of coil 1 on both sides around the outermost turn of the opposite coil (Green arrow)

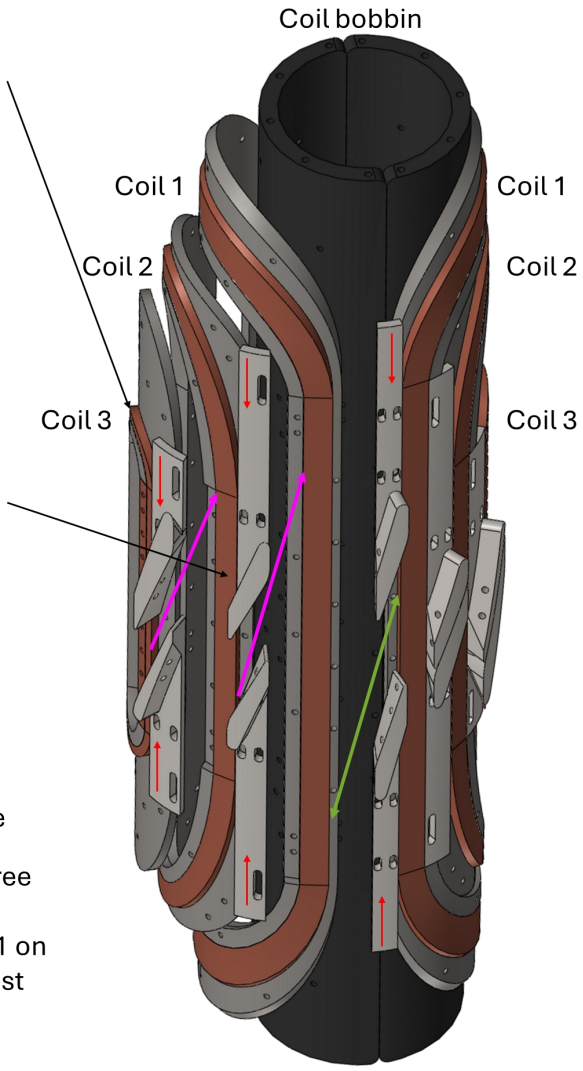

Figure 3.21: Overall summary of coil assembly process

3.3 Experimental Setup and Conduction Cooling Operation

To operate the assembled coil in a conduction-cooled environment, an appropriate experimental setup is required. The main data to be measured from the coil is the magnetic field distribution at the center. Therefore, a field-mapper was installed along with the conduction cooling system to measure the magnetic field at the center. For this purpose, the chamber of the conduction cooling system was designed with a room-temperature bore at the center. Additionally, to verify the stable operation of the coil, temperature and voltage were measured in real time by installing temperature sensors and voltage taps. After installing the magnet, cooling was performed using a cryocooler, and the cooling profile was analyzed using the previously mentioned thermal circuit model. The temperature gradient within the coil was also measured and compared with previous analysis results.

3.3.1 Experimental System Construction

The data to be measured from the fabricated magnet includes 1) magnetic field distribution; 2) voltage of each coil; and 3) temperature. Each measurement requires specific equipment and experimental setup. First, a field-mapper was designed and installed to measure the magnetic field distribution. Figure 3.22 shows the schematic and actual installation of the field mapper. The field-mapper's external frame is approximately 1 m$\times$1 m$\times$2 m in size, with stepper motors mounted on the top metal frame for positional control in three axes, allowing precise positioning to 0.01 mm. A rod about 1 m long, attached to the position control unit of the field-mapper, is inserted into the room-temperature bore of the conduction cooling chamber, with a Hall sensor mounted at the end of the rod to measure the magnetic field. The Hall sensor used in this experiment is the Lakeshore HGCT-3020 model, operated via the Lakeshore Model 121 DC current source. The Hall sensor outputs a voltage signal in the presence of a magnetic field, and calibration was performed in a room-temperature environment as shown in Figure

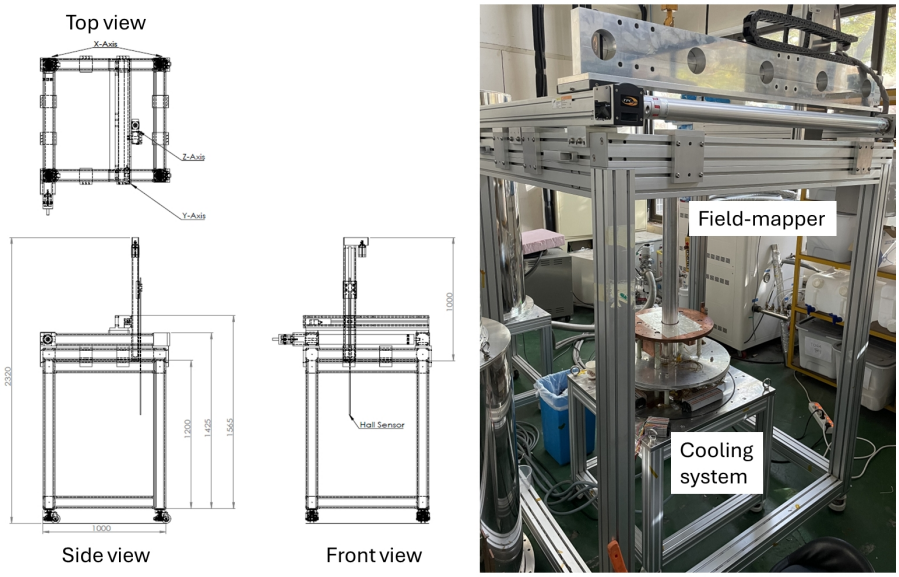

Figure 3.22: Drawings of the field-mapper used in the experiment and photos of the actual installation

3.23, allowing the voltage signal to be converted into magnetic field measurements.

The voltage output from the Hall sensor and the coil is at a similar mV-level, so the same data acquisition system (DAQ) was used to measure both voltages. The DAQ used includes the SCXI-1000(chassis), 1125(voltage input module), and 1305(Bayonet Neill-Concelman terminal), all from National Instruments, as shown in Figure 3.24 (a). The sampling rate during measurement was 5 Hz. Lastly, temperature sensors and monitors were used to measure the temperature of different parts of the magnet and cooling system. For temperature sensors, DT-670 silicon diode sensors from Lakeshore were used, and the temperature monitors were the Lakeshore Model 224 and Model 336, shown in Figure 3.24 (b). Since the magnet in this study aims to create a uniform magnetic field distribution, stable operation of the current source is essential. The power supply used for the experiment was the MercuryiPS from Oxford Instruments, as shown in Figure 3.24 (c), which offers a current stability of 2 mA. Creating a vacuum environment is essential in conduction cooling to prevent heat intrusion from

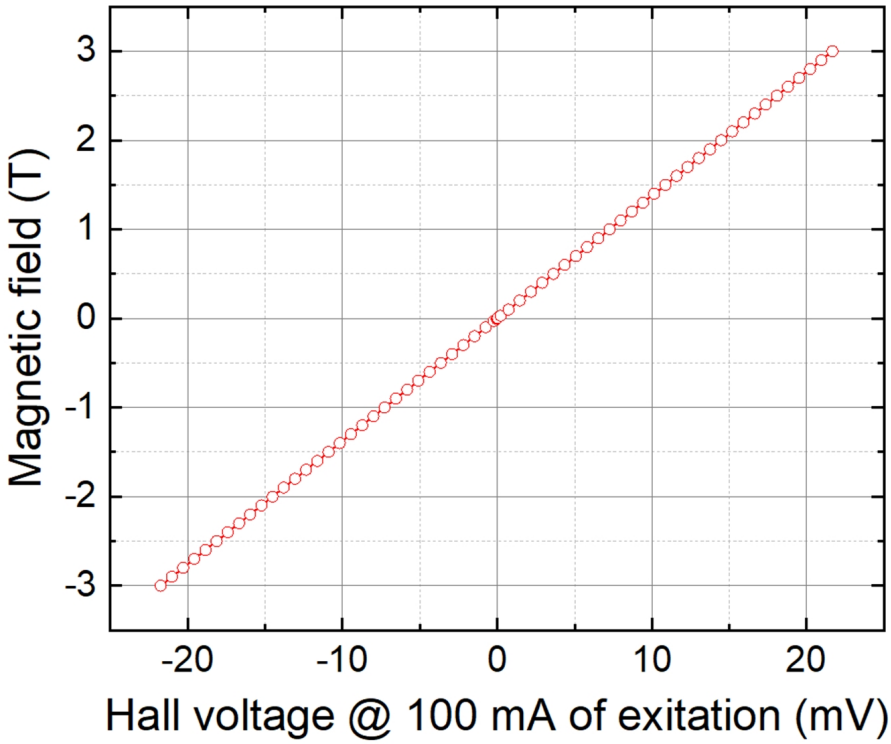

Figure 3.23: Calibration results of Hall sensor used in the experiment

convection. In this experiment, a rotary pump and a turbo pump were used to achieve a vacuum level of less than 10^{-6} Torr. The equipment used to measure the vacuum level was the DualGauge from Pfeiffer.

The method of assembling and installing the magnet and experimental equipment is shown in Figure 3.25. Figure 3.25 (a) illustrates the signals output from the magnet, cooling system, and field-mapper, which are read and processed by the measurement devices. The conduction cooling chamber is located inside the field-mapper, with the magnet assembled inside the chamber. The magnet outputs temperature and voltage signals, which are read by the measurement equipment; the cooling chamber outputs temperature readings, and the field-mapper outputs Hall voltage signals. These signals are monitored and recorded in real-time on a PC. A photo of the actual magnet installation is shown in Figure 3.25 (b). As previously described, the field-mapper is

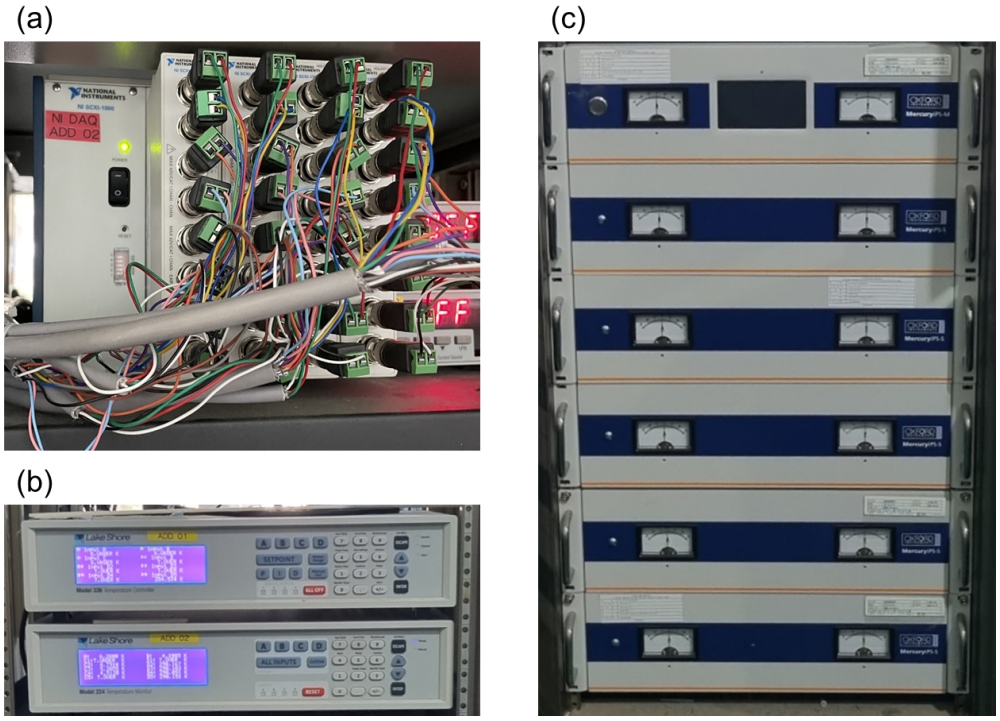

Figure 3.24: Equipment used in the experiment. (a) SCXI-1125 for voltage measurement, (b) temperature monitor Model 224 and 336 for temperature measurement, (c) MercuryiPS used as the power supply.

positioned externally, with a rod containing the Hall sensor inserted from above into the room-temperature bore. The magnet is cooled by direct contact between the bobbin and the copper plate attached to the second stage, and additional cooling channels were established using copper braided wire (shown as thin yellow wires in the figure). Relatively thick copper braided wire was used to supply current to the magnet from the current leads of the cooling system. Temperature sensors were attached throughout the magnet to monitor temperature, and voltage taps inserted in the coils were used to measure voltage at various points.

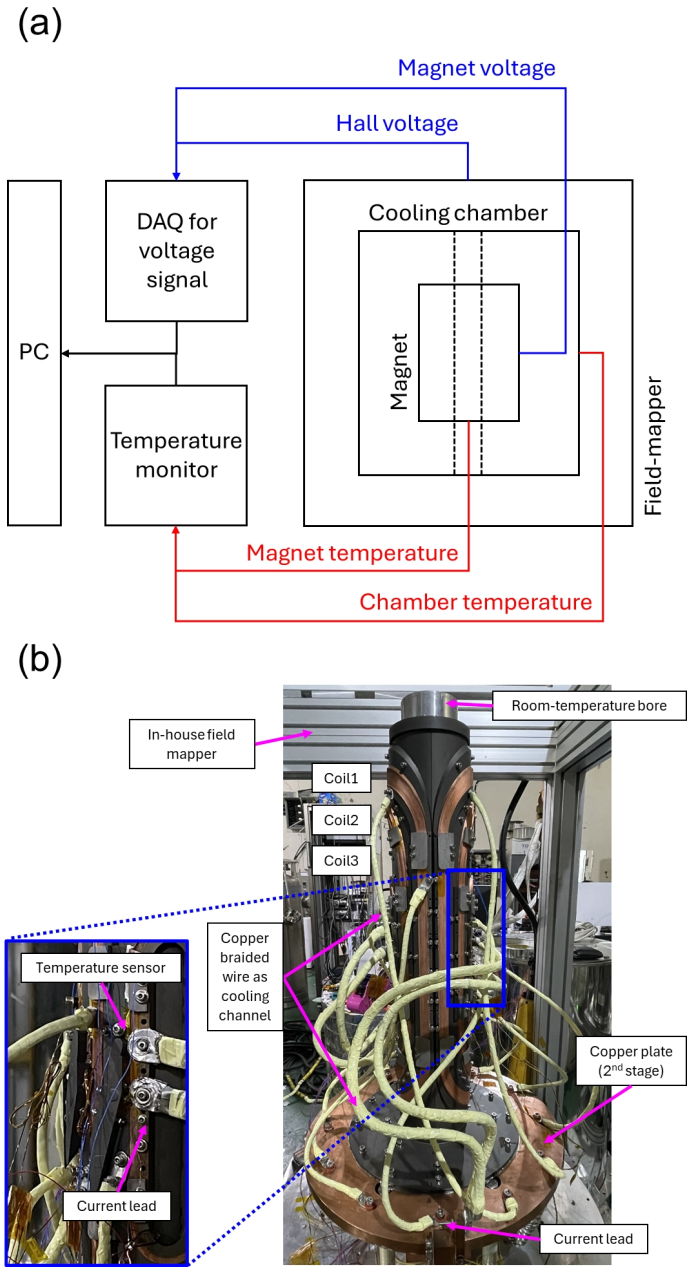

Figure 3.25: Overall experimental setup. (a) Schematic diagram of data extraction points and measurement data processing method, (b) Experimental setup of the main magnet.

3.3.2 Cooling Results and Cryogenic Properties

The assembled magnet was cooled using the conduction cooling system, and the main temperature profile is shown in Figure 3.26. The total time required to cool the magnet was 29.2 hours. The temperature of the first stage cold head stabilized at 45.7 K, and the surface temperature of the radiation shield attached to the first stage stabilized at 51.0 K. The temperature of the second stage cold head, where the magnet was installed, stabilized at 8.7 K. As shown in small inlet in the figure, temperature measurements taken from sensors attached to the surface of the magnet's bobbin showed that the lowest point on the bobbin reached 10.1 K, while the highest point reached 11.3 K. Based on the predictions in Figure 3.16, the temperature gradient of approximately 1.2 K suggests a thermal resistance of about 0.02 K/W between the coil and the copper plate of the second stage.

Using the thermal circuit model from Figure 3.14, along with the parameters in Table 3.4 and Figure 3.15, thermal analysis was conducted to interpret the cooling profile. The thermal contact resistance values between each node were initially estimated from previous experimental data and then optimized to minimize discrepancies with the measured results. For the analysis, assumptions about the level of thermal intrusion were necessary. The primary sources of thermal intrusion were through the current leads and radiative heat. Based on the cooling map in Figure 3.11, a total thermal intrusion of approximately 54 W was estimated, with the first stage dissipating about 53.98 W and the second stage dissipating around 0.02 W at equilibrium. With these assumptions, the overall thermal resistance in the cooling system was interpreted to be around 0.01 K/W. The analysis results are shown in Figure 3.27. This analysis model will also be used to analyze the temperature rise due to bypass currents during charging and discharging.

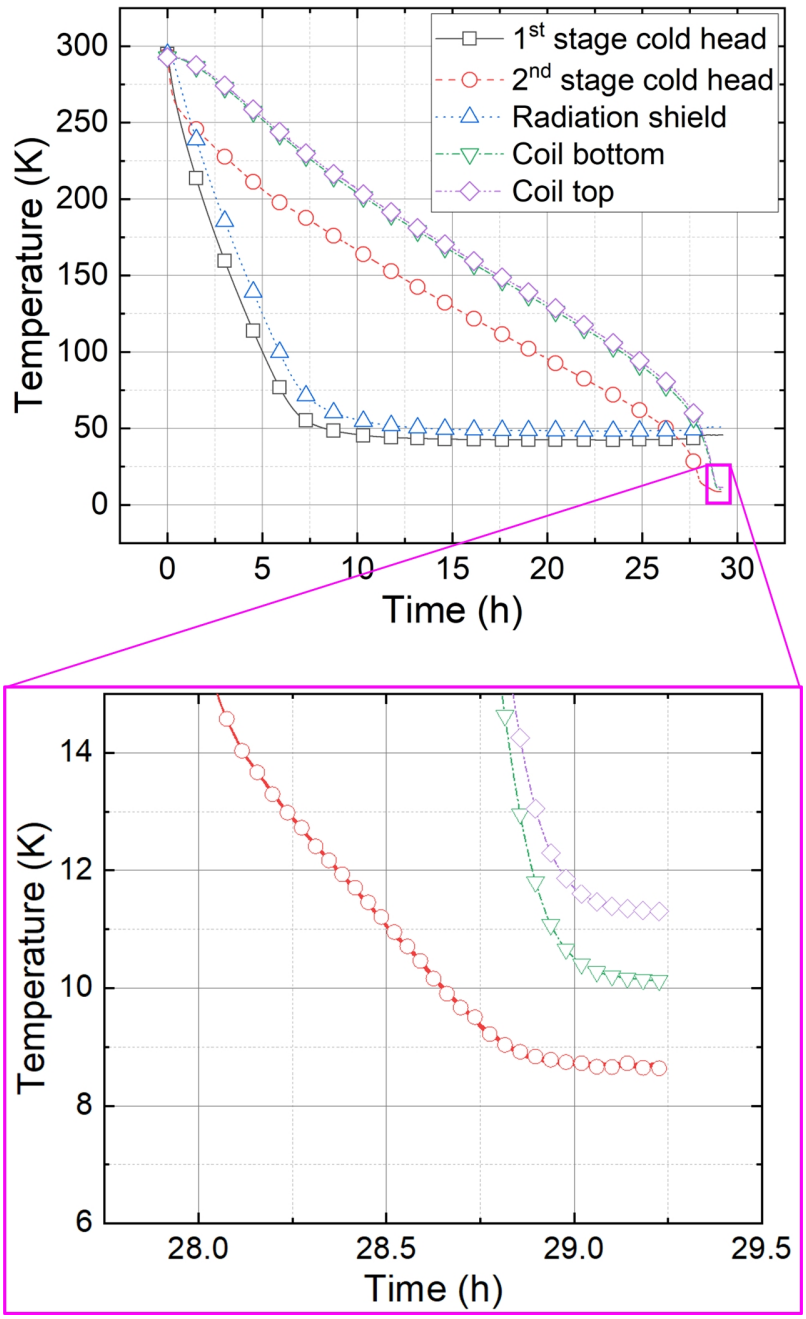

Figure 3.26: Overall cooling profile and thermal gradient measurement results at the final temperature

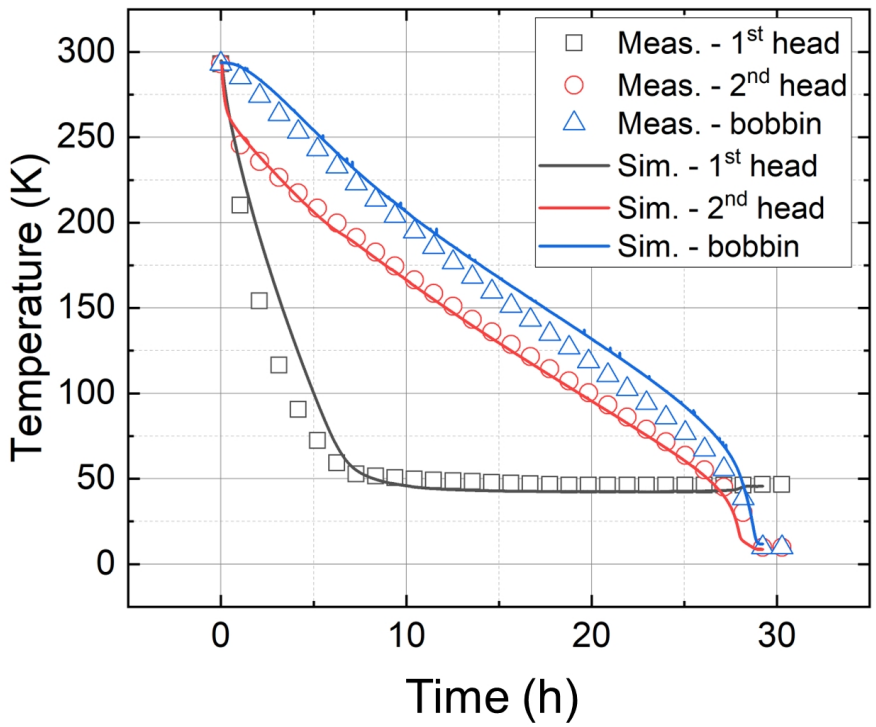

Figure 3.27: Comparison of the thermal circuit model analysis results with the measured cooling profile

3.4 Summary of Design and Fabrication of Demo Magnet

The preceding sections of this chapter provided a detailed discussion of the design, fabrication, and cooling method for the 0.7 T dipole magnet, the primary subject of analysis and experimentation. However, before these techniques were developed, a process of trial and error was conducted using a demo magnet. This section provides a brief summary of the demo magnet. The demo magnet was relatively small, was tested in a liquid nitrogen environment, and had a central magnetic field strength of only about 0.1 T. A comparison will be made between the issues identified in the demo magnet and the improvements applied to the 0.7 T magnet.

3.4.1 Main Differences between the Dipole Magnet with a Center Field of 0.7 T and Demo Magnet

Demo magnet was produced prior to the 0.7 T saddle-shaped dipole magnet discussed in this study. The purpose of the demo magnet was to minimize conductor usage by testing and experimenting on a smaller scale, allowing for the identification and improvement of potential issues before conducting experiments on the primary magnet. The design, analysis, fabrication, and operational methods previously discussed were refined based on the test results of the demo magnet. Therefore, detailed descriptions of the design and fabrication steps are omitted here, and a summary is provided in this section. The main differences between the demo magnet and the 0.7 T magnet are shown in Table 3.6.

The demo magnet was produced twice with the same design, using different winding techniques. The first was wound in an NI manner to confirm the current-bypassing characteristics, and the second applied a 2-ply winding method, a form of cabling, to verify high-speed charge-discharge characteristics. The 2-ply winding technique is a type of cowinding in which two REBCO wires are stacked together, with each turn configured as REBCO-REBCO-insulation(Kapton) to allow current sharing only be-

Table 3.6: Comparison of the key differences between the demo magnet and the main magnet

Factors	**Demo magnet**	**0.7 T saddle-shaped dipole main magnet**
Winding technique	NI / 2-ply	NI
Widning diameter	80 mm	110 mm
Axial length	250 mm	550 mm
The number of coil pairs	2	3
Shape of coil end-part	superellipse (n=3)	ellipse (n=2)
Center magnetic field	0.1 T	0.7 T
Magnetic field uniformity	8.8×10^{-4} @ 15 mm reference radius	1.9×10^{-4} @ 15 mm reference radius
Electrical connection between coils	Soldered lap joint	Solder-free lap joint
Mechanical support at straight section	N/A	Wedge structure
Cooling method	Liquid nitrogen (77 K)	Conduction cooling (15 K)

tween the two adjacent conductors. To simplify fabrication, the demo magnet was relatively small in size and was made with two coil pairs instead of three.

In the case of the demo magnet, the shape of the end-part (curved section) was designed as a superellipse rather than an ellipse to test for curvature continuity with the straight section. The central magnetic field strength was also lower, around 0.1 T, and the magnetic field uniformity was designed to be lower over the same reference radius. Coil-to-coil connections were made by soldering to form lap joints, implemented as shown in Figure 3.28. This method was chosen because, to avoid bending the conductor and to bring it outwards for soldering, the surfaces of the two conductors were not parallel, making a conventional lap joint impossible. The demo magnet did not have a

reinforcement structure for the straight section, and the cooling was conducted only in a liquid nitrogen environment for tests.

3.4.2 Problems identified during Fabrication and Test of Demo Magnet and Corresponding Improvements

When the demo magnet was produced as described above, several issues were identified during the design, construction, and operation processes, as outlined below.

- **[Design]** It was determined that two coil pairs were insufficient to achieve adequate magnetic field uniformity. Increasing the number of coil pairs raises the difficulty and time required for fabrication, but it also adds more adjustable variables in the design, thereby enhancing magnetic field uniformity. Based on this, the design was modified to include three coil pairs.

- **[Design]** Although designing the coil's end-part as a superellipse can theoretically ensure curvature continuity, it proved to have minimal effect in practice. Instead, it created sections where the winding surface angle changed more steeply, making the manual winding process with the universal joint more challenging. Therefore, an elliptical shape was applied instead of a superellipse, resulting in a relatively easier winding process.

- **[Construction]** During winding, the absence of clamps to hold the straight sections caused deformation of the coil shape. This occurred because the straight sections experienced almost no compressive stress from winding tension. Although tension appeared to be applied while winding each turn, it actually loosened in the straight sections during the transition to the next turn due to factors like friction between conductors. To address this, clamps were applied every 180 degrees to maintain pressure, ensuring that the straight sections remained taut and tension was sustained until the winding was complete.

- **[Construction]** To create soldered lap joints for electrical connections between coils, additional space was required specifically for these joints. In the demo magnet, a cylindrical structure was added at the bottom of the coil to fabricate the joint on its side, which was both spatially inefficient and introduced inductance and magnetic field effects that could impact coil operation. Additionally, oxidation of the lap joint over time was observed. To address these issues, a solder-free lap joint was introduced, with coil connections implemented by drawing the conductor continuously between coils.

- **[Operation]** Operating in a 77 K liquid nitrogen environment limited the achievable magnetic field level. Additionally, since the Hall sensor was placed inside liquid nitrogen during magnetic field mapping, temperature changes could alter the sensor's sensitivity, and vibrations from nitrogen boiling caused noise in the Hall sensor signal. To address these issues, experiments were conducted using a conduction cooling system with a room-temperature bore.

- **[Operation]** Without reinforcement for the straight sections, significant shape deformation due to thermal contraction was observed. As will be discussed later, this shape change severely degraded the uniformity of the magnetic field. To address this, a wedge-shaped reinforcement structure was applied to the straight sections to maintain pressure, and the magnet was operated in this stabilized configuration.

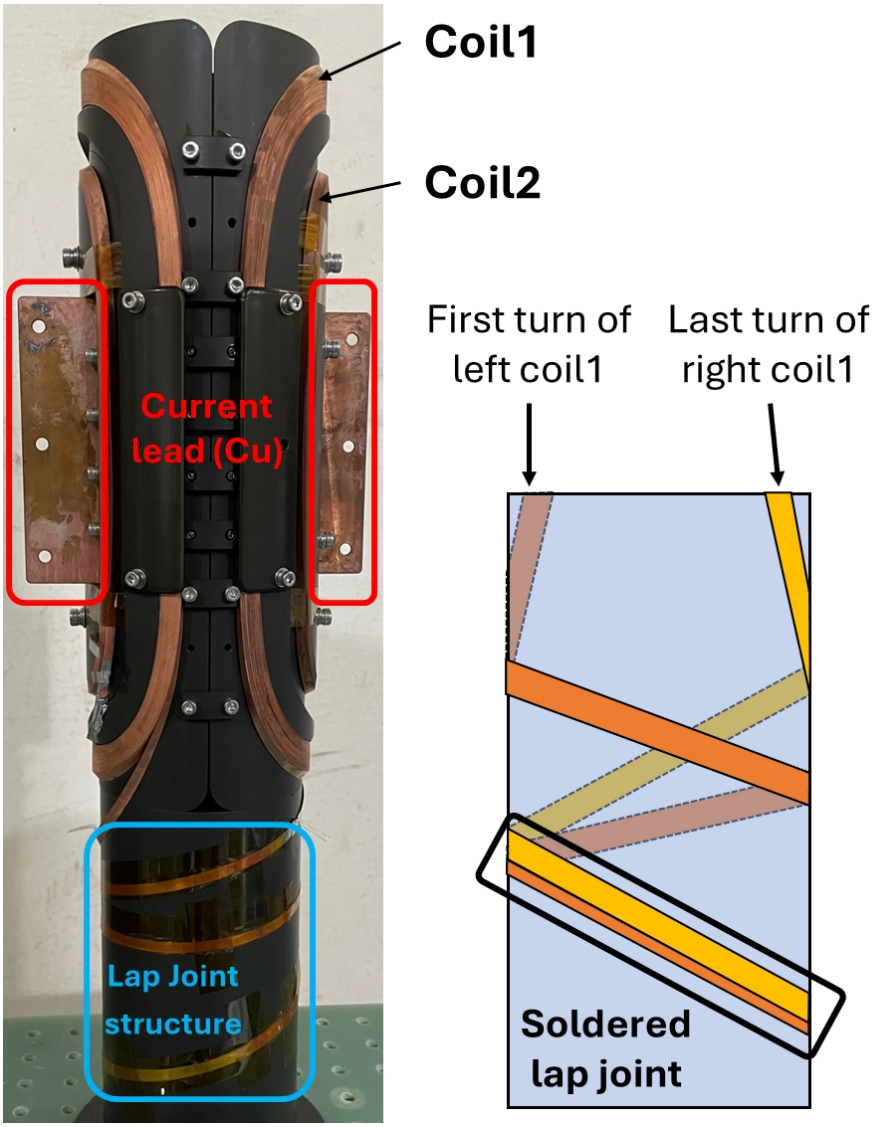

Figure 3.28: Photograph of the demo magnet fabrication and the implementation method for soldering lap joints

Chapter 4

EXPERIMENTAL RESULTS AND ANALYSIS OF HTS SADDLE-SHAPED DIPOLE MAGNET

This chapter describes the experimental results for the fabricated magnet. The magnet was operated in a conduction cooling environment and achieved the target central magnetic field. However, the measured magnetic field uniformity was lower than the designed value. This issue appears to result from shape deviations during fabrication, measurement errors, and screening current. Additionally, the temporal stability of the magnetic field under sustained current in driven-mode operation was examined. To improve magnetic field uniformity, a ferroshim was designed and fabricated, and measurements confirmed an improvement in uniformity.

4.1 Experimental Results and Analysis for HTS Dipole Magnet

The results of the magnet's conduction cooling environment experiments can be summarized as follows: 1) center magnetic field of 0.7 T achieved; 2) pre-compensation magnetic field uniformity of 14×10^{-4}; 3) temporal stability of field uniformity below 0.38×10^{-4}/hour. Current sweep reversal (CSR) technique, which helps improve

magnetic field uniformity through screening current, was applied to measure potential improvements. However, the effect of CSR was minimal, as confirmed by screening current analysis results calculated using the widthwise-segmented circuit model.

4.1.1 Experiment Procedures

The overall process of experiments conducted after cooling was progressed as follows.

- **Charge-Discharge Test**: The magnet was charged to the target current of 295 A. Due to the NI winding of the magnet, magnetic field charging delay occurred due to current bypassing, which can help identify parameters like contact resistivity based on the extent of this delay. Temperature increases during the charging and sudden-discharge processes were measured to determine the heat generation in the NI magnet.

- **Measurement of Magnetic Field Distribution**: The magnetic field distribution at a current of 200 A was measured using the field-mapper to check for deviations from the designed uniformity. Since the reference radius for the designed magnetic field uniformity was 15 mm, the magnetic field was measured at 12 points spaced 30 degrees apart along circumferences with radii of 5, 10, and 15 mm from the center. The current was set to 200 A instead of 295 A to serve as a control for the CSR test.

- **Current Sweep Reversal Test**: CSR is an operational technique designed to counteract the reduction in magnetic field uniformity caused by screening currents. This method involves applying a current slightly above the target current and then reducing it back to the target level, which helps offset the current distribution effects caused by screening current during the charging process. The effect of CSR on the saddle-shaped magnet was observed by measuring the magnetic field uniformity.

- **Comparison of Magnetic Field Uniformity by Current Level**: To measure the changes in magnetic field distribution caused by screening current, experiments were conducted at operating currents of 50 A, 100 A, and 150 A, and the uniformity was measured for each case.

In chronological order, after these experiments were completed, a ferroshim was fabricated and tested to correct the magnetic field uniformity, and finally, an experiment was conducted to measure the magnet's critical current.

4.1.2 Basic Operations Results

In an NI magnet, heat generation occurs during charging and discharging due to current bypass characteristics. Since the amount of heat generated is proportional to the charging rate, a very slow charging rate must be used to prevent temperature rise. In this experiment, the charging rate was limited to set below 2 A/min for all tests.

The results of charging up to 295 A are shown in Figure 4.1. Figure 4.1 (a) displays the current profile up to 295 A and the central magnetic field profile, while (b) shows the voltage graph for each coil. The central magnetic field reached 0.717 T at 295 A, showing a deviation of approximately 0.4% from the designed value. This minor deviation is likely due to shape imperfections from the fabrication process. Since coil2s contained solder-free lap joints, the internal resistance value can be measured from the voltage while holding the current. Figure 4.2 shows the results of the sudden-discharge experiment. To avoid potential damage from heat generation during a sudden-discharge at higher current, the test was conducted at 50 A. Figure 4.2 (a) shows the measured current, voltage, and central magnetic field, while (b) displays the coil-specific voltage at the point of sudden discharge. From the coil voltages, the inductance of each coil was verified, and the contact resistivity for each coil was analyzed. The coil parameters measured from the experimental results are shown in Table 4.1.

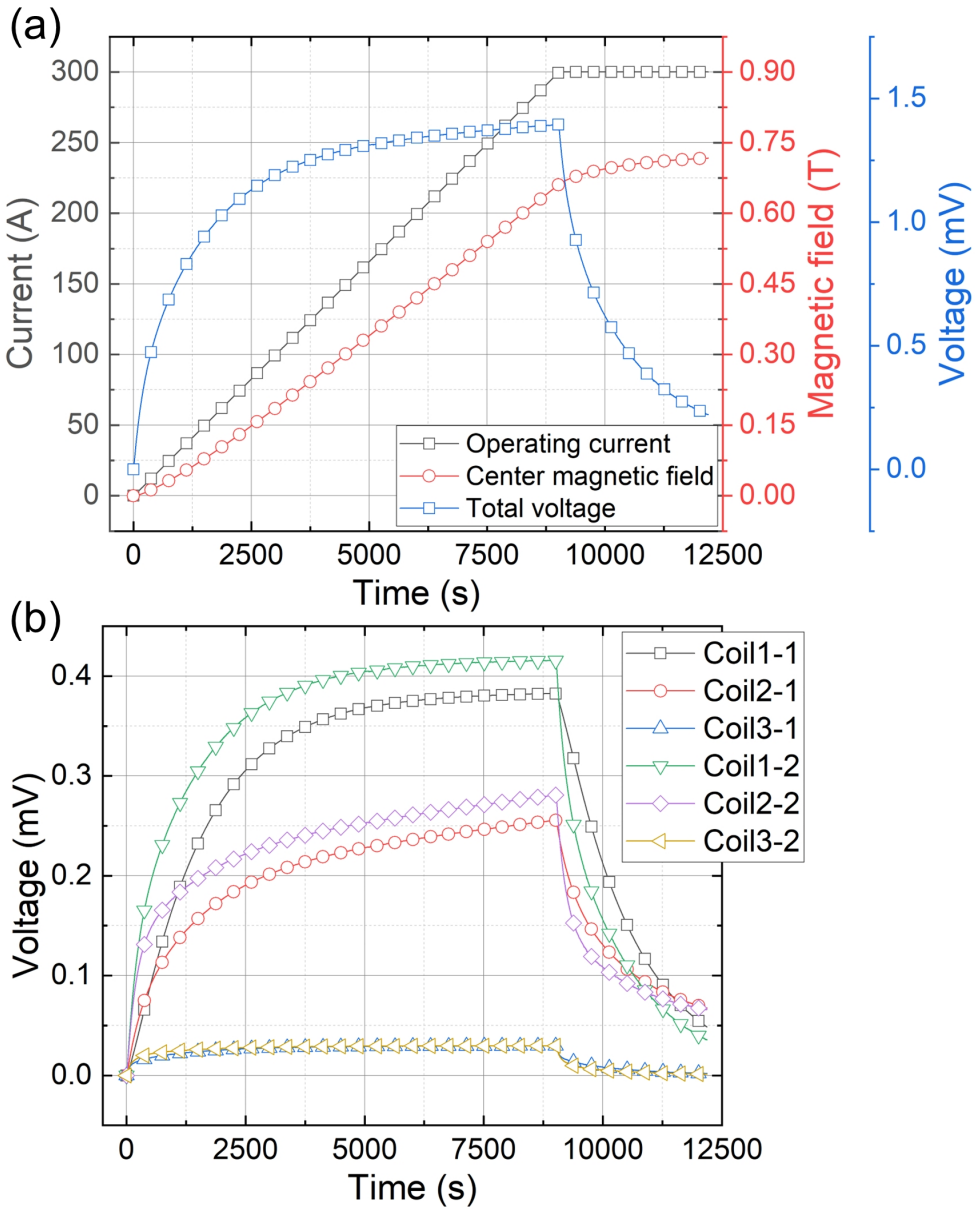

Figure 4.1: Magnet charging experiment results. (a) Current charging profile at 295 A and measurement results of central magnetic field charging delay, (b) Voltage measurement results for each coil.

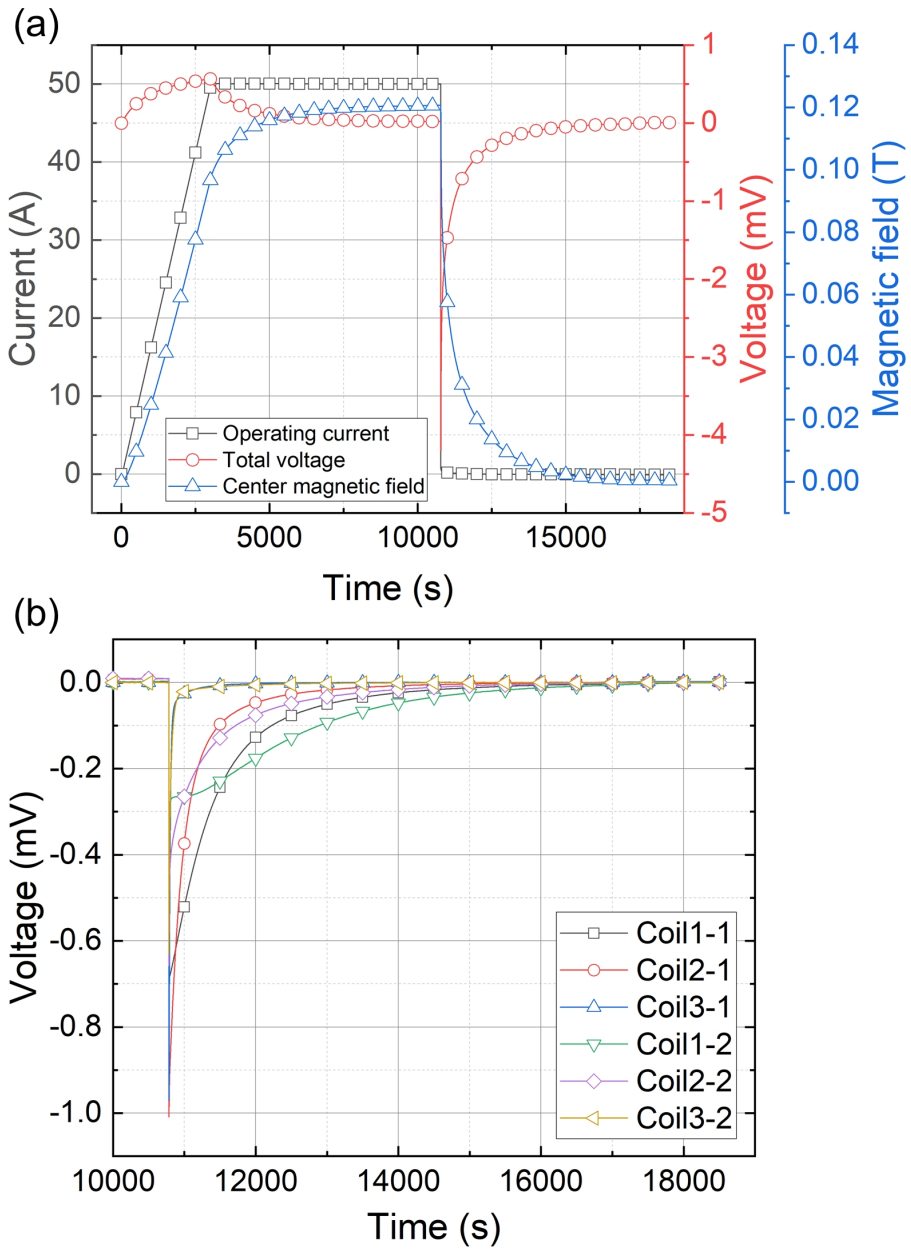

Figure 4.2: Magnet sudden-discharge experiment results. (a) Measurement results of current, magnetic field, and voltage during the entire operation process, including sudden-discharge, (b) Voltage measurement results for each coil at the moment of sudden-discharge.

Table 4.1: Measured characteristic resistance and contact resistivity

Parameter	**Unit**	**Coil 1-1**	**Coil 1-2**	**Coil 2-1**	**Coil 2-2**	**Coil 3-1**	**Coil 3-2**
Characteristic resistance	[μΩ]	4.1	24.8	9.0	22.0	7.9	7.9
Contact resistivity	[μΩcm^2]	1.9	12.1	4.1	9.9	4.6	4.6
Time constant	[min]			20.0			

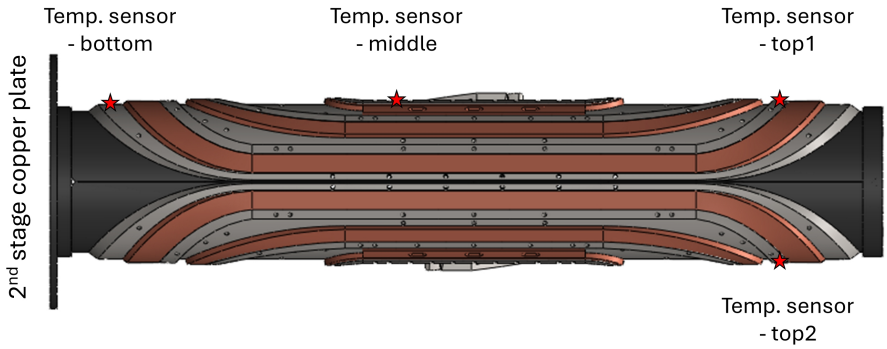

Figure 4.3: Temperature sensor attachment locations

The contact resistance parameters of the coil measured from the experimental results are shown in the table. The contact resistivity was found to range from 1.9 μΩcm^2 to 12.1 μΩcm^2, which is consistent with typical results from NI magnet experiments. In the demo magnet experiment discussed later, insufficient reinforcement of the straight section led to significantly higher contact resistivity, whereas in this magnet, it was indirectly confirmed that sufficient pressure was applied to the straight section.

These analysis results can also be used to interpret temperature rise during charging and sudden discharge of the magnet. In the circuit model for NI magnets, heat generation is modeled as follows:

$$Q = \sum_{k=1}^{N_{coil}} I_{r,k}^2 R_{c,k}, \tag{4.1}$$

where Q, N_{coil}, $I_{r,k}$, and $R_{c,k}$ represent the Joule loss, the number of coils, radial current flowing each coil, and the characteristic resistance of each coil, respectively. Figure 4.3 presents the sensor attachment locations corresponding to the analysis results.

The analysis results for temperature rise during the previous 295 A charging process and during sudden discharge are shown in Figure 4.4. Figure 4.4 (a) shows that at a charging rate of 2 A/min, temperature rise occurred due to heat generated in the copper current lead as the operating current increased to 295 A. Temperature was measured with sensors attached to the bottom, center, and top of the coil bobbin, with a maximum temperature rise of 8.0 K observed. The analysis results using the thermal circuit model closely matched the measured results. Additionally, Figure 4.4 (b) shows the measured temperature rise during the sudden discharge experiment, with the analysis results accurately replicating the measurements.

The mechanical analysis results for the magnet were not quantitatively verified due to the inability to directly measure strain using methods such as strain gauges. Instead, from a qualitative perspective, the magnet successfully operated without issues, reaching its target current. This suggests, as observed in the analysis results shown in Figure 3.10, that excessive strain was not applied to the magnet. However, it was confirmed that displacement occurred in the coil.

Figure 4.5 (a) shows the winding state before the experiment, while (b) shows the state after an attempt to cool the system, during which the target temperature of 10 K was not achieved, and the magnet was subsequently warmed up without applying current. Visible displacement occurred in the curved section of Coil 1, indicating an upward deformation. This displacement trend aligns with the displacement analysis results from thermal contraction shown in Figure 2.17. While quantitative measurements were not conducted, the process of thermal contraction is observed to cause displacement in the direction of the coil lifting away.

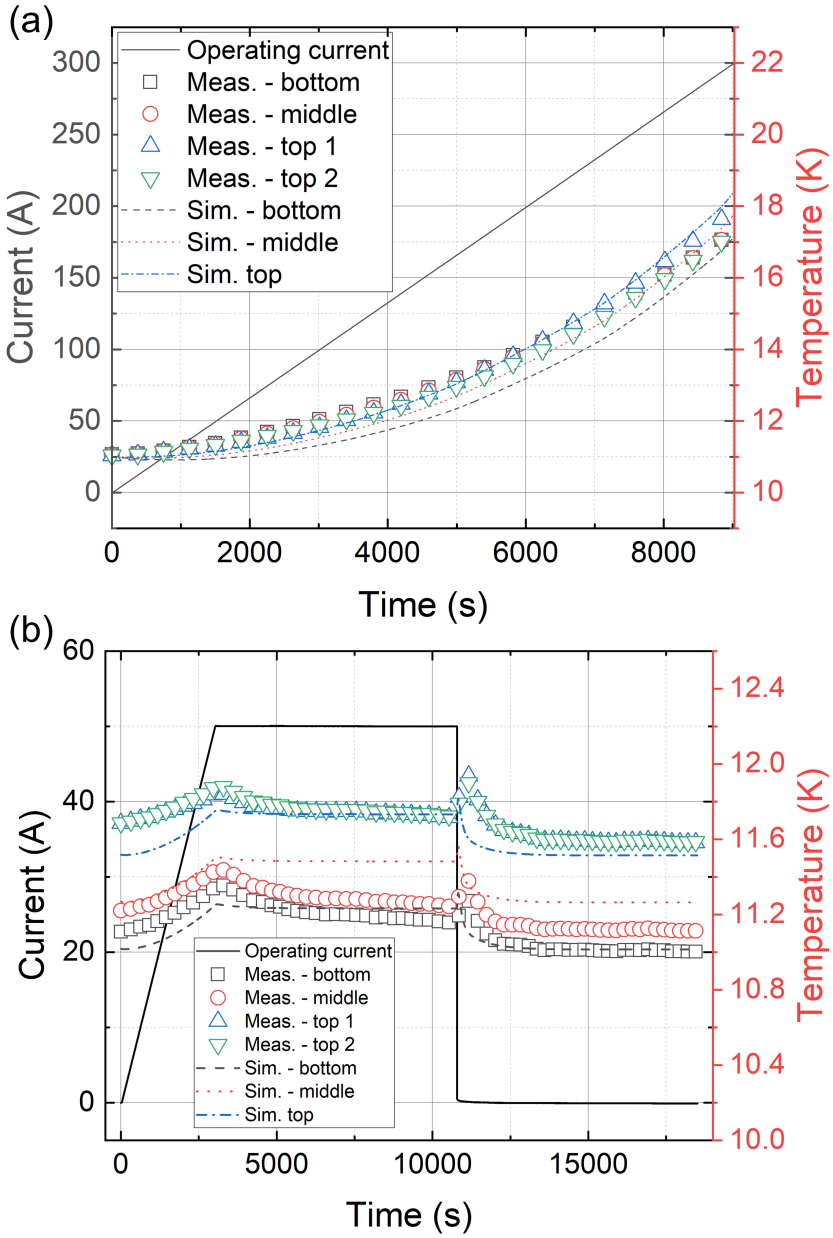

Figure 4.4: Thermal analysis results during magnet charging and sudden-discharge. (a) Comparison of thermal analysis results during the charging process up to 295 A at a rate of 2 A/min, (b) Comparison of thermal analysis results during the sudden-discharge scenario.

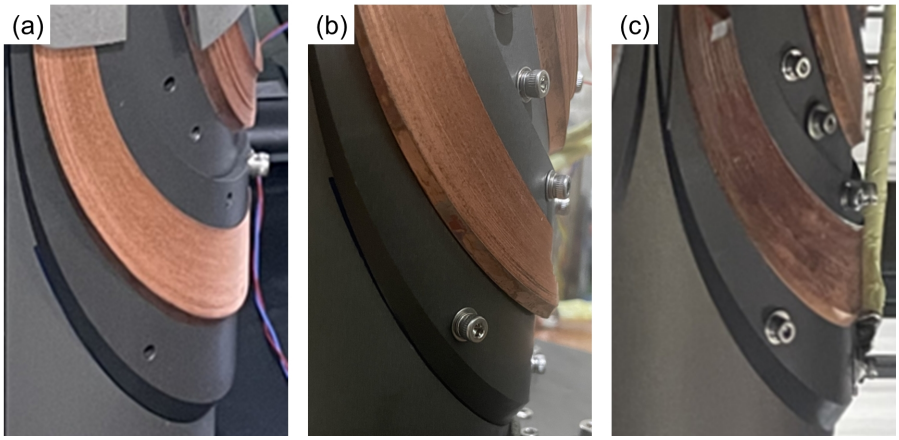

Figure 4.5: Observation of deformation during operation. (a) Winding state of coil1's curved section before the experiment, (b) State after cooling only, (c) State after cooling and operation completion.

Figure 4.5 (c) shows the winding state after cooling, current application, and the conclusion of all experiments, when the magnet was removed from the cooling chamber. At this point, the winding had returned toward the bobbin, consistent with the analysis results. These observations confirmed that the assumptions were reasonable.

Magnetic field uniformity was measured with the magnet charged to 200 A. Due to the magnetic field charging delay caused by the current-bypassing characteristics of the no-insulation magnet, a sufficiently long waiting period was required after the current had been fully charged. Since there is no clear standard for how long to wait for magnetic field relaxation, temporal stability of the magnetic field was measured to establish a guideline. The results of the magnetic field distribution measurement are shown in Figure 4.6. The magnetic field was measured at 37 points in total: the center, 12 points along a 5 mm radius circumference, 12 points along a 10 mm, and 12 points along a 15 mm. Measurements were repeated six times, and the measurement times were normalized by a time constant of 20.0 minutes. The results indicated that the magnetic field distribution was not fully stabilized at 6.8 times the time constant, while nearly identical magnetic field distributions were observed after 10 times the

time constant. At this point, the uniformity value defined in (2.28) was measured to be 14.0×10^{-4} at a 15 mm radius, which is significantly lower than the designed value of 1.9×10^{-4}. This result will be compared with cases where CSR and ferroshim were applied to determine whether magnetic field uniformity improved.

Finally, the critical current of the magnet was measured to compare it with the predicted value. During the design process, a 20% critical current margin was set based on the assumption that the operating temperature would remain constant at 15 K. However, since temperature variations under actual operating conditions are difficult to predict before measurements, the design was carried out under this assumption.

Before current charging, the actual magnet showed a temperature of approximately 10 K. When the current was charged to the point of thermal runaway quench, the maximum measured temperature was 19.1 K, with an operating current of 331 A at that point. This result supports the earlier conclusion that the 'widthwise average method' predicts the critical current more accurately than the 'widthwise minimum method'.

Assuming a current of 331 A flows at a temperature of 19.1 K, the widthwise critical current distribution at the innermost and outermost turns of each coil is shown in Figure 4.7. As evident in the results, there are points along the width where the critical current is significantly exceeded. However, since the widthwise average did not reach the operating current, 331 A was achievable. The location with the lowest widthwise average critical current was at the junction of the straight and curved sections of coil 1. The critical current was calculated to be 338 A, showing a 2.1% deviation.

Figure 4.8 (a) shows the current, voltage, and magnetic field graphs during the quench event at 331 A. While it is difficult to confirm if the quench occurred precisely at the predicted location, it was verified that the quench occurred in coil1-1. Figure 4.8 (b) presents the critical current load-line analysis. The red star indicates the operating condition where the quench occurred, confirming that the critical current was reached at an operating temperature between 19 K and 20 K. These results demonstrate that the widthwise average method effectively predicts and analyzes the critical current.

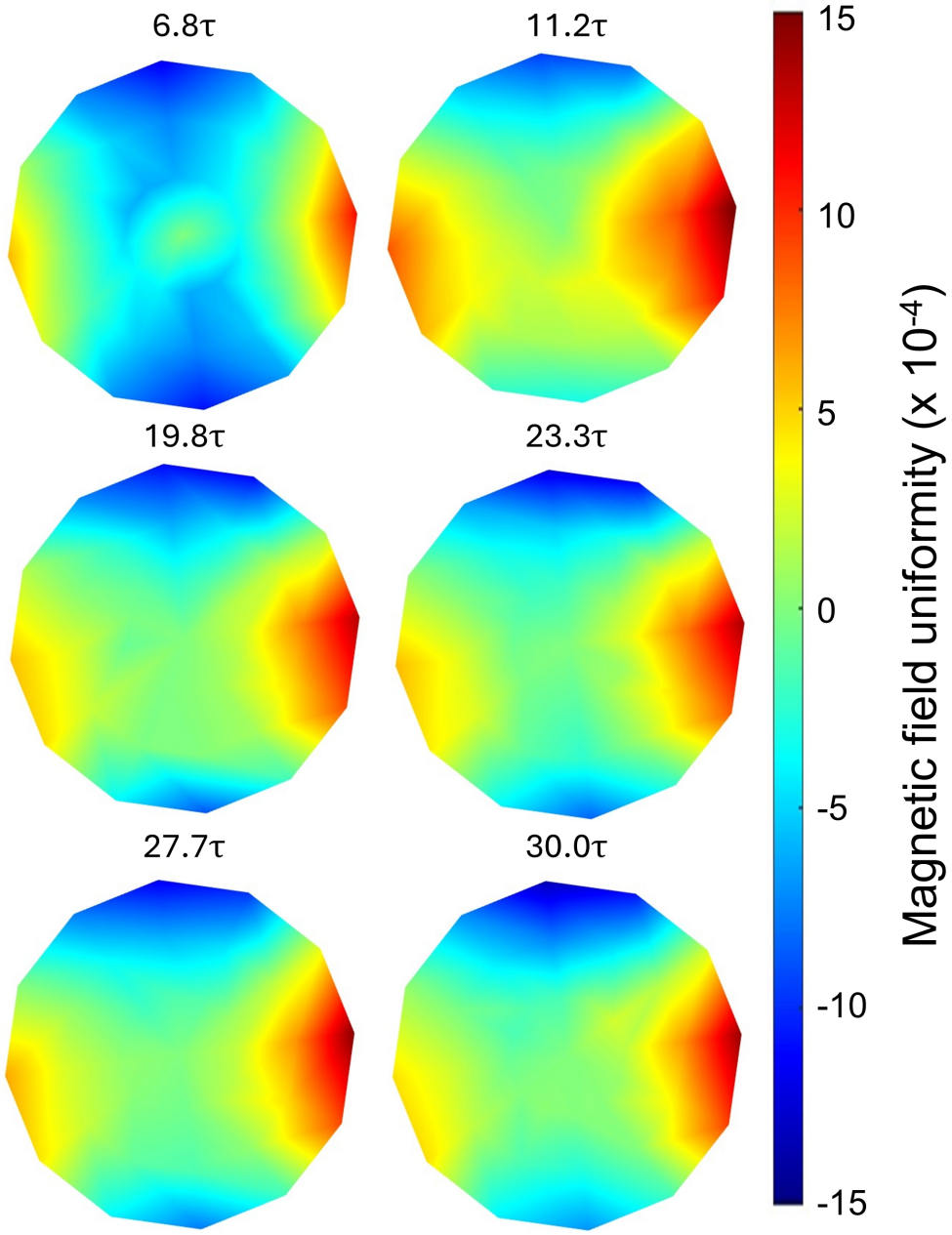

Figure 4.6: Measurement results of magnetic field uniformity over time (normilzed by time constant, 20 minutes)

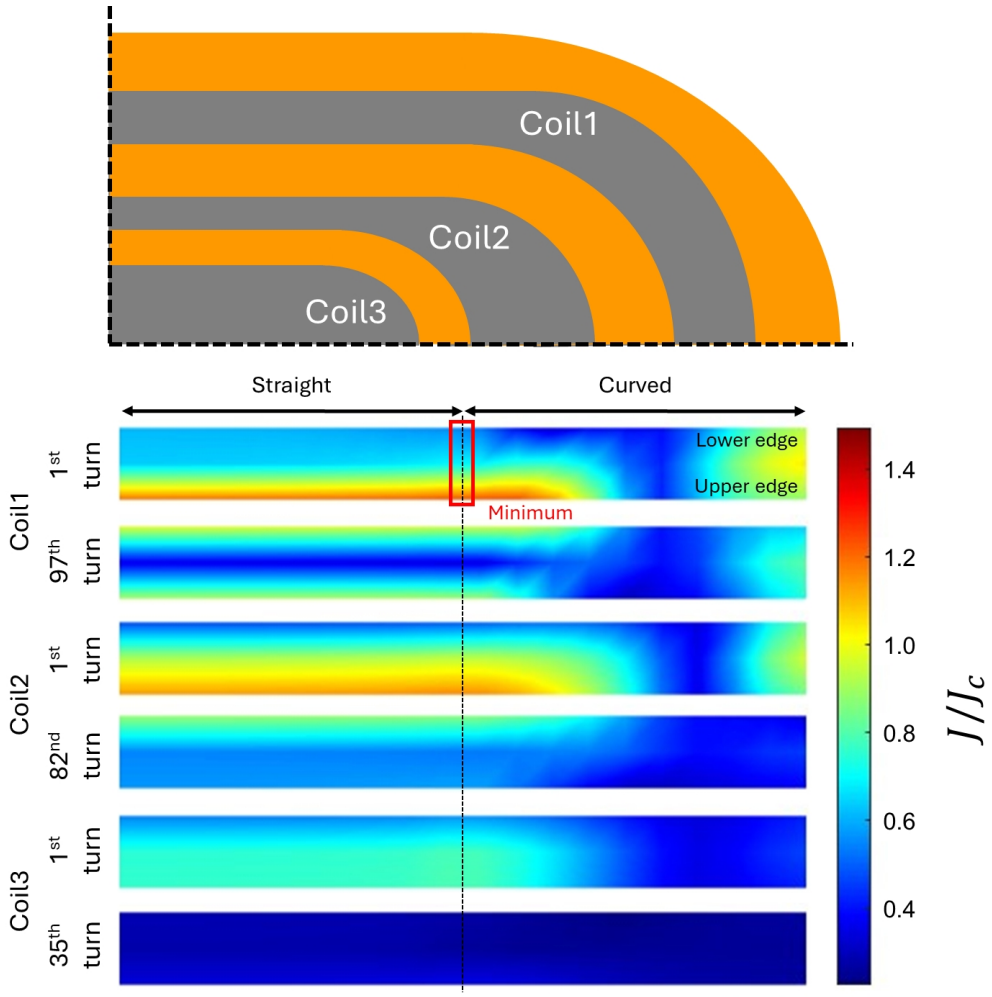

Figure 4.7: Analysis results of critical current distribution at the innermost and outermost turns of each coil

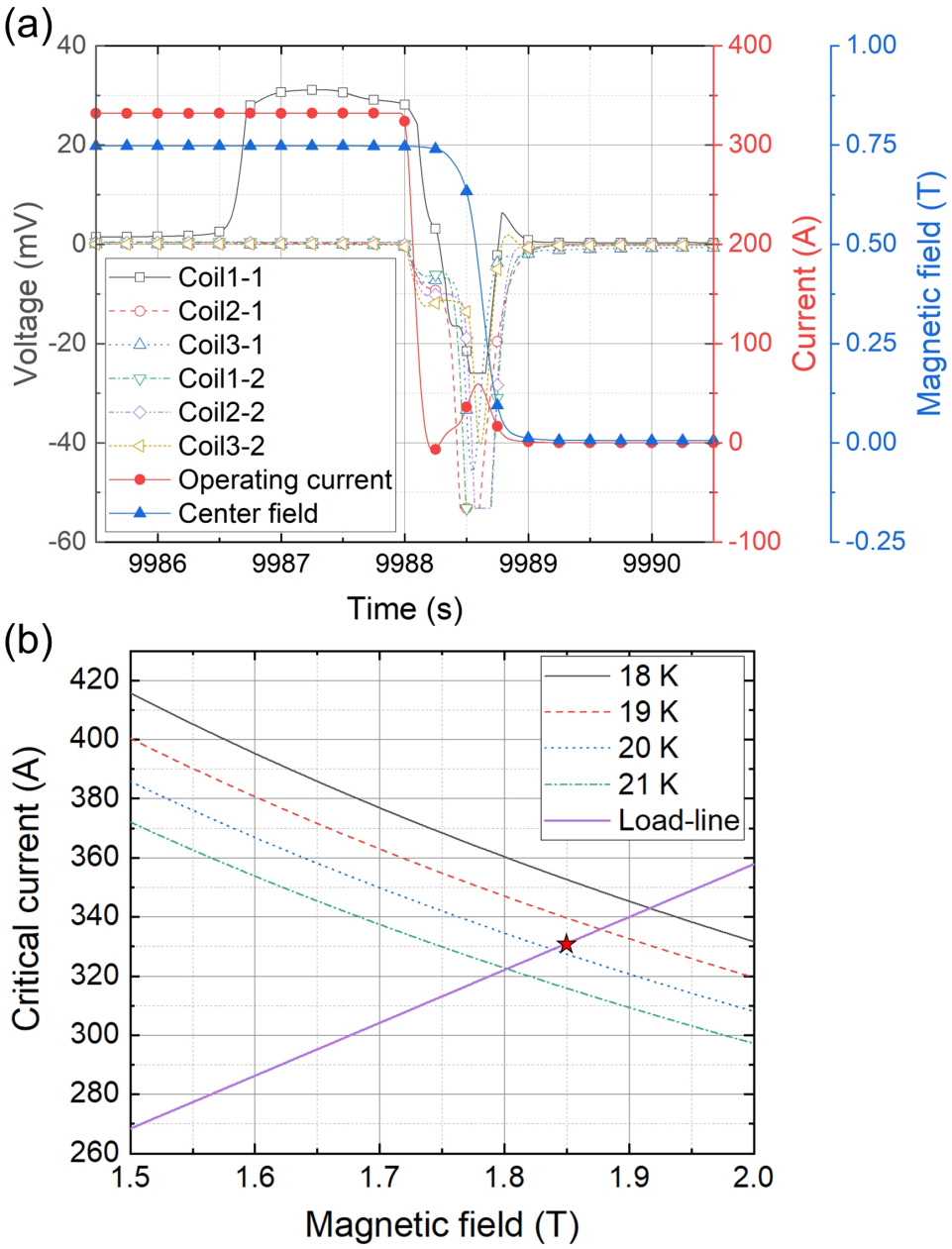

Figure 4.8: Quench results and critical current prediction. (a) Coil data at quench occurrence at 331 A, (b) Load-line margin calculation results considering temperature.

4.1.3 Current Sweep Reversal Operation Results and Screening Current Analysis Results

The CSR technique is designed to improve magnetic field uniformity degraded by screening currents through adjustments in magnet operation [141, 142]. The application method is relatively simple: the operating current of the magnet is temporarily charged beyond the target current, and then lowered back to the target level. This approach leverages the fundamental properties of screening currents. In superconductors, where resistance is zero, current is first charged from the outer layers, forming screening currents. If the current is charged directly to the target level, it remains unevenly distributed, with most of the current concentrated near the edges, and this imbalance is not easily resolved. However, by briefly increasing the current above the target level and then reducing it, a negative current density forms on the outer layers, partially mitigating the magnetic field distortion caused by screening currents. CSR takes advantage of this characteristic and has been used in solenoid magnets for NMR and MRI to improve magnetic field uniformity. However, this technique had not been applied to saddle-shaped magnets before and was introduced for the first time in this study.

The operating sequence applied in the experiment is shown in Figure 4.9. When CSR was not applied, the magnet was charged to 200 A over 200 minutes at a rate of 1 A/min, followed by magnetic field distribution measurements. When CSR was applied, the magnet was charged to 220 A, 10% higher than the target current, over 220 minutes at the same rate of 1 A/min. Afterward, the system was allowed to relax for 10 times the time constant until the magnetic field and current distribution stabilized. The current was then reduced back to 200 A at 1 A/min, and the magnetic field distribution was measured.

The magnetic field distribution measured after applying CSR is shown in Figure 4.10. Although the measurement was not conducted at exactly the same time points as in the previous experiment, data was collected up to 28.8 times the time constant to cover a comparable time range. The magnetic field distribution was found to be nearly

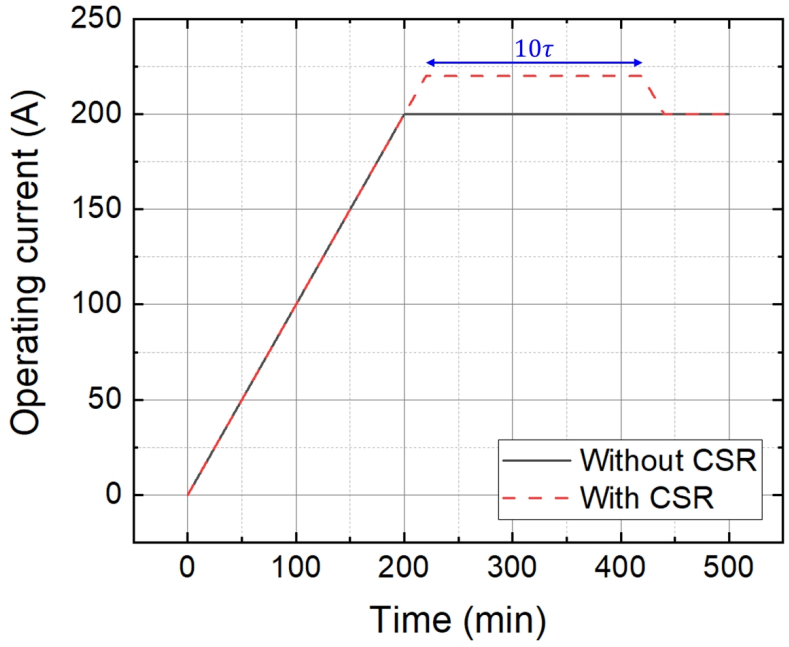

Figure 4.9: CSR operation protocol used in the experiment

identical to that measured without CSR. The magnetic field uniformity was also measured to be 13.8×10^{-4}, showing little difference from the reference. To explain this negligible difference, screening current analysis was conducted using the previously described widthwise-segmented circuit model.

The analysis results of the current distribution are shown in Figure 4.11. Since it is challenging to depict all current distributions over time, the results compare the reference scenario with the CSR-applied scenario. In the reference scenario, charging was completed in 200 minutes, followed by a stabilization process for the current distribution. In contrast, for the CSR scenario, charging was completed in 220 minutes, followed by an additional waiting period of 200 minutes corresponding to ten times the time constant, then 20 minutes to lower the current to 200 A, and finally waiting for the current distribution to stabilize. Therefore, the current distribution was compared at the following points for both scenarios: immediately after charging was completed, at 420

minutes, and at 640 minutes (considered as the point of stabilized current distribution).

The analysis results revealed differences in the characteristic resistance of each coil, which determines the NI properties, leading to varying effects of current charging delays. Additionally, when CSR was applied, the current distribution after discharge became relatively uniform. In contrast, in the reference case without CSR, the current distribution remained significantly non-uniform even after a long time. The differences in the magnetic field caused by these current distributions were analyzed and are shown in Figure 4.12. The magnetic fields generated by the current distributions at 640 minutes and the differences compared to those generated by a uniform current distribution are presented.

The overall trend in magnetic field differences varies between the two cases. Without CSR, the overall magnetic field is greater than that of a uniform current distribution, whereas with CSR, the magnetic field is smaller. This indicates that the top and bottom edges of the coil's width significantly influence the magnetic field. However, the differences in the magnetic field are approximately 20 μT. Considering that the central magnetic field is 0.5 T, the impact on magnetic field uniformity is around 0.4×10^{-4}. This is smaller than the measurement error of the Hall sensors and other measurement equipment used in the experiment, indicating that the magnetic field distortion caused by screening currents is at a level that is extremely difficult to distinguish in the experimental environment of this study.

The minimal impact of screening currents on the magnetic field distribution was also confirmed through another experiment. Before the ferroshim installation, the magnetic field distribution was measured at different operating current levels. The operating currents chosen for comparison were 50, 100, and 150 A. These levels were selected because the current distribution within the conductor at lower operating currents differs from that at 200 A, and if the effect of screening currents were significant, differences in the magnetic field distribution would be observable.

The experimental results are shown in Figure 4.13. After completing the charging

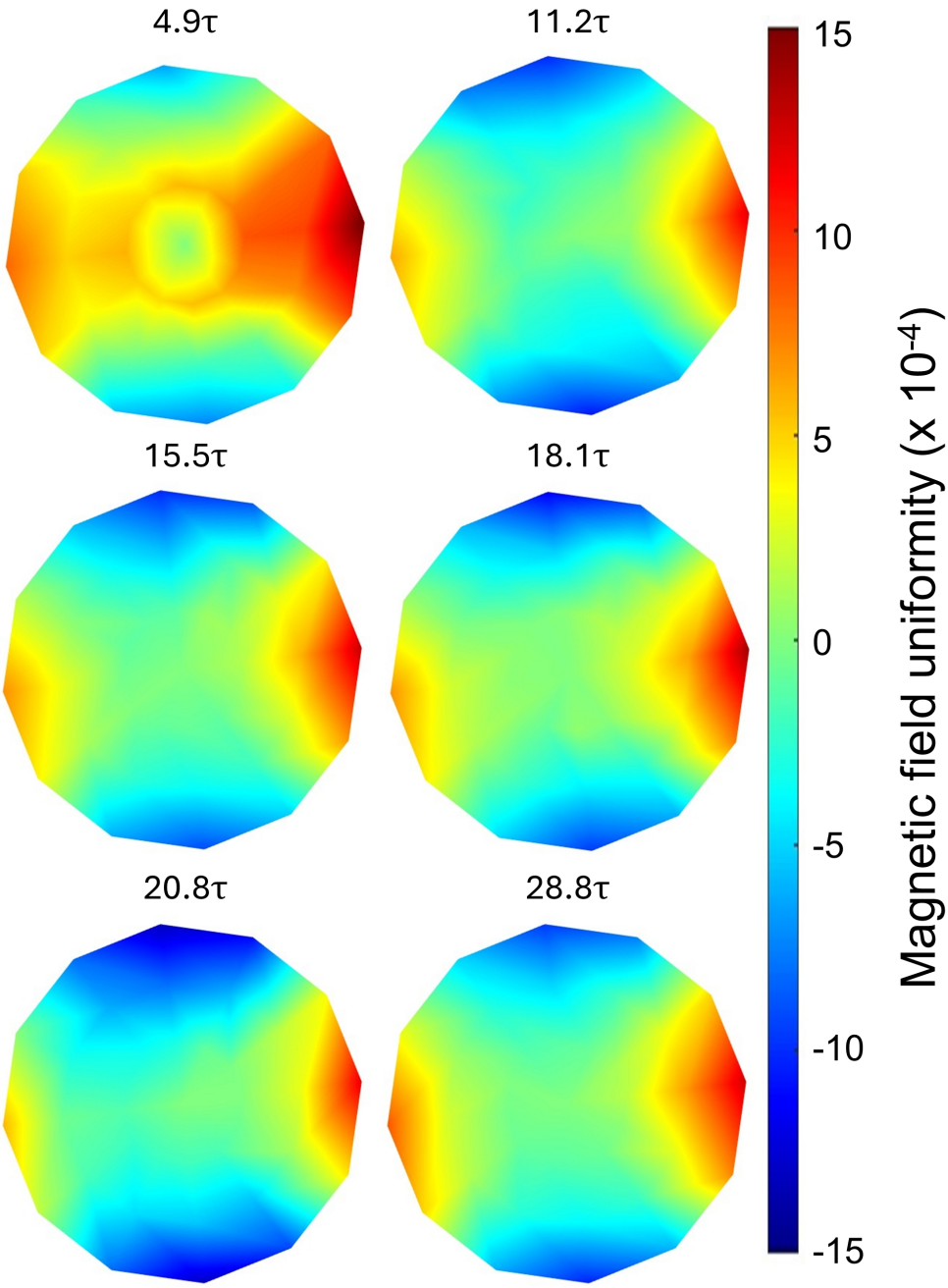

Figure 4.10: Measurement results of magnetic field uniformity over time with the application of the CSR method

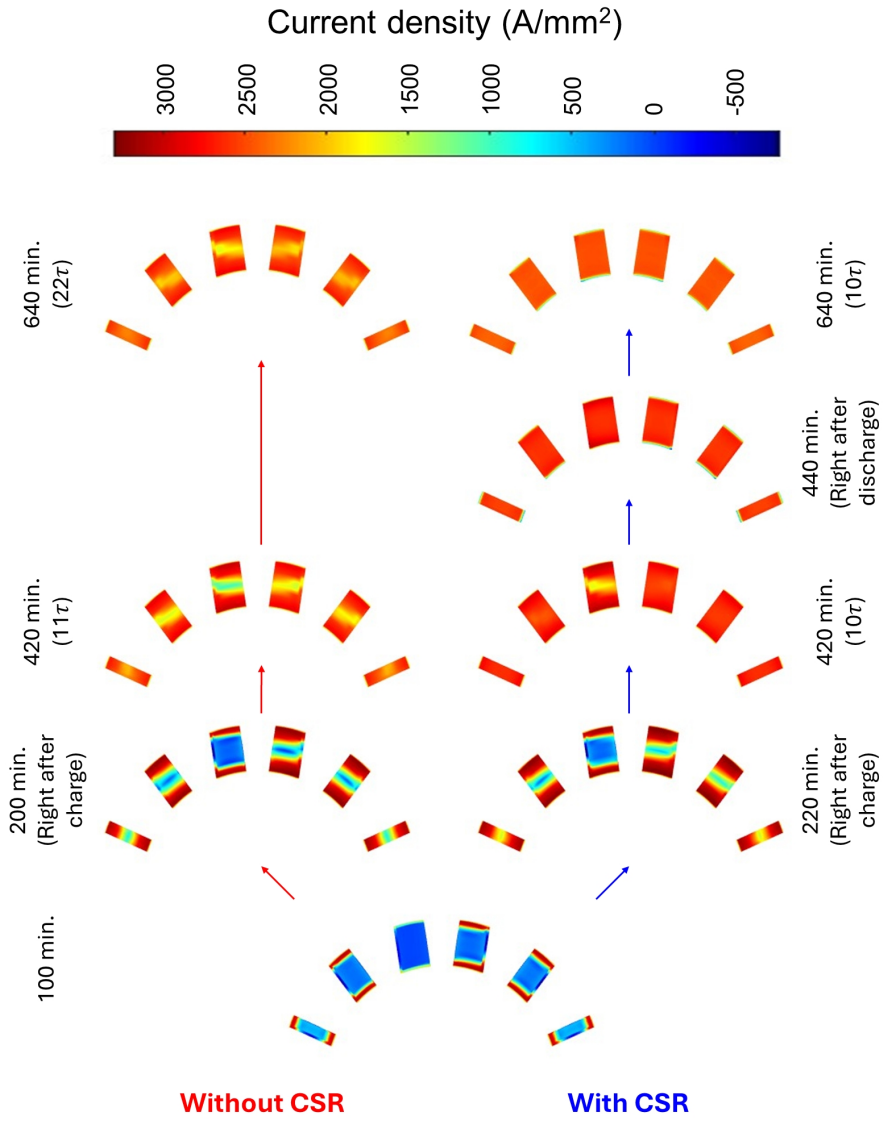

Figure 4.11: Analysis of current distribution with and without CSR operation

for each operating current and waiting for a time exceeding 10τ, field mapping was performed. The measurements revealed that changes in the magnetic field distribution due to different operating currents were minimal. This observation aligns with the previous analysis of screening currents in the context of CSR.

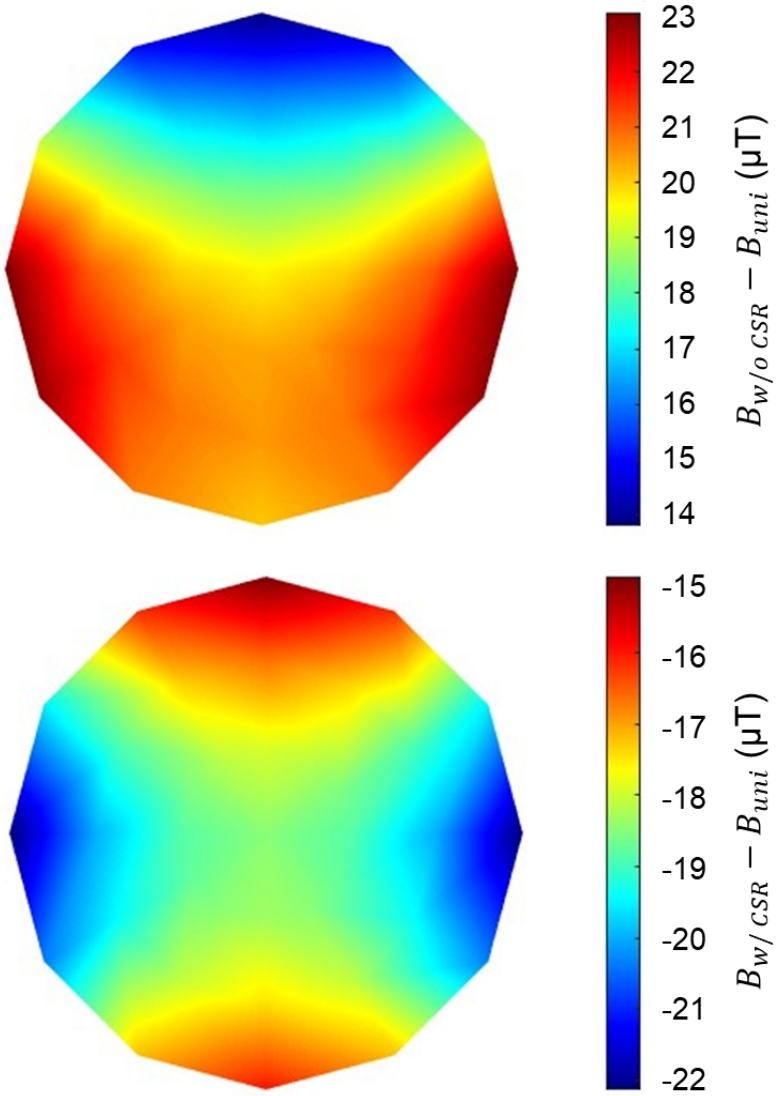

Figure 4.12: Analysis of the difference between the magnetic field considering screening currents and the magnetic field from uniform current distribution

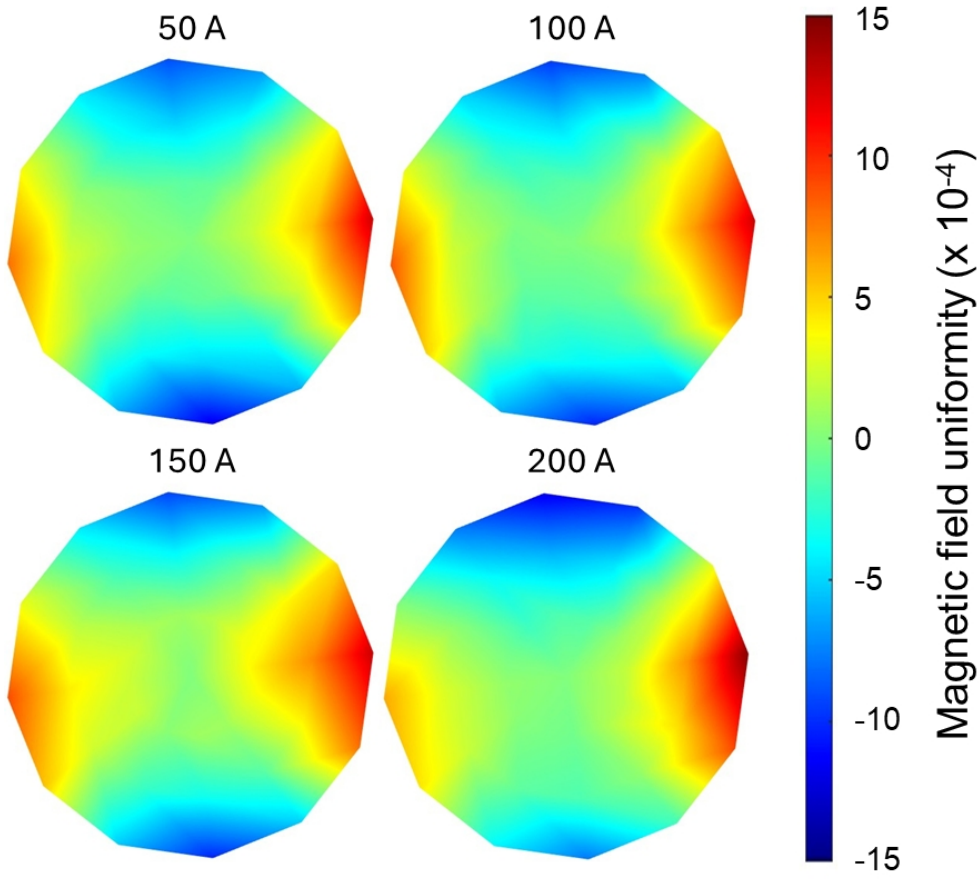

Figure 4.13: Measured results of magnetic field uniformity at different operating current levels

4.1.4 Analysis of Current and Magnetic Field Distribution Based on Ramping-rate

The ramping-rate of a dipole magnet varies depending on its application. In the case of NI magnets, achieving a very fast charging rate of around 1 T/s is challenging due to the current-bypassing characteristics. This makes them unsuitable for applications requiring such high speeds, such as in synchrotrons, where rapid speed is needed to stabilize the orbit while increasing beam energy. However, when used as DC magnets, they can operate with much slower charging rates. Even when utilized as DC magnets, NI magnets exhibit variations in the magnetic field distribution depending on the charging profile. This is due to the combined effects of shielding currents and the NI characteristics. In this study, we used a widthwise-segmented circuit model to analyze the differences in current distribution and magnetic field distribution caused by these two factors depending on the ramping rate. Although direct experiments were not conducted, the analysis allowed us to infer the performance of the magnet in scenarios where it is applied to particle accelerators.

In the previous subsection, the measurement and analysis results were based on a magnet charging rate of 1 A/min without applying CSR. In this analysis, additional simulations were conducted assuming charging rates of 10 A/min and 100 A/min. Figure 4.14 shows the current distribution analysis results for each case immediately after charging (at the point when 200 A was reached). In the case of 100 A/min, the charging rate was too fast, resulting in most of the current bypassing the intended path. On the other hand, for 10 A/min, some current was charged, but a delay in charging is observed, particularly in the upper coil1.

Figure 4.15 illustrates the magnetic field distribution analysis results for each case. Horizontally, it shows the magnetic field distribution immediately after current charging and after the magnetic field stabilizes (following a wait of 10 times the time constant). Vertically, it compares the cases for each current charging rate. In the magnetic field distribution immediately after current charging, mT-scale magnetic field

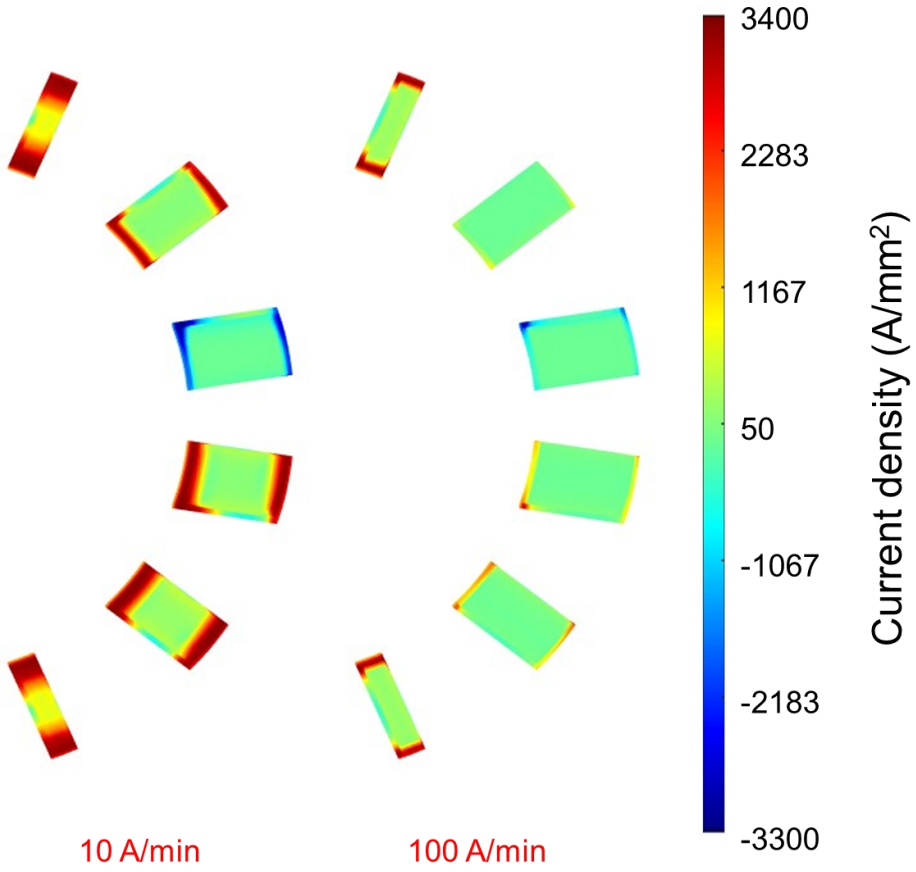

Figure 4.14: Current distribution immediately after charging for cases with faster current ramping-rates.

non-uniformity was observed. Figure 4.16 shows the magnetic field uniformity represented as a contour on a log-scale. This level of non-uniformity can induce errors on the order of 100 in terms of magnetic field uniformity, making it unsuitable for use in accelerators. However, after waiting 10 times the time constant, μT-scale magnetic field non-uniformity was observed, which can be corrected using techniques such as ferroshimming. Since differences in magnetic field distribution exist for each case, even when used as DC magnets, there is likely an optimal charging rate. This optimal point can be identified using the analysis model proposed in this study.

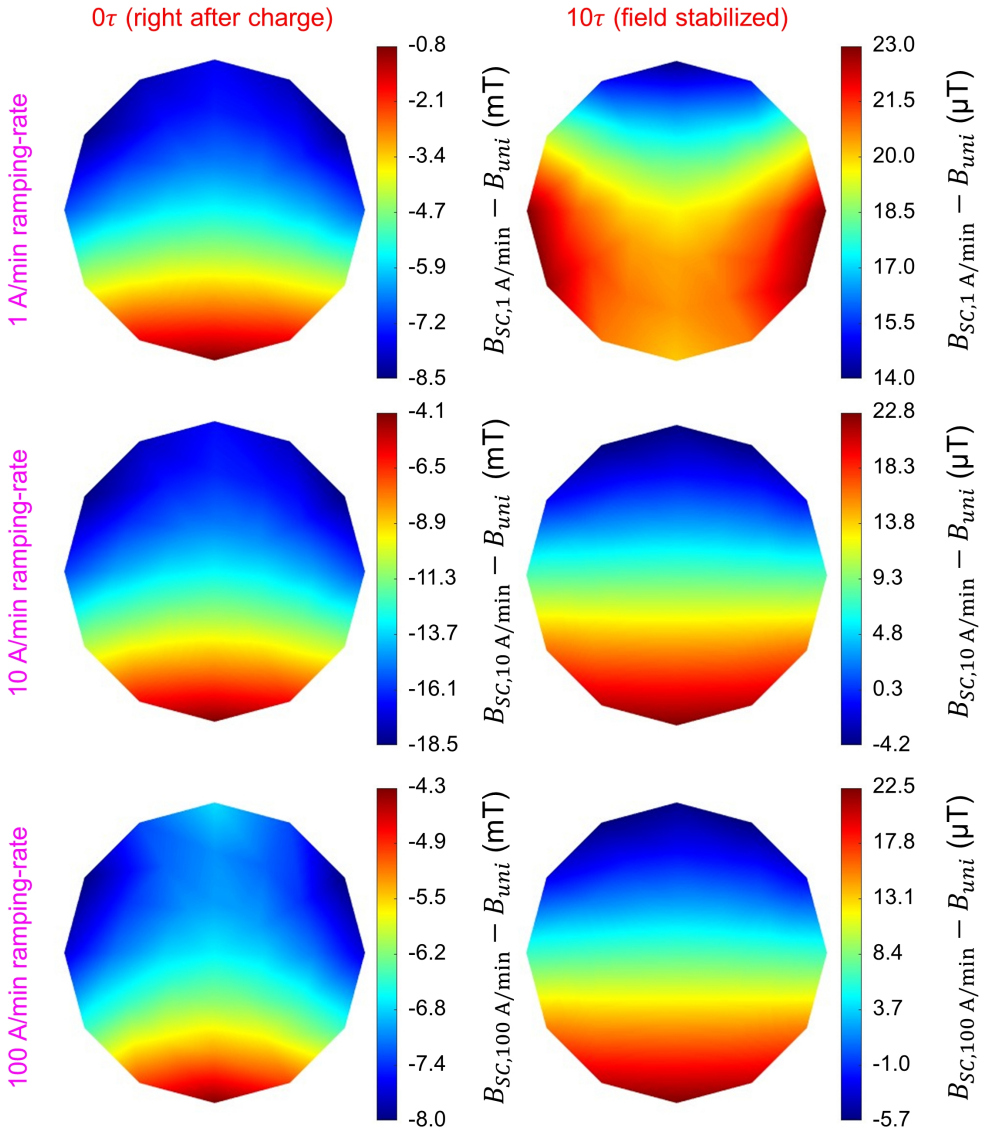

Figure 4.15: Magnetic field distribution analysis for each current ramping-rate case.

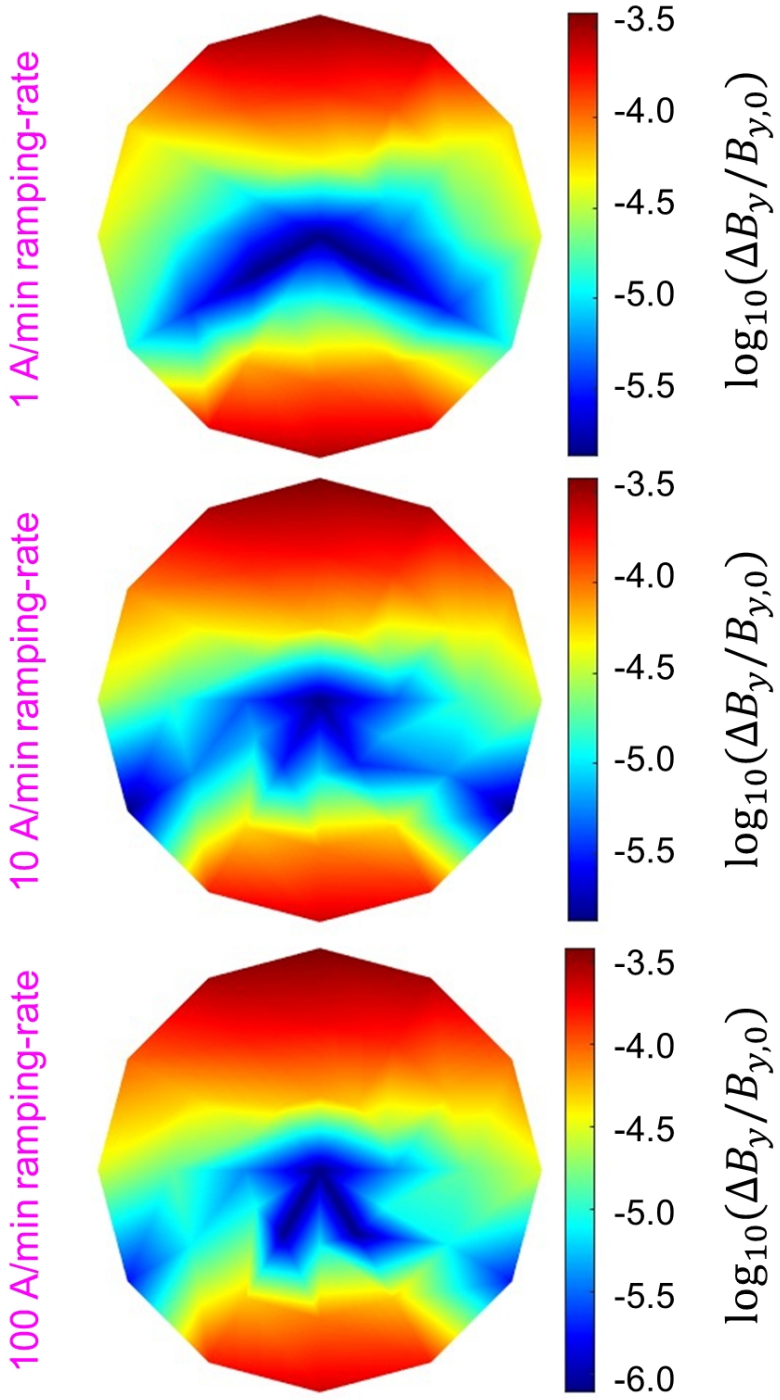

Figure 4.16: Log representation of magnetic field uniformity after 10τ has passed.

4.1.5 Quench Test and Analysis Results

As mentioned earlier, the analysis of critical current estimation matched the experimental results, confirming that the magnet experienced a quench at 331 A. Chronologically, the critical current measurement and quench experiments were conducted after all ferroshim-related experiments discussed in the following sections. This sequence was chosen because a quench could cause coil damage, leading to resistance development or excessive mechanical stress, potentially deforming the coil structure.

The magnet underwent two extreme operating conditions: a sudden discharge at 337 A and a quench at 331 A. These two cases were distinguished based on the experimental results shown in Figure 4.17. As discussed in the section on critical current estimation, the minimum critical current point occurred at the boundary between the straight and curved sections of the innermost turn of coil1. This was experimentally verified at the voltage taps installed at the wedge structure connecting coil1 and coil2 and at both terminals of coil1. In Figure 4.17, the blue graph represents the voltage across the region connecting coil1-1 and coil2-1, while the red graph shows the voltage across terminals of coil1-1. Both experiments showed similar voltage rise patterns. However, the first experiment, identified as a sudden discharge, showed the central magnetic field decaying very slowly, consistent with the characteristics of a sudden discharge in NI magnets. In contrast, the second experiment, determined to be a thermal runaway quench, showed the central magnetic field vanishing completely in less than one second.

In this experiment, no specific quench protection method was applied. This decision was made because conventional quench protection techniques, such as dump resistors, are largely ineffective for NI magnets. Additionally, experimental data was needed to understand extreme scenarios where protection circuits or heaters fail to operate. The REBCO conductor used in the experiment has a copper stabilizer thickness of approximately 15 to 20 μm, resulting in a copper matrix cross-sectional area ranging from 0.123 to 0.164 mm^2. Since the REBCO layer thickness is around 1 μm,

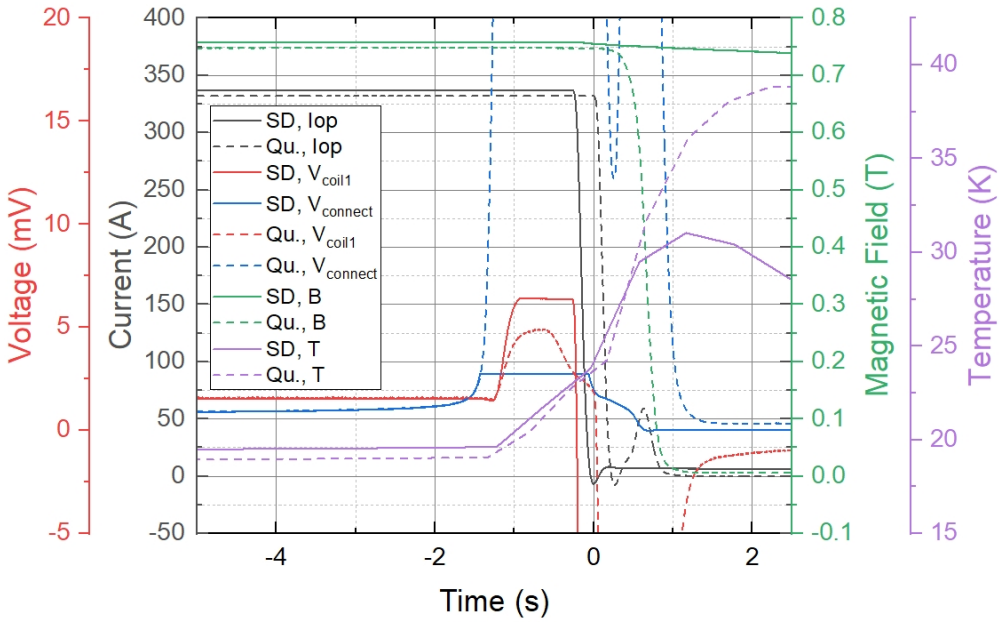

Figure 4.17: Comparison of sudden-discharge and quench experiment results

its cross-sectional area is approximately 0.004 mm^2. Furthermore, the RRR (Residual Resistivity Ratio) of the copper in the conductor was measured at about 61 in [143]. Based on this, the calculated Z-function values for the copper are as follows: $Z(150\,\mathrm{K}, 0) = 9.4 \times 10^{16}$ A^{2}s/m^4; and $Z(300\,\mathrm{K}, 0) = 13.5 \times 10^{16}$ A^{2}s/m^4. Using these values, the time required for the normal zone temperature to rise to 150 K and 300 K while the current continues to flow undetected was calculated to be 0.023 and 0.033 seconds, respectively. Considering the experimental sampling rate of 2 Hz, this rapid temperature rise is too fast to prevent coil damage.

From Figure 4.17, the degree of resistance generated during a quench event can be inferred. Unlike sudden-discharge behavior, which exhibits current bypass characteristics, the time constant during the quench decreased to 0.694 seconds. Given that the magnet's inductance is 39.1 mH, the effective resistance generated during the quench can be calculated as 56.3 mΩ. Understanding how this resistance increases over time is crucial for accurate quench analysis. However, due to the highly complex physical

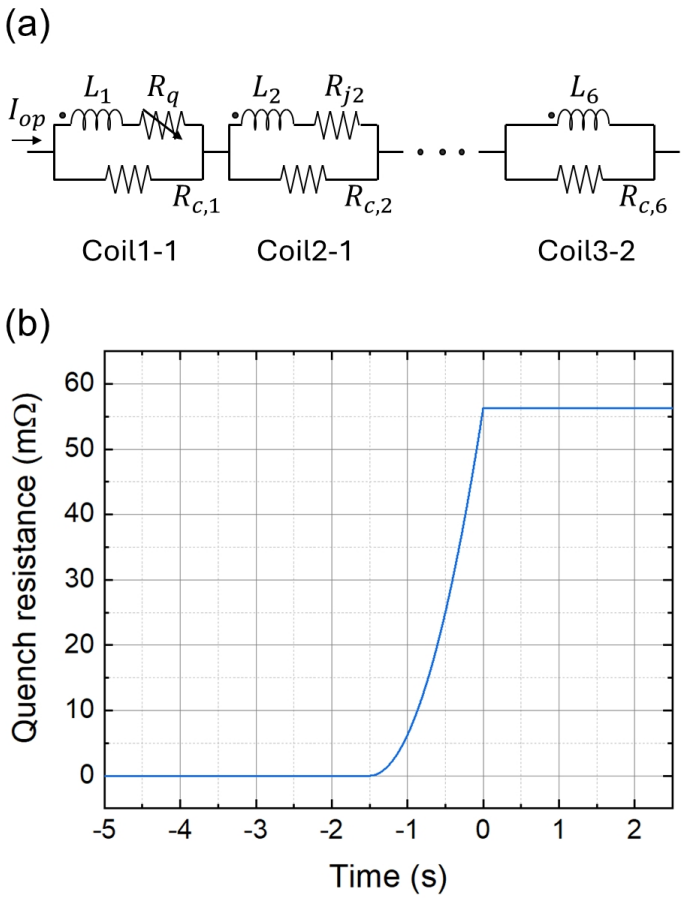

Figure 4.18: Quench analysis model and assumptions. (a) Lumped circuit model used for quench analysis, (b) Resistance evolution modeling over time during quench.

phenomena involved, finding an appropriate analytical model and predicting parameter changes remains challenging. Although this study did not establish a comprehensive model for quench behavior, the existing lumped-circuit analysis model and the previously discussed thermal circuit model were applied to compare the electromagnetic field, voltage, and temperature profiles with experimental results.

Figure 2 4.18 illustrates the lumped-circuit electromagnetic model used for quench analysis. Parameters such as inductance, characteristic resistance, and joint resistance were consistent with previously measured data, but the model simulated a scenario

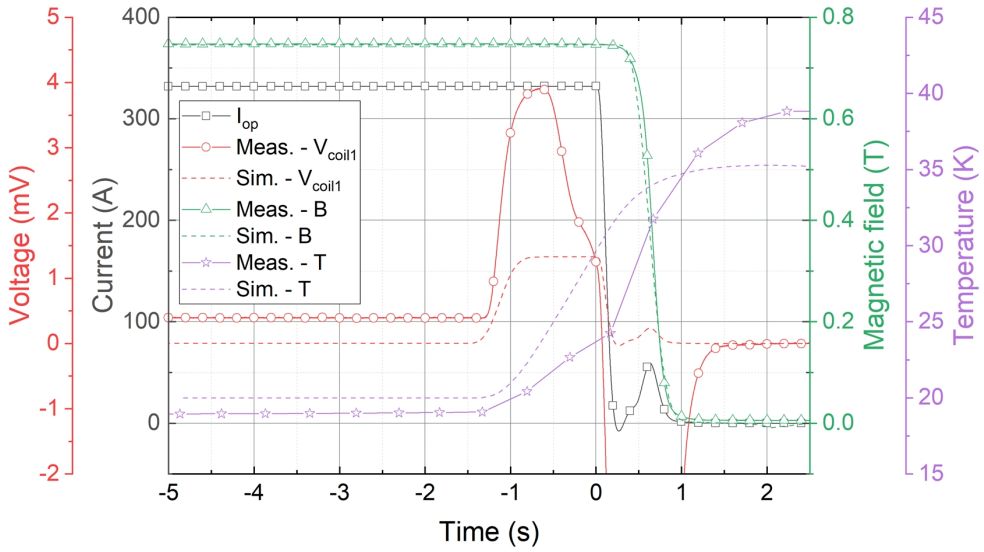

Figure 4.19: Comparison of quench measurement and simulation results

where resistance emerges in coil1-1 due to the quench. To achieve this, the resistance was modeled as forming just before the quench and reaching 56.3 mΩ immediately at the quench initiation (t = 0), as shown in Figure 4.18 (b). The resistance's gradual increase was approximated using a quadratic function. While this approximation lacks a direct physical basis, iterative simulations were conducted to identify a configuration that closely matched the experimental results.

The quench analysis results are shown in Figure 4.19. While not all results align perfectly, the rate of magnetic field decay closely matches the experimental observations with negligible error. Additionally, the temperature rise at the locations where the temperature sensors were attached exhibits a similar trend, with a difference of approximately 5 K. For voltage, achieving matching results is challenging if the local behavior of the coil is not adequately modeled. In this analysis, discrepancies in the voltage profile remain, emphasizing the need for further research to incorporate factors such as the transition of contact resistivity for more accurate voltage estimation during quench [144].

4.2 Magnetic Field Uniformity Enhancement After Assembly of Ferroshim

In the previous section, it was confirmed that the measured magnetic field uniformity was lower than the designed value. The primary causes of this discrepancy can be attributed to the effects of screening currents and shape errors. From the CSR experiment results and subsequent analysis, it was determined that the influence of screening currents is minimal. Therefore, the distortion in the magnetic field is presumed to result from shape errors, which could potentially be minimized through additional reinforcement structures and impregnation techniques. However, given the current technological limitations, it is challenging to completely eliminate shape errors arising during the manufacturing process. Thus, a method to compensate for magnetic field distortion caused by shape errors is necessary. In this study, the ferroshim technique was applied to enhance magnetic field uniformity. A design and fabrication method for ferroshim was developed, and its effectiveness was demonstrated by installing it in the warm bore of the magnet.

4.2.1 Design and Fabrication of Ferroshim

The process of improving magnetic field uniformity using coils or iron pieces is called shimming. This method is classified into active shimming and passive shimming depending on whether the control is achieved through an applied current. Active shimming involves creating coils with copper wire at room temperature or with superconducting wire in a cryogenic environment and adjusting the current applied to these coils to achieve a more uniform magnetic field. In contrast, passive shimming uses ferromagnetic iron pieces placed inside the magnet's bore, utilizing their magnetization to enhance magnetic field uniformity. For HTS magnets, such techniques have been used in NMR applications to achieve extremely high uniformity, particularly with ferroshims, reaching sub-ppm levels of magnetic field uniformity. However, there are

few examples of such methods being applied to saddle-shaped magnets. Conventional saddle-shaped dipole magnets typically use an iron core, improving magnetic field uniformity through end-part optimization of the core. Since the magnet in this study lacks an iron core, a method similar to the ferroshim technique used in NMR was applied to enhance the magnetic field uniformity.

The ferroshim was fabricated by attaching small iron pieces of a thickness designed based on magnetic field uniformity requirements onto an aluminum cylinder, following a method similar to that used in NMR magnets. The aluminum cylinder has a diameter of 50 mm and a height of 150 mm. The iron pieces were made from AISI 1008 carbon steel, with the thickness adjusted using steel plates in 1-mil (=1/1000 inch) increments. For the ferroshim to function effectively, the steel pieces must undergo sufficient magnetization. The magnetization of the AISI 1008 carbon steel pieces used in this experiment follows the B-H curve shown in Figure 4.20. When the magnetic field strength exceeds approximately 2×10^4 A/m, the steel converges to a magnetic dipole generating around 2.1 T of magnetic field. In the case of applying ferroshim to this magnet, the magnetic flux density is 0.5 T, corresponding to a magnetic field strength of about 4×10^5 A/m, which is expected to sufficiently magnetize the steel pieces. The design was conducted based on this prediction. However, subsequent results revealed that some areas did not undergo adequate magnetization, and quantitative analyses were performed to address this issue.

While increasing the number of iron pieces attached to the aluminum cylinder allows for more optimization variables and finer design, excessively small iron pieces reduce manufacturability. Therefore, the dimensions of each iron piece were fixed at 6 mm$\times$10 mm. The cylinder surface was divided into 26 segments circumferentially and 15 segments along its height, forming the basis for the design.

The design was optimized using (2.39) as follows:

$$\text{Min.} \quad f(x_1, x_2, \cdots, x_{390}) = \max\left(\left|\frac{(B_{y,R_{ref}}+B^f_{y,R_{ref}})-(B_{y,0}+B^f_{y,0})}{B_{y,0}+B^f_{y,0}}\right|\right), \quad (4.2)$$

$$\text{subject to} \quad 0 \le x_i \le 1 \text{ mm } (i = 1, 2, \cdots, 390), \quad (4.3)$$

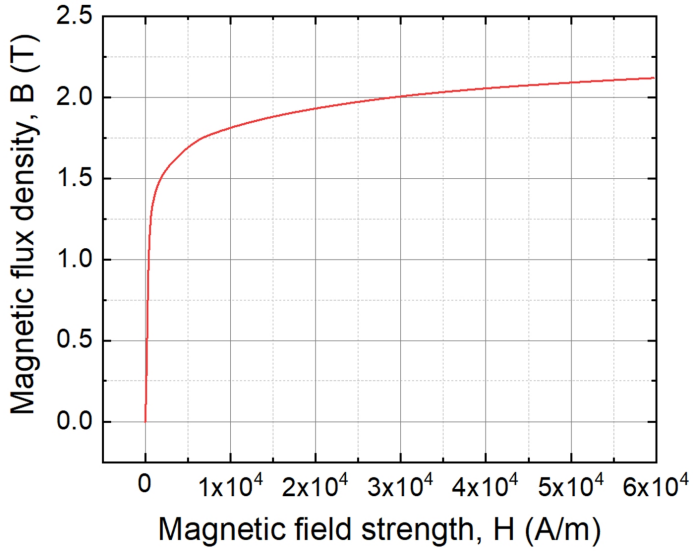

Figure 4.20: B-H curve of AISI 1008 carbon steel.

where x_i, $B^f_{y,0}$, and $B^f_{y,R_{ref}}$ represent thickness of i^{th} piece of iron shim, magnetic field at the center generated by ferroshim, and magnetic field along the reference radius generated by ferroshim, respectively. The thickness was limited to 1 mm because setting the ferroshim thickness to 40 mils or more makes the iron pieces difficult to bend, complicating fabrication. Additionally, a larger difference between the inner and outer radii of the iron piece could result in excessive design errors.

The ferroshim design, developed through the optimization process, is shown in Figure 4.21. The numbers in the table represent the thickness of the iron pieces in mils, and the color intensity in each cell is proportional to the thickness for easier comparison. Connecting the left and right edges of the table forms a cylindrical shape, representing the actual ferroshim configuration. The optimization results indicated that the magnetic field uniformity improved by over 54%, decreasing from 14.0×10^{-4} to 6.4×10^{-4}.

The iron sheets used for ferroshim fabrication had unit thicknesses of 1, 2, 3, 4, and 5 mils. For example, to achieve a thickness of 18 mils, three 5-mil sheets and one

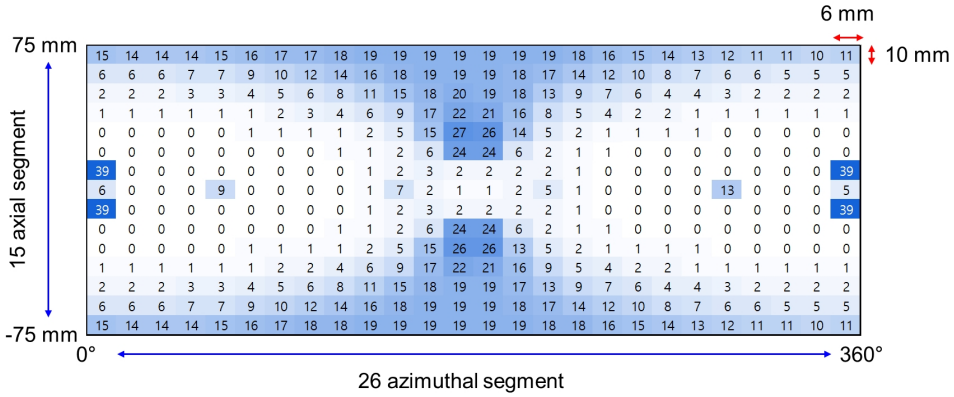

Figure 4.21: Thickness design results for the ferroshim positioned on the side surface of the cylinder.

3-mil sheet were combined. The unit thickness was limited to a maximum of 5 mils to prevent difficulty in bending the sheets and to minimize shape errors. Additionally, when neighboring iron pieces in the azimuthal direction had thicknesses differing by 5 mils (e.g., 10 mils and 11 mils), a single 12 mm-wide piece was cut instead of cutting two 6 mm-wide pieces. This approach improved manufacturing efficiency. The iron pieces were attached to the surface of the aluminum cylinder using commercial Kapton tape. The fabricated ferroshim is shown in Figure 4.22 (a), while (b) illustrates the installed ferroshim aligned within the warm bore of the magnet.

4.2.2 Validation of Spatial Magnetic Field Uniformity Enhancement

After installing the ferroshim, the magnetic field distribution was measured in the same manner as before. This time, no CSR operation was applied, and the results were compared to the reference. The measurements showed that the magnetic field uniformity, which was predicted to improve from 14.0×10^{-4} to 6.4×10^{-4}, only improved to a level of 9.5×10^{-4}. The measured magnetic field distribution is shown in Figure 4.23. While the distribution pattern appears similar to the reference, the uniformity improved to 72% (39%p increase) of the target level. It was also observed that the magnetic field

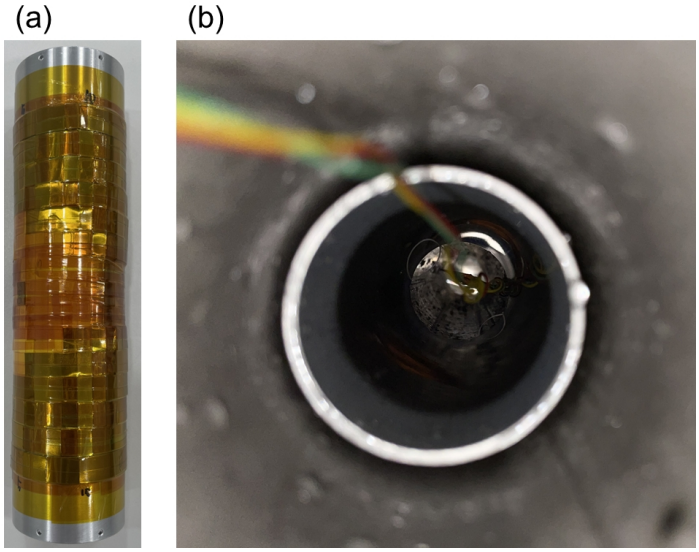

Figure 4.22: Ferroshim fabrication and installation results. (a) Photograph of the fabricated ferroshim, (b) Photograph of the ferroshim installed in the warm bore of the magnet.

distribution remained unstable before 10 times the time constant, as previously noted.

Figure 4.24 illustrates the difference in the magnetic field with and without the ferroshim. Overall, the magnetic field was higher when the ferroshim was applied. For high-field magnets exceeding 3 T, ferroshim typically reduces the central magnetic field due to the magnetization of the iron pieces around 2.1 T. However, in this case, when the magnetic field uniformity was measured at approximately 200 A, the central magnetic field was around 0.5 T, and the magnetized iron pieces increased the central magnetic field instead. The increase in the central magnetic field ranged from a maximum of 1.01 mT to a minimum of 0.64 mT.

The reason why the magnetic field uniformity did not improve as much as designed is attributed to insufficient magnetization of the iron pieces. This conclusion is supported by two analyses. The first analysis focuses on the increase in the central magnetic field due to the magnetization of the iron pieces. Before the ferroshim in-

stallation, the measured central magnetic field was 0.4992 T, while the designed value after installation was 0.5024 T. However, the measured value after the ferroshim installation was 0.5001 T, showing an increase of only 27% of the designed value. This result is illustrated in Figure 4.25, suggesting that the magnetization of the iron pieces likely reached only 27% of the intended 2.1 T.

The second analysis involves repeated simulations of the magnetic field distribution to estimate the level of magnetization in the iron pieces. The top-left of Figure 4.26 shows the magnetic field distribution when the iron pieces are fully magnetized to 2.1 T, while the top-right shows the distribution without the ferroshim. The bottom-left represents the actual measurement results, which fall between the two extremes. By varying the degree of magnetization and comparing the resulting distributions, it was found that a magnetization level of approximately 36% most closely matches the measured distribution, as shown in the bottom-right. In this case, the magnetic field uniformity remains at 9.5×10^{-4}. These two analyses suggest that the iron pieces were magnetized to a level between 27% and 36%, and their magnetization did not reach the intended 2.1 T. Consequently, the magnetic field uniformity could not improve to the designed level. To further improve magnetic field uniformity, a more detailed analysis of the material properties is required, and it will also be necessary to explore ferroshim using alternative materials.

The spatial magnetic field uniformity measurement results indicate that this magnet is not yet suitable for direct application in practical devices. In comparison, conventional LTS saddle dipole magnets exhibit magnetic field uniformity of less than 1×10^{-4}, which is approximately 10 times better than this magnet. The insufficient magnetic field uniformity of this magnet is due to areas that remain under-magnetized because of the low central magnetic field. Additionally, the ferroshim was constructed with only a single layer, necessitating further improvements. With such enhancements, this magnet could leverage its advantages of being more compact and not requiring cryogenic coolants, making it viable for practical applications.

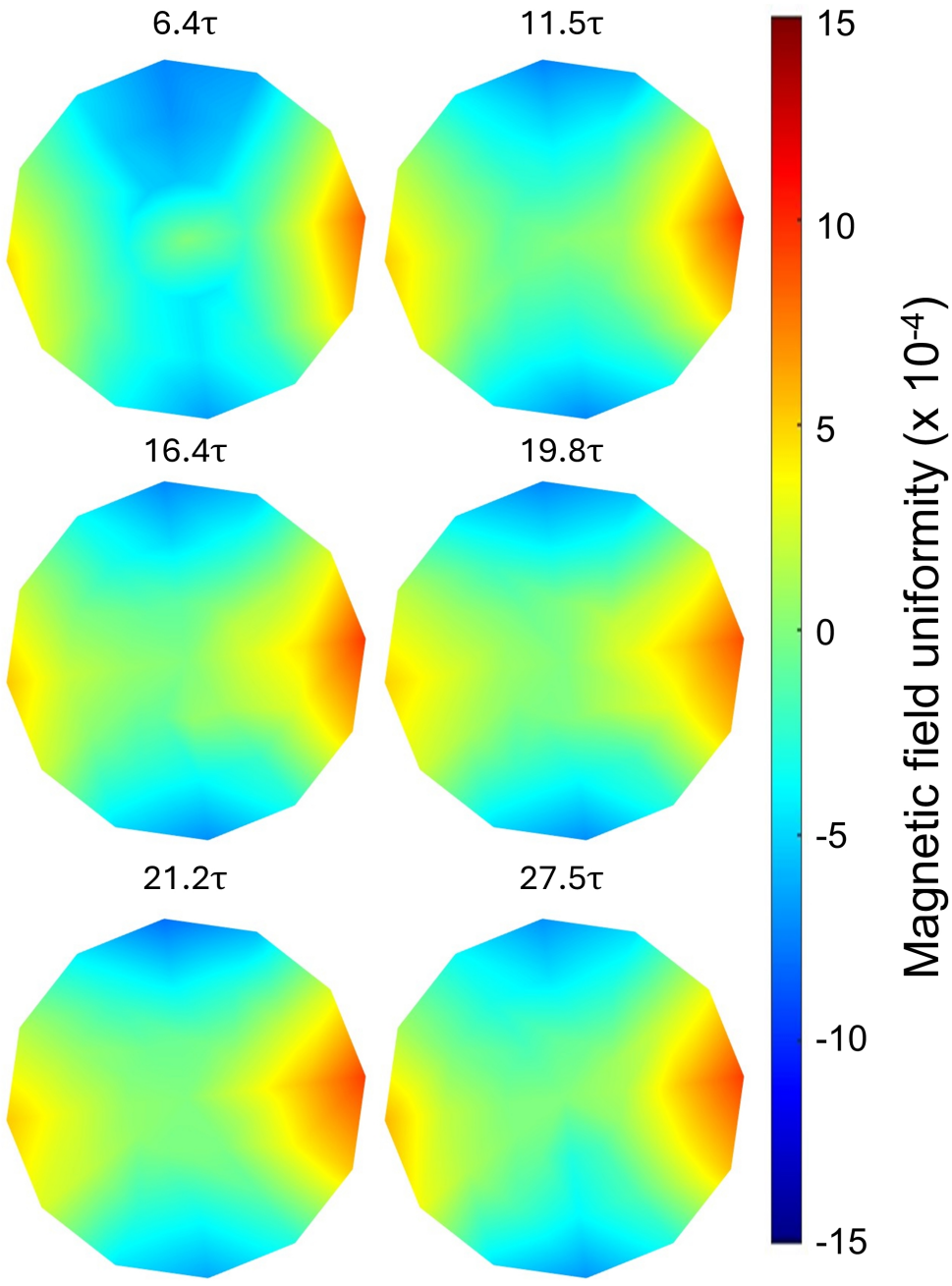

Figure 4.23: Measurement results of magnetic field uniformity over time after ferroshim installation

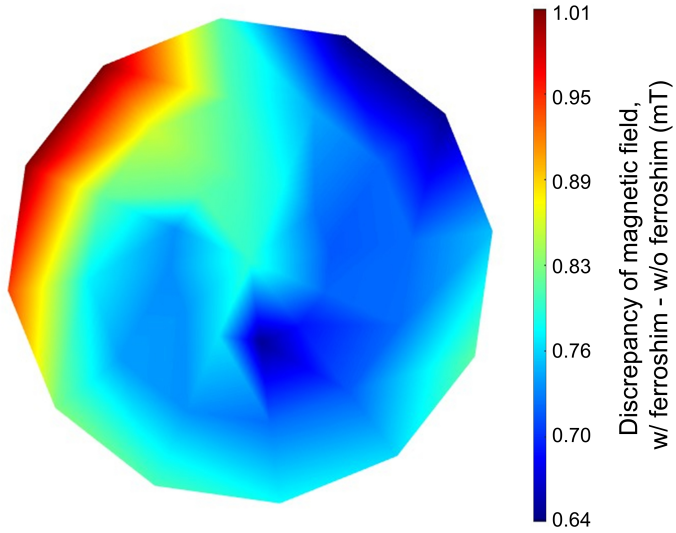

Figure 4.24: Discrepancy in magnetic field distribution between two cases: 1) with ferroshim; and 2) without ferroshim

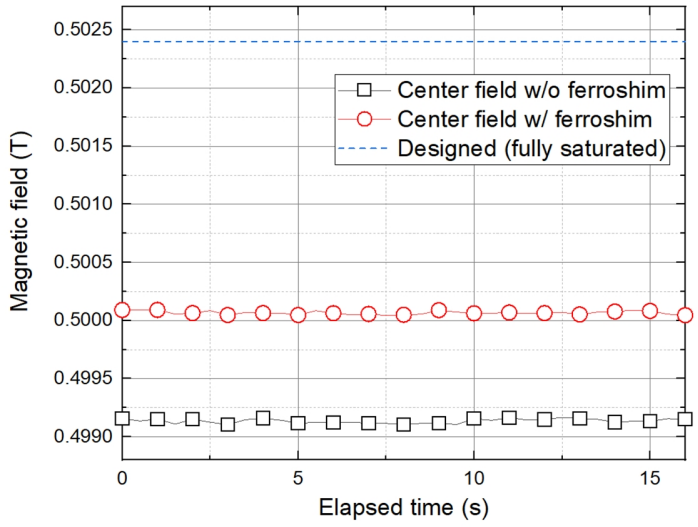

Figure 4.25: Comparison between the measured increase in the central magnetic field after ferroshim installation and the corresponding analytical results

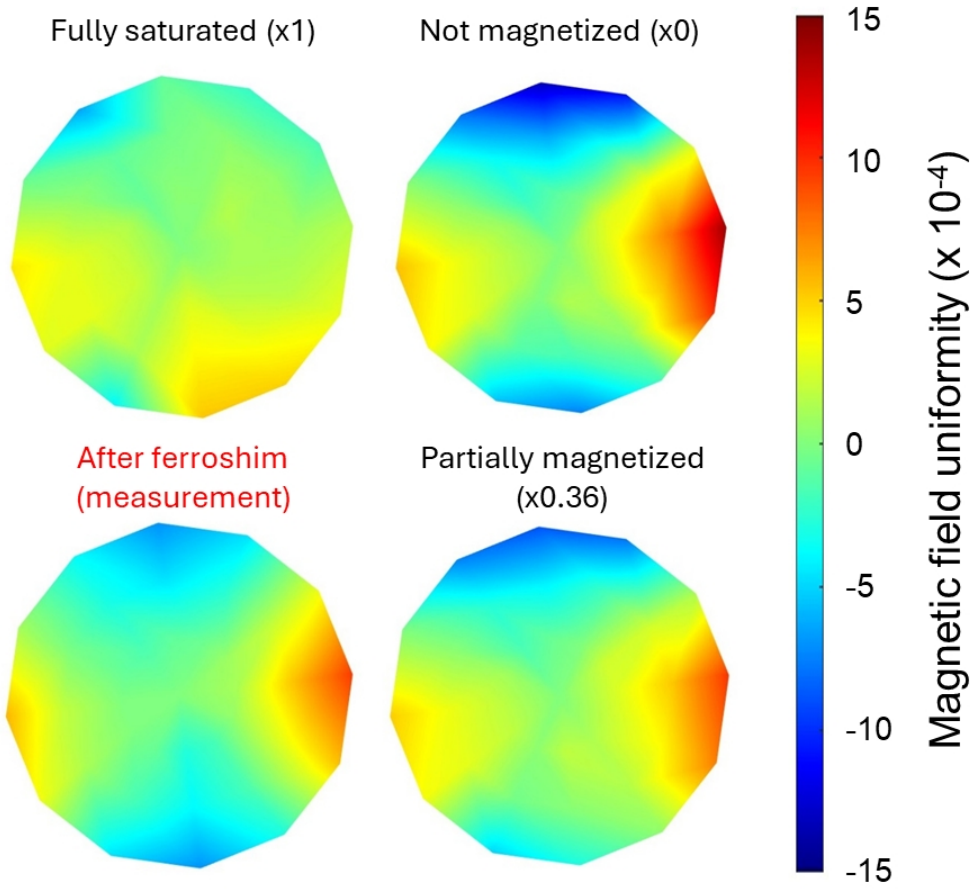

Figure 4.26: Comparison of the analytical results for the magnetic field distribution based on different levels of ferroshim magnetization

4.2.3 Harmonic Analysis and Temporal Magnetic Field Stability

Harmonic analysis was performed on the previously presented magnetic field distribution using (2.29). Repeated measurements of magnetic field uniformity revealed continuous variations, which were analyzed from the perspective of temporal stability. The temporal changes in magnetic field uniformity are shown in Figure 4.27. Compared to the reference measurement results without CSR or ferroshim applied, CSR showed an improvement in magnetic field uniformity that was negligible. However, with ferroshim applied, significant improvements were observed at 10 mm and 15 mm reference radii, while changes at the 5 mm radius were minimal. This is likely because the actual magnetic field values within smaller measurement radii exhibited less noticeable differences, making them harder to observe.

Additionally, the temporal variations of each harmonic component are shown in Figure 4.28. Panels (a), (b), and (c) represent the quadrupole, sextupole, and octupole components, respectively, while panels (d), (e), and (f) show the skew quadrupole, skew sextupole, and skew octupole components. To enable an absolute size comparison, the y-axis range was standardized with a minimum-to-maximum interval of 6. Theoretically, in a perfectly symmetric magnet, only odd-order normal components, such as the dipole and sextupole, should remain, with no skew components present. The measurement results indicated that, aside from the dipole component, the sextupole component was the most prominent, which aligns reasonably well with theoretical expectations. However, small contributions from other components were also observed. These minor deviations are likely attributed to geometric imperfections during the fabrication and operational processes.

The above results can be compared with those of the existing LTS dipole magnets. The prototype dipole magnet manufacturing results for CERN's LHC can be found in [50], where the quadrupole component (b2) was around 1.0, the sextupole component (b3) was around -8.9, and the octupole component (b4) was nearly nonexistent. The skew quadrupole (a2), skew sextupole (a3), and skew octupole (a4) components

Table 4.2: Comparison of harmonic components with LTS dipole magnet

Harmonic components	LTS magnet [50]	NI HTS magnet with ferroshim
Quadrupole (b2)	1.0	0.4
Sextupole (b3)	-8.9	-3.6
Octupole (b4)	0.0	-0.4
Skew quadrupole (a2)	0.2	-0.6
Skew sextupole (a3)	0.8	-0.4
Skew octupole (a4)	0.0	0.4

were approximately 0.2, 0.8, and 0.0, respectively. These comparison results are summarized in Table 4.2. Due to the smaller reference radius compared to the reference, a direct comparison of harmonic components is challenging, but it was still possible to achieve sufficiently high uniformity levels in similar-sized regions. However, the LTS magnets, which were used alongside other magnet systems, incorporated technologies to correct the magnetic field. Therefore, for this magnet to be applicable in practical applications, further improvements in magnetic field uniformity are necessary. In addition, higher-order harmonic components were observed to be larger compared to LTS magnets, likely due to design constraints caused by the shape of the REBCO conductors. Future studies will need to focus on optimizing the number and arrangement of coils to reduce these higher-order components.

The maximum variation in magnetic field uniformity over time was 0.38×10^{-4}/hour, observed during the CSR measurement. The temporal stability of each harmonic component was analyzed to remain below the identified maximum threshold. However, in particle accelerator systems, separate magnets are installed and operated to adjust these harmonic components. Magnets such as quadrupoles, sextupoles, and octupoles are utilized to minimize the impact of higher-order harmonic components of the magnetic field on beam operation. Therefore, achieving stable control over the temporal stability of each harmonic component is essential for the efficient operation of the

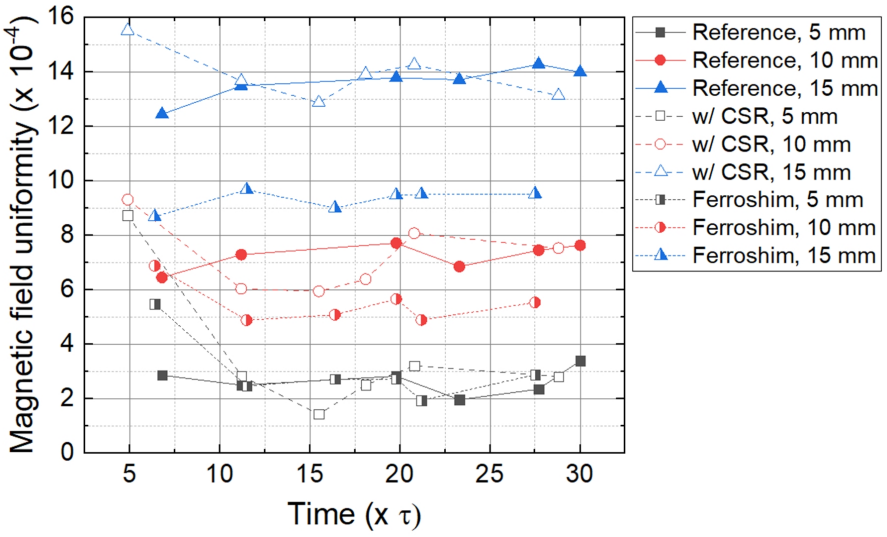

Figure 4.27: Temporal stability measurement results of magnetic field uniformity

system. By adopting technologies such as NI applied to this magnet, it is possible to achieve potentially high magnetic fields even in a compact size while ensuring spatial magnetic field uniformity and temporal stability. These technologies can be applied to medical particle accelerators, providing a level of magnetic field uniformity that ensures precise and consistent particle beam paths.

Additionally, they enable efficient use of space and eliminate the need for cryogenics, thereby reducing long-term operational costs. Still, to utilize saddle-shaped magnets in practical applications, further improvement in temporal stability will be necessary. Factors contributing to measurement errors in stability include position control errors of the field mapper and control errors of the power supply. For evaluating magnetic field distributions in actual applications, the wire method [145, 146] has been proposed and is currently in use, offering the potential for more accurate measurements if implemented. Additionally, high-precision power supplies used for operating high-uniformity magnets like NMR systems are expected to enhance the uniformity of saddle-shaped dipole magnets if adopted.

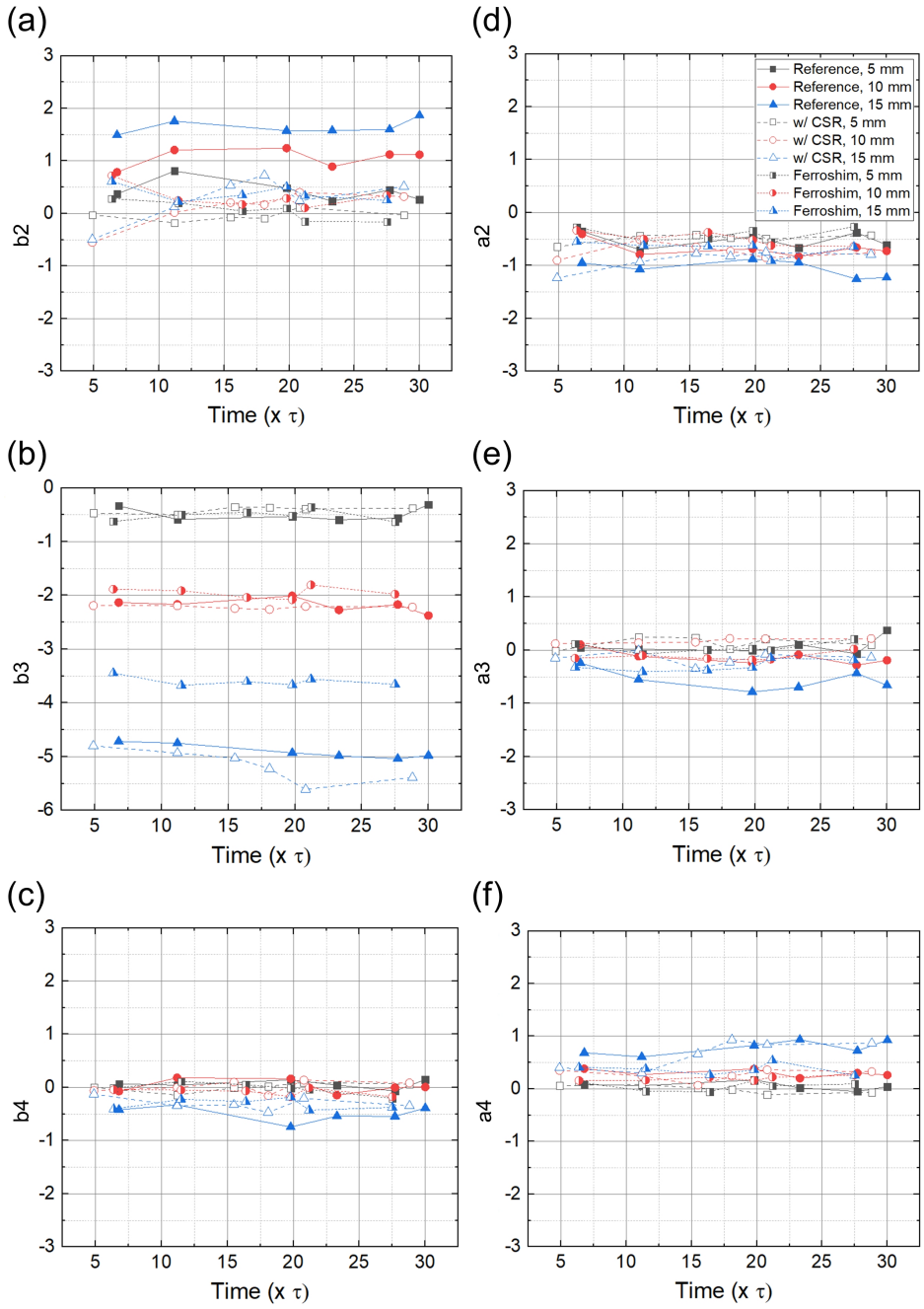

Figure 4.28: Temporal stability measurement results for each harmonic component of the magnetic field

4.3 Test Results and Analysis of Demo Magnet

The demo magnet was tested earlier, before the magnet fabrication and operation processes were well established, which led to the identification of several issues. This section analyzes the experimental results of the demo magnet and examines the causes of the problems encountered. These issues were resolved in the subsequent 0.7 T magnet. The demo magnet was tested twice: first as an NI magnet and second as a 2-ply winding magnet for fast-ramping experiments. In the NI magnet test, the magnetic field distribution was measured, and the effects of shape deviation and screening current on the field distribution were analyzed. In the 2-ply magnet test, fast-ramping operation in a liquid nitrogen environment was tested, and the results were interpreted using a distributed circuit model.

4.3.1 Screening Current and Shape Deformation Affecting Magnetic Field Distribution

The NI demo magnet [108] achieved a central magnetic field of 0.11 T, with current bypass characteristics clearly observed. The measured parameters are shown in Table 4.3. Figure 4.29 shows the measured voltage, current, and magnetic field data, along with the results interpreted using the lumped circuit model. The coil parameters were also determined using the lumped circuit model. Figures 4.29 (a), (b), (c), and (d) show the data when the magnet was charged and discharged at a rate of 0.5 A/s, while (e), (f), (g), and (h) show the results of the sudden-discharge experiment. Through these two experiments, the magnet parameters with the smallest deviation from the measured values were identified.

While typical NI coils have a contact resistivity of around 10 $\mu\Omega cm^2$, this magnet experiment recorded contact resistivity values ranging from 71 $\mu\Omega cm^2$ to as high as 231 $\mu\Omega cm^2$. Considering that contact resistivity is influenced by the pressure applied to the conductor, these high values indicate that the pressure between conductors was

Table 4.3: Measurement results of coil parameters for the demo magnet

Magnet parameter	**Unit**	**Coil 1-1**	**Coil 1-2**	**Coil 2-1**	**Coil 2-2**
Total inductance	[mH]		3.83		
Characteristic resistance	[μΩ]	470.4	245.4	141.5	123.8
Contact resistivity	[μΩcm^2]	231	118	79	71
Joint parameter	**Unit**				
Resistance of lap joint	[nΩ]		216		
Total inductance of lap joint	[nH]		340		

very low. The straight section reinforcement structure not only prevents mechanical damage to the magnet but can also help make the contact resistance lower and more uniform.

The shape deformation in the straight sections was visibly noticeable. As shown in Figure 4.30, observing the straight sections immediately after removing the magnet from liquid nitrogen revealed severe deformation due to thermal contraction. This deformation can significantly impact the magnetic field distribution. To assess the extent of this influence, the shape deformation in each coil's straight section was modeled as a rotation of the conductor, as illustrated in Figure 4.30. This assumption was chosen for its simplicity and because it closely resembles the observed deformation. In this model, coil2, which had relatively fewer turns and a smaller winding radius (resulting in less deformation in the straight section), was assumed to have no deformation, with an angle of rotation Δ set only for coil1s. Additionally, since observed deformations in the straight sections were asymmetrical, the rotation angles for each straight section were set differently in this model.

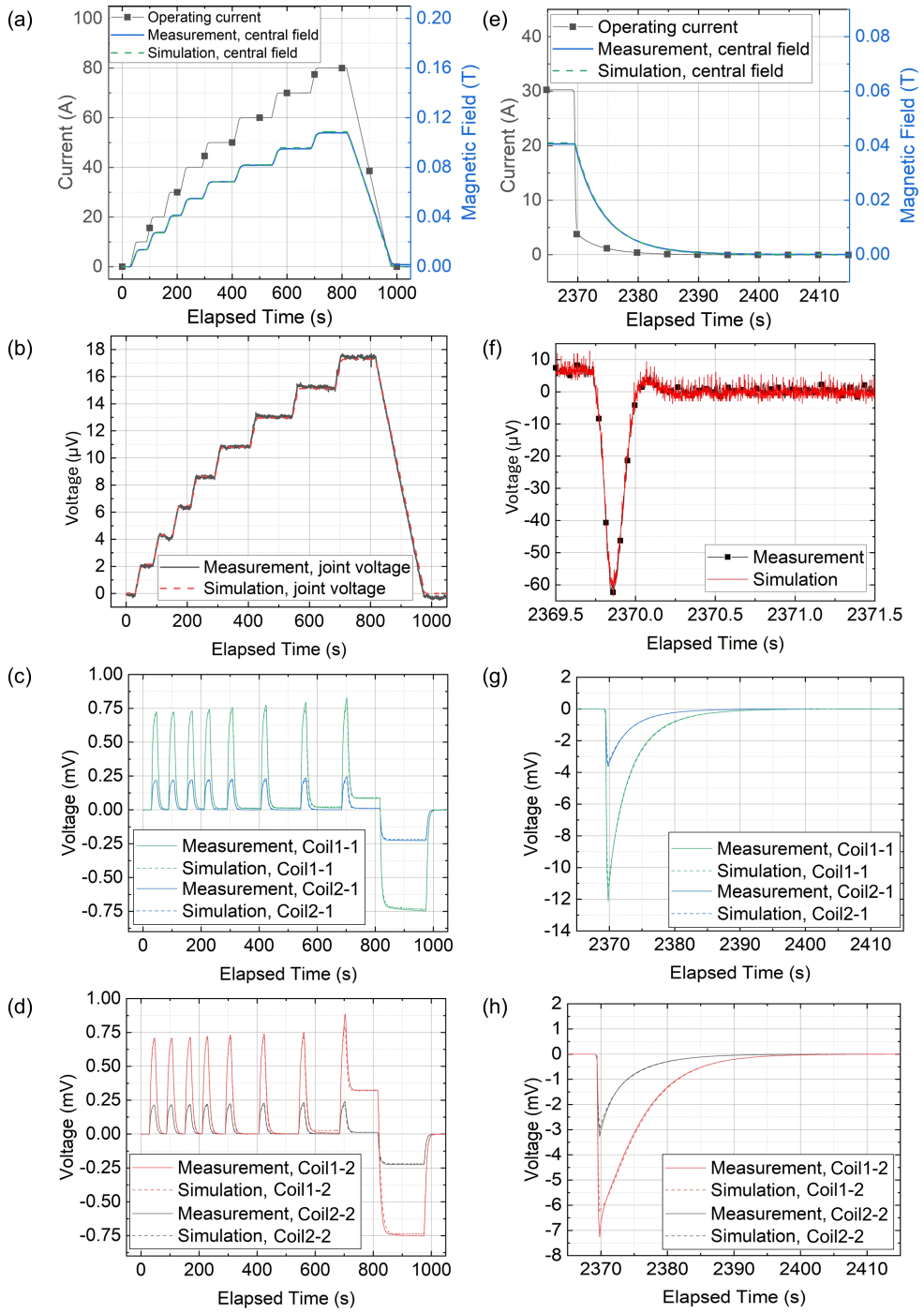

Figure 4.29: Measurement results of charging and sudden-discharge experiments for the demo magnet

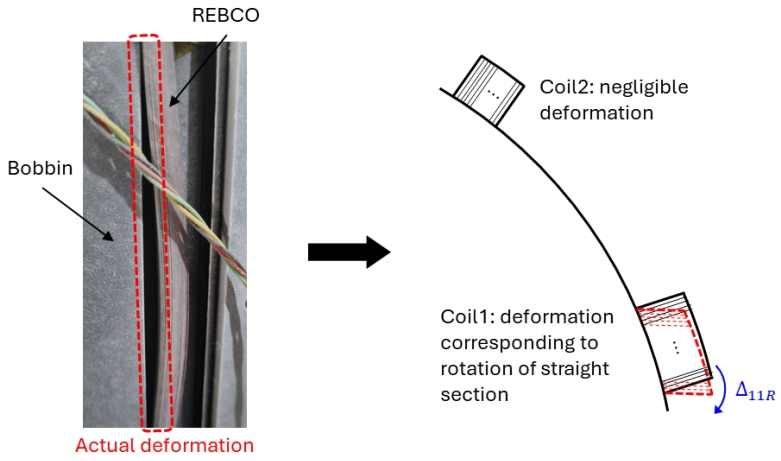

Figure 4.30: Photographs of the coil's straight section deformation and a schematic diagram of the modeling approach

The magnetic field distribution at the magnet's center was measured using the same field mapper. However, in the case of the demo magnet, the central bore was designed as a rectangular shape rather than circular, making it challenging to measure the magnetic field distribution along the circumference. Therefore, the magnetic field distribution was measured in a rectangular area 20 mm wide and 10 mm high, with measurements taken every 5 mm horizontally and vertically. The magnetic field uniformity within this area, relative to the central magnetic field, was 37×10^{-4}, which was significantly higher than the designed value. This discrepancy was suspected to result from the previously mentioned shape deformation. For quantitative analysis, the FEM-circuit sequential model was used. The deformation angles in coil1's straight sections were divided into right and left segments, labeled as Δ_{11R}, Δ_{11L}, Δ_{12R}, and Δ_{12L}. These angles were varied and repeatedly calculated to find the combination that minimized the deviation from the measured magnetic field distribution. The resulting angles were 20, 33, 37, and 27 degrees, respectively.

The magnetic field distribution within the measurement range is shown in Figure 4.31, with the mapping points and order indicated by arrows in the upper-right corner.

The results were analyzed and compared under four combinations based on the consideration of screening currents and shape deformation. The analysis showed that shape deformation had a greater effect on the magnetic field distribution than screening currents. To quantify this, the average error across 15 measurement points was calculated and represented. The errors between the measurements and analysis for the four cases were 0.21%, 0.20%, 0.09%, and 0.07%, respectively. This indicated that shape deformation contributed approximately 0.13%p error, while screening currents contributed about 0.02%p error. Notably, the analysis that accounted for both screening currents and shape deformation showed only a 0.07% error compared to the measurements, confirming the usefulness of the assumed rotation angles for shape deformation and the analysis model.

Additionally, the magnetic field distribution along the axial direction of the magnet was measured using the field mapper, and the error compared to the analysis results was evaluated. The experimental and analytical results are shown in Figure 4.32 (a). Here as well, the smallest error between analysis and measurement occurred when both screening currents and shape deformation were considered. Figure 4.32 (b) shows the analysis results for the current distribution. This result represents the current distribution calculated by the FEM-circuit sequential model, normalized with respect to the critical current. This quantitative analysis improved the accuracy of the analytical model and enhanced the completeness of the fabrication process, including structures like the straight section reinforcement.

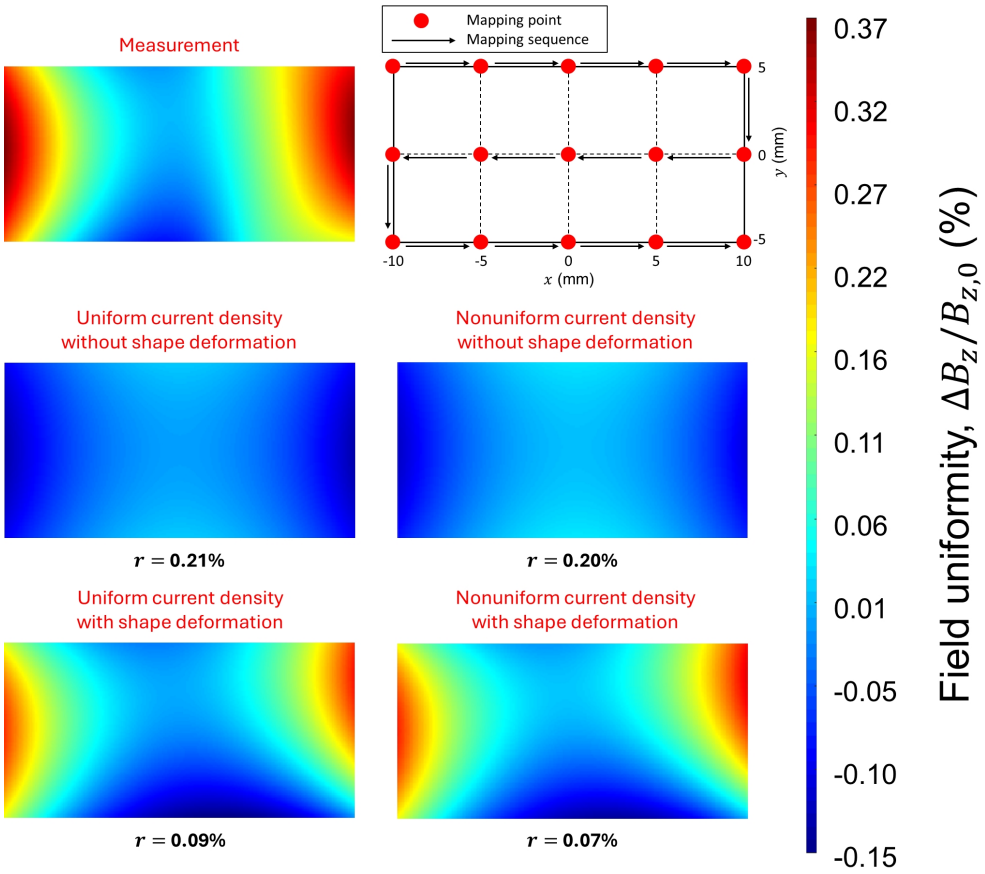

Figure 4.31: Measurements and calculation results for the transverse magnetic field distribution. The location of the mapped points and the sequence are presented.

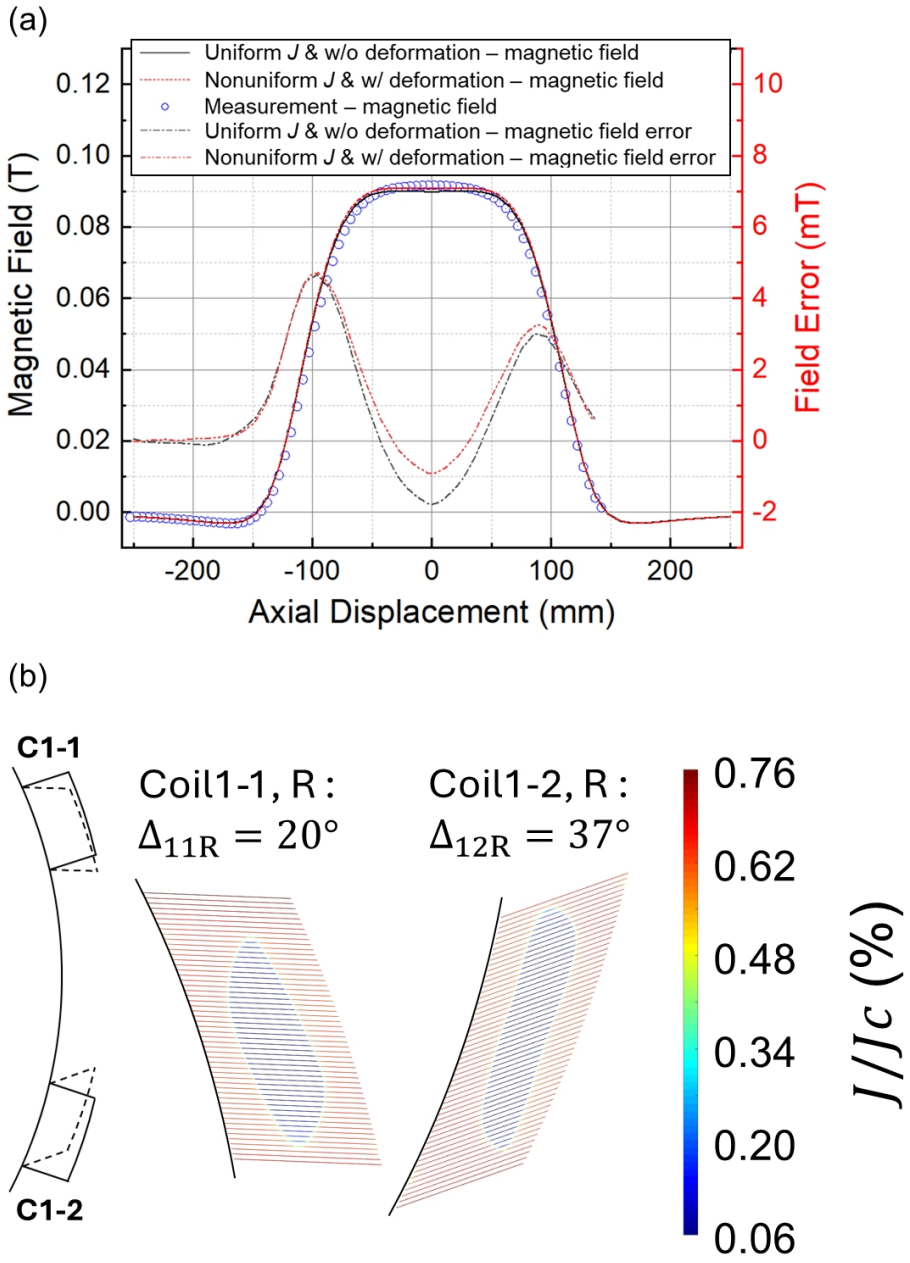

Figure 4.32: Analysis results of NI Demo magnet. (a) Measurement and calculation results for the axial magnetic field distribution, (b) FEM-circuit sequential model results for the demo magnet.

4.3.2 Fast-ramping Results and Analysis with Distributed Circuit Method

The demo magnet fabricated with 2-ply winding was designed to enable fast-ramping, unlike other technologies [147]. It was aimed at achieving a rapid charging rate exceeding 1 T/s and was tested in liquid nitrogen rather than a conduction cooling system. For fast-ramping experiments in a conduction cooling system, improvements in the cooling system would be required, based on an analysis of eddy current losses and AC losses caused by rapid changes in the magnetic field. All settings for this experiment were identical to the previous experiments, except for the current power supply. The power supply used in this experiment was the Genesys from TDK-Lambda, as it supports charge-discharge rates of up to 1000 A/s.

To analyze this magnet, a distributed circuit model, as shown in Figure 4.33, was used. This circuit is similar to the turn-distributed circuit model discussed in previous sections, but with the turn-to-turn contact path removed and instead modeled with two parallel conductors. Additionally, a contact resistance was added between the two conductors. Determining this resistance value through voltage and magnetic field analysis is challenging, as any changes in voltage and magnetic field due to the resistance fall below the resolution of the measurements. Therefore, a value of 10 $\mu\Omega cm^2$ was used for analyzing voltage and magnetic field, and additional analysis was conducted on current distribution between the conductors based on varying contact resistance values.

The experimental results and analysis using the distributed circuit model are shown in Figure 4.34. Figures 4.34 (a), (b), and (c) show the measurements and analysis results when a current control command of 100 A/s was applied, while (d), (e), and (f) show the results for a 1000 A/s command. Due to the power supply's limitations, the actual current waveform deviated slightly from the command. The measurement and analysis results showed good agreement. In the voltage data, the analysis exhibited more noise than the measurements because the derivative of the measured current values was used in the analysis. The magnetic field measurements indicated a magnetic

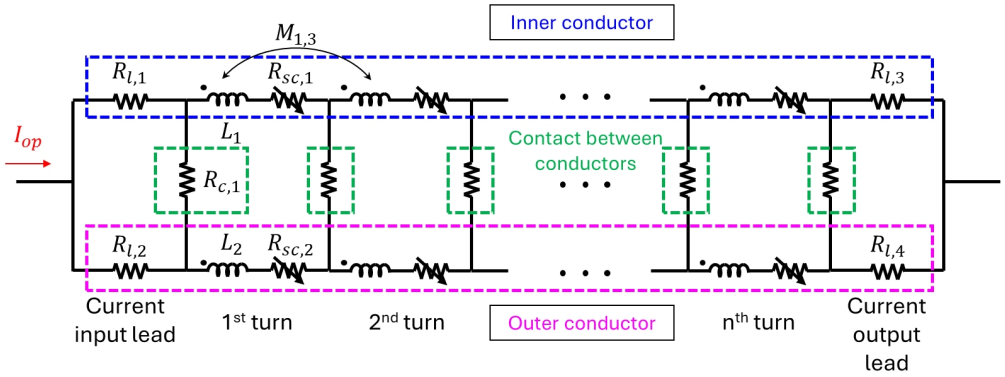

Figure 4.33: A distributed-circuit model for analyzing the experimental results of the demo magnet with 2-ply winding

field proportional to the current, similar to a conventional insulated magnet, with a maximum instantaneous charging rate measured at 1.4 T/s. Additionally, when charging to 100 A at 1000 A/s, the average charging rate until reaching the initial target current was measured at 0.51 T/s. Although conducted in liquid nitrogen, the experiment achieved the target charging rate of over 1 T/s.

The analysis of current distribution between the two conductors based on contact resistivity, using the circuit analysis model, is shown in Figure 4.35 (a). Analyses were conducted for contact resistivity values of 1, 10, 100, and 1000 $\mu\Omega cm^2$, with the lead resistance for each conductor set to the same value. While a contact resistivity of 1000 $\mu\Omega cm^2$ is uncommon in typical no-insulation settings, it is achievable with techniques like metal-insulation that can artificially increase contact resistivity. The results indicate that as contact resistivity increases, the current gradient decreases, likely due to the equal resistance of the current leads, meaning higher contact resistivity shifts the current distribution influence toward lead resistance. Conversely, when the contact resistivity is as low as 1 $\mu\Omega cm^2$, current primarily flows through a single conductor due to the difference in inductance between the two conductors. This suggests that the critical current of a 2-ply magnet could be less than the simple sum of the critical currents

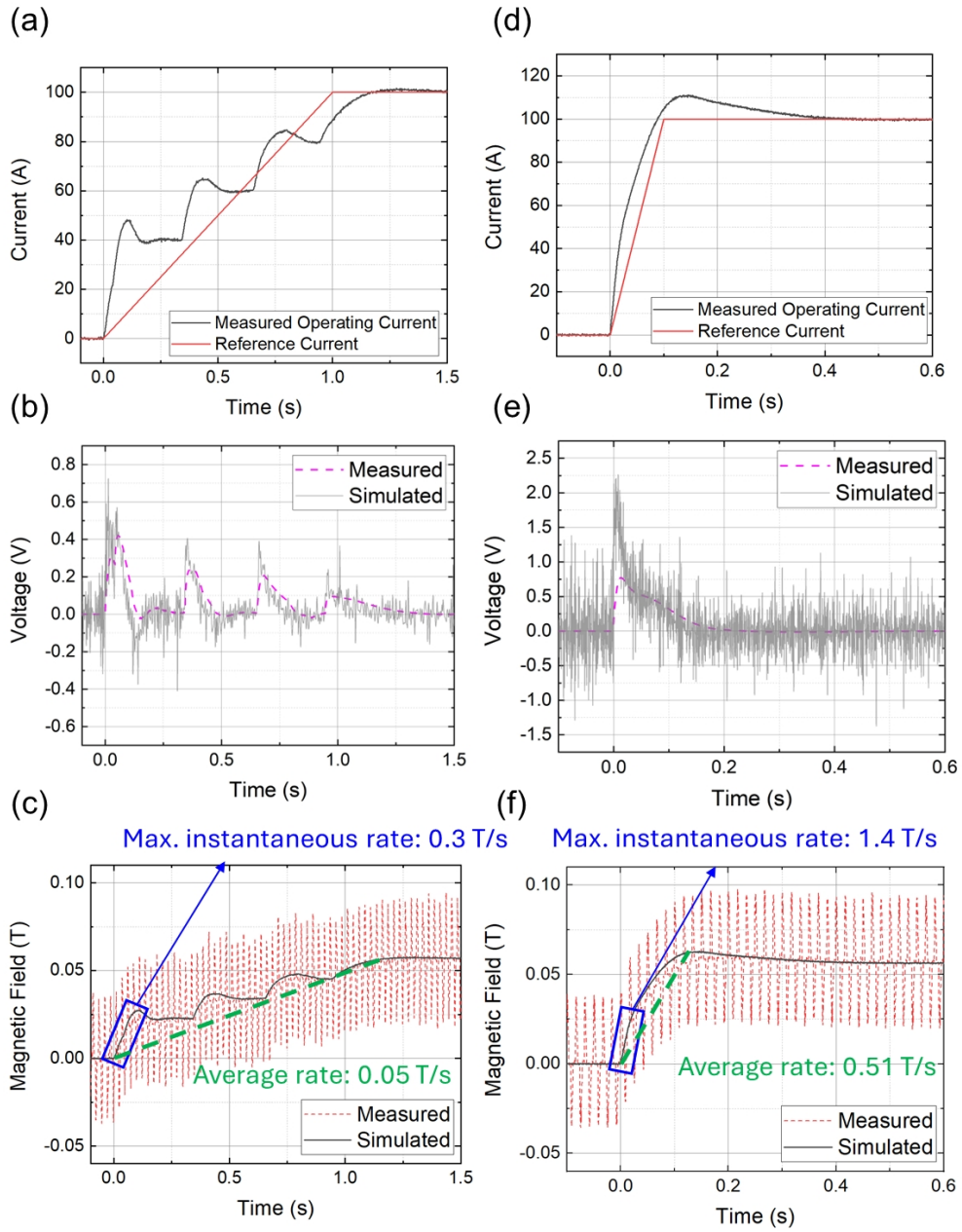

Figure 4.34: Fast-ramping experimental measurements and analysis results for the 2-ply winding demo magnet

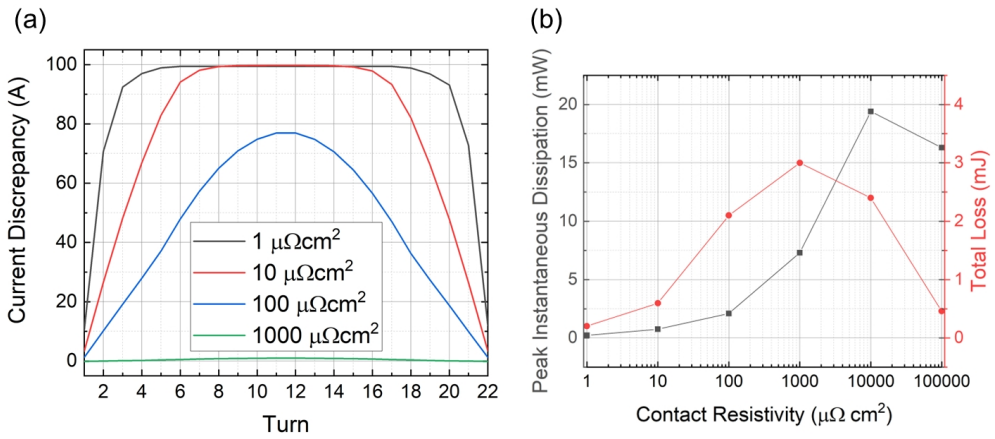

Figure 4.35: Based on contact resistivity between conductors, (a) analysis results of current difference, and (b) of Joule heating.

of both conductors.

Additionally, as shown in Figure 4.35 (b), the heat generation based on contact resistivity between conductors was calculated. The analysis suggests that for the 2-ply demo magnet used in the experiment, heat generation is maximized when the contact resistivity is around 1000 $\mu\Omega cm^2$ to 10000 $\mu\Omega cm^2$, indicating that to minimize heat generation, the contact resistivity should either be minimized or increased to a very high value. Since there are practical limits to increasing contact resistivity, minimizing contact resistivity between conductors is likely the more effective approach to reduce heat generation.

Chapter 5

CONCLUSION

This study aimed to develop analytical models, fabrication techniques, and operational methods required for applying a no-insulation (NI) high-temperature superconductor (HTS) saddle-shaped dipole magnet to particle accelerators. Furthermore, it sought to validate these developed techniques through experimental verification. Unlike existing research on NI HTS magnets, which has addressed and resolved various issues, this study faced unique challenges due to two specific factors: 1) the nonplanar saddle-shape; and 2) the demand for high magnetic field uniformity in dipole magnets.

First, the saddle-shape represents a nonplanar coil geometry distinct from the widely studied solenoid, racetrack, or D-shaped configurations. As a result, new analytical models had to be developed and validated, covering a range of topics from straightforward inductance calculations to complex analyses of current and magnetic field distributions caused by screening current, as well as mechanical property evaluations under 3D conditions. Additionally, unlike planar magnets that primarily use pancake coil windings, the saddle-shaped coil required decisions on bobbin design and the establishment of winding and fabrication techniques, necessitating further research.

Second, applying dipole magnets to particle accelerators demands a high level of magnetic field uniformity. However, instances of developing highly uniform magnets using NI HTS technology remain rare and are typically limited to solenoid configura-

tions, such as in NMR applications. In NI magnets, the current bypassing characteristic leads to more complex internal current distributions within the coil. Coupled with the pronounced impact of screening current caused by the wide tape geometry of REBCO conductors, this makes predicting the magnetic field uniformity particularly challenging. Therefore, this study also focused on developing correction methods to address the inherent factors that degrade the magnetic field uniformity produced by dipole magnets.

This study is divided into three primary parts: 1) development of analytical models for saddle-shaped dipole magnets; 2) design, fabrication, and operation of a dipole magnet for validation; and 3) experimental validation of the analytical models and development of methods for improving magnetic field uniformity. Each part addresses specific challenges and contributes to advancing the field.

In the first part, focused on analytical model development, solutions were proposed for challenges specific to saddle-shaped dipole magnets and general issues observed in NI magnets. To analyze screening current in saddle-shaped magnets, the study developed advanced models such as the FEM-circuit sequential model and the widthwise-segmented circuit model, building upon existing lumped and distributed circuit models. To enhance the efficiency of circuit analysis, methods like vectorization techniques and leveraging coil symmetry for faster inductance calculations were introduced. Additionally, a magnetic field analysis method for non-planar coils was established, along with a structured harmonic analysis approach to evaluate field uniformity. Beyond the saddle shape, estimating the critical current in NI magnets has been a widely recognized challenge. This difficulty arises due to the critical current gradient along the width of REBCO conductors and significant temperature gradients within magnets that use conduction cooling instead of cryogens. To address these issues, the widthwise average method was proposed to resolve the critical current gradient problem, and a load-line analysis technique was developed to account for the effects of both magnetic fields and temperatures. Lastly, for mechanical analysis, which becomes more complex

with saddle-shaped geometries, new modeling approaches were introduced. A winding path analysis method was proposed to avoid hard-way bending in coil-end regions, a common issue in saddle-shaped magnets. Boundary conditions for 3D geometries were established, enabling effective calculations of magnetic and thermal stresses, and a comprehensive mechanical analysis method was developed to ensure the magnet's structural integrity during operation.

The second part of this study describes the design, fabrication methods, cooling, and operation techniques for the dipole magnet used in validation experiments. The main magnet used in the experiments was designed with a central magnetic field of 0.7 T and a winding diameter of 110 mm. To achieve optimal performance, an optimization technique with magnetic field uniformity as the objective function was applied. The design process involved a parameter sweep from 2D cross-sectional analysis to a full 3D model to finalize the optimal design. Additionally, the analytical models developed in the first part were applied to evaluate the electromagnetic and mechanical stability of the magnet during the design phase. The magnet was cooled using a two-stage GM cryocooler conduction cooling system, necessitating thermal analysis to simulate the cooling process and assess the need for additional cooling channels. Based on these design results, the saddle-shaped coil was fabricated. The non-planar geometry required more complex multi-axis rotations and linear motions compared to traditional winding methods. To address this challenge, universal joints were implemented, enabling the successful winding of the coil. For electrical connections between coils, a solder-free lap joint was proposed to minimize damage to the REBCO conductors. This technique was applied during the magnet assembly process, and its effectiveness was validated. Additionally, a field-mapper was installed to measure the magnetic field uniformity, and a comprehensive experimental setup was established to monitor voltage, magnetic field, and temperature during operation. Finally, this section includes a separate discussion on the demo magnet, fabricated prior to the main magnet. The demo magnet's development highlights challenges encountered during the process and provides logi-

cal justification for the solutions that were implemented in the main magnet's design and fabrication. This approach underscores the iterative learning process that informed the successful development of the main magnet.

The final part of this study presents the experimental results for the dipole magnet. The main magnet was successfully charged to its target current of 295 A, with experiments including sudden-discharge tests at 50 A to derive coil parameters and confirm thermal characteristics. These results verified that the magnet operated as designed and exhibited the expected NI characteristics. Additionally, the winding geometry of the coil was inspected during each experimental step, enabling validation of the mechanical analysis. The magnetic field uniformity, measured when the magnet was charged to 200 A, was 14.0×10^{-4}, which is significantly lower than the designed value of 1.9×10^{-4}. This discrepancy was attributed primarily to shape deformation, while the influence of screening currents on uniformity was found to be minimal. This conclusion was further supported by current sweep reversal (CSR) experiments, a method commonly used in HTS magnets to mitigate magnetic field distortion caused by screening currents. CSR was applied to the dipole magnet for the first time in this study. However, no significant improvement in field uniformity was observed, aligning with analytical predictions. Additional tests at operating currents of 50 A, 100 A, and 150 A further confirmed that the effect of screening currents on the magnetic field was negligible.

To improve magnetic field uniformity, the ferroshim technique was employed, utilizing the magnetization of iron shims to enhance uniformity. Unlike conventional dipole magnets that use iron cores or yokes, the magnet developed in this study lacked such structures. Instead, ferroshims were installed in the warm bore of the magnet. An optimization process was conducted on the measured magnetic field distribution to determine the optimal thickness of the iron shims. These shims were fabricated by attaching iron pieces of the designed thickness onto an aluminum pipe. Installing the ferroshim improved the field uniformity to 9.5×10^{-4}, although this improvement was

still below the expected level. This shortfall was attributed to incomplete saturation of the iron shims. Furthermore, the temporal stability of the magnetic field uniformity was measured to be less than 0.38. A quench test was conducted on the main magnet to validate the developed critical current estimation model, and the observed quench phenomenon in the dipole magnet was analyzed using both electromagnetic and thermal simulations for comparison. Lastly, experimental results from the demo magnets produced in two iterations (NI and 2-ply winding) were discussed. The NI demo magnet experiments revealed the effects of shape deformation and screening currents on the magnetic field distribution, while the 2-ply demo magnet, operated under liquid nitrogen cooling, demonstrated a fast-ramping capability exceeding 1 T/s. These findings provide a comprehensive reference for the future development of high-field HTS dipole magnets.

Appendix

A Fundamental Physics of Superconductivity

A.1 Superconductivity

Superconductivity is a phenomenon where certain materials exhibit zero electrical resistance and expel magnetic flux fields under specific conditions. This remarkable behavior was first discovered in 1911 by Heike Kamerlingh Onnes in mercury at temperatures close to absolute zero [148]. Since then, superconductivity has become a cornerstone of advanced technologies, with applications ranging from powerful magnets in medical imaging (MRI) to particle accelerators and quantum computing. Superconductors are characterized by two defining properties:

- **Zero Electrical Resistance:** In the superconducting state, materials allow the flow of electrical current without any energy loss, making them ideal for applications requiring high efficiency.
- **Meissner Effect:** This phenomenon describes the complete expulsion of magnetic fields from the interior of a superconductor when it transitions into the superconducting state. Unlike ideal conductors, which can still support static magnetic fields, superconductors actively repel them, indicating a fundamental departure from conventional electromagnetism.

In 1935, Fritz and Heinz London formulated the London equations to establish a foundational framework for the electrodynamics of superconductors, particularly fo-

cusing on the expulsion of magnetic flux from their interior [149]. These equations involve a modification of Maxwell's equations, leading to a differential equation for the magnetic flux density inside a superconductor:

$$\nabla^2 \mathbf{B} = \frac{1}{\lambda_L^2} \mathbf{B}, \tag{1}$$

where λ_L represents London penetration depth. Solving this equation reveals that the magnetic flux density decays exponentially as it penetrates the superconductor. The London depth represents the scale of this decay and depends on the temperature as:

$$\lambda_L \propto \frac{1}{\sqrt{1 - (\frac{T}{T_c})^4}}, \tag{2}$$

where T and T_c represent the temperature and the critical temperature, respectively. While the London equations capture key aspects of superconducting behavior, such as the Meissner effect, they are oversimplified and unable to describe all electrodynamic phenomena in superconductors. For instance, they do not account for the microscopic quantum mechanics underlying superconductivity, which was later addressed by the BCS theory and Ginzburg-Landau theory.

After the discovery of superconductivity, numerous physicists endeavored to uncover its underlying mechanisms and explain its unique physical behaviors. In 1957, John Bardeen, Leon Cooper, and John Robert Schrieffer introduced the first microscopic theory of superconductivity, known as the BCS theory [150]. This theory describes superconducting current as a superfluid consisting of Cooper pairs, which are pairs of electrons bound together through interactions mediated by phonons as shown in Figure A.1.

A Cooper pair behaves as a boson, possessing an integer spin quantum number (0, 1, 2, ...), unlike a single electron, which is a fermion with a half-integer spin quantum number (1/2, 3/2, 5/2, ...). Although electrons naturally experience Coulomb repulsion, the electron-phonon interaction induces a stronger effective attraction between them, facilitating the formation of these pairs. Once Cooper pairs are formed, breaking them

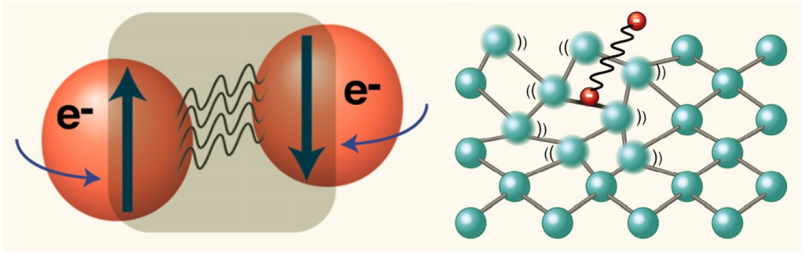

Figure A.1: Schematic diagram illustrating the concept of a Cooper pair [151].

requires a significant amount of energy, unlike the relatively small energy needed to alter the state of a single electron in a normal metal.

The energy required to break a Cooper pair is called the energy gap (Δ). This gap can be directly observed in tunneling experiments, and its temperature dependence is described by the BCS theory [152], which provides a quantitative prediction as follows:

$$\Delta(T) = \Delta(0)\sqrt{\cos\left(\frac{\pi}{2}\left(\frac{T}{T_c}\right)^2\right)}, \tag{3}$$

where $\Delta(0)$ represent gap energy at absolute 0 K. This characteristic energy gap is a defining feature of superconductors and plays a critical role in their unique properties.

A.2 Classification of Superconductors

Superconductors can be categorized into type-I and type-II based on their distinct physical properties. The key criterion for distinguishing between these two types is the Ginzburg-Landau dimensionless parameter, $\kappa = \lambda_L/\xi$, which represents the ratio of two characteristic lengths: the London penetration depth λ_L and the coherence length ξ.

The coherence length is the minimum distance over which the superconducting electron density can vary significantly. On the other hand, the London penetration depth corresponds to the depth at which a magnetic field is expelled from a superconductor. λ_L is closely linked to the density of superconducting electrons, while depends on the Fermi velocity and the energy gap of the material. Together, these parameters

determine the sign of the surface free energy in the superconductor, which ultimately dictates its classification.

The distinction between type-I and type-II superconductors can be summarized using the following criteria:

- **Type-I Superconductors:** Characterized by $\kappa < 1/\sqrt{2}$. It exhibits complete expulsion of the magnetic field (Meissner effect) until a critical field is reached, beyond which the superconducting state collapses entirely.

- **Type-II Superconductors:** Characterized by $\kappa > 1/\sqrt{2}$. It allows partial penetration of magnetic fields in the form of quantized vortices between the lower critical field H_{c1} and the upper critical field H_{c2}, forming a mixed state. Beyond H_{c2}, the material transitions to the normal state.

This classification provides a framework to understand and predict the magnetic and superconducting behaviors of various materials under different conditions.

The critical magnetic field can be estimated using the principles derived from Ginzburg-Landau theory [148]. At the critical magnetic field, fluxoids are packed as closely as the coherence length permits. Each fluxoid core carries a magnetic flux approximately equal to $\pi\xi^2 B_{c,2}$, which corresponds to the quantum of magnetic flux Φ_0. Therefore, the relationship can be expressed as follows:

$$B_{c,2} = \frac{\Phi_0}{2\pi\xi^2}, \tag{4}$$

where Φ_0 represents the quantum of magnetic flux, with a value of 2.067×10^{-15} Wb.

Another way to classify superconductors is based on their critical temperature T_c. Generally, low-temperature superconductors (LTS) are materials that exhibit superconductivity below 30 K, while high-temperature superconductors (HTS) are those that exhibit superconductivity at temperatures above this threshold. Some engineers specializing in HTS applications argue that HTS materials should ideally have above 77 K, the boiling point of liquid nitrogen, to facilitate practical cooling systems. Most metal-

lic superconductors have far below 77 K and are categorized as LTS, whereas the majority of ceramic-based superconductors fall into the HTS category. The conventional BCS theory predicted that superconductivity could not exist above approximately 30 K. However, in 1986, Karl Alexander Müller and Johannes Georg Bednorz discovered the first HTS in lanthanum-barium-copper oxide (LBCO) at 35 K [153]. Since then, HTS materials in the cuprate family, including LBCO and YBCO, have been shown to exhibit superconductivity beyond the explanatory scope of BCS theory. Alternative models such as the Lawrence-Doniach model and the anisotropic Ginzburg-Landau model have been developed to analyze the layered structures characteristic of HTS materials [154]. In these models, layered superconductors are treated as stacked arrays of two-dimensional superconductors coupled through Josephson tunneling effects. Using the anisotropic Ginzburg-Landau model, the critical magnetic field must be calculated along different lattice directions modeled as ab-plane and c-axis.

HTS exhibits nonlinear resistance in the mixed state, a condition where the superconductor can no longer maintain perfect diamagnetism. This nonlinear behavior poses a significant challenge, prompting physicists to explain it using microscopic theories. For HTS materials, particularly in cuprates, the mixed state is often categorized into two phases: the vortex-glass state and the vortex-fluid state.

In the vortex-glass state, Lorentz forces act between the transport currents and the quantized magnetic flux lines within normal state cores, referred to as vortices. These vortices are formed by circulating currents. According to Abrikosov's vortex lattice theory, imperfections in the material can pin these vortices. If the Lorentz force is small enough, the vortices remain stationary, resulting in zero resistance. However, when the transport current density J_t and temperature increase, the Lorentz force combined with thermal fluctuations can exceed the pinning force, causing vortices to move. This movement disrupts the superconducting state, marking the transition to the vortex-fluid state.

Thermal fluctuations play a significant role in HTS due to its high critical temper-

ature, making the energies required for vortex motion relatively small. The transition from the vortex-glass state to the vortex-fluid state is defined by the glass-melting temperature T_g, also referred to as the vortex-glass critical temperature. Researchers like D. Fisher have used scaling analysis to describe the vortex-glass phase [155]. Below T_g, the nonlinear relationship between the electric field E and current density J can be expressed as:

$$\frac{E}{J} \approx e^{-(\frac{J_T}{J})^{\alpha}}, \tag{5}$$

where α is a specific constant. In HTS, $J_T \approx J_c$, highlighting the impact of thermal fluctuations on critical current density. Subsequent research on the nonlinear electromagnetic behavior of HTS expanded into detailed analyses of current distribution, including transport current density and screening current density J_{sc}. These studies have led to the development of various models, with the 'power law' E-J relationship becoming the standard for analyzing HTS current density [155]:

$$E = E_c(\frac{J}{J_c})^n, \tag{6}$$

where n is the power-law exponent that describes the steepness of the E-J curve. This law has become integral to understanding and modeling the behavior of HTS under practical operating conditions. The fundamental nonlinear characteristics of superconductivity concerning temperature, current density, and magnetic field make analysis challenging from both microscopic and macroscopic perspectives, leading to difficulties in magnet analysis. From the perspective of magnet design, the development of sophisticated macroscopic analysis models is essential.

B Basics on Beam Physics and Particle Accelerator

B.1 Principles of Beam Dynamics

Beam dynamics is the cornerstone of particle accelerator physics, detailing the behavior of charged particles under electromagnetic forces within the confines of an accel-

erator. The primary goal is to precisely guide, confine, and accelerate particle beams along a predefined trajectory, minimizing beam loss and ensuring long-term stability. Dipole magnets play a fundamental role by creating uniform magnetic fields that bend particle trajectories, enabling the circular motion essential in synchrotrons, cyclotrons, and storage rings. This section expands on key principles of beam dynamics with detailed explanations, mathematical formulations, and their practical significance.

The motion of a charged particle in an electromagnetic field is governed by the Lorentz force law:

$$\mathbf{F} = q(\mathbf{E} + \mathbf{v} \times \mathbf{B}), \tag{7}$$

where $\mathbf{F}$, q, and v represent force acting on the particle, charge of the particle, and velocity of the particle, respectively. In particle accelerators, the electric field primarily accelerates particles, while the magnetic field is used to steer their trajectories. Dipole magnets are specifically designed to produce a uniform magnetic field, perpendicular to the beam's direction, resulting in a centripetal force that bends the particle's trajectory.

The governing equations describing the motion of a beam under a magnetic field can be derived. Here, the beam's direction of propagation is defined as the s-direction. For the actual trajectory in relation to the ideal orbit, the horizontal component of the deviation is along the x-direction, and the vertical component is along the z-direction. Assuming the beam undergoes a rotation by an angle ϕ in the horizontal plane, which is perpendicular to the z-axis, the unit vectors for the x- and s-components, $\mathbf{x}_0$ and $\mathbf{s}_0$, are transformed as follows through the rotation transformation.

$$\mathbf{x}_0 = \mathbf{x}_{0,i} \cos\phi + \mathbf{s}_{0,i} \sin\phi, \tag{8}$$

$$\mathbf{s}_0 = -\mathbf{x}_{0,i} \sin\phi + \mathbf{s}_{0,i} \cos\phi, \tag{9}$$

where $\mathbf{x}_{0,i}$ and $\mathbf{s}_{0,i}$ are initial unit vectors. By differentiating both equations, the time

derivatives of the unit vectors can be obtained as follows:

$$\dot{\mathbf{x}}_0 = \frac{1}{R}\dot{s}\mathbf{s}_0, \tag{10}$$

$$\dot{\mathbf{s}}_0 = \frac{1}{R}\dot{s}\mathbf{x}_0, \tag{11}$$

where R represents the radius of the orbit. Then, the position vector $\mathbf{r}$ and its first and second derivatives can be written in the genral form as follows:

$$\mathbf{r} = \mathbf{r}_0 + x\mathbf{x}_0 + z\mathbf{z}_0, \tag{12}$$

$$\dot{\mathbf{r}} = \dot{x}\mathbf{x}_0 + \dot{z}\mathbf{z}_0 + (1 + \frac{x}{R})\dot{s}\mathbf{s}_0, \tag{13}$$

$$\ddot{\mathbf{r}} = (\ddot{x} - (1 + \frac{x}{R})\frac{\dot{s}^2}{R})\mathbf{x}_0 + \ddot{z}\mathbf{z}_0 + (\frac{2}{R}\dot{x}\dot{s} + (1 + \frac{x}{R})\ddot{s})\mathbf{s}_0. \tag{14}$$

The time derivatives can be replaced by derivates of spatial coordinate as follows:

$$\dot{x} = x'\dot{s} \tag{15}$$

$$\ddot{x}\ x''\dot{s}^2 + x'\ddot{s}. \tag{16}$$

Using these relations, (12) can be formulated as follows:

$$\dot{\mathbf{r}} = x'\dot{s}\mathbf{x}_0 + z'\dot{s}\mathbf{z}_0 + (1 + \frac{x}{R})\dot{s}\mathbf{s}_0, \tag{17}$$

$$\ddot{\mathbf{r}} = (x''\dot{s}^2 + x'\ddot{s} - (1 + \frac{x}{R})\frac{\dot{s}^2}{R})\mathbf{x}_0 + (z''\dot{s}^2 + z'\ddot{s})\mathbf{z}_0 + (\frac{2}{R}x'\dot{s}^2 + (1 + \frac{x}{R})\ddot{s})\mathbf{s}_0. \tag{18}$$

With the assumption that only the transverse components of magnetic field exists because of the relativistic velocity of the particle, (7) can be organized as follows:

$$\ddot{\mathbf{r}} = \frac{e}{m}(\dot{\mathbf{r}} \times (B_x, B_z, 0)) = \frac{e}{m}(-(1 + \frac{x}{R})\dot{s}B_z, (1 + \frac{x}{R})\dot{s}B_x, x'\dot{s}B_z - z'\dot{s}B_x), \tag{19}$$

where m represents the mass of particle. Then, (17) and (19) lead to the relations as follows:

$$x''\dot{s}^2 + x'\ddot{s} - (1 + \frac{x}{R})\frac{\dot{s}^2}{R} = -\frac{e}{m}B_z(1 + \frac{x}{R})\dot{s}, \tag{20}$$

$$z''\dot{s}^2 + z'\ddot{s} = \frac{e}{m}B_x(1 + \frac{x}{R})\dot{s}. \tag{21}$$

Finally, the governing equations for particle motion in the magnetic field can be expressed with particle momentum p and the momentum deviation Δp as follows:

$$x'' + (\frac{1}{R^2} - k)x = \frac{1}{R}\frac{\Delta p}{p}, \tag{22}$$

$$z'' + kz = 0. \tag{23}$$

In the governing equations, $\frac{1}{R}$ corresponds to the dipole strength while k the quadrupole strength.

The generation of high-flux photon beams for accelerator-based light sources fundamentally relies on synchrotron radiation, a phenomenon where electromagnetic radiation is emitted as high-energy electron beams are deflected by magnetic fields, as illustrated in Figure B.2. The emitted photon spectrum spans a wide range of energies, and the critical energy E_c, which marks the spectral peak of the radiated photons, is directly proportional to the strength of the magnetic field. The total radiated power by the particle with relativistic velocity can be formulated as follows [10]:

$$P_s \frac{e^2 c}{6\pi\epsilon_0}\frac{1}{(m_0c^2)^2}((\frac{dp}{d\tau})^2 - \frac{1}{c^2}(\frac{dE}{d\tau})^2), \tag{24}$$

where τ is the proper time.

Then, the type of acceleration can be categorized by linear and circular. For the linear acceleration, the time derivative of energy can be expressed as follows:

$$\frac{dE}{d\tau} = v\frac{dp}{d\tau}. \tag{25}$$

In this case, the radiated power can be formulated as:

$$P_s = \frac{e^2 c}{6\pi\epsilon_0}\frac{1}{(m_0c^2)^2}(\frac{dE}{dx})^2. \tag{26}$$

However, considering the practical limit of the electric field level, the radiation of electromagnetic energy during linear acceleration is negligible.

The circular acceleration is caused by the magnetic field. This is the dominant component in synchrotron radiation compared to the linear one. The change of momentum

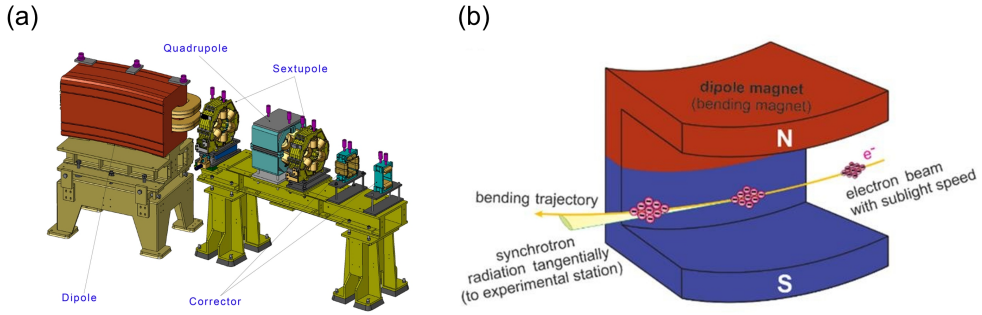

Figure B.2: The magnet system of a particle accelerator and the role of the dipole magnet. (a) Dipole, quadrupole, and sextupole magnets installed in a synchrotron [156], (b) Synchrotron radiation emitted by deflecting an electron beam using dipole magnets [157].

can be expressed as follows:

$$\frac{dp}{dt} = p\frac{v}{R}. \tag{27}$$

In this case, the radiation power by the circular acceleration can be formulated as:

$$P_s = \frac{e^2 c}{6\pi\epsilon_0}\frac{1}{(m_0c^2)^2}\frac{E^4}{R^2}. \tag{28}$$

Increasing the beam energy leads to an increase in the radiated power, but it necessitates an upgrade of the entire accelerator system. Alternatively, replacing the current electromagnets with higher-field magnets offers another way to enhance the radiated power. The power radiated during circular acceleration is proportional to the square of the magnetic field strength, as the bending radius decreases inversely with an increase in the magnetic field. The critical energy of beam can be expressed as follows:

$$E_c = \frac{3hq\gamma^2}{4\pi m\beta}|\mathbf{B}|, \tag{29}$$

where h, γ, and β represent the Planck constant, the Lorentz factor, and the speed of beam normalized by the speed of light, respectively. Increasing the magnetic field strength in a dipole magnet ultimately means reducing the overall system radius or achieving higher beam energy.

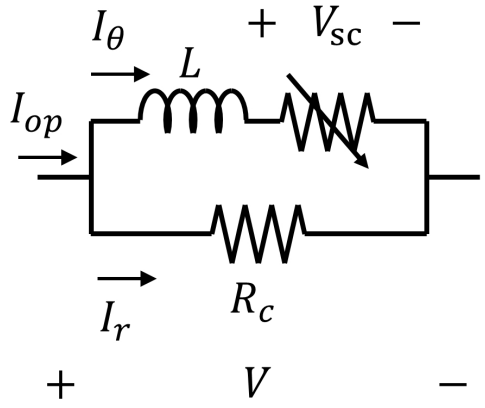

Figure C.3: Lumped circuit model for an NI HTS coil or magnet

C Conventionally Used Simulation Models for NI Magnets

C.1 Lumped and Distributed Circuit Model

The circuit models for NI HTS coils can be divided into two categories: 1) lumped circuit models and 2) distributed circuit models. Both types incorporate inductive and resistive elements and have been experimentally validated by numerous research groups. Depending on the analysis objectives, these models are applied to study the electromagnetic behavior of the coils.

The lumped circuit model for an NI (or its variation) HTS coil includes self-inductance, index resistance, and a characteristic resistance representing the resistive path for the bypass current as shown in Figure C.3 [78, 95, 158]. When multiple NI HTS coils are involved, mutual inductances between specific coils are also taken into account. Due to the limited number of circuit elements required, this model enables fast and accurate analysis of the coil's terminal voltage and the central magnetic field. It has been applied across different scales, from single-pancake coils to large magnets, and for both normal operation and quench conditions. However, this model cannot capture local electromagnetic behaviors within the coil. The governing equation for

this model is calculated as follows:

$$V = L\frac{dI_\theta}{dt} + V_{sc}(I_\theta) = R_c I_r, \tag{30}$$

$$I_{op} = I_\theta + I_r, \tag{31}$$

$$V_{sc}(I_\theta) = E_c l(\frac{I_\theta}{I_c})^n, \tag{32}$$

$$\therefore \frac{dI_\theta}{dt} = \frac{1}{L}(R_c I_{op} - R_c I_\theta - E_c l(\frac{I_\theta}{I_c})^n). \tag{33}$$

The voltage-current characteristics can be determined by solving this nonlinear ODE. Due to the nonlinearity introduced by the index resistance, numerical methods like the backward differentiation formula (BDF) [159] or the Runge-Kutta method [160] are used to find the solution.

The distributed circuit model divides the coil into smaller elements, enabling the investigation of local behaviors since each element is represented by individual circuit components. This model includes the self-inductance of each element, mutual inductances between elements, index resistance, and the characteristic resistance for each bypass current path. Although it demands more computation time than the lumped circuit model due to the larger number of elements, it is commonly used for specific purposes, such as analyzing local behaviors related to coil defects, quench effects, or nonuniform current density caused by screening currents.

The turn-distributed-circuit model is a widely used type of distributed circuit model [161]. In this approach, each turn of the NI HTS coil is treated as an individual circuit element as shown in Figure C.4. Accordingly, the number of azimuthal current paths and bypass current paths corresponds to the total number of turns.

The governing equation for this model can be derived as follows:

$$\mathbf{V} = \mathbf{M}\frac{d\mathbf{I}_\theta}{dt} + \mathbf{V}_{sc}(\mathbf{I}_\theta) = \mathbf{R}_c \mathbf{I}_r, \tag{34}$$

$$\mathbf{I}_\theta = (I_{\theta,1}, I_{\theta,2}, \cdots, I_{\theta,N})^T, \tag{35}$$

$$\mathbf{I}_r = (I_{r,1}, I_{r,2}, \cdots, I_{r,N})^T, \tag{36}$$

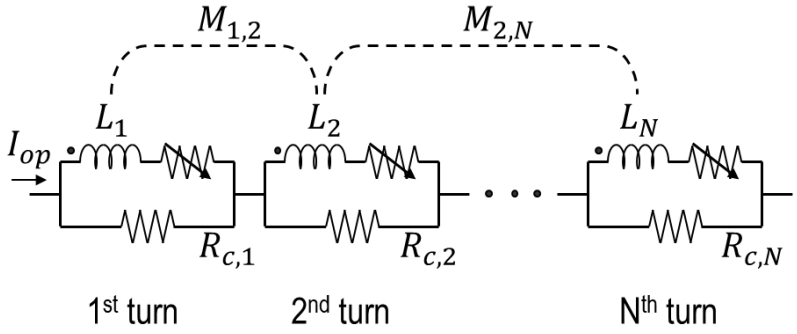

Figure C.4: Turn-distributed circuit model of an NI HTS coil

$$\mathbf{M} = \begin{pmatrix} L_1 & M_{1,2} & \cdots & M_{1,N} \\ M_{2,1} & L_2 & \cdots & M_{2,N} \\ \vdots & \vdots & \ddots & \vdots \\ M_{N,1} & M_{N,2} & \cdots & L_N \end{pmatrix} \tag{37}$$

$$\mathbf{V}_{sc}(\mathbf{I}_\theta) = (E_c l_1 (\frac{I_{\theta,1}}{I_{c,1}})^n, E_c l_2 (\frac{I_{\theta,2}}{I_{c,2}})^n, \cdots, E_c l_N (\frac{I_{\theta,N}}{I_{c,N}})^n)^T, \tag{38}$$

$$\mathbf{R}_c = \text{diag}(R_{c,1}, R_{c,2}, \cdots, R_{c,N}), \tag{39}$$

$$\mathbf{I}_\theta + \mathbf{I}_r = (I_{op}, I_{op}, \cdots, I_{op})^T = \mathbf{I}_{op}, \tag{40}$$

$$\therefore \frac{d\mathbf{I}_\theta}{dt} = \mathbf{M}^{-1}(\mathbf{R}_c \mathbf{I}_{op} - \mathbf{R}_c \mathbf{I}_\theta - \mathbf{V}_{sc}(\mathbf{I}_\theta)), \tag{41}$$

where $I_{\theta,i}$, $I_{r,i}$, $I_{c,i}$, L_i, $M_{i,j}$, l_i, $R_{c,i}$, and N represent the azimuthal current flowing through i^{th} turn, radial current flowing through i^{th} turn, critical current of i^{th} turn (which is determined by magnetic field, inclination angle, and temperature), self-inductance of i^{th} turn, mutual inductance between i^{th} and j^{th} turns, length of i^{th} turn, characteristic resistance of i^{th} turn, and the number of total turns, respectively.

The above equation is also highly nonlinear, and a stiff matrix can arise if there are abrupt changes in the index resistance. Therefore, methods such as the BDF or the Runge-Kutta method should be used with consideration of stability of the numerical solver during the solving process.

Lastly, the partial element equivalent circuit (PEEC) model is an analysis method that divides the coil's turns into smaller segments [140, 162–164]. This model has also been utilized in various studies, primarily for quench analysis and AC operation analysis. Compared to the previously mentioned models, the PEEC model is the most complex and requires the longest computation time. Researches are ongoing to develop techniques to reduce the computation time. The governing equation for the conventional PEEC model as shown in Figure C.5 is calculated as follows based on Kirchhoff's current law (the first equation) and voltage law (the second and third ones):

$$\mathbf{C}\mathbf{I}_\theta + \mathbf{D}\mathbf{I}_r = (I_{op}, 0, \cdots, 0)^T|_{sN\times 1}, \tag{42}$$

$$\mathbf{C}^T\mathbf{V} = \mathbf{M}\frac{d\mathbf{I}_\theta}{dt} + \mathbf{V}_{sc}(\mathbf{I}_\theta), \tag{43}$$

$$\mathbf{D}^T\mathbf{V} = \mathbf{R}_c\mathbf{I}_r, \tag{44}$$

$$C_{i,j} = \begin{cases} 1 & (i = j) \\ -1 & (i = j+1)\ , \\ 0 & (\text{otherwise}) \end{cases} \tag{45}$$

$$D_{i,j} = \begin{cases} 1 & (i = j) \\ -1 & (i = j+s)\ , \\ 0 & (\text{otherwise}) \end{cases} \tag{46}$$

$$\mathbf{M} = \begin{pmatrix} L_1 & M_{1,2} & \cdots & M_{1,sN} \\ M_{2,1} & L_2 & \cdots & M_{2,sN} \\ \vdots & \vdots & \ddots & \vdots \\ M_{sN,1} & M_{sN,2} & \cdots & L_{sN} \end{pmatrix}, \tag{47}$$

$$\mathbf{R}_c = \text{diag}(R_{c,1}, R_{c,2}, \cdots, R_{c,sN-s+1}), \tag{48}$$

$$\mathbf{I}_\theta = (I_{\theta,1}, I_{\theta,2}, \cdots, I_{\theta,sN})^T, \tag{49}$$

$$\mathbf{I}_r = (I_{r,1}, I_{r,2}, \cdots, I_{r,sN-s+1})^T, \tag{50}$$

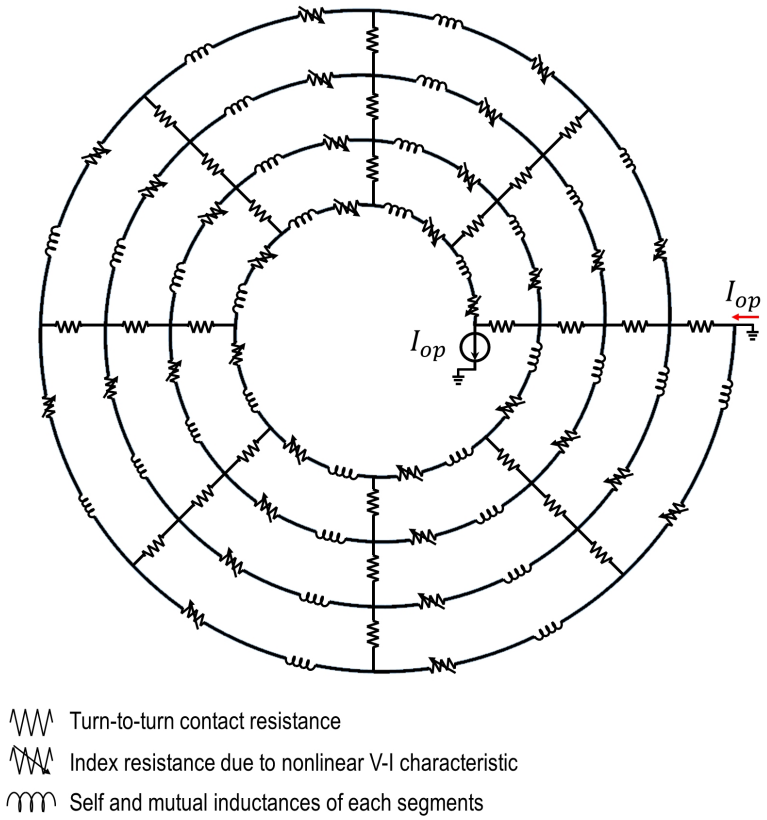

Figure C.5: Partial element equivalent circuit model of an NI HTS coil

$$\mathbf{V}_{sc}(\mathbf{I}_\theta) = (E_c l_1(\frac{I_{\theta,1}}{I_{c,1}})^n, E_c l_2(\frac{I_{\theta,2}}{I_{c,2}})^n, \cdots, E_c l_{sN}(\frac{I_{\theta,sN}}{I_{c,sN}})^n)^T, \tag{51}$$

where $I_{\theta,i}$, $I_{r,i}$, $I_{c,i}$, L_i, $M_{i,j}$, l_i, $R_{c,i}$, s, and N represent the azimuthal current flowing through i^{th} element, radial current flowing through i^{th} element, critical current of i^{th} element (which is determined by magnetic field, inclination angle, and temperature), self-inductance of i^{th} element, mutual inductance between i^{th} and j^{th} element, length of i^{th} element, characteristic resistance of i^{th} element, the number of azimuthal segments of each turn, and the number of total turns, respectively. Due to positional relationship between each node, the size of system matrices $\mathbf{C}$ and $\mathbf{D}$ are $sN \times sN$ and $sN \times (sN - s + 1)$, respectively.

To find the solution of the above equation, the rank of the matrix must be adjusted

to $w = sN - s + 1$. Therefore, the equations can be rearranged through the following partition of matrices:

$$\mathbf{C} = \begin{pmatrix} \mathbf{C}_1|_{w\times w} & \mathbf{0}|_{w\times(s-1)} \\ \mathbf{C}_2|_{(s-1)\times w} & \mathbf{C}_3|_{(s-1)\times(s-1)} \end{pmatrix}, \tag{52}$$

$$\mathbf{D} = \begin{pmatrix} \mathbf{D}_1|_{w\times w} \\ \mathbf{D}_2|_{(s-1)\times w} \end{pmatrix}, \tag{53}$$

$$(\mathbf{C}^T)^{-1}\mathbf{M} = \begin{pmatrix} \mathbf{M}_1|_{w\times w} & \mathbf{M}_2|_{w\times(s-1)} \\ \mathbf{M}_3|_{(s-1)\times w} & \mathbf{M}_4|_{(s-1)\times(s-1)} \end{pmatrix}, \tag{54}$$

$$\mathbf{I}_\theta = \begin{pmatrix} \mathbf{I}_{\theta,1}|_{w\times 1} \\ \mathbf{I}_{\theta,2}|_{(s-1)\times 1} \end{pmatrix}, \tag{55}$$

$$\mathbf{V}_{sc} = \begin{pmatrix} \mathbf{V}_{sc,1}|_{w\times 1} \\ \mathbf{V}_{sc,2}|_{(s-1)\times 1} \end{pmatrix}, \tag{56}$$

$$\mathbf{I}_{op} = (I_{op}, 0, \cdots, 0)^T|_{w\times 1}. \tag{57}$$

Then, the governing equation can be derived as follows:

$$\mathbf{I}_r = \mathbf{D}_1^{-1}\mathbf{I}_{op} - \mathbf{D}_1^{-1}\mathbf{C}_1\mathbf{I}_{\theta,1} = \mathbf{P}_1\mathbf{I}_{op} + \mathbf{Q}_1\mathbf{I}_{\theta,1}, \tag{58}$$

$$\mathbf{I}_{\theta,2} = -\mathbf{C}_3^{-1}\mathbf{D}_2\mathbf{P}_1\mathbf{I}_{op} - \mathbf{C}_3^{-1}(\mathbf{D}_2\mathbf{Q}_1 + \mathbf{C}_2)\mathbf{I}_{\theta,1} = \mathbf{P}_2\mathbf{I}_{op} + \mathbf{Q}_2\mathbf{I}_{\theta,1}, \tag{59}$$

$$\begin{aligned} &\mathbf{D}_1^T(\mathbf{M}_1\frac{d\mathbf{I}_{\theta,1}}{dt} + \mathbf{M}_2\frac{d\mathbf{I}_{\theta,2}}{dt} + \mathbf{V}_{sc,1}) \\ &\qquad + \mathbf{D}_2^T(\mathbf{M}_3\frac{d\mathbf{I}_{\theta,1}}{dt} + \mathbf{M}_4\frac{d\mathbf{I}_{\theta,2}}{dt} + \mathbf{V}_{sc,2}) = \mathbf{R}_c\mathbf{I}_r, \end{aligned} \tag{60}$$

$$\begin{aligned} \therefore \frac{d\mathbf{I}_{\theta,1}}{dt} = \mathcal{M}^{-1}(&\mathbf{R}_c\mathbf{Q}_1\mathbf{I}_{\theta,1} - \mathbf{D}_1^T\mathbf{V}_{sc,1} \\ &- \mathbf{D}_2^T\mathbf{V}_{sc,2} + \mathbf{R}_c\mathbf{P}_1\mathbf{I}_{op} - \mathcal{N}\frac{d\mathbf{I}_{op}}{dt}), \end{aligned} \tag{61}$$

$$\mathcal{M} = \mathbf{D}_1^T(\mathbf{M}_1 + \mathbf{M}_2\mathbf{Q}_2) + \mathbf{D}_2^T(\mathbf{M}_3 + \mathbf{M}_4\mathbf{Q}_2), \tag{62}$$

$$\mathcal{N} = (\mathbf{D}_1^T\mathbf{M}_2 + \mathbf{D}_2^T\mathbf{M}_4)\mathbf{P}_2. \tag{63}$$

The above formulae are for the basic PEEC model, and in the case of the model

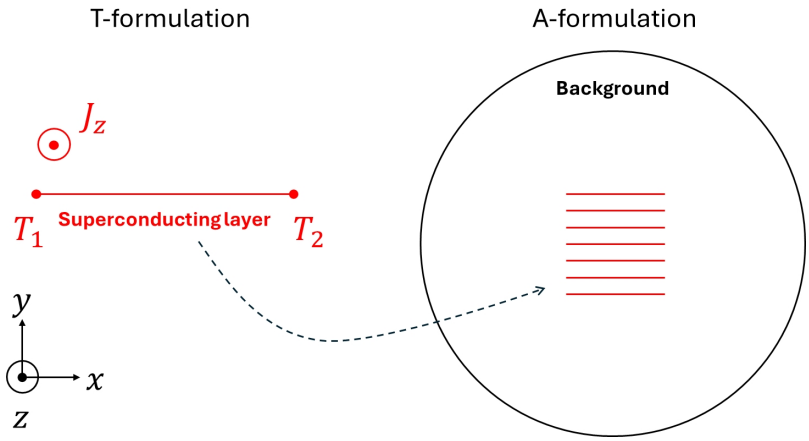

Figure C.6: Schematic drawing for T-A formulation method. T formulation is used to simulate superconducting layers while A formulation is used to simulate the backgroud outside superconducting layers.

suggested in this dissertation, the screening current analysis was performed by adding a widthwise segmentation of the conductor.

C.2 Finite Element Method with T-A formulation

The T-A formulation [165, 166] efficiently simulates the nonuniform current density due to screening current. The REBCO tapes are modeled as one-dimensional elements, and only these one-dimensional areas are formulated by the current vector potential $\mathbf{T}$ as shown in Figure C.6. The other area is formulated by the magnetic vector potential $\mathbf{A}$. The governing equations and boundary condition are as follows:

$$-\frac{\partial \mathbf{B}}{\partial t} = \nabla \times (\rho \nabla \times \mathbf{T}), \tag{64}$$

$$\mathbf{J} = \nabla \times (\frac{1}{\mu} \nabla \times \mathbf{A}) = \sigma \mathbf{E}, \tag{65}$$

$$\mathbf{E} = -\frac{\partial \mathbf{A}}{\partial t}, \tag{66}$$

$$I_{op} = (T_1 - T_2)\delta, \tag{67}$$

where T_1 and T_2 are the current vector potentials at the edge of the 1D area.

D Additional Analysis on Screening Current

D.1 Effect of Current Source's Ripple on Screening Current Induced Field

The widthwise-segmented circuit model proposed in this study enables the analysis of the effect of the current source on screening currents. The current source used in the experiment is the MercuryiPS from Oxford Instruments, as mentioned in the text. This current source has a current ripple of 2 mA, and a case where the operating current changes, as shown in Figure D.7, was assumed.

In this model, the current offset was set to 200 A, with the ripple modeled as a sine function with an amplitude of 2 mA. A period of 1 second was assumed. The resulting current distribution caused by this operating current was analyzed, and the difference in magnetic field distribution between the peak and trough of the current ripple was evaluated. The results are shown in Figure D.8. The analysis reveals differences in the magnetic field distribution, with the magnetic field at the peak being greater than that at the trough. However, the ripple in the magnetic field is on the nT scale, which is negligible and does not significantly impact the target magnetic field uniformity. The ripples that vary significantly over time due to the current bypass paths in NI magnets are found to have little impact on the magnetic field. This analysis quantitatively demonstrates the influence of the current source on the magnetic field distribution.

D.2 Analysis of Screening Current Induced Voltage

Quantifying screening currents is generally challenging. The most commonly used approach involves measuring the magnetic field, either by comparing the absolute magnitude of the central magnetic field or, as in this study, by comparing the magnetic field distribution. However, this method requires high precision in magnetic field measurements, which increases the complexity and cost of the experimental setup.

Other parameters, such as strain and AC loss, can also be used, but they are even

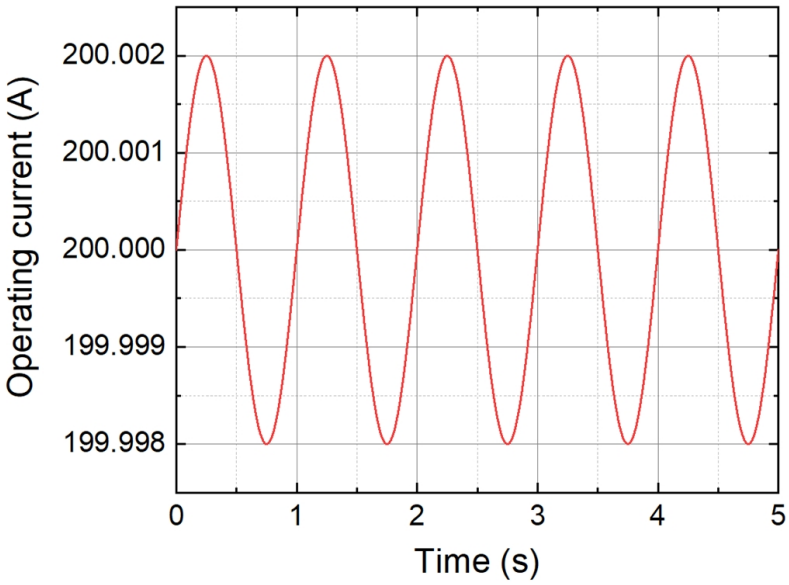

Figure D.7: Operating current profile considering current ripple from the current source.

more difficult to measure and are prone to significant measurement errors. As an alternative, screening currents can be quantified using voltage. When screening currents occur, the effective inductance changes, causing variations in voltage, even in coils without resistance. Figure D.9 provides an example of measuring voltage induced by screening currents. In the experiment, the NI coil used showed different voltage profiles during the first and second current charging phases, despite having no resistance. This difference indicates that the screening currents differ in each case due to the hysteresis of the screening currents. This behavior can be replicated using the widthwise-segmented circuit model.

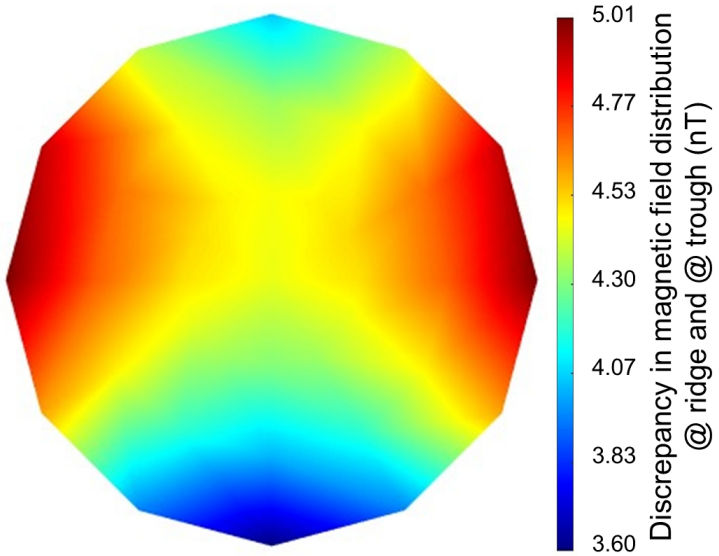

Figure D.8: Magnetic field ripple caused by the presence of current ripple.

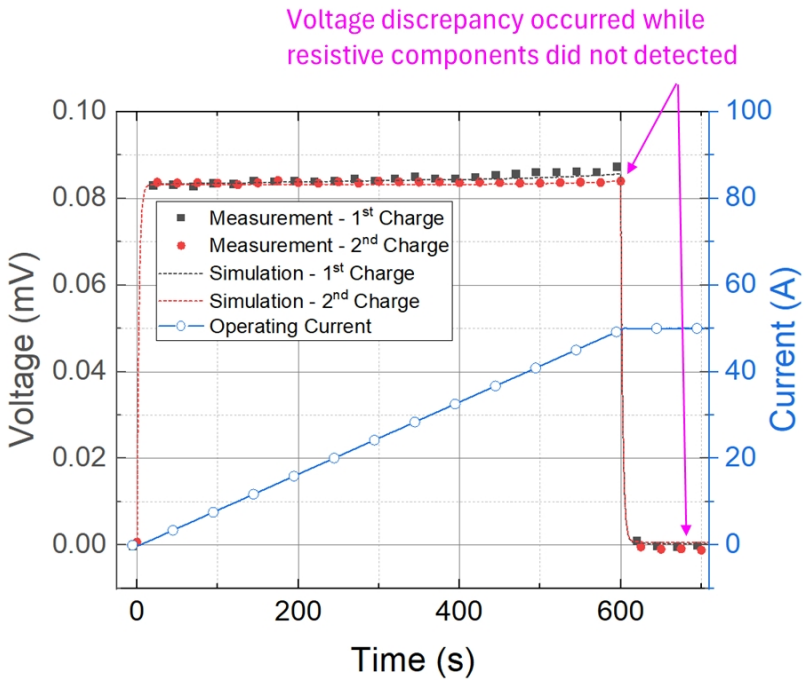

Figure D.9: Example of measurement and analysis of screening current induced voltage.

Bibliography

[1] E. Todesco and P. Ferracin, "Limits to High Field Magnets for Particle Accelerators," *IEEE Trans. Appl. Supercond.*, vol. 22, no. 3, pp. 4 003 106–4 003 106, 2012.

[2] L. Rossi and L. Bottura, "Superconducting Magnets for Particle Accelerators," *Rev. Accel. Sci. Technol.*, vol. 5, pp. 51–89, 2012.

[3] L. Bottura, S. A. Gourlay, A. Yamamoto, and A. V. Zlobin, "Superconducting Magnets for Particle Accelerators," *IEEE Trans. Nucl. Sci.*, vol. 63, no. 2, pp. 751–776, 2015.

[4] L. Bottura, S. Prestemon, L. Rossi, and A. V. Zlobin, "Superconducting Magnets and Technologies for Future Colliders," *Front. Physics*, vol. 10, p. 935196, 2022.

[5] F. Zimmermann, "Accelerator Technology and Beam Physics of Future Colliders," *Front. Physics*, vol. 10, p. 888395, 2022.

[6] A. Canepa and M. D'Onofrio, "Future Accelerator Projects: New Physics at the Energy Frontier," *Front. Physics*, vol. 10, p. 916078, 2023.

[7] S. Gourlay, T. Raubenheimer, and V. Shiltsev, "Challenges of Future Accelerators for Particle Physics Research," *Front. Physics*, vol. 10, p. 920520, 2022.

[8] L. Bottura, "High Field Accelerator Magnets for Next Generation Colliders–Motivation, Goals, Challenges and R&D Drivers," in *The High Luminosity Large Hadron Collider: New Machine for Illuminating the Mysteries of the Universe*. World Scientific, 2024, pp. 615–641.

[9] E. Wilson, *An Introduction to Particle Accelerators*. Oxford University Press, 2001.

[10] K. Wille, *The Physics of Particle Accelerators: An Introduction*. Clarendon Press, 2000.

[11] O. Brüning, H. Burkhardt, and S. Myers, "The Large Hadron Collider," *Prog. Part. Nucl. Phys.*, vol. 67, no. 3, pp. 705–734, 2012.

[12] R. Wolf, *The Higgs Boson Discovery at the Large Hadron Collider*. Springer, 2015, vol. 264.

[13] M. Mangano *et al.*, "Future Circular Collider," *no. CERN-ACC-2018-0056, Dec*, 2018.

[14] M. Benedikt *et al.*, "Future Circular Colliders," *Annual Review of Nuclear and Particle Science*, vol. 69, no. 1, pp. 389–415, 2019.

[15] M. Benedikt, A. Blondel, P. Janot, M. Mangano, and F. Zimmermann, "Future Circular Colliders Succeeding the LHC," *Nat. Phys.*, vol. 16, no. 4, pp. 402–407, 2020.

[16] M. Benedikt and F. Zimmermann, "Future Circular Collider: Integrated Programme and Feasibility Study," *Front. Physics*, vol. 10, p. 888078, 2022.

[17] I. Agapov *et al.*, "Future Circular Lepton Collider FCC-ee: Overview and Status," *arXiv preprint arXiv:2203.08310*, 2022.

[18] M. Benedikt *et al.*, "Future Circular Hadron Collider FCC-hh: overview and status," *arXiv preprint arXiv:2203.07804*, 2022.

[19] D. Stratakis *et al.*, "A Muon Collider Facility for Physics Discovery," *arXiv preprint arXiv:2203.08033*, 2022.

[20] C. Accettura *et al.*, "Towards a Muon Collider," *Eur. Phys. J. C*, vol. 83, no. 9, pp. 1–110, 2023.

[21] K. Black *et al.*, "Muon Collider Forum Report," *J. Instrum.*, vol. 19, no. 02, p. T02015, 2024.

[22] E. Aschenauer *et al.*, "eRHIC Design Study: an Electron-ion Collider at BNL," *arXiv preprint arXiv:1409.1633*, 2014.

[23] National Academies of Sciences and Division on Engineering and Physical Sciences and Board on Physics and Committee on US-Based Electron-Ion Collider Science Assessment, *An Assessment of US-based Electron-ion Collider Science*. National Academies Press, 2018.

[24] E. Aschenauer *et al.*, "The Electron–ion Collider: Assessing the Energy Dependence of Key Measurements," *Rep. Prog. Phys.*, vol. 82, no. 2, p. 024301, 2019.

[25] "Future Circular Collider," https://home.cern/science/accelerators/future-circular-collider.

[26] M. Palmer, "An Overview of the US Muon Accelerator Program," 2013.

[27] "U.S. Department of Energy Selects Brookhaven National Laboratory to Host Major New Nuclear Physics Facility," https://www.bnl.gov/newsroom/news.php?a=116996.

[28] "China's Designs for a Future Circular Collider," https://cerncourier.com/a/chinas-designs-for-a-future-circular-collider/.

[29] X. Lou, "The Circular Electron Positron Collider," *Nat. Rev. Phys.*, vol. 1, no. 4, pp. 232–234, 2019.

[30] J. Song, L. Xin-Chou, R. Man-Qi, X. Qing-Jin, and Z. Hong-Bo, "The Circular Electron Positron Collider: Its Physics, Technology, and Status," *Physics*, vol. 48, no. 3, pp. 148–158, 2019.

[31] G. Jie, "CEPC: A Proposed Circular Electron-Positron Collider as a Higgs Factory," *AAPPS Bulletin*, vol. 30, no. 4, 2020.

[32] L. Brouwer *et al.*, "Design and Test of a Curved Superconducting Dipole Magnet for Proton Therapy," *Nucl. Instrum. Methods Phys. Res. Sect. A-Accel. Spectrom. Dect. Assoc. Equip.*, vol. 957, p. 163414, 2020.

[33] L. Bottura *et al.*, "Performance of the LHC Final Prototype and First Pre-series Superconducting Dipole Magnets," *IEEE Trans. Appl. Supercond.*, vol. 12, no. 1, pp. 211–214, 2002.

[34] M. Conte and W. W. MacKay, *An Introduction to the Physics of Particle Accelerators*. World Scientific, 2008.

[35] L. Rossi and O. Brüning, "Introduction to the HL-LHC Project," in *The High Luminosity Large Hadron Collider: The New Machine for Illuminating the Mysteries of Universe*. World Scientific, 2015, pp. 1–17.

[36] F. Savary *et al.*, "The 11 T dipole for HL-LHC: Status and Plan," *IEEE Trans. Appl. Supercond.*, vol. 26, no. 4, pp. 1–5, 2016.

[37] G. Apollinari *et al.*, "High-Luminosity Large Hadron Collider (HL-LHC). Technical Design Report V. 0.1," Fermi National Accelerator Lab.(FNAL), Batavia, IL (United States), Tech. Rep., 2017.

[38] A. Dainese, M. Mangano, A. B. Meyer, A. Nisati, G. Salam, and M. A. Vesterinen, "Report on the Physics at the HL-LHC, and Perspectives for the HE-LHC," *CERN Yellow Reports: Monographs*, vol. 7, 2019.

[39] O. Brüning and L. Rossi, "The High Luminosity Large Hadron Collider–HL-LHC," in *The High Luminosity Large Hadron Collider: New Machine for Illuminating the Mysteries of the Universe*. World Scientific, 2024, pp. 1–53.

[40] D. E. Kim, H. S. Han, H.-G. Lee, K.-H. Park, H. Suh, and J. Young-Gyu, "Magnet System for PLS-II Project," in *Particle Accelerator Conference (PAC 09)*, 2010, p. MO6PFP032.

[41] "KEKB B factory design report," 6 1995.

[42] L. Dallin, I. Blomqvist, M. de Jong, E. Hallin, D. Lowe, and R. Silzer, "The Canadian Light Source: An Update," in *PACS2001. Proceedings of the 2001 Particle Accelerator Conference (Cat. No. 01CH37268)*, vol. 4. IEEE, 2001, pp. 2680–2682.

[43] L. Dallin *et al.*, "Gradient Dipole Magnets for the Canadian Light Source," in *Proc. PAC*, 2002, pp. 2340–2343.

[44] E. Bondarchuk *et al.*, "Magnets for the PETRA-III Project," *IEEE Trans. Appl. Supercond.*, vol. 16, no. 2, pp. 220–223, 2006.

[45] N. Marks and M. Lieuvin, "Design of the Accelerator Magnets for the ESRF," *IEEE Trans. Magn.*, vol. 24, no. 2, pp. 741–744, 1988.

[46] M. Preger and C. Sanelli, "The DAFNE Main Ring Magnet Prototypes," 1996.

[47] S. Sanfilippo *et al.*, "Magnets for the Upgrade of the Swiss Light Source at the Paul Scherrer Institute-Design, Production, Measurement Challenges," *IEEE Trans. Appl. Supercond.*, vol. 34, no. 5, pp. 1–5, 2023.

[48] R. Erickson, S. DeBarger, C. Spencer, and Z. Wolf, "Dipole Magnets for the SLAC 50 GeV A-Line Upgrade," in *Proceedings Particle Accelerator Conference*, vol. 2. IEEE, 1995, pp. 1366–1368.

[49] G. S. LeBlanc, M. Boland, and Y. Tan, "The Australian Synchrotron Project Storage Ring and Injection System Overview," in *Proceedings of EPAC*, vol. 4, 2004.

[50] L. Bottura, P. Pugnat, A. Siemko, J. Vlogaert, and C. Wyss, "Performance of the LHC Final Design Full Scale Superconducting Dipole Prototypes," *IEEE Trans. Appl. Supercond.*, vol. 11, no. 1, pp. 1554–1557, 2001.

[51] I. DIPOLES, "Construction and Testing of Arc Dipoles and Quadrupoles for the Relativistic Heavy Ion Collider (RHIC) at BNL," 1996.

[52] L. C. Teng, R. A. Carrigan, C. Rubbia, D. B. Cline, and A. B. Tollestrup, "The Tevatron," 1978.

[53] H. E. Fisk, "Superconducting Magnets," Fermi National Accelerator Lab.(FNAL), Batavia, IL (United States), Tech. Rep., 1987.

[54] H. Hirabayashi, "Development of Superconducting Magnets for Beam Lines and Accelerator at KEK," *IEEE Trans. Magn.*, vol. 17, no. 1, pp. 728–731, 1981.

[55] A. Ageyev *et al.*, "Study of the Models of Superconducting Dipole Magnet for the UNK," in *11th International Conference on Magnet Technology (MT-11) Volume 1*. Springer, 1990, pp. 111–116.

[56] R. Gupta, S. Kahn, and G. Morgan, "Coil and Iron Design for SSC 50 mm Magnet," Brookhaven National Lab., Upton, NY (USA), Tech. Rep., 1990.

[57] A. Gabard, D. George, M. Negrazus, L. Rivkin, V. Vrankovic, and Y. Kolokolnikov, "A 2.9 Tesla Room Temperature Superbend Magnet for the Swiss Light Source at PSI," in *Proceedings of IPAC2011*, 2011.

[58] A. McInturff *et al.*, "ISABELLE Ring Magnets," *IEEE Trans. Magn.*, vol. 13, no. 1, pp. 275–278, 1977.

[59] A. Milanese *et al.*, "Design of the EuCARD High Field Model Dipole Magnet FRESCA2," *IEEE Trans. Appl. Supercond.*, vol. 22, no. 3, pp. 4 002 604–4 002 604, 2011.

[60] G. Willering *et al.*, "Tests of the FRESCA2 100 mm Bore Nb_3Sn Block-coil Magnet to a Record Field of 14.6 T," *IEEE Trans. Appl. Supercond.*, vol. 29, no. 5, pp. 1–6, 2019.

[61] S. Caspi, "LBNL Cos-theta Nb_3Sn Dipole Magnet D20," *Nb_3Sn Accelerator Magnets: Designs, Technologies and Performance*, pp. 133–156, 2019.

[62] D. R. Chichili *et al.*, "Fabrication of the Shell-type Nb_3Sn Dipole Magnet at Fermilab," *IEEE Trans. Appl. Supercond.*, vol. 11, no. 1, pp. 2160–2163, 2001.

[63] S. A. Gourlay, S. O. Prestemon, A. V. Zlobin, L. Cooley, and D. Larbalestier, "The US Magnet Development Program Plan," 2016.

[64] X. Wang, "LBNL ReBCO Dipole Development," in *HiTAT workshop*, 2023.

[65] J. van Nugteren *et al.*, "Powering of an HTS Dipole Insert-magnet Operated Standalone in Helium Gas between 5 and 85 K," *Supercond. Sci. Technol.*, vol. 31, no. 6, p. 065002, 2018.

[66] J. van Nugteren, G. Kirby, J. Murtomäki, G. DeRijk, L. Rossi, and A. Stenvall, "Toward REBCO 20 T+ Dipoles for Accelerators," *IEEE Trans. Appl. Supercond.*, vol. 28, no. 4, pp. 1–9, 2018.

[67] T. Nes *et al.*, "Design of a Cloverleaf-racetrack Dipole Demonstrator Magnet with Dual ReBCO Conductor," *IEEE Trans. Appl. Supercond.*, vol. 32, no. 6, pp. 1–5, 2022.

[68] A. Zlobin, "Conceptual Design of A 20 T Dipole Based on Hybrid REBCO/Nb3Sn Cos-theta Coil," *arXiv preprint arXiv:2408.11023*, 2024.

[69] K. Koyanagi *et al.*, "Development of Saddle-shaped Coils Using Coated Conductors for Accelerator Magnets," *IEEE Trans. Appl. Supercond.*, vol. 23, no. 3, pp. 4 100 404–4 100 404, 2012.

[70] S. Takayama *et al.*, "Design and Test Results of Superconducting Magnet for Heavy-ion Rotating Gantry," in *Journal of Physics: Conference Series*, vol. 871, no. 1. IOP Publishing, 2017, p. 012083.

[71] X. Wang *et al.*, "Development and Performance of a 2.9 Tesla Dipole Magnet Using High-temperature Superconducting CORC® Wires," *Supercond. Sci. Technol.*, vol. 34, no. 1, p. 015012, 2020.

[72] Y. Liu, P. Song, M. Xiao, L. Shao, M. Guan, and T. Qu, "Design of a 3 T REBCO Dipole Magnet Considering Screening Current Induced Magnetic Field and Its First Test Result at 77 K," *IEEE Trans. Appl. Supercond.*, 2024.

[73] S. Nam *et al.*, "Major Upgrade Activity of the PLS in PAL: PLS-II," *PAC09, Vancouver, Canada*, pp. 3172–3174, 2009.

[74] "Large Hadron Collider (LHC) Dipole Magnet Cutaway." [Online]. Available: https://cds.cern.ch/record/2764842

[75] T. Shen *et al.*, "Design, Fabrication, and Characterization of a High-field High-temperature Superconducting Bi-2212 Accelerator Dipole Magnet," *Phys. Rev. Accel. Beams*, vol. 25, no. 12, p. 122401, 2022.

[76] K. R. Bhattarai *et al.*, "Understanding Quench in No-insulation (NI) REBCO Magnets through Experiments and Simulations," *Supercond. Sci. Technol.*, vol. 33, no. 3, p. 035002, 2020.

[77] S. Noguchi, "Electromagnetic, Thermal, and Mechanical Quench Simulation of NI REBCO Pancake Coils for High Magnetic Field Generation," *IEEE Trans. Appl. Supercond.*, vol. 29, no. 5, pp. 1–7, 2019.

[78] S. Hahn, D. K. Park, J. Bascunan, and Y. Iwasa, "HTS Pancake Coils without Turn-to-turn Insulation," *IEEE Trans. Appl. Supercond.*, vol. 21, no. 3, pp. 1592–1595, 2010.

[79] Y. Yanagisawa, Y. Xu, X. Jin, H. Nakagome, and H. Maeda, "Reduction of Screening Current-induced Magnetic Field of REBCO Coils by the Use of Multi-filamentary Tapes," *IEEE Trans. Appl. Supercond.*, vol. 25, no. 3, pp. 1–5, 2014.

[80] E. Berrospe-Juarez, F. Trillaud, V. M. Zermeño, and F. Grilli, "Screening Current-induced Field and Field Drift Study in HTS Coils Using TA Homogenous Model," in *Journal of Physics: Conference Series*, vol. 1559, no. 1. IOP Publishing, 2020, p. 012128.

[81] Y. Yan, Y. Li, and T. Qu, "Screening Current Induced Magnetic Field and Stress in Ultra-high-field Magnets Using REBCO Coated Conductors," *Supercond. Sci. Technol.*, vol. 35, no. 1, p. 014003, 2021.

[82] B. A. Glowacki, W. J. Nuttall, and R. H. Clarke, "Beyond the Helium Conundrum," *IEEE Trans. Appl. Supercond.*, vol. 23, no. 3, pp. 0 500 113–0 500 113, 2013.

[83] M. Green and B. Strauss, "Estimating the Operating Cost of Superconducting Magnet Systems at Various Operating Temperatures," *IEEE Trans. Appl. Supercond.*, vol. 26, no. 4, pp. 1–5, 2016.

[84] P. Vedrine *et al.*, "Iseult/INUMAC Whole Body 11.7 T MRI Magnet Status," *IEEE Trans. Appl. Supercond.*, vol. 20, no. 3, pp. 696–701, 2010.

[85] U. Bong *et al.*, "Design, Construction, and Operation of a 2 T 240 mm Conduction-cooled Defect-irrelevant Winding (RE)$Ba_2Cu_3O_{7-x}$ Magnet," *Rev. Sci. Instrum.*, vol. 93, no. 7, 2022.

[86] J. Bang *et al.*, "A Customized Electric Heater to Mitigate Screening Current by Optimal Control on Temperature Distribution in a High-temperature Superconductor Coil," *J. Appl. Phys.*, vol. 132, no. 18, 2022.

[87] S. Pamidi, C. Kim, and L. Graber, "High-temperature Superconducting (HTS) Power Cables Cooled by Helium Gas," in *Superconductors in the Power Grid*. Elsevier, 2015, pp. 225–260.

[88] Q. Wu, P. Song, Y. Yan, Z. Shi, M. Song, and T. Qu, "Design and Testing of a Gas-helium Conduction Cooled REBCO Magnet for a 300 kVar HTS Synchronous Condenser Prototype," *IEEE Trans. Appl. Supercond.*, vol. 30, no. 4, pp. 1–5, 2020.

[89] S. Hahn *et al.*, "'Defect-irrelevant' Behavior of a No-insulation Pancake Coil Wound with REBCO Tapes Containing Multiple Defects," *Supercond. Sci. Technol.*, vol. 29, no. 10, p. 105017, 2016.

[90] ——, "Construction and Test of 7-T/68-mm Cold-bore Multiwidth No-insulation GdBCO Magnet," *IEEE Trans. Appl. Supercond.*, vol. 25, no. 3, pp. 1–5, 2014.

[91] D. Park, W. Lee, J. Bascuñán, H. M. Kim, and Y. Iwasa, "A Cryogen-free 25-T REBCO Magnet with the Extreme-no-insulation Winding Technique," *IEEE Trans. Appl. Supercond.*, vol. 32, no. 6, pp. 1–5, 2022.

[92] S. Yoon, J. Kim, K. Cheon, H. Lee, S. Hahn, and S.-H. Moon, "26 T 35 mm all-$GdBa_2Cu_3O_{7-x}$ Multi-width No-insulation Superconducting Magnet," *Supercond. Sci. Technol.*, vol. 29, no. 4, p. 04LT04, 2016.

[93] J. Kim *et al.*, "Design, Construction, and Operation of an 18 T 70 mm No-insulation (RE)$Ba_2Cu_3O_{7-x}$ Magnet for an Axion Haloscope Experiment," *Rev. Sci. Instrum.*, vol. 91, no. 2, 2020.

[94] J. Bang *et al.*, "Harmonic Errors of a 9.4 T All-REBCO NMR Magnet Affected by Screening Current and Geometric Inconsistency of Coated Conductors," *Sci Rep*, vol. 14, no. 1, p. 19146, 2024.

[95] S. Hahn *et al.*, "45.5-tesla Direct-current Magnetic Field Generated with a High-temperature Superconducting Magnet," *Nature*, vol. 570, no. 7762, pp. 496–499, 2019.

[96] Y. Suetomi, S. Takahashi, T. Takao, H. Maeda, and Y. Yanagisawa, "A Novel Winding Method for a No-insulation Layer-wound REBCO Coil to Provide a Short Magnetic Field Delay and Self-protect Characteristics," *Supercond. Sci. Technol.*, vol. 32, no. 4, p. 045003, 2019.

[97] Y. Suetomi *et al.*, "Quench and Self-protecting Behaviour of an Intra-layer No-insulation (LNI) REBCO Coil at 31.4 T," *Supercond. Sci. Technol.*, vol. 34, no. 6, p. 064003, 2021.

[98] J.-B. Song, X. Chaud, B. Borgnic, F. Debray, P. Fazilleau, and T. Lécrevisse, "Construction and Test of a 7 T Metal-as-insulation HTS Insert under a 20 T High Background Magnetic Field at 4.2 K," *IEEE Trans. Appl. Supercond.*, vol. 29, no. 5, pp. 1–5, 2019.

[99] T. Lécrevisse, X. Chaud, P. Fazilleau, C. Genot, and J.-B. Song, "Metal-as-insulation HTS Coils," *Supercond. Sci. Technol.*, vol. 35, no. 7, p. 074004, 2022.

[100] J. Liu *et al.*, "World Record 32.35 Tesla Direct-current Magnetic Field Generated with an All-superconducting Magnet," *Supercond. Sci. Technol.*, vol. 33, no. 3, p. 03LT01, 2020.

[101] Z. Hartwig *et al.*, "The SPARC Toroidal Field Model Coil Program," *IEEE Trans. Appl. Supercond.*, vol. 34, no. 2, p. 0600316, 2024.

[102] G. Brittles and R. Bateman, "Stability and Quench-dynamic Behaviour of Tokamak Energy REBCO QA coils," in *Talks at WAMHTS-5*, 2019.

[103] L. Bottura, E. Felcini, G. De Rijk, and B. Dutoit, "GaToroid: a Novel Toroidal Gantry for Hadron Therapy," *Nucl. Instrum. Methods Phys. Res. Sect. A-Accel. Spectrom. Dect. Assoc. Equip.*, vol. 983, p. 164588, 2020.

[104] J. Park, "5 T High Temperature Superconductor 3 Pole Wavelength Shifter Magnet for Accelerator-based Light Sources," PhD thesis, Seoul National University, February 2024, available at 10.23170/snu.000000181582.11032.0001503.

[105] C. Sanabria *et al.*, "Development of a High Current Density, High Temperature Superconducting Ccable for Pulsed Magnets," *Supercond. Sci. Technol.*, vol. 37, no. 11, p. 115010, 2024.

[106] H. Winick, *Synchrotron Radiation Sources: a Primer*. World Scientific, 1994, vol. 1.

[107] X. Wang *et al.*, "Turn-to-turn Contact Characteristics for an Equivalent Circuit Model of No-insulation ReBCO Pancake Coil," *Supercond. Sci. Technol.*, vol. 26, no. 3, p. 035012, 2013.

[108] G. Kim *et al.*, "Investigation on Nonuniform Current Density and Shape Deformation Affecting the Magnetic Field Performance of a Saddle-shaped No-insulation HTS Cosine–theta Dipole Magnet," *Supercond. Sci. Technol.*, vol. 36, no. 8, p. 084002, 2023.

[109] L. Qin *et al.*, "Refined Circuit Model for Current Distribution of the No-insulation HTS Insert Magnet," *Supercond. Sci. Technol.*, vol. 34, no. 7, p. 075002, 2021.

[110] G. Kim *et al.*, "Fast Current Distribution Simulation Method for No-insulation HTS Coil with Defects," *IEEE Trans. Appl. Supercond.*, vol. 32, no. 6, pp. 1–5, 2022.

[111] F. W. Grover, *Inductance Calculations: Working Formulas and Tables*. Courier Corporation, 2004.

[112] J. Bang, "Simulation and Mitigation of Screening Current in High-Temperature Superconductor Magnet for Magnetic Resonance Application," PhD thesis, Seoul National University, August 2022.

[113] S. Ahn, G. Kim, S. H. Park, J. Park, and S. Hahn, "Fast Computation of Inductance of Saddle-shaped HTS Coil," in *2023 Summer Conference of KSSC*, 2023.

[114] D. Hilton, A. Gavrilin, and U. Trociewitz, "Practical Fit Functions for Transport Critical Current versus Field Magnitude and Angle Data from (RE)BCO Coated Conductors at Fixed Low Temperatures and in High Magnetic Fields," *Supercond. Sci. Technol.*, vol. 28, no. 7, p. 074002, 2015.

[115] "High-temperature Superconducting Wire Critical Current Database, SuNAM SAN04200 2G HTS," https://htsdb.wimbush.eu/dataset/5182354.

[116] G. Kim *et al.*, "Investigation on Effective Critical Current of REBCO Conductor under Widthwise Magnetic Field Gradient," in *2024 Winter Conference of KSSC*, 2024.

[117] Y. Iwasa, *Case Studies in Superconducting Magnets: Design and Operational Issues*. Springer science & business media, 2009.

[118] H. Liang *et al.*, "Design of the Integral Field Measurement System of Dipole Magnets," *IEEE Trans. Appl. Supercond.*, vol. 28, no. 3, pp. 1–5, 2018.

[119] Y. Zhu, W. Kang, F. Chen, W. Chen, X. Wu, and M. Yang, "An Improved Design Method for Conventional Straight Dipole Magnets," *arXiv preprint arXiv:1701.07600*, 2017.

[120] H. S. Suh *et al.*, "Design, Development, and Test of the Magnets for PAL-XFEL," in *Proceedings of FEL2015*, 2015.

[121] K. Wachowicz, "Evaluation of Active and Passive Shimming in Magnetic Resonance Imaging," *RES. REP. NUCL. MED.*, pp. 1–12, 2014.

[122] G. Kim, K. Choi, J. Park, U. Bong, J. Bang, and S. Hahn, "A Simulation-based Design Study of Superconducting Zonal Shim Coil for a 9.4 T Whole-body MRI Magnet," *Prog. Supercond. Cryog.*, vol. 22, no. 1, pp. 12–16, 2020.

[123] D. Park, J. Lee, J. Bascuñán, Z. Li, and Y. Iwasa, "Prototype REBCO Z1 and Z2 Shim Coils for Ultra High-field High-temperature Superconducting NMR Magnets," *Sci Rep*, vol. 10, no. 1, p. 21946, 2020.

[124] A. Belov *et al.*, "Passive Shimming of the Superconducting Magnet for MRI," *IEEE Trans. Appl. Supercond.*, vol. 5, no. 2, pp. 679–681, 1995.

[125] M. C. Ahn, "Passive Shimming Design with Commercially Available Rectangular Shim Sheets on a Cylinder for HTS NMR Magnets," *Prog. Supercond. Cryog.*, vol. 20, no. 2, pp. 29–33, 2018.

[126] J. Y. Jang *et al.*, "Experimental Study of a Room-temperature Shimming Technology Employing Genetic Algorithm for NMR/MRI Superconducting Magnets," *IEEE Trans. Appl. Supercond.*, vol. 33, no. 5, pp. 1–5, 2023.

[127] S. Russenschuck, *Field Computation for Accelerator Magnets: Analytical and Numerical Methods for Electromagnetic Design and Optimization*. John Wiley & Sons, 2011.

[128] L. Rossi and E. Todesco, "Electromagnetic Design of Superconducting Dipoles based on Sector Coils," *Phys. Rev. Accel. Beams*, vol. 10, no. 11, p. 112401, 2007.

[129] A. Mate, "The Frenet-Serret Formulas," *Brooklyn Collage Of The City University Of New York, izdano*, vol. 19, 2017.

[130] T. Luo, H. Chen, and G. S. Kassab, "Resliced Image Space Construction for Coronary Artery Collagen Fibers," *PLoS One*, vol. 12, no. 9, p. e0184972, 2017.

[131] T. Nes, G. de Rijk, A. Kario, and H. Ten Kate, "Differential Geometry Method for Minimum Hard-way Bending 3D Design of Coils with ReBCO Tape Conductor," *Supercond. Sci. Technol.*, vol. 35, no. 10, p. 105011, 2022.

[132] U. Bong, "Applicability of No-insulation High-temperature Superconductor Field Winding to Superconducting Synchronous Motor," PhD thesis, Seoul National University, August 2022.

[133] N. Simon, E. Drexler, and R. P. Reed, "Properties of Copper and Copper Alloys at Cryogenic Temperatures: Final Report," National Inst. of Standards and Technology (MSEL), Tech. Rep., 1992.

[134] Y. Touloukian, "Recommended Values of the Thermophysical Properties of Eight Alloys, Major Constituents and Their Oxides," Tech. Rep., 1966.

[135] R. J. Corruccini and J. J. Gniewek, *Thermal Expansion of Technical Solids at Low Temperatures: A Compilation from the Literature*. US Department of Commerce, National Bureau of Standards, 1961, vol. 29.

[136] R. I. Rousseau and A.-H. Bouzid, "The Tightening and Untightening Modeling and Simulation of Bolted Joints," *Machines*, vol. 12, no. 9, p. 654, 2024.

[137] Q. Yu, H. Zhou, and L. Wang, "Finite Element Analysis of Relationship Between Tightening Torque and Initial Load of Bolted Connections," *Adv. Mech. Eng.*, vol. 7, no. 5, p. 1687814015588477, 2015.

[138] R. Radebaugh, "Cryocoolers: the State of the Art and Recent Developments," *J. Phys.-Condes. Matter*, vol. 21, no. 16, p. 164219, 2009.

[139] "ULVAC Refrigerator (CRYO)," https://showcase.ulvac.co.jp/en/products/refrigerator/.

[140] G. Kim *et al.*, "A Numerical Method for Spatially-distributed Transient Simulation to Replicate Nonlinear 'Defect-irrelevant' Behaviors of No-insulation HTS Coil," *Supercond. Sci. Technol.*, vol. 34, no. 11, p. 115004, 2021.

[141] Y. Yanagisawa *et al.*, "Effect of Current Sweep Reversal on the Magnetic Feld Stability for a Bi-2223 Superconducting Solenoid," *Physica C*, vol. 469, no. 22, pp. 1996–1999, 2009.

[142] Y.-G. Kim, Y. H. Choi, D. G. Yang, H.-J. Shin, M. C. Ahn, and H. Lee, "Study for Reducing the Screening Current-induced Field in a 10-MHz No-insulation Magnet Using Current Sweep Reversal Method," *IEEE Trans. Appl. Supercond.*, vol. 25, no. 3, pp. 1–5, 2014.

[143] M. Bonura and C. Senatore, "High-field Thermal Transport Properties of REBCO Coated Conductors," *Supercond. Sci. Technol.*, vol. 28, no. 2, p. 025001, 2014.

[144] G. Kim *et al.*, "Experimental Study for Modified Lumped-Circuit Model to Analyze Saddle-Shaped No-Insulation HTS Coil Operated in Overcurrent Situation," *IEEE Trans. Appl. Supercond.*, 2023.

[145] A. Grau *et al.*, "Characterization of 30-cm-long Superconducting Undulator Coils with the Magnetic Measurement System CASPER II," *IEEE Trans. Appl. Supercond.*, vol. 26, no. 4, pp. 1–4, 2016.

[146] S. Gerstl *et al.*, "First Characterization of a Superconducting Undulator Mockup with the CASPER II Magnetic Measurement System," in *6th Int. Particle Accelerator Conf.(IPAC'15), Richmond, VA, USA, May 3-8, 2015*. JACOW, Geneva, Switzerland, 2015, pp. 2815–2817.

[147] G. Kim *et al.*, "Distributed-Circuit Method for Replication of Fast-Ramping of Saddle-Shaped REBCO Dipole Magnet Wound With Two-Tape Bundled Conductor," *IEEE Trans. Appl. Supercond.*, 2023.

[148] M. Tinkham, *Introduction to Superconductivity*. Courier Corporation, 2004, vol. 1.

[149] A. C. Rose-Innes, *Introduction to Superconductivity*. Pergamon, 1978, vol. 2.

[150] J. Bardeen, L. N. Cooper, and J. R. Schrieffer, "Microscopic Theory of Superconductivity," *Phys. Rev.*, vol. 106, no. 1, p. 162, 1957.

[151] F. Wang and D.-H. Lee, "The Electron-Pairing Mechanism of Iron-Based Superconductors," *Science*, vol. 332, no. 6026, pp. 200–204, 2011. [Online]. Available: https://www.science.org/doi/abs/10.1126/science.1200182

[152] B. Mühlschlegel, "Die Thermodynamischen Funktionen des Supraleiters," *Zeitschrift für Physik*, vol. 155, no. 3, pp. 313–327, 1959.

[153] J. G. Bednorz and K. A. Müller, "Possible High T_c Superconductivity in the Ba-La-Cu-O system," *Zeitschrift für Physik B Condensed Matter*, vol. 64, no. 2, pp. 189–193, 1986.

[154] S. J. Chapman, Q. Du, and M. D. Gunzburger, "On the Lawrence–Doniach and Anisotropic Ginzburg–Landau Models for Layered Superconductors," *SIAM J. Appl. Math.*, vol. 55, no. 1, pp. 156–174, 1995.

[155] D. S. Fisher, M. P. Fisher, and D. A. Huse, "Thermal Fluctuations, Quenched Disorder, Phase Transitions, and Transport in Type-II Superconductors," *Phys. Rev. B*, vol. 43, no. 1, p. 130, 1991.

[156] "Accelerator Magnet," https://www.nsrrc.org.tw/English/organizationDetail.aspx?Dept_UID=8.

[157] L. Kong, R. P. Gamage, J. Zhao, T. Rathnaweera, and Z. Ma, "Tensile Behaviors of Granite: Grain Scale Cracking and Fracture Process Zone," in *ARMA US Rock Mechanics/Geomechanics Symposium*. ARMA, 2019, pp. ARMA–2019.

[158] G. Kim *et al.*, "Experimental Study and Frequency Domain Analysis on Metal-insulation HTS Coil," *IEEE Trans. Appl. Supercond.*, vol. 32, no. 4, pp. 1–5, 2022.

[159] C. Fredebeul, "A-BDF: a Generalization of the Backward Differentiation Formulae," *SIAM J. Numer. Anal.*, vol. 35, no. 5, pp. 1917–1938, 1998.

[160] J. Butcher, "Runge-Kutta Methods," *Scholarpedia*, vol. 2, no. 9, p. 3147, 2007.

[161] K. Choi *et al.*, "Upper Limit Estimation of Resistive Heating Made by No-insulation HTS Magnet Having Defects," *IEEE Trans. Appl. Supercond.*, vol. 31, no. 5, pp. 1–5, 2021.

[162] T. Wang *et al.*, "Analyses of Transient Behaviors of No-insulation REBCO Pancake Coils during Sudden Discharging and Overcurrent," *IEEE Trans. Appl. Supercond.*, vol. 25, no. 3, pp. 1–9, 2015.

[163] C. Im *et al.*, "Mesh Dependency on a Partial Element Equivalent Circuit Model for an NI HTS Coil," *IEEE Trans. Appl. Supercond.*, vol. 31, no. 5, pp. 1–5, 2021.

[164] G. Kim *et al.*, "Analysis of Nonuniform Contact Resistivity Distribution on No-insulation HTS Racetrack Coil," *IEEE Trans. Appl. Supercond.*, vol. 33, no. 5, pp. 1–5, 2023.

[165] F. Liang *et al.*, "A Finite Element Model for Simulating Second Generation High Temperature Superconducting Coils/stacks with Large Number of Turns," *J. Appl. Phys.*, vol. 122, no. 4, 2017.

[166] F. Huber, W. Song, M. Zhang, and F. Grilli, "The TA Formulation: an Efficient Approach to Model the Macroscopic Electromagnetic Behaviour of HTS Coated Conductor Applications," *Supercond. Sci. Technol.*, vol. 35, no. 4, p. 043003, 2022.

초 록

입자 가속기는 가까이는 암치료를 위해, 보다 멀리서는 입자 물리학을 비롯한 첨단과학의 연구를 위해 사용되어 우리의 삶과 밀접하게 연결되어 있다. 세계 각국은 기존의 입자 가속기 성능을 높이거나 새로운 장치를 만들기 위한 기술 개발을 수행하고 있다. 대표적인 사례로 유럽의 CERN이 운영하고 있는 대형 강입자 충돌기는 질량을 매개하는 힉스 보존을 검출하는데 성공했으며, 표준 모형을 비롯한 현대물리학의 비밀을 파헤치기 위해 고휘도 대형 강입자 충돌기의 개발을 진행하고 있다. 입자 가속기가 다루는 입자 빔은 전자, 양성자, 중이온 등이 존재하며, 이들을 목적에 맞게 제어하기 위해서는 운전 조건에 일치하는 위치와 속도를 유지시키기 위한 장치가 필요하다. 전하를 갖는 입자를 제어할 수 있는 대표적인 방식은 자기장이 가하는 로렌츠힘을 이용하는 것이다. 따라서 입자 가속기에는 높은 자기장을 갖는 자석이 이용되고 있다. 현재까지는 주로 1 T 수준의 상대적으로 낮은 자기장 영역에 대해서는 상전도 구리 자석, 더 높은 자기장 영역에 대해서는 NbTi 저온초전도 자석이 이용되었으며 최근에는 Nb_3Sn 저온초전도 자석 위주로 개발되고 있다. 또한, 가속기의 성능을 높이기 위해 자석의 자기장을 높여야하므로 고온초전도 자석을 적용하려는 시도가 등장하고 있으나 아직은 초기 단계에 머물고 있어 연구가 필요하다.

기존에도 고온초전도체인 REBCO 선재를 이용해 가속기를 위한 이극 자석을 개발하려는 시도가 이루어진 바 있다. 하지만 무절연 기술을 적용하여 이극 자석을 개발한 사례는 없었다. 이극 자석의 복잡한 형상으로 인한 제작의 어려움과 무절연 자석의 전류 우회 특성이 야기하는 자기장 균일도의 불안정성으로 인해 무절연 자석을 사용하는 것이 어려웠다. 또한, 실제 응용분야에 대한 자석 개발로 이어지기

위해서는 고온초전도 선재에서 발견되고 있는 여러 어려움들이 먼저 해결되어야 한다. 대표적으로 REBCO 선재를 통해 만든 자석의 임계전류를 예상하는 것부터 어려움이 존재한다. 입사되는 자기장의 세기뿐만 아니라 입사각도에 의해서도 임계전류가 바뀌는 특성으로 인해 선재의 폭방향으로도 임계전류의 분포가 크게 발생할 수 있으며, 이는 자석의 설계와 운전을 어렵게 만든다. 무절연 자석에서 발생하는 차폐전류, 기계적 응력, 퀜치 현상 등의 문제 역시 해결이 요구되는 연구 주제들이다.

본 연구에서는 무절연 고온초전도 기술을 이용한 이극 자석의 입자 가속기에의 적용 가능성에 대해 논의하였다. 이를 위하여 기존에 제시된 자석 해석 모델을 개선하거나, 새로이 모델을 개발하여 자석의 설계와 해석에 적용하였다. 본 연구는 크게 1) 해석 모델 개발, 2) 이극 자석 설계, 제작, 운전, 3) 측정 결과 및 자기장 균일도 개선으로 구성되었다. 이극 자석이 갖는 안장 형상으로 인해 기존의 유한요소법 기반의 차폐전류 해석이 어려우므로 분산회로 모델을 적용하기 위해 회로 해석 기법, 인덕턴스 계산 속도 향상법, 3차원 자기장 해석 기법의 모델을 개발하였다. 고온초전도 선재의 임계전류 문제를 해결하기 위해 최초로 표준데이터를 정의하고 폭방향 평균기법을 제시하여 실험을 통해 검증하였다. 무절연 이극 자석의 성능과 개발된 모델을 검증하기 위하여 중심 자기장 0.7 T 자석을 설계하고 권선 및 조립 기법을 개발하여 자석을 제작하였으며, 자석 냉각을 위한 전도 냉각 시스템과 자기장 균일도 측정을 위한 매핑 시스템을 구축하였다. 이러한 장치들을 이용해 무절연 이극 자석을 최초로 성공적으로 운전하고 목표한 중심 자기장이 도출됨을 검증하였다. 자기장 균일도 측정 실험을 진행하여 해석 모델과 비교하여 오차를 분석하였고, 측정된 자기장 균일도를 개선하기 위해 페로심(ferroshim) 기법을 도입하여 설계하고 제작하여 균일도가 개선됨을 확인하였다. 마지막으로 실제 고자기장 무절연 고온초전도 이극 자석 개발을 위한 개선점과 추가 연구의 필요성을 정리하였다.

주요어: 고온초전도, 무절연 권선법, 입자 가속기, 안장형 자석, 이극 자석

학번: 2020-27571